Department of Exploration Geophysics

Effect of Fluid Distribution on Compressional Wave Propagation in Partially Saturated Rocks

Julianna J Toms

This thesis is presented for the Degree of
Doctor of Philosophy
of
Curtin University of Technology

April 2008

Declaration

To the best of my knowledge and belief this thesis contains no material previously published by any other person except where due acknowledgment has been made.

This thesis contains no material which has been accepted for the award of any other degree or diploma in any university.

Signature:

Date: 3 June 2008

For

Neville Toms

Acknowledgements

Firstly I would like to thank sincerely my supervisor Boris Gurevich for his assistance, guidance and support. Without his knowledge and valuable input my PhD would not be half the document it is.

I would like to thank Tobias Müller for his assistance and input into my research. I have enjoyed our technical discussions and collaborations.

I am very grateful to Lincoln Paterson and Greg Lupton for allowing me to use their X -ray tomographic images of partially saturated rock. These images have provided much stimulus for my research work.

Thanks are extended also to Dave Johnson for providing insight and technical discussion on the topic of patchy saturation.

Thank you Radim Ciz for code, collaborations and technical discussions.

For this study I was under the financial support of CSIRO studentship and WACUPS scholarships, for this I would like to thank CSIRO and CSIRO Petroleum. Thank you to Kevin Dodds and Milovan Urosevic who recognized my potential and supported my scholarship applications.

I would like to thank Deirdre Hollingsworth and Robert Verstandig for assistance in administration and IT areas, which seem all too hard at times.

To the many friends I have made both inside and outside the department, thank you for keeping my spirits high and making me feel welcome.

To my husband Colin Stewart, thank you for weathering the PhD storm in good humour.

Finally, I would like to acknowledge my father Neville Toms for his thoughtfulness, generosity, encouragement and sacrifices. Thank you for sparking my intellectual curiosity early on and supporting my many and varied academic pathways.

Thank you all for making this possible.

Julianna

Table of Contents

1. Introduction, Basic Theory and Thesis Overview

2. Fluid Distribution from Saturation Experiments on Porous Rock

3. Patchy Saturation Models for Complex and Irregular Fluid Distribution

4. Extension of the APS Framework

5. Numerical Analysis of APS Shape Parameter

6. Conclusions

List of Figures

List of Tables

Abstract

Partial saturation of porous rock by two fluids substantially affects compressional wave propagation. In particular, partial saturation causes significant attenuation and dispersion due to wave-induced fluid flow. Such flow arises when a passing wave induces different fluid pressures in regions of rock saturated by different fluids. When partial saturation is mesoscopic, i.e. existing on a length scale much greater than pore scale but less than wavelength scale, significant attenuation can arise for frequencies 10-1000 Hz. Models for attenuation and dispersion due to mesoscale heterogeneities mostly assume fluids are distributed in a regular way. Recent experiments indicate mesoscopic heterogeneities have less idealised distributions and distribution affects attenuation/dispersion. Thus, theoretical models are required to simulate effects due to realistic fluid distributions.

The thesis focus is to model attenuation and dispersion due to realistic mesoscopic fluid distributions and fluid contrasts. First X-ray tomographic images of partially saturated rock are analysed statistically to identify spatial measures useful for describing fluid distribution patterns. The correlation function and associated correlation length for a specific fluid type are shown to be of greatest utility. Next a new model, called 3DCRM (CRM stands for continuous random media) is derived, utilizing a correlation function to describe the fluid distribution pattern. It is a random media model, is accurate for small fluid contrast and approximate for large fluid contrast. Using 3DCRM attenuation and dispersion are shown to depend on fluid distribution.

Next a general framework for partial saturation called APS (acoustics of partial saturation) is extended enabling estimation of attenuation and dispersion due to arbitrary 1D/3D fluid distributions. The intent is to construct a versatile model enabling attenuation and dispersion to be estimated for arbitrary fluid distributions, contrasts and saturations. Two crucial parameters within APS called shape and frequency scaling parameters are modified via asymptotic analysis using several random media models (which are accurate for only certain contrasts in fluid bulk moduli and percent saturation). For valid fluid contrasts and saturations, which satisfy certain random media

conditions there is good correspondence between modified APS and the random media models, hence showing that APS can be utilized to model attenuation and dispersion due to more realistic fluid distributions.

Finally I devise a numerical method to test the accuracy of the analytical shape parameters for a range of fluid distributions, saturations and contrasts. In particular, the analytical shape parameter for randomly distributed spheres was shown to be accurate for a large range of saturations and fluid contrasts.

Chapter 1

Introduction, Basic Theory and Thesis Overview

1.0 Introduction

Partial saturation of porous rock by two or more different fluids can occur in a multitude of geological settings. For instance, gas, oil and brine commonly share the available pore-space in the upper part of gas capped reservoirs. Underground aquifers can become infiltrated by contaminating fluids. Earthquake events can induce ground water variations and in turn; aftershocks have been linked to changes in pore fluid distribution. In order to better assist the interpretation of seismic data acquired for the purposes of detecting hydrocarbons, monitoring or tracking saltwater intrusions into ground water aquifers, or for analysing recorded waveforms from earthquake events, knowledge of how partial fluid saturation affects elastic wave propagation is required.

The propagation of elastic waves in fluid saturated porous media is usually described by Biot’s equations of poroelasticity (Biot 1956a; 1956b; 1962). In the low-frequency (static) limit these equations yield the so-called Gassmann’s equation (Gassmann 1951), which expresses the undrained static bulk modulus of the porous medium as a function of the properties of the dry frame and the saturating fluid. Both Biot’s and Gassmann’s equations assume that the porous medium is saturated with a single Newtonian fluid (liquid or gas).

Extending Biot-Gassmann theory to model wave propagation in porous media saturated by two or more immiscible fluids is not trivial. Immiscibility implies that the fluids are not dissolved into one another and a distinct fluid-fluid interface exists which separates each fluid (Bear 1988). When two immiscible fluids are distributed on a relatively fine scale, they can be regarded as a single composite fluid whose compressibility (inverse of bulk modulus) is given by an average of its constituent compressibilities (using the so-called Wood equation (Wood 1941)). In this circumstance, Gassmann’s equation can be applied to determine an effective bulk modulus of the porous medium, in which the fluid bulk modulus is now given by the composite average. This case is often referred to as uniform saturation, and implies full pressure equilibration between the two fluids.

This pressure equilibration can only be achieved if the frequency is sufficiently low so that the characteristic length of fluid diffusion in the pore-space is large compared to the largest spatial scale of fluid mixing. If the frequency is higher, the pressure in the two fluids will not have enough time to equilibrate, resulting in a higher undrained bulk modulus and wave velocity. Hence, the presence of two fluids in the pores (so called partial saturation) causes an additional dispersion and attenuation of elastic waves, which is related to relaxation of pore fluid pressures. The frequency dependency of wave velocity and attenuation in a partially saturated medium is controlled by the size, shape and spatial distribution of fluid pockets and permeability and elastic moduli of the solid matrix as well as the properties of the two fluids.

In the last 30 years a numbers of models have been introduced that correspond to different spatial configurations of fluid pockets. Most of these models assume regular fluid patterns such as a cubic lattice of gas pockets of a fixed shape in a liquid-saturated background medium (White 1975; Johnson 2001; Pride et al. 2004). However, spatially regular distribution of the fluids may not always give an adequate representation of the real distribution. Moreover, it has been shown (Gurevich & Lopatnikov 1995; Müller & Gurevich 2004) that random and periodic 1D distributions of two different fluids yield very different attenuation/dispersion pairs. Although 1D alternating fluid distributions may not be realistic, this result gives an additional motivation to studies of wave propagation in porous media with random spatial fluid distributions. Recent results show that this approach is promising (Ciz et al. 2005; Ciz et al. 2006; Toms et al. 2006).

1. 1 Elastic Wave Propagation in Fully Fluid Saturated Porous Media

Biot's equations of dynamic poroelasticity (Biot 1956a; 1956b; 1962) provide a general framework for modelling elastic wave propagation through porous fluid saturated media. The equations were derived using a Lagrangian view point with generalised coordinates given by the average solid and fluid displacements. A dissipation function was introduced, which depended only upon relative solid and fluid motion. Subsequently, Biot's equations have been rederived using a number of different mathematical techniques, such as volume averaging methods (Pride et al. 1992) and homogenization for periodic structures (Levy 1979; Auriault 1980; Burridge & Keller 1981). All of these methods yield exactly the same macroscopic equations, thus confirming the validity of Biot's original formulation.

The basic assumptions of Biot's equations (Biot 1956a; 1956b; 1962) are:

I) The porous rock frame is homogeneous and isotropic. It has uniform porosity ϕ, bulk modulus K_d, shear modulus μ_0, density ρ_0 and permeability κ, and consists of only one grain type, characterized by bulk modulus K_g, shear modulus μ_g and density ρ_g.

II) The porous rock is fully saturated by only one fluid having viscosity η, fluid bulk modulus K_f, and density ρ_f.

III) Relative motion between solid and fluid is governed by Darcy's law.

IV) The wavelength of the passing wave is substantially larger than the size of the largest grains or pores.

Biot's wave equations describing average solid ***u*** and fluid displacement ***U*** can be written in the frequency domain (with time dependence $\exp(-i\omega t)$ implied) as (Biot 1962)

$$(H-\mu)\,\mathrm{grad}\,\mathrm{div}\,\mathbf{u}+\mu\nabla^2\mathbf{u}+\alpha M\,\mathrm{grad}\,\mathrm{div}\,\mathbf{w}+\omega^2\left(\rho\mathbf{u}+\rho_f\mathbf{w}\right)=0\,, \qquad (1.1.1)$$

$$\alpha M\,\mathrm{grad}\,\mathrm{div}\,\mathbf{u}+M\,\mathrm{grad}\,\mathrm{div}\,\mathbf{w}+\omega^2\left(\rho_f\mathbf{u}+q\mathbf{w}\right)=0\,, \qquad (1.1.2)$$

where $\mathbf{w} = \phi(\mathbf{U} - \mathbf{u})$ represents the average fluid displacement relative to the solid, $\rho = (1-\phi)\rho_g + \phi\rho_f$ is the density of the porous fluid-saturated rock, $\alpha = 1 - K_d / K_g$ is so called the Biot-Willis coefficient (Biot & Willis 1957), and H, μ, and M are material properties (defined later in this section page 6). Parameter $q(\omega)$ is a frequency-dependent coefficient responsible for viscous and inertial coupling between the solid and fluid motion, and is given by

$$q = \rho_f \left[\frac{\chi}{\phi} + \frac{i\eta}{\kappa^*(\omega)\omega\rho_f} \right]. \tag{1.1.3}$$

Here $\chi \geq 1$ is the tortuosity, a dimensionless parameter which is responsible for inertial coupling between solid and fluid motion and $i = \sqrt{-1}$. The parameter κ^* is the dynamic hydraulic permeability, which in general, is frequency-dependent and responsible for viscous coupling. For sufficiently low frequencies (lower than Biot's characteristic frequency $f_c = \phi\eta / (2\pi\kappa\rho_f)$), fluid flow within the pore channels can be regarded as Poiseuille flow. This means that the flow is laminar (i.e. the Reynolds number of the flow which expresses the ratio of inertial forces to viscous forces, is less than a critical Reynolds number (Bear 1980)). In this case the first bracketed term in the right-hand side of (1.1.3) can be neglected (Bourbie et al. 1987) and the dynamic permeability reduces to the steady-state permeability κ, giving

$$q = \frac{i\eta}{\kappa\omega}. \tag{1.1.4}$$

For most rocks and soils Biot's characteristic frequency f_c turns out to be about 10^5 Hz or higher. Therefore, for most seismic and acoustic applications the low-frequency version of Biot's theory is adequate.

For a homogeneous porous medium equations (1.1.1) and (1.1.2) form a system of six linear partial differential equations with constant coefficients for six components of two vector-functions **u** and **w**. By considering a solution of these equations dependent upon only one coordinate, say *x*, we can reduce equations (1.1.1) and (1.1.2) to a system of six second-order linear ordinary differential equations with one independent variable x. The equations for u_y, u_z, w_y, and w_z describe the propagation of two identical shear modes with two orthogonal polarisations. These shear waves are very similar in nature to classical shear waves in an isotropic viscoelastic medium. The remaining system of two equations for u_x, w_x has a solution of the form

$$\begin{pmatrix} u_x \\ w_x \end{pmatrix} = \begin{pmatrix} u_{x0} \\ w_{x0} \end{pmatrix} \exp(ikx), \tag{1.1.5}$$

where wavenumber k is the root of its characteristic equation, that is, an eigenvalue of the linear algebraic system obtained by substituting (1.1.5) into (1.1.1) and (1.1.2). The characteristic equation is quadratic in k^2, and thus yields two pairs of complex roots $\pm k_+$ and $\pm k_-$. This shows that in a porous medium there exist two types of compressional waves with complex velocities $v_{+,-} = \omega / \mathrm{Re}\{k_{+,-}\}$ and attenuation factors (inverse quality factors) $Q^{-1}_{+,-} = \mathrm{Im}\{k^2_{+,-}\} / \mathrm{Re}\{k^2_{+,-}\}$.

The compressional waves are termed fast (+) and slow (-) *P*-waves and occur when solid and fluid particle motion is in phase or out of phase, respectively. The fast wave is a direct analog of the normal compressional wave in an elastic or viscoelastic solid; it exhibits small amounts of attenuation and phase velocity dispersion (see Figure 1.1.1). On the other hand, the slow *P*- wave behaves very differently at low and high frequencies. At low frequencies $f << f_c$, the wavenumber of the slow *P-wave* is given by $k_-^2 = i\omega\eta / \kappa N$ where $N = ML/H$. In this frequency regime, the slow *P-wave* is highly attenuated and is analogous to diffusion or heat conduction. On the other hand, at high frequencies $f >> f_c$ the slow *P*-wave is propagatory with the propagation velocity approaching $c_f \chi^{-1/2}$, where c_f is sound velocity in the free fluid.

For frequencies less than Biot's characteristic frequency, the fast *P* and shear wave numbers are given by (Berryman 1998)

$$k_+^2 = \frac{\omega^2}{v_+^2}\left(1+\frac{i}{Q_+}\right), k_s^2 = \frac{\omega^2}{v_s^2}\left(1+\frac{i}{Q_s}\right), \tag{1.1.6}$$

where $v_+ = \sqrt{H/\rho}$ is the fast *P-wave* velocity and $v_s = \sqrt{\mu/\rho}$ is the shear wave velocity. In this frequency range the attenuation (inverse quality factors) for fast *P* and shear waves are $Q_+^{-1} = \omega\kappa\rho_f\left(1-v_0^2/v_+^2\right)^2/\eta\rho$ and $Q_s^{-1} = \omega\kappa\rho_f/\eta\rho$, where $v_0 = \sqrt{\alpha M/\rho_f}$. Parameter H that appears in the expression for the fast *P-wave* velocity v_+ is called the saturated *P-wave* modulus, and can be written as $H = K + 4\mu/3$, where K and μ are the undrained bulk and shear moduli of the fluid-saturated porous medium given by the equations:

$$K = K_d + \alpha^2 M, \tag{1.1.7}$$

$$M = \left[(\alpha-\phi)/K_g + \phi/K_f\right]^{-1}, \tag{1.1.8}$$

$$\mu = \mu_0, \tag{1.1.9}$$

where the analogous P-wave modulus for a dry medium is given by $L = K_d + 4\mu_0/3$.

Equations (1.1.7) - (1.1.9) have first been derived by Gassmann (1951) and are referred to as Gassmann's equations. For Gassmann's equations to be applicable, several conditions must be met. The pore-space within the rock must be connected so that pore fluid can achieve equilibration. Thus, fluid pressure effects due to isolated pore-spaces are not accounted for. Furthermore, the frequency must be sufficiently low, so that, fluid pressures induced by a passing wave have enough time for pressure equilibration.

In essence, Gassmann's equations define elastic wave velocities in fluid saturated porous media in the low frequency limit. These equations are widely used in the petroleum industry for estimating seismic wave velocities in hydrocarbon reservoirs (Wang 2001; Smith 2003). However, in general, seismic wave propagation often violates the quasi-static assumption, causing deviations from Gassmann's results. In particular, wave attenuation and phase velocity dispersion cannot be modelled with Gassmann's equation. To account for these effects Biot's theory is often utilized.

Wave attenuation and phase velocity dispersion within Biot type media is caused by global or macroscopic fluid flow, which is called "Biot's loss". It occurs when pore fluids develop spatial gradients in fluid pressure induced over the wavelength of an incident compressional wave. This drives fluid flow relative to the rock frame, causing wave energy to be lost through viscous dissipation.

Although Biot's theory provides a mechanism for the dissipation and dispersion of elastic waves, it is generally accepted that it cannot adequately explain observed magnitudes of attenuation and dispersion, especially within the low frequency regime (Johnston et al. 1979; Winkler 1985; Gist 1994; Bukingham 2000). However, it is widely accepted that Biot's theory is correct in predicting the existence of the slow *P*-wave. It has been confirmed by a number of laboratory experiments (Plona 1980; Nagy et al.. 1990; Kelder & Smeulders 1997).

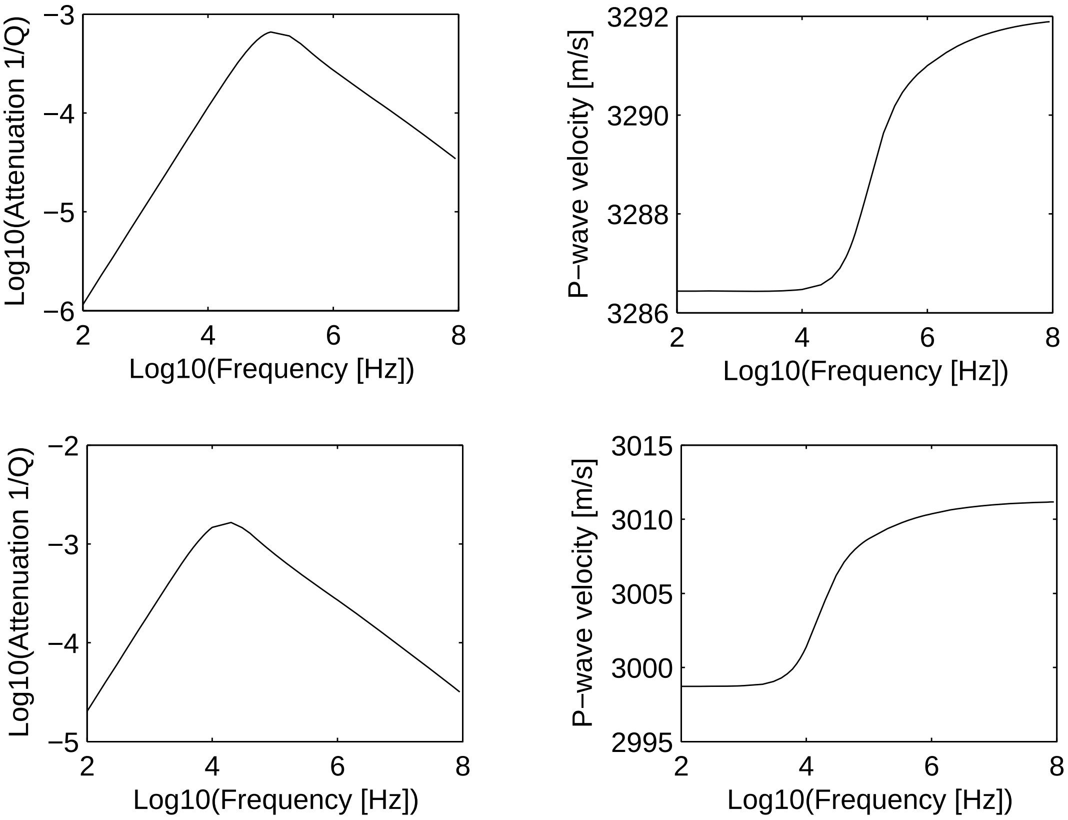

Figure 1.1.1: Biot's attenuation (inverse quality factor) and dispersion for porous rock containing different fluids. (Top) 100 % water saturated and (bottom) 100% heavy gas saturation of porous rock. Very modest amounts of attenuation and dispersion are predicted at high frequencies using Equations 1.1.6.

1.2 Elastic Wave Propagation in Partially Fluid Saturated Porous Media

Partial fluid saturation of porous rock by multiple types of pore fluids was first proposed as a cause for the mismatch between experimental measurements of attenuation and phase velocity dispersion, and theoretical predictions given by Biot's theory (Biot 1956a; 1956b; 1962). JE White and his co-authors were the first to show theoretically that partial fluid saturation can cause significant attenuation and phase velocity dispersion (White 1975; White et al. 1976). Experimental studies conducted around the same time (Domenico 1976; Gregory 1976) also indicated that partial fluid saturation of porous rock causes different phase velocity behaviour then fully saturated porous rock.

Since 1970s, the study of elastic wave propagation in partially fluid saturated media has become a field of interest in its own right, generating a number of experimental (Gist 1994; Murphy 1984; 1985; Cadoret et al. 1995; Cadoret et al. 1998), numerical (Dutta & Ode 1979a; Dutta & Ode 1979b; Dutta & Seriff 1979; Carcione et al. 2003; Helle et al. 2003) and theoretical studies designed to elucidate key features that cause attenuation and phase velocity dispersion.

There are a number of different approaches to theoretically modelling attenuation and dispersion due to the presence of partial fluid saturation. Each approach emphasizes a particular physical aspect, thought to significantly affect attenuation and dispersion estimates. Broadly speaking, most approaches focus on:

I) Porescale distribution of immiscible fluids: These models are often called local or “squirt” flow models (Mavko & Nur 1979; Palmer & Traviola 1980; Murphy et al. 1986; Jones 1986). Attenuation and phase velocity dispersion arise due to fluid flow occurring between gas and liquid filled areas of the same pore or crack.

II) Mesoscale distribution of immiscible fluids: fluid heterogeneities occur on the scale greater than the pore scale, but less than wavelength scale. Fluid heterogeneities can be modelled using a periodic distribution (White 1975; Johnson 2001; Pride et al. 2004; White et al. 1976) or a random distribution (Müller & Gurevich 2004; Ciz et al. 2005; Toms et al. 2005). Attenuation and phase velocity dispersion arises due to induced pressure gradients on the mesoscale, which causes fluid to flow.

III) Defining an effective pore fluid: incorporating free bubble oscillations (Bedford & Stern 1982; Lopatnikov & Gorbachev 1987; Smeulders & van Dogen 1997; Aurialt et al. 2002). Attenuation can arise due to viscous and thermal damping, which occurs when the free gas bubble oscillates in response to pressure fluctuations in the surrounding pore liquid.

There are many different types of porous rocks, such as sandstones, limestones, shales etc, which are often saturated by different combinations of pore fluids, such as water, oil and gas. As such, in some situations, one theoretical approach may be more applicable than another.

Category I models are good for situations where porous rocks are known to contain a large number of very compliant grain contacts or cracks. This becomes especially important for laboratory studies where rock samples have undergone distortion due to removal from in situ conditions, which can either induce fracturing on the grain scale or cause the opening of otherwise closed grain contacts, due to changes in confining pressure (Pride et al. 2004). Furthermore, certain rock samples or in situ rocks which contain significant grain-scale heterogeneities are also suitable, such as with carbonate rocks which possess both intergranular and intragranular porosity (Assefa et al. 1999) or for sandstones having either imperfectly cemented grain contacts (Murphy et al. 1986) or an assemblage of smaller irregularly shaped intra-pore minerals (Best et al. 1994).

In those circumstances, wetting fluids like water preferentially saturate grain contacts and cracks, whilst non-wetting fluids like gas assume larger rounder pore-spaces (Murphy et al. 1986). In response to a passing wave, spatial gradients in fluid pressure develop which cause fluid to flow between grain cracks, contacts etc and rounder pore-spaces. This occurs because cracks, contacts etc are more compliant (mechanically weaker) than rounder pore-spaces.

This type of pore scale fluid flow also known as local (or squirt) flow causes attenuation and phase velocity dispersion. The reason is that when wave frequencies are sufficiently low, there is enough time for fluid to flow between grain cracks into surrounding pores etc, whilst at higher frequencies there isn't sufficient time. This means that a porous rock at lower frequencies is less stiff than at higher frequencies resulting in lower wave velocities. At intermediate wave frequencies, phase velocity is frequency-dependent and attenuation is a maximum.

A possible limitation of most squirt flow models is that they assume specific pore scale geometries. In particular, Murphy et al. (1986) assumes that the grain contact is perfectly flat and adjacent to a spherical pore, whilst Mavko and Nur (1979) model a multitude of idealised geometries, such as flat, triangular and parabolic pore shapes. Thus appropriate application of these models requires knowledge of rock characteristics on the pore scale, which isn't always available, certainly for in situ applications. However, the increasing use of X-ray microtomographic imaging (Arns et al. 2004) with numerical algorithms (Arns et al. 2002; Saenger et al. 2007) that compute elastic properties from porescale images of real rock, will provide a direct means of relating elastic properties to pore structure. Hence, these studies may serve to improve our understanding of squirt flow mechanisms etc and thus provide direction on how squirt flow models for certain rock types should be framed.

As it is well known that bubbles affect the acoustic properties of a liquid (Silberman 1957; van Wijngaarden 1972; Commander & Prosperetti 1989), category III models are best suited to applications where fluid-fluid interaction is considered important. In a free liquid the presence of bubbles has two interconnected effects on the acoustic properties of the liquid, which can also affect wave propagation when that fluid saturates porous rock.

Firstly, the presence of bubbles affects the compressibility of the liquid; this changes the propagation velocity of waves. Secondly, pressure fluctuations within the liquid stemming from wave propagation, forces bubbles to oscillate about their equilibrium radius. This causes attenuation, as wave energy is transferred into energy which drives bubble oscillations. As sound wave attenuation has a maximum at the resonant frequency of the bubble, it is anticipated that these models will be of most use at high frequencies, as the resonant frequency of the bubble is inversely proportional to bubble radius which is typically small (Silberman 1957).

On the other hand, category II models are best suited to applications where wave frequencies are low and the porous rock is saturated by relatively large (mesoscopic) fluid patches. For the rest of this Chapter, I will focus only on category II models; however I wish to acknowledge that both category I and category III models are important.

1.2.1 Mesoscopic Distribution of Fluids

Fluid heterogeneities existing on a scale which is greater than pore scale, but less than wavelength scale are called mesoscopic. A mesoscopic distribution of two pore fluids can arise due to variations in porosities, permeabilities and grain types within a porous rock. These features will cause pore fluids to be preferentially located in different positions, e.g., in a way shown in Figure 1.2.1.1

On the pore scale, numerical studies (Knight et al. 1990; Silverstein & Fort 2000a; 2000b; 2000c; Berkowitz & Hansen 2001) have shown that water preferentially locates in grain contacts and smaller pore-spaces, whilst gas prefers larger rounder pore-spaces. Presumably, the same physics which dictates fluid distribution on the pore scale, such as minimization of interfacial surface area, between grains and fluids, and fluids and fluids, history of fluid saturation, processes of fluid saturation, wettability of the rock, capillary effects etc will also influence fluid distribution on the mesoscale, in addition to gravitational forces which leads to the separation of fluids that have significantly different densities (i.e reservoir scale-gas cap rocks).

Mesoscopic fluid distributions have been observed in recent experiments (Cadoret et al. 1995; 1998; Monsen & Johnstad, 2005). In these studies, clusters or patches of different pore fluids are distributed throughout the porous rock samples. These experiments have revealed that the shape and distribution of mesoscopic fluid patches depends upon the degree of saturation and also upon the process of fluid saturation.

X-ray tomographic images of Cadoret et al. (1995) show that imbibition experiments, where water displaces gas, produce more or less regular patches of fluids distributed uniformly throughout the porous rock at high water saturations, whilst drainage or evaporative experiments, where the reverse fluid substitution process occurs, produce gas clusters distributed non-uniformly through out the porous rock at high water saturations.

As drainage and imbibition produce different saturation patterns at the same level of saturation, differences in attenuation and phase velocity measurements have been attributed to differences in fluid distribution. Moreover, phase velocities measured from drainage experiments are appreciably higher than those from imbibition experiments (Cadoret et al. 1995; Knight & Nolen-Hoeskema 1990) and differences between attenuation values have also been observed (Cadoret et al. 1998). Hence, estimates of attenuation and phase velocity are affected by the distribution of immiscible fluids.

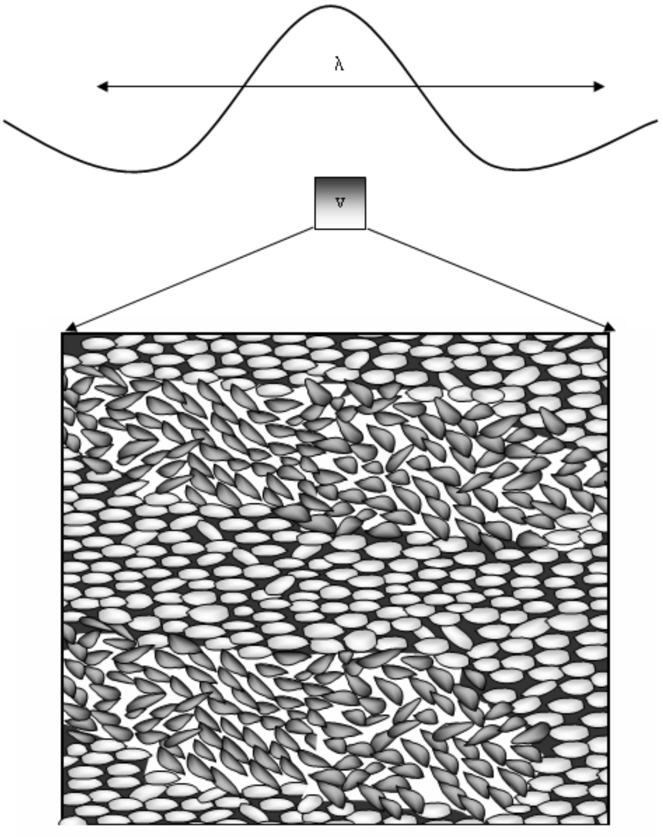

Figure 1.2.1.1: Mesoscale distribution of two different pore fluids within a porous rock having lithological variations. The scale of fluid heterogeneities is greater then pore scale, but much less then wavelength scale

1.2.2 Low and High Frequency Elastic Moduli

In response to a passing compressional wave, the porous framework of grains is compressed and rarefied on time scales imposed by the wave speed. When spatial heterogeneities in saturating fluids (and/or rock properties) exist, the compression or rarefaction of the frame causes spatial gradients in fluid pressure to develop. Providing that heterogeneities exist on length scales less than a wavelength, but greater than pore scale, gradients in fluid pressure develop on the mesoscale. This drives the so called mesoscopic fluid flow, which causes the attenuation of elastic energy and the dispersion of a propagating wave form.

In the limiting cases of very low and very high wave frequencies, theoretical values of phase velocities can be determined. For intermediate wave frequencies, phase velocities are frequency-dependent and lie between these limiting values. Following Mavko and Murkerji, (1998), Johnson (2001), Müller and Gurevich (2004), the upper and lower-frequency limits on phase velocities are presented below.

For a porous rock having only heterogeneities in saturating fluids, Norris (1993) has shown that the distribution of fluid pressures is governed by the diffusion equation with a diffusion length of

$$\lambda_d = \sqrt{\frac{\kappa N}{\omega \eta}} ,$$

where $N = ML/H$, ω is wave frequency, and L and H are *P-wave* moduli of the dry and fluid-saturated rock, respectively.

When the frequency ω of the incident wave is sufficiently low and the characteristic patch size of fluid heterogeneities is less then the diffusion length λ_d , there is enough time for fluid to flow and equilibrate at a constant pressure. In this limit, Wood's law (Wood, 1941) can be applied to determine an effective fluid bulk modulus K_f given by,

$$K_W^{-1} = S_1/K_{f1} + S_2/K_{f2} , \tag{1.2.2.1}$$

where S_1, S_2 are volume concentrations of fluids having bulk moduli K_{f1}, K_{f2}.

Once the effective bulk modulus of the pore fluid is defined, Gassmann's relations (1.1.7)-(1.1.9) can be applied to estimate the low-frequency phase velocity for a partially fluid saturated rock (Figure 1.2.2.1). This quasi-static limit is known as uniform saturation or Gassmann-Wood limit.

Conversely, when the wave frequency ω is sufficiently high, and the characteristic patch size is larger than the diffusion length λ_d, there isn't enough time for pressure equilibration and fluid flow effects can be ignored. In this circumstance, patches of rock will remain at different pressures. Then, application of Gassmann's theory on individual patches allows the saturated bulk modulus of each patch to be determined. According to Gassmann's equation (1.1.9), the saturated shear modulus of each patch is independent of fluid bulk modulus. Thus Hill's theorem (Hill 1963) can be applied to determine the overall saturated bulk modulus:

$$[K_H + 4\mu/3]^{-1} = S_1/(K_1 + 4\mu/3) + S_2/(K_2 + 4\mu/3), \qquad (1.2.1.2)$$

Where K_1 and K_2 are the saturated bulk moduli determined by applying Gassmann's theory on each fluid patch (Figure 1.2.2.1). This high-frequency or no-flow limit is known as patchy or Gassmann-Hill limit.

The elastic moduli in both the low- and high frequency limits are given by real numbers and are frequency independent. Johnson (2001) has shown that 1) for any non-zero saturation the homogeneous moduli are always smaller than those for patchy saturation, and 2) at intermediate frequencies the bulk modulus lies between these limits. Thus for any intermediate saturation level the partially fluid saturated rock exhibits frequency-dependent phase velocity.

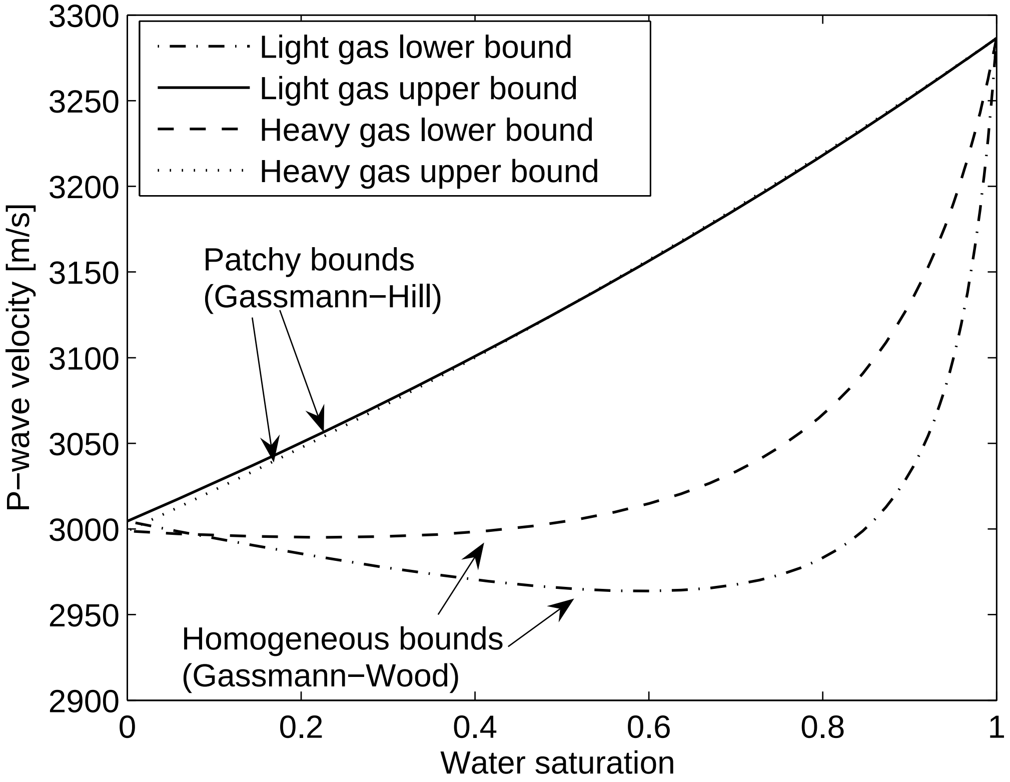

Figure 1.2.2.1: Lower and upper bounds on P-wave velocities for partially water saturated porous rocks with light gas or heavy gas inclusions.

1.3. Regular Cell Models

1.3.1 White's Models

There are a number of approaches to modelling attenuation and phase velocity dispersion due to mesoscopic fluid flow. Most approaches assume that heterogeneities in fluid content or lithology are distributed periodically throughout the porous medium. This approach was proposed by White et al. (1976) and White (1975), who were the first to illustrate that significant amounts of attenuation and phase velocity dispersion could arise from mesoscopic fluid flow. White et al. (1976) modelled fluid heterogeneities as periodically alternating layers of gas and water in a uniform solid frame. White (1975) modelled fluid heterogeneities as a periodic array of spherical gas inclusions, embedded within a water saturated rock having uniform frame properties, see (Figure 1.3.1.1).

In these approaches, an elementary composite volume consisting of porous rock saturated by each fluid is considered representative of the entire periodic system of fluid heterogeneities. In 1D, the representative volume spans the interface between different fluid layers from the centre of each layer. In 3D, the representative volume is spherical enclosing a single gas inclusion. See Figure 1.3.1.1.

In White et al. (1976) and White (1975), the frequency-dependent complex bulk modulus is derived by considering the ratio of the imposed pressure amplitude to the corresponding fractional change in volume (including effects of fluid flow). Later these models were recast using Biot's equations of dynamic poroelasticity (Biot 1962) for 1D periodic layering by Norris (1993) and for 3D spherical gas inclusions by Dutta and Ode (1979a; 1979b). These studies validated the conclusions that wave induced fluid flow causes attenuation and phase velocity dispersion, and demonstrated that Biot's theory of poroelasticity provides a powerful and versatile tool to study this phenomenon.

Recently, two more general models for patchy saturation have been developed which also utilize 3D regular patch geometries (Johnson 2001; Pride et al. 2004). These new models allow attenuation and phase velocity to be determined for arbitrary shaped fluid inclusions. However, explicit analytical expressions are only given for White’s periodic layering and concentric sphere geometries.

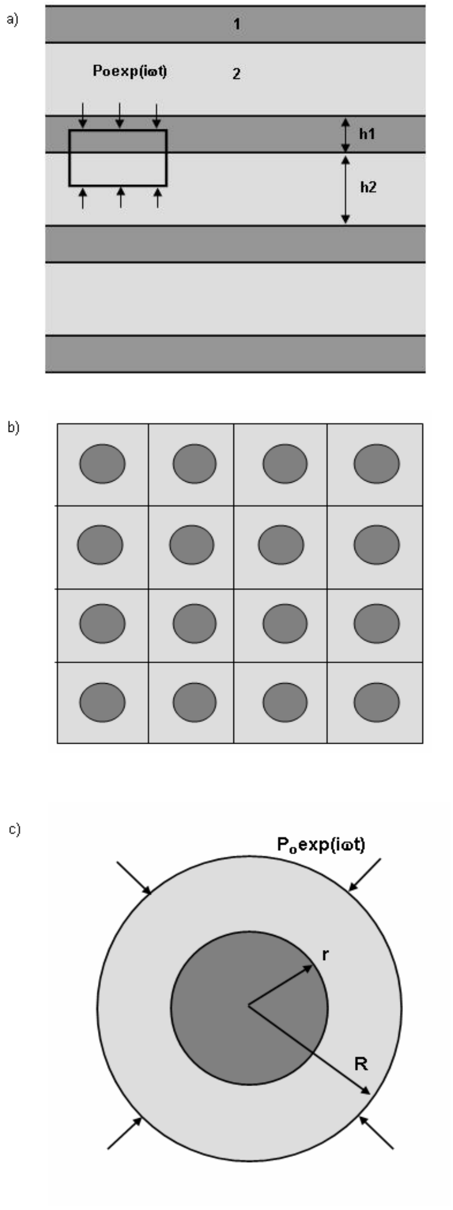

Figure 1.3.1.1: White’s periodic fluid distribution geometries. (a) Shows 1D periodic layering and its composite volume. (b) Shows spherical inclusions distributed in a 3D periodic array and (c) the composite volume used to approximate the 3D periodic array

1.3.2 The APS Framework -Johnson's Model

The Acoustics of Patchy Saturation (APS) model of Johnson (2001) will be utilized extensively in Chapters 4 and 5. Here I will give a precursory introduction, leaving the detailed discussions to subsequent chapters.

Johnson's APS (Acoustics of Patchy Saturation) approach was developed within the context of low-frequency Biot's theory. The dynamic bulk modulus $K(\omega)$ of a partially fluid saturated porous rock is developed by firstly considering its response to low and high wave frequencies (however where 'high frequency' is still assumed smaller than Biot's characteristic frequency $f_c = \phi\eta/(2\pi\kappa\rho_f)$).

When wave frequencies are sufficiently low, the rock is "relaxed" as fluid pressure is equilibrated. In this limit the low frequency asymptote of $K(\omega)$ converges to Gassmann-Wood limits (see Section 1.2.2),

$$K_J(\omega) = K_{BGW}\left[1 - i\omega T + o(\omega)\right]. \tag{1.3.2.1}$$

Here T is a parameter which depends on: percent fluid saturation, contrast between pore-fluid properties and fluid patch geometry. This parameter only has analytical solutions for very simple fluid distributions, such as White's concentric spheres, etc. The general expression for T is

$$T = \frac{\phi^2 K_{BGW}}{\kappa V}\int g(r)\Phi(r)dV \tag{1.3.2.2}$$

In Equation (1.3.2.2)

$$g(r) = \frac{\alpha\left(1/K_W - 1/K_f(r)\right)}{\alpha - \phi K_d\left(1/K_g + 1/K_W\right)} \tag{1.3.2.3}$$

where K_W is the effective fluid modulus given by Wood's law (Equation 1.2.2.1) and $K_f(r)$ is the fluid bulk modulus at some spatial position *r*, and $\Phi(r)$ is a solution to the potential equation:

$$\nabla \cdot \left[\frac{-1}{\eta(r)} \nabla \Phi \right] = g(r) \tag{1.3.2.4}$$

Here $\eta(r)$ is fluid viscosity at position *r*.

Equations (1.3.2.1) and (1.3.2.4) can only be analytically solved for simple fluid distributions. For periodic layering (Johnson, 2001):

$$T = \frac{K_{BGW}\phi^2}{6\kappa(L_1 + L_2)} \left\{ \eta_1 g_1^2 L_1^3 + 3\eta_1 g_1 g_2 L_1^2 L_2 + 3\eta_2 g_1 g_2 L_1 L_2^2 - \eta_2 g_2^2 L_2^3 \right\}, \tag{1.3.2.5}$$

where L_1 and L_2 are layer widths. In analogy to the concentric sphere model of White et al. (1976) and Johnson (2001); Krzikalla et al. (2006) derived the T coefficient for concentric circles in a two-dimensional medium (corresponding in 3D to circular cylinders):

$$T = \frac{K_{BGW}\phi^2}{8\kappa R_2{}^2} \left\{ \left[\eta_2 g_2^2 + 2g_1 g_2(\eta_1 - \eta_2) - \eta g_1^2 \right] R_1^4 - 2g_1 g_2 (\eta_1 - \eta_2) R_1^2 R_2^2 \right.$$
$$\left. + 4\eta_2 g_2 (g_1 - g_2) \ln\left(\frac{R_1}{R_2} \right) R_1^2 R_2^2 - \eta_2 g_2^2 R_2^4 \right\}, \tag{1.3.2.6}$$

where R_1 and R_2 are radii for the inclusion and host. For the concentric sphere model (Johnson, 2001):

$$T = \frac{K_{BGW}\phi^2}{30\kappa R_2^3} \left\{ \left[3\eta_2 g_2^2 + 5(\eta_1 - \eta_2) g_1 g_2 - 3\eta_1 g_1^2 \right] R_1^5 - 15\eta_2 g_2 (g_2 - g_1) R_1^3 R_2^2 \right.$$
$$\left. + 5g_2 \left[3\eta_2 g_2 - (2\eta_2 + \eta_1) g_1 \right] R_1^2 R_2^3 - 3\eta_2 g_2^2 R_2^5 \right\}. \tag{1.3.2.7}$$

Conversely, when wave frequencies are sufficiently high, the rock is “unrelaxed” as fluid pressures are unequilibrated. In this limit, the high frequency asymptote of $K(\omega)$ converges to Gassmann-Hill limit (see Section 1.2.2), leading to an expansion of the form

$$K_J(\omega) = K_{BGH}\left[1 - G(-i\omega)^{-1/2} + o\left(\omega^{-1/2}\right) \right]. \tag{1.3.2.8}$$

Here G depends on: contrast between pore-fluid properties and volume to surface ratio of the patches, such that

$$G = \frac{\kappa K_{BGH}}{\eta_1\sqrt{D_1} + \eta_2\sqrt{D_2}} \frac{\int \left|\Delta p_f\right|^2 ds}{\left|P_e\right|^2 V}, \tag{1.3.2.9}$$

where η_i and D_i are viscosity and diffusivity of fluid *i*, ds/V is the surface area to volume ratio of the fluid inclusion and $|\Delta p_f| / |P_e|$ is the change in pore pressure due to external pressure applied on the sample.

For intermediate wave frequencies, the dynamic response of the porous rock is constructed using a branching function, which ensures causality of the solution and convergence to lower-frequency (Equation 1.3.2.1) and higher-frequency (Equation 1.3.2.8) limits. The dynamic saturated bulk modulus is given by:

$$K_J(\omega) = K_{BGH}(1 - \delta bf(\omega)), \qquad (1.3.2.10)$$

with a branching function of

$$bf(\omega) = \left[1 - \zeta + \zeta\sqrt{1 - i\omega\tau/\zeta^2}\right]^{-1}, \qquad (1.3.2.11)$$

and fluid contrast factor

$$\delta = \frac{(K_{BGH} - K_{BGW})}{K_{BGH}}. \qquad (1.3.2.12)$$

The branching is defined in terms of two parameters. The first is called the shape parameter

$$\zeta = (K_{BGH} - K_{BGW})^3 / (2K_{BGW} K_{BGH}^2 TG^2). \qquad (1.3.2.13)$$

and controls the shape of the attenuation curve. The second is called the frequency scaling parameter

$$\tau = (K_{BGH} - K_{BGW})^2 / (K_{BGH} G)^2 \;, . \qquad (1.3.2.14)$$

and controls the frequency at which attenuation reaches its maximum value.

Utilizing this theory, Tserkovnyak and Johnson (2002) deduced values for the specific surface area and effective patch size from experimental data (Cadoret et al. 1995; 1998). They found that APS theory could be used to interpret geometrical measures of partial fluid saturation from attenuation and phase velocity measurements. Their interpretation produced effective patch sizes which were in general plausible; however the volume to surface ratios exceeded theoretical limits at large water saturations. Tserkovnyak and Johnson (2002b) have extended the approach to incorporate surface tension at the interface between pore fluids.

1.3.3 Double Porosity Dual Permeability -Pride and Berryman

A more general approach based broadly on similar principles as APS theory was recently developed by Pride and Berryman (2004a; 2004b). This approach yields estimates of attenuation and phase velocity in a general double-porosity dual-permeability medium. The theory utilizes Biot's equations (Biot 1962) of poroelasticity to determine the poroelastic response of a composite body comprising two different poroelastic materials (each described by Biot's equations of poroelasticity).

Central to the double-porosity dual-permeability theory is a model for fluid transport (Pride and Berryman 2004b). That is, they aim to directly model mesoscopic fluid flow arising between different regions of rock. They assume that it is proportional to fluid pressure differences (between each material), with a frequency-dependent proportionality coefficient γ. The average rate ξ_{inc} at which fluid volume is transferred from material 1 into material 2 is given by

$$-i\omega\xi_{inc} = \gamma(\omega)(p_{f1} - p_{f2}), \qquad (1.3.3.1)$$

where p_{fi} refers to fluid pressure in material i. It is this quantity ξ_{inc} that represents mesoscopic fluid flow, when wave frequency is much less than Biot's characteristic frequency. This flow is responsible for significant attenuation and dispersion of compressional waves.

The fluid transport coefficient γ in Equation (1.3.3.1) is obtained using a similar approach to that of Johnson (2001). That is, the fluid transport coefficient is only exactly determined at low and high frequency limits. To estimate γ at intermediate frequencies, Pride and Berryman (2004b) use a branching function given by

$$\gamma(\omega) = \gamma_m \sqrt{1 - i\frac{\omega}{\omega_m}}\ , \qquad (1.3.3.2)$$

which converges to theoretically derived low and high frequency limits. The parameters ω_m and γ_m depend on mesoscopic geometry and constituent properties (see Pride et al. 2004).

In the important case where one porous phase is entirely embedded in the other, the double porosity equations of Pride and Berryman (2004a, 2004b) reduce to an effective Biot's theory having complex frequency-dependent coefficients. That is, the drained bulk modulus $K_d(\omega)$, saturated bulk modulus $K_{sat}(\omega)$ and fluid modulus $M(\omega)$ all depend on wave frequency. This is possible because in this case the flux into and out of the volume element for the embedded fluid is zero. Wave attenuation and velocity dispersion are then modelled by substituting these equations into the wave slowness obtained from Biot's theory. Hence, attenuation and dispersion due to heterogeneities in rock (or fluid properties) can be predicted for both the low and high frequency regimes of Biot's theory. This shall be shown in Figure 1.3.3.1.

Pride et al. (2004) specialised the general results of Pride and Berryman (2004a, 2004b). to the specific case of patchy saturation, where only heterogeneities in saturating fluids exist. They also derive analogous results for squirt flow. Rather then list the multitude of equations required to use their theory, I shall show below a patchy saturation version that I simplified assuming that the frequency is much lower than Biot's characteristic frequency.

The saturated P-wave modulus is

$$H(\omega) = -\frac{1}{A_2}\left(A_1 + \frac{A_3^{\,2}}{A_4 + A_2\dfrac{\gamma}{i\omega}}\right) + \frac{4}{3}\mu\,, \tag{1.3.3.3}$$

where γ is the fluid transport coefficient given by Equation (1.3.3.2). The A_i coefficients are:

$$A_1 = \frac{\alpha}{K_d B_0} \tag{1.3.3.4}$$

$$A_2 = \frac{-\alpha}{K_d^{\,2} B_0}\left(1 - \alpha B_0\right) \tag{1.3.3.5}$$

$$A_3 = \frac{\alpha^2}{K_d^{\,2}}\left(\frac{v_1 v_2}{B_1 B_2}\right)\left(B_1 - B_2\right) \tag{1.3.3.6}$$

$$A_4 = \frac{-\alpha^2 \beta}{K_d^{\,3} B_0}\left(1 - \alpha B_0\right) + \frac{\alpha^2 v_1 v_2}{K_d B_1 B_2}\left(1 - \alpha B_0^{*}\right). \tag{1.3.3.7}$$

Here $B_i, (i = 1,2)$ are Skempton coefficients for regions of rock saturated by fluid one and fluid two. The Skempton coefficient is a ratio of the change in fluid pressure of the undrained rock due to changes in confining pressure (Shempton 1954). That is, it is a measure of induced fluid pressure and is given by (Pride et al. 2004):

$$B_i = \frac{\alpha}{\alpha + \dfrac{\phi K_d}{K_{f_i} K_s}\left(K_s - K_{f_i}\right)}.$$

In Equations (1.3.3.4)-(1.3.3.7), B_0 and B_0^* are harmonic and arithmetic averages of the Skempton coefficients for the two phases,

$$\frac{1}{B_0} = \left\langle \frac{1}{B} \right\rangle = \frac{v_1}{B_1} + \frac{v_2}{B_2},$$

$$B_0^* = \left\langle B \right\rangle = B_1 v_1 + B_2 v_2,$$

and

$$\beta = \frac{v_1 v_2}{B_0}\left[\alpha - \frac{\left(1 - K_d / K_{BGH}\right)}{B_0^*}\right] \Bigg/ \left[\alpha - \frac{\left(1 - K_d / K_{BGH}\right)}{B_0}\right].$$

Figure 1.3.3.1 shows (a) attenuation and (b) velocity calculated using Pride and Berryman’s (P.B) patchy saturation model; this is compared against Equation (1.3.3.3). Clearly, Equation (1.3.3.3) is a good approximation at low frequencies, as the predicted attenuation and velocity curves are identical to P.B. (a) Shows two attenuation peaks, the first at low frequencies is due to mesoscopic fluid flow, whilst the second at higher frequencies is due to macroscopic fluid flow. There is a large difference in the magnitude of attenuation, at high frequencies as Equation (1.3.3.3) does not account for macroscopic flow (which is negligible at low frequencies).

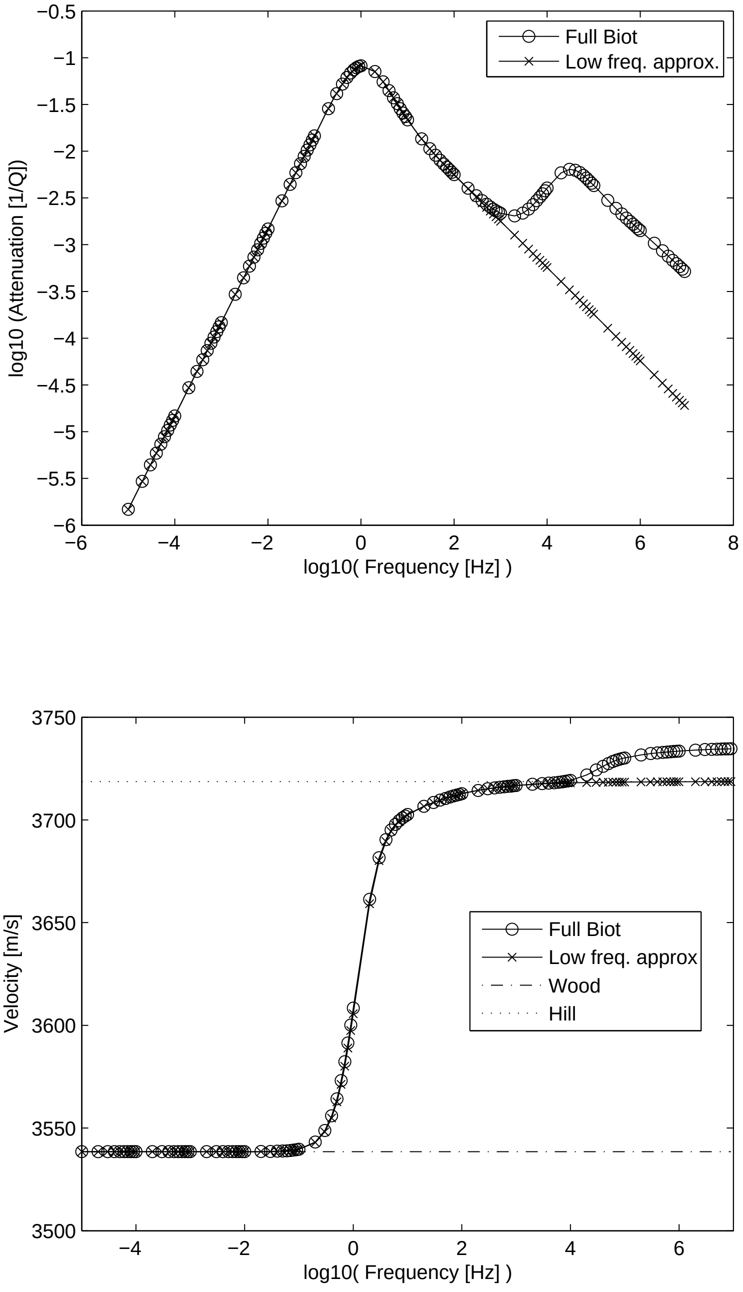

(a)

(b)

Figure 1.3.3.1: Attenuation and dispersion due to the Pride et al. (2004) patchy saturation model and approximation. (a) Attenuation and (b) velocity modelled using Pride et al. (2004) full Biot's model (solid line with circles) and modelled using my low frequency approximation Equation (1.3.3.3).

1.3.4 Comparison of Regular Cell Concentric Sphere Models

Here I model attenuation and dispersion using three regular cell models (White, Johnson, Pride and Berryman approaches) assuming the concentric sphere fluid geometry. The motivation is to identify whether differences in physical approaches used to account for mesoscopic fluid flow will affect attenuation and dispersion estimates. For 5% of air inclusions within an otherwise water saturated host rock of porosity 0.15, attenuation and phase velocity are shown in Figure 1.3.4.1 (a) and (b), respectively. These figures show that there is a good agreement between all periodic models for estimates of attenuation and phase velocity. In particular, (a) shows that attenuation at low frequencies is proportional to ω, whilst for high frequencies it is proportional to $\omega^{-1/2}$. (b) Shows that phase velocities converge to low (Gassmann-Wood) and high frequency (Gassmann-Hill) limits and at intermediate frequencies the phase velocities are bounded by those limits. Clearly, the differences in theoretical formulations do not affect attenuation and velocity estimates.

The regular cell approaches are limited to modelling attenuation and velocity dispersion due to wave induced flow arising between fluid heterogeneities that are identical in shape and distributed regularly throughout the porous medium. The use of idealised modelling geometries has clearly been helpful in identifying the effects of mesoscopic fluid flow. However, other types of patchy saturation models that allow more realistic fluid distributions to be modelled, like the random media approaches (Müller & Gurevich 2004; Ciz et al. 2006) are required in order to evaluate whether fluid distribution will influence attenuation and velocity estimates. We know from 1D analyses (Gurevich & Lopatnikov, 1995; Müller & Gurevich, 2004) that random and periodic 1D distributions of two different fluids yield very different attenuation/dispersion pairs. Although 1D alternating fluid distributions may not be realistic, this result gives additional motivation to studies of wave propagation in porous media with 3D random spatial fluid distributions.

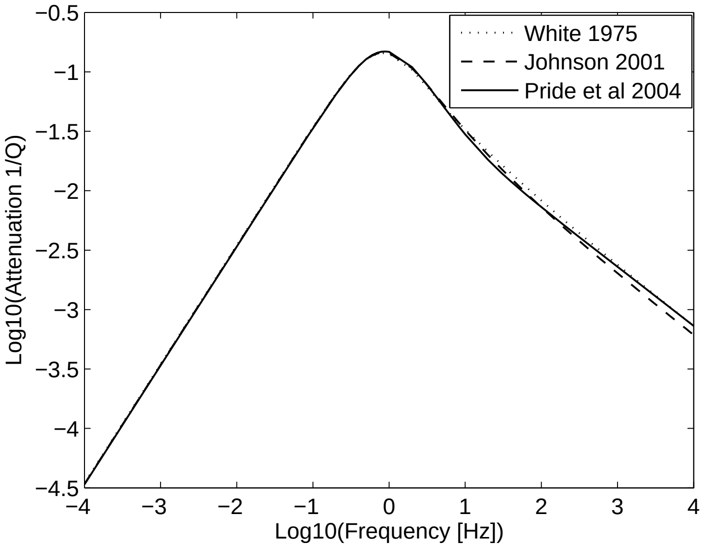

(a)

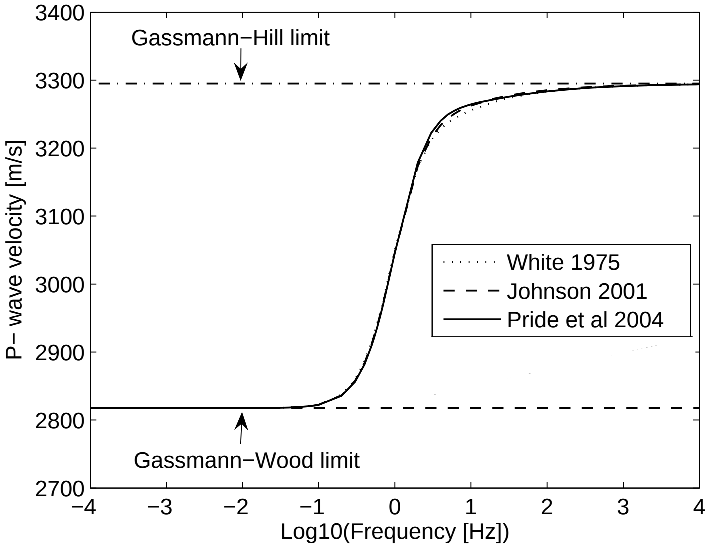

(b)

Figure 1.3.4.1: Attenuation and dispersion modelled using the regular cell approaches. (a) Attenuation and (b) velocity estimates modelled using the periodic models of White, Johnson and Pride et al. 2004. Very good agreement between all approaches for the case of 5 % air inclusions in an otherwise water saturated host rock of porosity 15%. The inclusion radius is 25 cm.

1.4 Thesis Overview – My Contribution

I once sent a dozen of my friends a telegram saying "flee at once- all is discovered". They all left town immediately. - Mark Twain

Well, fortunately (or unfortunately) I never received Twain's telegram, was he talking about patchy saturation? Yes and No. It is true that the effect has been identified and the physics is pretty much understood; however there are still two aspects of this phenomenon (amongst others) which require further research. They are (1) how fluid contrast and (2) fluid distribution influence patchy saturation signatures (attenuation and dispersion). Both aspects are interrelated and are the focus of my thesis.

My first study concerns fluid distribution, that is, how fluids are spatially arranged on a scale that is greater than pore scale but less than wavelength scale. Specifically, in Chapter 2, I examine a series of X-ray tomographic images of partially saturated rock. The objective is to identify which statistical measures are useful for characterizing mesoscopic fluid distributions and to study how those measures change as average gas saturation increases. From this chapter, I show that the correlation function and correlation length provide the most useful statistical information for spatial characterisation of mesoscopic fluid heterogeneities.

By learning how to describe fluid distribution (and changes in fluid distribution) from experimental data, we can identify how to characterise fluid distribution in our theoretical models. That is, if we want to model patchy saturation signatures (attenuation and dispersion) due to realistic fluid distributions, then we need a way of incorporating realistic spatial information into our theoretical models. In Chapter 3, I detail two models based on concepts of random media and build a new random media patchy saturation model. In particular, my model called 3DCRM implicitly assumes that fluid distribution is described by a correlation function. Hence it is well suited to modelling patchy saturation signatures due to realistic fluid distributions that arise in X-ray tomographic images. In this Chapter, I show how these signatures change for different types of correlation functions.

The Chapter 3 patchy saturation models allow us to connect realistic fluid distributions to patchy saturation signatures. However, the models are not without their limitations and restrictions. Perhaps the most significant of these is that they are in general accurate for low fluid contrast and approximate for large fluid contrast (fluid contrast refers to the difference between the bulk moduli of the fluids). That is, low contrast implies that there are only small differences in the fluid bulk moduli, this may occur with a water and oil in the system; whilst high contrast implies that there are large differences, such as with a water and gas system.

When modelling patchy saturation signatures due to realistic fluids, it is necessary to be able to take into account realistic fluid contrasts (in bulk moduli, viscosity etc), in addition to realistic fluid distributions. In Chapter 4, I express the patchy saturation models from Chapter 3 in a single framework, a unified parameterization. The framework utilized is APS (Section 1.2), which is valid for high contrast between fluids, but is analytically restricted to very simple geometries. Specifically, I derive expressions which allow APS to estimate attenuation and dispersion due to the fluid distributions employed by the Chapter 3 models.

Central to the APS framework is a branching function, which provides a simple way to approximate the dynamic solution at intermediate frequencies from knowledge of low and high frequency asymptotes. Via comparison with the Chapter 3 models, which predict attenuation and velocity explicitly over the entire frequency range, I show that the branching function provides an excellent approximation of frequency-dependent attenuation and velocity at intermediate frequencies. These comparisons are performed at fluid contrasts for which the Chapter 3 models are precise. Hence, the question remains can APS with modified parameters be used to model attenuation/dispersion when pore fluid contrast is large, such as with water and air.

In Chapter 5, I use numerical methods to examine how the shape parameter for a specific model varies as fluid contrast increases. The results of this analysis show that the shape parameter for a random distribution of spherical inclusions is governed well by the shapes parameters derived in Chapter 4 for most fluid contrasts.

Chapter 2

Fluid Distribution from Saturation Experiments on Porous Rock

2.0 Introduction

Understanding how the percentage of two (or more) different pore fluids will affect P-wave velocities is important for interpreting time lapse seismic data, in particular tracking fluid front movements. Application of Gassmann's fluid substitution relations (Gassmann 1951) in addition to fluid mixing equations like Brie et al.. (1995) or Wood's (1941) is one approach which could be used to make forward modelling estimates of P-wave velocities at different percentages of fluid saturation. However, the problem with these approaches is that partial fluid saturation effects such as mesoscopic fluid flow are completely ignored.

Mesoscale fluid flow arises when a passing wave induces different fluid pressures in regions of rock saturated by different fluid types, where mesoscale specifically refers to a length scale greater than pore scale, but less than wavelength scale. The presence of spatial gradients in fluid pressure causes fluid to flow relative to the rock frame. This causes dissipation of energy and results in the attenuation and dispersion of a propagating waveform. A number of different patchy saturation models accounting for the mesoscale distribution of fluid heterogeneities have been proposed: concentric sphere model of White et al. (1977), Acoustics of Patchy Saturation (APS) model of Johnson (2001) and the so-called Continuous Random Media (CRM model, Chapter 3) of Toms et al. (2006; 2007).

These theoretical models allow us to calculate dynamic-equivalent elastic moduli as a function of percent fluid saturation and wave frequency. However, one must assume either a fixed geometry of the patch distribution (such as periodically distributed spherical inclusions in White's model) or fluid distribution given by a specific correlation function (for CRM). Thus, the applicability of these models hinges on knowledge of the real spatial distribution of pore fluids in rocks. The spatial distribution is influenced by rock heterogeneity, the prior history of fluid movement, and density and viscous effects such as viscous fingering (Homsy 1987).

The most suitable tool to assist with imaging fluid distributions of partially saturated rocks is X-ray tomography. It is already routinely applied in petroleum engineering to image reservoir lithologies undergoing secondary and tertiary recovery processes (Wellington & Vinegar 1987, Dunsmuir et al.. 1991, Withjack et al.. 2003). It is also increasingly used for characterization of soils (Peyton et al.. 1992; De Gryze et al. 2006) and rocks (Arns et al. 2002; Arns et al. 2004); to produce input models for numerical algorithms which calculate transport properties of rocks (Arns et al. 2001; Knackstedt et al. 2004) and for calculation of elastic properties (Arns et al. 2002). In fact, it is being used in numerous other applications spanning the entire geoscience field (Ketcham & Carlson 2001).

The simultaneous acquisition of X-ray tomographic images and acoustic measurements during fluid saturation experiments on porous rock will provide the most direct means of relating velocity saturation information to pore fluid distribution. There have been several recent studies of this kind (Cadoret et al. 1995; Cadoret et al. 1998; Monsen & Johnstad 2005). Cadoret et al. (1995) use X-ray tomographic images to explain why velocities at the same percentage of water saturation may be different for drainage and imbibition experiments. Where the velocities differed the drainage images showed the presence of distinct gas bearing clusters (for water saturations greater than 80%), whilst the imbibition images showed no such clustering. This suggests that differences in fluid distribution will cause differences in velocity measurements. The same conclusion has been drawn for attenuation measurements (Cadoret et al. 1998).

Although X-ray tomographic images are central to the experiments of Cadoret et al. (1995) and Monsen and Johnstad (2005), the images themselves are only analysed qualitatively. That is, apart from identifying images which have clustering (Cadoret et al. 1995) or show fluid displacement in preferred directions (Monsen & Johnstad

2005), no further analysis of the fluid saturation patterns is performed. Thus, variations in velocities and attenuation are linked qualitatively to changes in fluid saturation patterns; missing still is a quantitative description.

In this chapter I examine a series of X-ray tomographic images (with mesoscale resolution) obtained from a drainage experiment performed on Mount Gambier Limestones (Paterson & Lupton 2003, unpublished results). The objective is to analyse fluid saturation patterns quantitatively, thus showing how they can be described and how they vary as saturation changes. In particular, the applicability and significance of correlation type measures on mesoscopic fluid patch patterns is investigated. Unfortunately, reliable velocity data was not acquired during the experiment so these results can not be linked to experimentally measured velocities.

The chapter is organised as follows: Section 1 describes Paterson's fluid saturation experiment and briefly outlines the basics of X-ray tomography. Section 2 covers processing of raw tomographic scans to produce saturation patterns. Section 3 is the main contribution, where I introduce and extract quantitative statistics which allow description of fluid saturation patterns. Section 4 summarizes the results, compiling a list of reasonable fluid assumptions for modelling velocities due to patchy saturation.

2.1 The Experiment

Paterson and Lupton (2003) performed a series of drainage experiments on Mount Gambier limestone samples. The experimental setup is shown in Figure 2.1.1. There is a cylindrical core sample encased in PVC pipe connected to pipe work which controls pressured fluid injection of nitrogen gas and subsequent water extraction. The medical X-ray imager is shown in the background, at various stages during the saturation experiment images are taken of the core sample.

The experiment proceeds by initially taking an image of the dry core sample. The core sample is then fully saturated with water. A vacuum is applied to ensure uniform saturation of the water through out the pore-space and to draw out any remaining air. An image is then taken of the fully water saturated sample. Then fluid replacement begins by injecting pressurized nitrogen gas into the end of the core. The flow rate is kept continuous at constant pressure (but not at a constant rate) throughout the experiment. Images were taken at different times.

The core samples are Mount Gambier limestone (MGL), which come from the Bruhn quarry in South Australia (www.bruhn.com.au). They generally have a high permeability (around 5 Darcy) and typical effective porosities in the range 36-44% Although the saturation experiments were performed on a number of different core samples, only one experiment (performed on sample MGL2a) is suitable for thorough analysis, as images are taken at both low and high gas saturations.

Figure 2.1.1: Paterson's (2003) experimental setup for imaging the core sample during the fluid replacement experiment.

2.1.2 X-ray Tomography

The X-ray tomography method was originally developed for medical applications, specifically the imaging of bones and soft tissue (Hounsfield 1972). Typical medical X-ray tomography machines, such as the one shown in Fig. 2.1.1 employ a single source which is rotated around the object being scanned. The source is an X-ray tube which emits a beam of photons that are received by a fixed set of detectors located in a ring around the object. They measure the intensity of the received X-ray which is related to the intensity of the source X-ray for homogeneous materials by Beer's Law (Wellington & Vinegar 1987)

$$I = I_0 \exp(-\mu x), \tag{2.1.2.1}$$

where μ is the linear attenuation coefficient of the scanned material and x is the distance travelled through the material. When the material is heterogeneous Beer's law is

$$I = I_0 \exp\left(\sum_i -\mu_i x_i\right), \qquad (2.1.2.2)$$

where μ_i is the linear attenuation coefficient of each material and x_i is the distance travelled through each material i.

Different types of heterogeneities (materials) in a porous rock such as saturating fluids and mineral grains can be imaged providing there is sufficient contrast in the linear X-ray attenuation coefficient of each type of material. The linear attenuation coefficient, in turn, depends on how atoms in a material absorb and scatter energy. Absorption of X-ray energy is due to the photoelectric effect, where the entire energy of the photon is transferred to the atom resulting in the emission of an electron. This effect is dominant for X-ray energies less than 100keV.

When X-ray energies are greater than 100keV but less than 10 MeV, Compton scattering dominates. This effect causes some of the photon energy to be transferred to the atom resulting in the emission of an electron and deflection of the photon in another direction. The degree of Compton scattering depends upon the electron density of the material. In general, the linear attenuation coefficient of a material can be expressed as the sum of photoelectric and Compton scattering terms:

$$\mu = \sigma(E)\rho_a + \left(b\bar{Z}^{3.8}/E^{3.2}\right)\rho_a, \qquad (2.1.2.3)$$

where is the Klein-Nishina coefficient and ρ_e is the electron density, $\bar{Z}$ is the effective atomic number, E is the photon energy in keV and $b = 9.8\times10^{-24}$ (Vinegar & Wellington 1986).

Although the detectors measure the intensity of the received X-rays, the output of a CT scanner is in Hounsfield units (HU). Hounsfield units come from the reconstruction of linear attenuation coefficients from the measured X-ray intensities using methods such as the Shepp-Logan filter (Shepp and Logan 1974). In general, medical imagers are calibrated such that the CT value of water is zero (HU) and the CT value of air is -1000 (HU). However, other types of calibration (Amos et al.

1995; Orsi & Anderson 1999; Johns et al. 1993) can be adopted, which linearly relate CT values to a materials bulk density, this is especially useful for geological applications.

As fluids such as water, brine, oil etc all have simular linear attenuation coefficients (and thus CT values), petroleum engineers often utilize dopants which are added to one of the fluids to increase the linear attenuation coefficient and thus create contrast in properties. Typical substances utilized are sodium iodide and bromide. In Paterson’s experiment sodium iodide was added to water to help distinguish it from Nitrogen.

Imaging of pore-spaces and individual mineral grains requires the use of high resolution tomography machines. Typically, pore scale imaging of most materials requires resolutions of 3 to 5 microns (Olafuyi et al. 2006). When combined with a typical field of view of 512 x 512 or 1024 x 1024 pixels, this limits the size of the scanned sample to 5 mm-1 cm. In Figure 2.1.1.1 we show porescale images of a typical sample of MGL containing no saturating fluids (Toms et al. 2008). The MGL samples have a very complicated microstructure composed of macroporosity, and microporosity (not resolvable at this scale). Variations in rock porosity will have a significant affect on the distribution of different pore fluids.

Porescale images of a drainage experiment performed on a Berea sandstone and mono-disperse bead pack show that the wetting fluid is present as pendular rings, bridges between adjacent grains and as lenses within pore throats (Turner et al. 2004). This degree of detail is not visible in the images obtained during the Paterson and Lupton (2003) experiments as the resolution of the medical imager utilized was less, but the field of view larger. The relatively large core samples have a radius of 0.050 m and length 0.24 m, and were imaged with a minimum pixel size of 0.36 mm. Hence, in order to visualize changes in fluid distribution the images must be processed as specified in the following section.

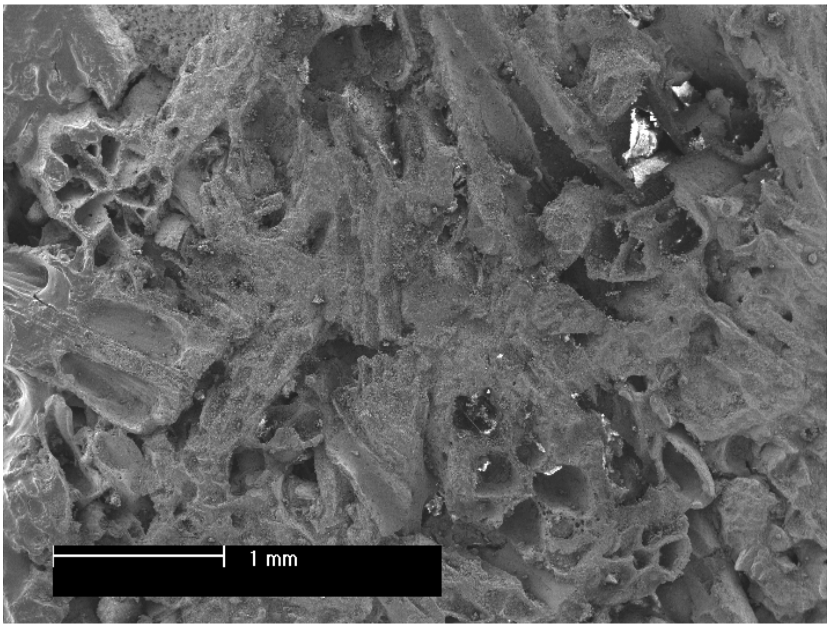

(a)

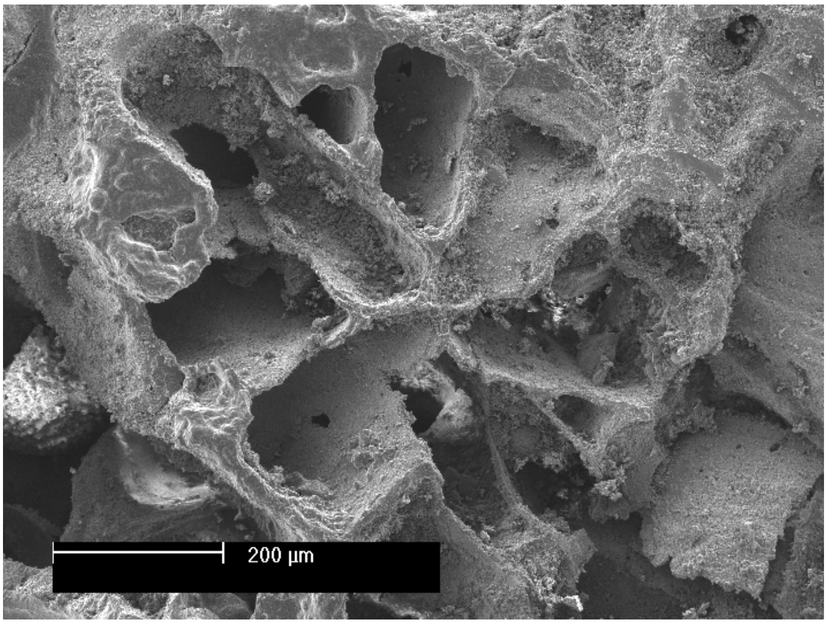

(b)

Figure 2.1.1.1 Porescale images of a typical sample of MGL containing no saturating fluids.

2.2 Processing Images

As the resolution of the tomographic scanner is not sufficient to image the interface between gas, water and mineral grains, the CT value of each pixel is approximately equal to the average of CT responses due to different percentages of mineral grains, pore-spaces, and pore fluids. That is, dry map pixels have CT values (See Figure 2.2.1 (a)) given by

$$CT_{DRY} \approx (1-\phi)CT_{GRAIN} + \phi CT_{AIR} \, , \tag{2.2.1}$$

where ϕ is rock porosity, and CT_{GRAIN} , CT_{AIR} are the CT values of the grains and air filled pore-spaces, respectively. Pixels belonging to the fully water saturated map have CT values (see Figure 2.2.1(b)) :

$$CT_{FULLSAT} \approx (1-\phi)CT_{GRAIN} + \phi CT_{WATER} \, , \tag{2.2.2}$$

whilst pixels of the partially saturated maps have CT values (see Figure 2.2.1 (c)) given by

$$CT_{PARTSAT} \approx (1-\phi)CT_{GRAIN} + \phi(v_2 CT_{WATER} + v_1 CT_{GAS}) \, , \tag{2.2.3}$$

where CT_{WATER} and CT_{GAS} are the CT values of water and nitrogen and v_1 and v_2 are the percentages of water and gas occupying the pore-space, respectively.

In essence, Equations (2.2.1-3) assume that the *CT* value of a pixel at mesoscale resolution is linearly related to *CT* values of its constituents in proportion to volume fractions. Thus for large differences in CT values, which may occur at interfaces between mineral grains and pore-spaces, the above approximations can have considerable errors. Ketchom and Carlson (2001) suggest that these errors can in general be ignored as mineral/grain interfaces are rotated randomly relative to the plane of the scan; however when the interfaces are parallel to the plane of the scan errors can be as high as 10%. A further assumption of the approach is that the grain space is mono-mineralic (or has constant X-ray density).

In general, the CT value (at mesoscale resolution) does not change greatly as the relative percentage of gas to water in the pore-space alters. That is, the change in CT value associated with changes in percentage gas saturation is much less than the CT values of the rock frame itself. Thus in order to identify regions of the core sample that contain gas; the processing procedure of Cadoret et al. (1995) is implemented. This procedure also removes CT artefacts arising from multi-mineralogical grain spaces.

Cadoret's procedure involves creating three different types of maps:

(1) *Porosity map = {fully water saturated image} – {dry image},*
(2) *Gas content map = {fully water saturated image} – {partially water saturated images},*
(3) *Gas saturation map = Gas content map / porosity map.*

The pixels in each of the created maps have CT values of:

$$(1)\quad CT_{POROSITY} = CT_{DRY-}CT_{FULLSAT} = \phi(CT_{WATER} - CT_{AIR}) \qquad \textit{(see Fig. 2.2.1(d)),} \tag{2.2.4}$$

$$(2)\quad CT_{GASCONT} = CT_{FULLSAT} - CT_{PARTSAT} = \phi v_1(CT_{WATER} - CT_{GAS}) \qquad \textit{(see Fig. 2.2.1(e)),} \tag{2.2.5}$$

$$(3)\quad CT_{GASSART} = \frac{CT_{GASCONT}}{CT_{POROSITY}} = \frac{v_1(CT_{WATER} - CT_{GAS})}{(CT_{WATER} - CT_{AIR})} \qquad \textit{(see Fig. 2.2.1(f)).} \tag{2.2.6}$$

In theory Equation (2.2.4) can be used to estimate spatial fluctuations in rock porosity (in addition to the average rock porosity). Unfortunately, it cannot be utilized in this study as the CT value of the doped water wasn't measured.

Determination of percentage gas saturation of each pixel comes from Equation (2.2.6), where it is assumed that the CT value of Nitrogen gas is close to the CT value of air. If this assumption is accepted then maps generated in Step (3) show the spatial location of gas saturating pores and the percentage of gas saturation in those pores. Pixel values range from 0 to 1, where 0 indicates fully water saturated pores and 1 indicates fully gas saturated pores, whilst intermediate pixel values indicate that the pore-space is of mixed gas-water composition. The average gas saturation $\langle v_1 \rangle$ of the core sample is calculated from the gas saturation of each pixel by

$$\langle v_1 \rangle = \frac{1}{N}\sum_{i=1}^{N} v_1(i), \tag{2.2.7}$$

where *N* is the total number of pixels.

To convert the images into binary media (which is necessary to extract certain types of quantitative statistics), a simple global-threshold-technique is applied; where pixels below a certain threshold value are counted as water, whilst above the threshold they are counted as gas. The threshold value utilized here is the arithmetic mean of the statistical distribution of pixel values. Thus the threshold value is representative of an average pixel that contains some percentage of gas, whilst pixels below (or above) the threshold are to be understood as containing less (or more) gas relative to the average pixel.

In Fig. 2.2.2 (a) – (m) the gas saturation maps are shown for the drainage experiment on MGL2a (only the inner square of the core sample is shown). During the initial stages of the experiment (Figure 2.2.2 (a)-(f)) gas saturations less than 20%) distinct patches of gas bearing pores exist. Once average gas saturations (Figure 2.2.2 (g)-(m)) have exceeded this value, distinct clusters of gas bearing pores are no longer visible.

In Figure 2.2.3 the gas saturation map (left) is compared with its corresponding binary map (right). It shows that applying a threshold about the mean produces a binary map which preserves the main features of the full gas saturation map. This is true for most scans; however more elaborate thresholding techniques like indicator kriging could be used (Oh & Lindquist 1999).

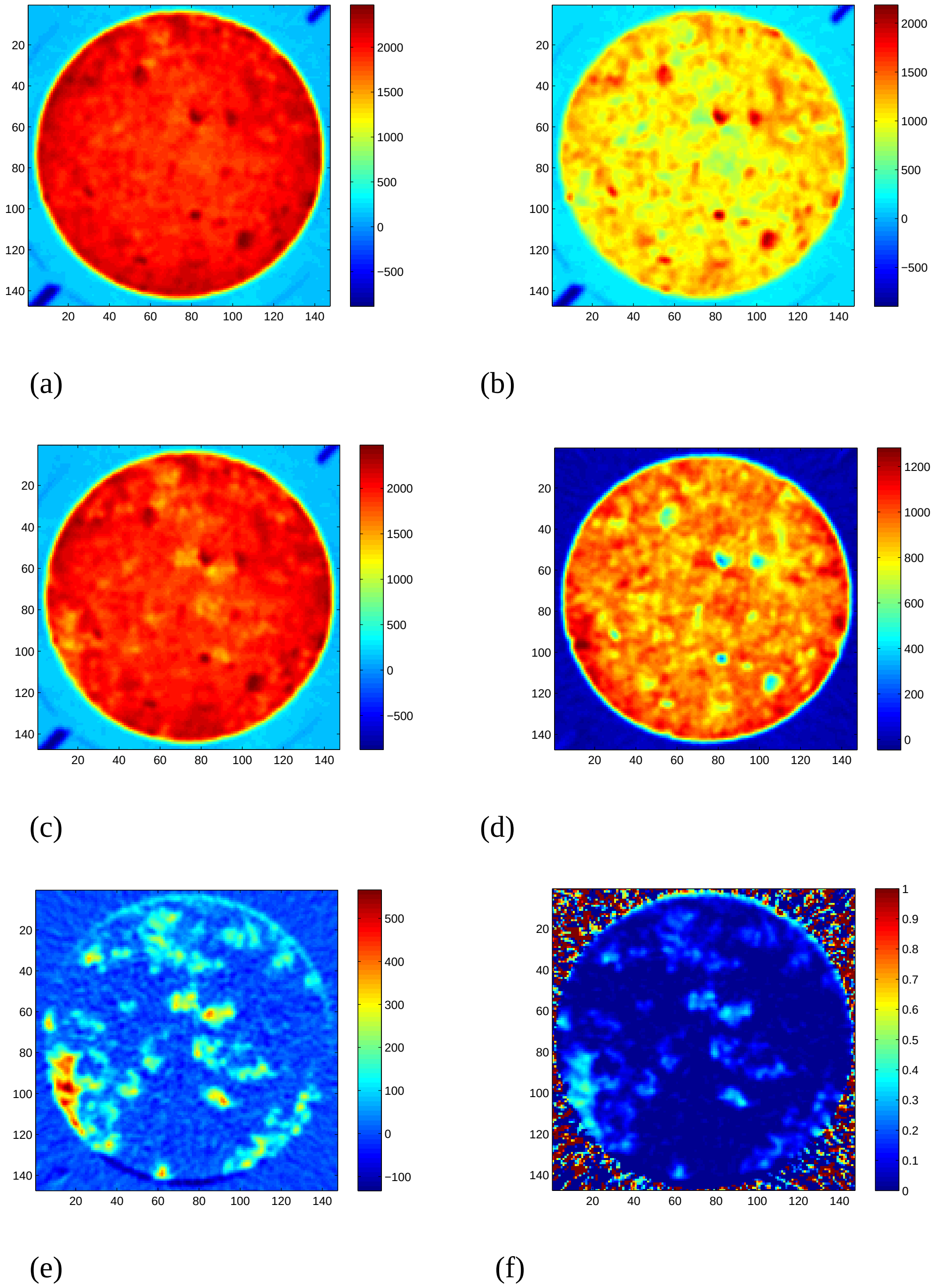

(a) (b)

(c) (d)

(e) (f)

Figure 2.2.1 X-ray images and fluid heterogeneity maps. X-ray images of (a) dry core (b) fully water saturated core and (c) partially water saturated core, (d) Porosity map, (e) gas content map and (f) gas saturation map. The colour bar in (a-e) refers to CT values, whilst the colour bar in (f) refers to percent gas saturation divided by 100.

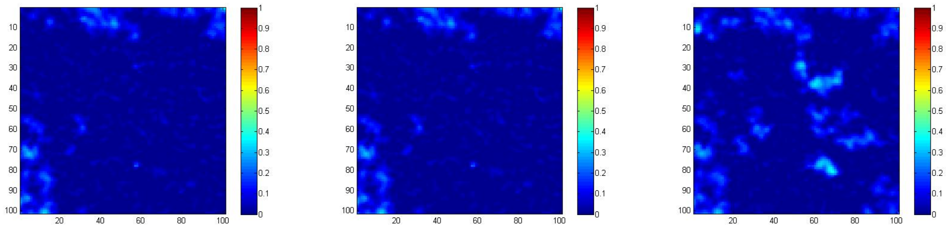

(a) Scan 3 (b) Scan 4 (c) Scan 5

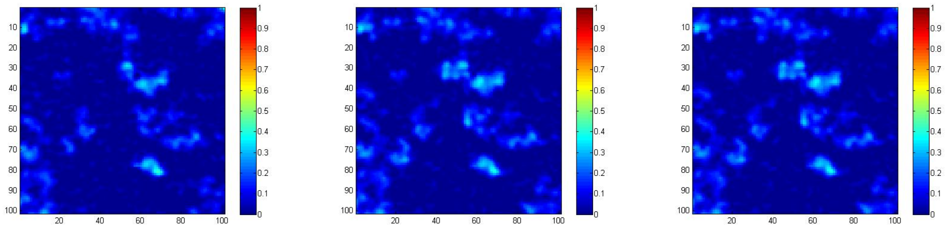

(d) Scan 6 (e) Scan 7 (f) Scan 8

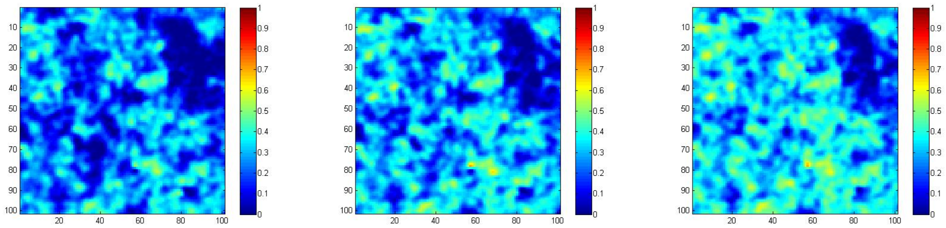

(h) Scan 15 (i) Scan 16 (j) Scan 17

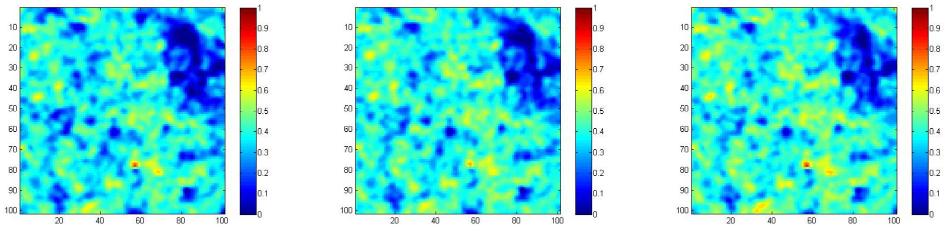

(k) Scan 18 (l) Scan 19 (m) Scan 20

Figure 2.2.2 Gas saturation maps for Scans 3 through to 20. The colour bar indicates the average gas saturation of a pixel. Red corresponds to 100 % gas saturation, whilst blue corresponds to 100 % water saturation. Intermediate colours such as green and yellow, indicate pixels of mixed gas-water composition.

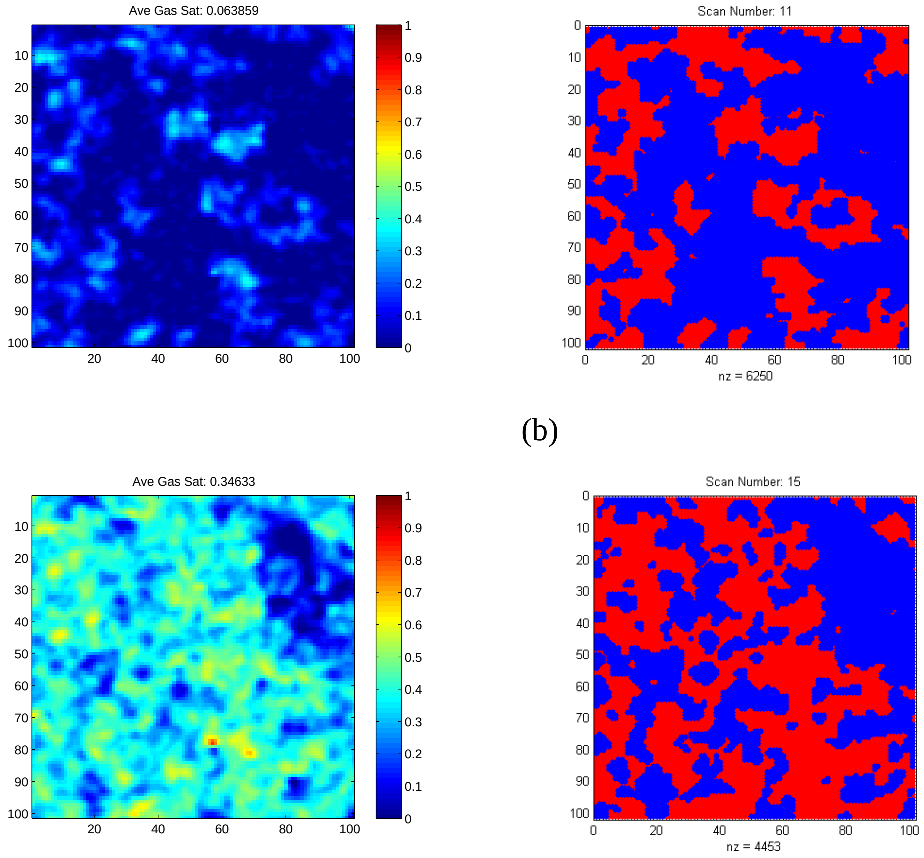

(a) (b)

(c) (d)

Figure 2.2.3: Example of global thresholding applied to saturation maps (a) Scan 11 and (c) Scan 15 to create binary maps (b) and (d)

2.3 Statistical Analysis of the Binary Maps

As the drainage experiment proceeds, the gas saturation maps (Figure 2.2.2 (a)-(m)) become more complicated as more of the pore-space becomes affected by the presence of gas. To characterise the fluid distribution (and changes in fluid distribution) of each mesoscale image, descriptive statistics (such as the correlation function, correlation length, linear path function, etc) are extracted from the binary images using Monte Carlo methods. By comparing statistics derived from each map, it is possible to characterise changes in fluid distribution caused by changes in gas saturation.

For each binary map an indicator function is defined which describes the segmentation of the map into different subdomains. The indicator function is given by

$$I^{(i)}(r;\omega) = \begin{cases} 1 & if \quad r \in V_i(\omega) \\ 0 & otherwise \end{cases}, \tag{2.3.1}$$

where $I^{(1)}$ is the indicator function for the gas saturated domain V_1 and $I^{(2)}$ is the indicator function for the water saturated domain V_2.

The role of the indicator function can be elucidated by considering all points $r_g = \{(x,y) : (x,y) \in V_1\}$ belonging to the gas saturated domain and the values assumed by the different indicator functions. For this set of points the indicator function for the gas saturated domain $I^{(1)}(r_g) = 1$, whilst the indicator function for the water saturated zone $I^{(2)}(r_g) = 0$. For all points belonging to the water saturated domain, the reverse is true. Hence, $I^{(1)}(r) + I^{(2)}(r) = 1 \ \forall \quad r = (x,y) \in V = V_1 \cup V_2$.

The average of either indicator function $I^{(i)}(r)$ is equal to the volume concentration of that domain, that is $\langle I^{(i)} \rangle = \varphi_i$. This is equivalent to the probability that a randomly chosen point on the map will belong to either the gas saturated (or water saturated) domain. That is $\langle I^{(1)} \rangle = P\{I^{(1)}(r) = 1\} = \varphi_1$ and $\langle I^{(2)} \rangle = P\{I^{(2)}(r) = 1\} = \varphi_2$. It is not necessarily the case that the volume concentration of the gas saturated domain is equal to the average gas saturation of the partially saturated core sample, that is ($\varphi_1 \neq v_1 \quad \therefore \quad \varphi_2 \neq v_2$).

2.3.1 Autocorrelation Functions and Correlation Length

The autocorrelation function $\chi(r)$ for the binary map is related to the indicator functions of the gas and water saturated domains by

$$\chi(dr) = \left\langle I^{(1)}(r) - \varphi_1 \right\rangle \left\langle I^{(1)}(r + dr) - \varphi_1 \right\rangle = \left\langle I^{(2)}(r) - \varphi_2 \right\rangle \left\langle I^{(2)}(r + dr) - \varphi_2 \right\rangle , \qquad (2.3.1.1)$$

where dr is the scalar distance separating two points. Relation (2.3.1.1) is appropriate for isotropic maps where $\chi(r)$ does not vary with line orientation (see Section 2.3.1.2). As the indicator function of each domain is equivalent to the probability of a random point residing in that domain, the correlation function can be determined from

$$\chi(r) = S^{(1)}(r, r + x) - \varphi_1^2 = S^{(2)}(r, r + x) - \varphi_2^2 , \qquad (2.3.1.2)$$

where $S^{(1)}(r, r + x)$ and $S^{(2)}(r, r + x)$ are the two point probability functions for the gas and water saturated domains, respectively.

The two point probability function refers to the probability that two random points displaced by a scalar distance dx reside in the same domain. That is, $S^{(1)}(r, r + x)$ is the probability that two random points will reside in the gas saturated domain and $S^{(2)}(r, r + x)$ is the probability that two random points will reside in the water saturated domain. Clearly as the distance separating the points reduces to zero the two point probability functions reduce to one point probability functions

$$\lim_{x \to 0} S^{(i)}(r, r + x) = S^{(i)}(r, r) = S^{(i)}(r) = \varphi_i , \qquad (2.3.1.3)$$

accordingly. Moreover, if no long range order exists the two point probability function converges to

$$\lim_{dx \to \infty} S^{(i)}(r, r + dx) = \varphi_i^2 . \qquad (2.3.1.4)$$

Substitution of Equations (2.3.1.3) and (2.3.1.4) into Equation (2.3.1.2) shows that the correlation function has limiting values of $\chi(0) = \varphi_1 - \varphi_1^2 = \varphi_1 \varphi_2$ and $\chi(\infty) = 0$.

To determine the correlation function for each binary map, we extract the two point probability function using Monte Carlo methods. From Equation (2.3.1.2) it is clear that the correlation function can be determined using either two-point probability functions for the gas or water saturated domain. Here I choose to extract the two point probability function corresponding to the gas saturated domain. Note that the two point probability function of the water saturated domain can be calculated from the two point probability function for the gas saturated domain using

$$S^{(2)}(r, r+dx) = S^{(1)}(r, r+dx) - \varphi_1^2 + \varphi_2^2 = S^{(1)}(r, r+dx) + 1 - 2\varphi_1 . \qquad (2.3.1.5)$$

The one point probability function for the gas saturated domain is determined by randomly sampling the image at one point and recording the total number of times that one point corresponds to gas saturated domain. This total is divided by the total number of points sampled to give the one point probability density function. It is equivalent to the volume fraction of the gas saturated domain within the binary map.

The two point probability function of the gas saturated domain is obtained by randomly sampling the image at two points separated by scalar distances dx_s. A record is made of the total number of times both sample points simultaneously reside in the gas saturated domain for each scalar distance dx. Refer to Figure 2.3.1.1 for an illustration of which events are counted in the record. To determine the two point probability density function, the record is divided by the total number of times the binary map was sampled at each scalar distance.

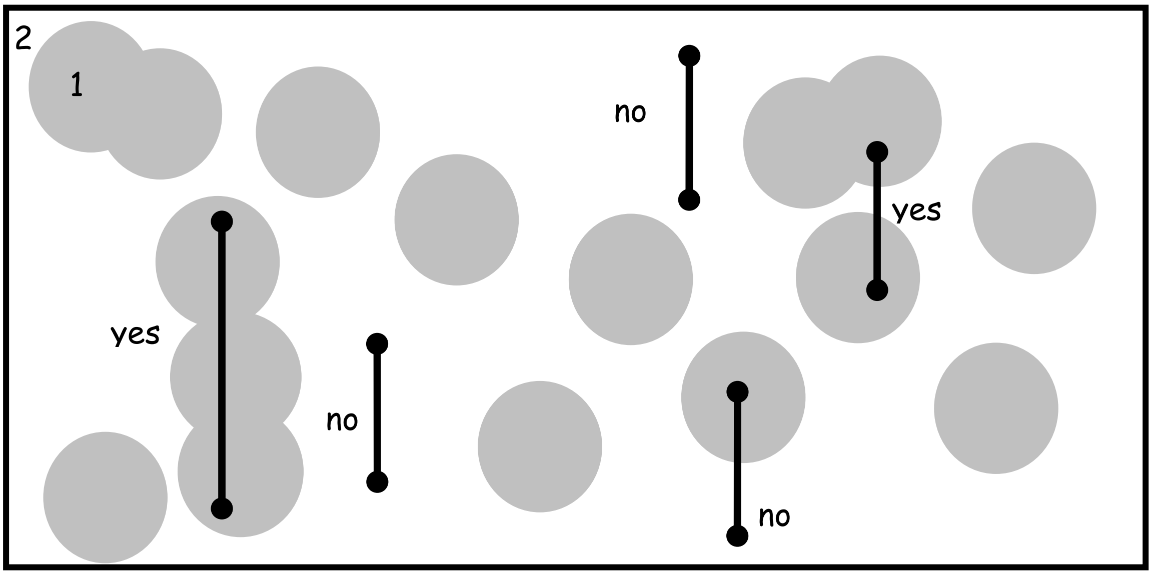

(a)

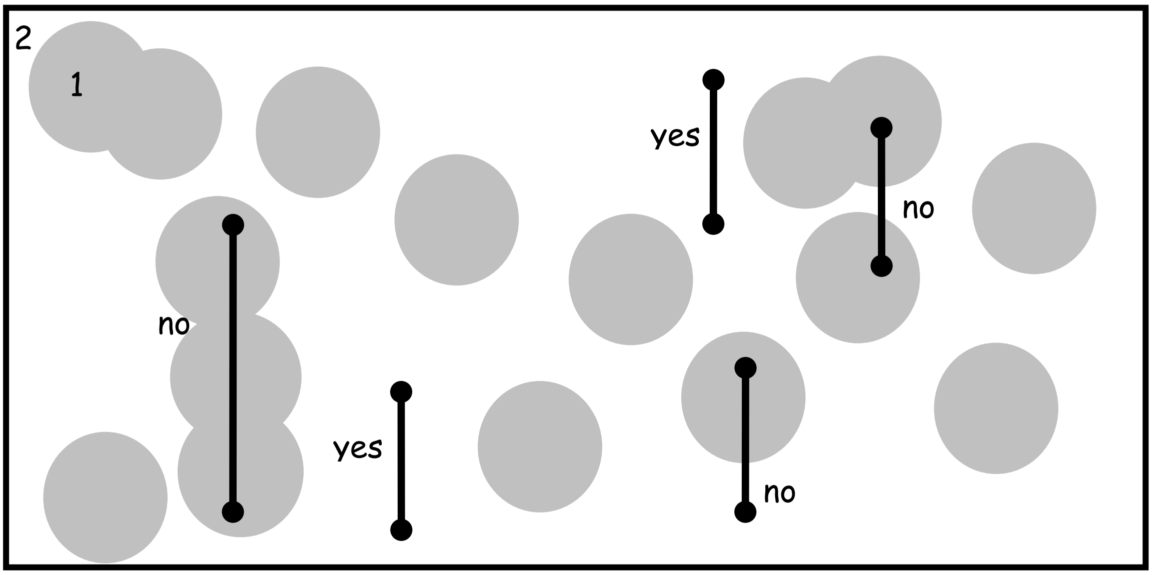

(b)

Figure 2.3.1.1: Cartoon representation of two point probability functions. (a) Two point probability function for the grey phase 1. (b) Two point probability function for the white phase 2.

2.3.1.1 Correlation Function of Binary Map with and without Periodic Boundary Conditions

The computational domain of each binary map is finite. As the scalar distance between random points on the map increases, the total number of potential pairs of sample points decreases. For instance, when the scalar distance is equal to the size of the map, only pairs of points residing on the map edge can be sampled; no other combination is possible. In general, the statistical sample size decreases as the scalar distance between points increases. This affects the accuracy of the correlation function at larger offsets.

To minimize the effect small statistical sizes have on the two point probability function (and thus the correlation function), boundary conditions can be applied on the edge of the map. The most widely used boundary conditions are periodic in character (Gadjdošík et al. 2006; Torquato 2002), which can be easily implemented by replicating the map spatially, as per Figure 2.3.1.1.1 (b). The adoption of periodic boundary conditions ensures statistical consistency with the original map and an increased statistical sample size at larger scalar distances.

Another type of boundary condition, which can be implemented, relies upon deriving statistically equivalent binary maps by transforming the original map by certain types of transformations. These statistically equivalent maps can be added to the edges of the original map in order to expand the computational domain. In particular, the binary map can be rotated 90, 180 and 270 degrees and flipped horizontally about the middle column or flipped vertically about the middle row. A random representation of the original binary map is then formed by randomly rotating or flipping the additional boundary condition maps. This can be seen in Figure 2.3.1.1.1(c).

Alternatively, no boundary conditions can be added to the edge of the map (see Figure 2.3.1.1.1(a)). In which case, the correlation function at long offsets should be disregarded. Figure 2.3.1.1.2 (a) - (b), compares correlation functions extracted from each of type of representation: no boundary conditions (dotted line), periodic boundary conditions (dashed line) and random boundary conditions (solid line) for gas saturations of 6% and 48%. All three curves are in good correspondence for small offsets and thus extraction of the Debye correlation length (see Section 2.3.1.4) from either correlation function will be consistent.

As offsets become large (but still less than half the sample width), there is reasonable correspondence between periodic and random map correlation functions. However, correlation functions extracted from the no B.C map differ significantly. For offsets greater than half the sample width (but still less than the width of the sample) the periodic and random map correlation functions differ. The reason is that the periodic map correlation function is an even function (symmetric) about the mid point of the sample width whilst the random map is not.

Figure 2.3.1.1.3 shows for gas saturations of (a) 6% and (b) 48% that correlation functions extracted from thresholded (binary) maps having periodic (dashed line) and random (solid line-circles) representations are different from correlation functions from non-thresholded maps (continuous) of periodic (dash-dotted line) and random representation (solid line solid circles). Furthermore, there are considerable differences between the non-thresholded correlation functions. This results from the artificial manner in which maps are added to the boundaries of the original map. That is, large differences in pixel values may arise across the map boundaries, destroying the continuous variation of the pixel values. Thus boundary maps should not be added when extracting correlation functions from continuous maps.

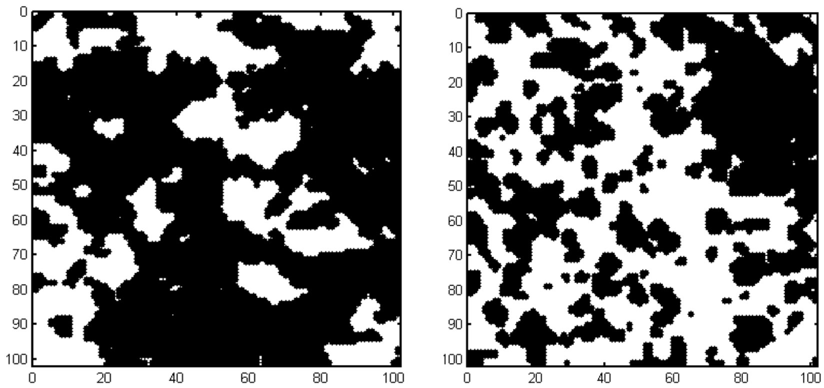

(a) Binary Maps

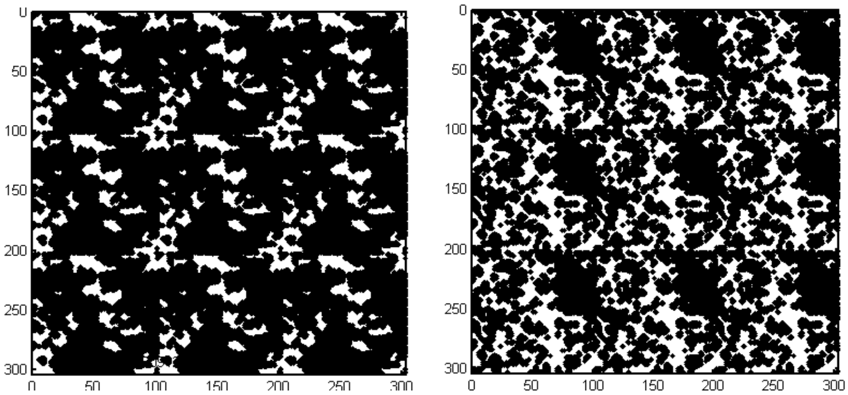

(b) Periodic Representations

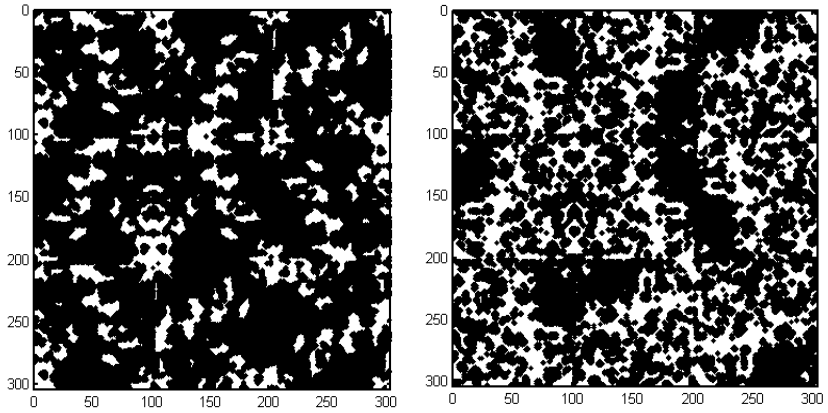

(c) Random Representations

Figure 2.3.1.1.1: Various representations of the binary maps for Scan 11 and Scan 23

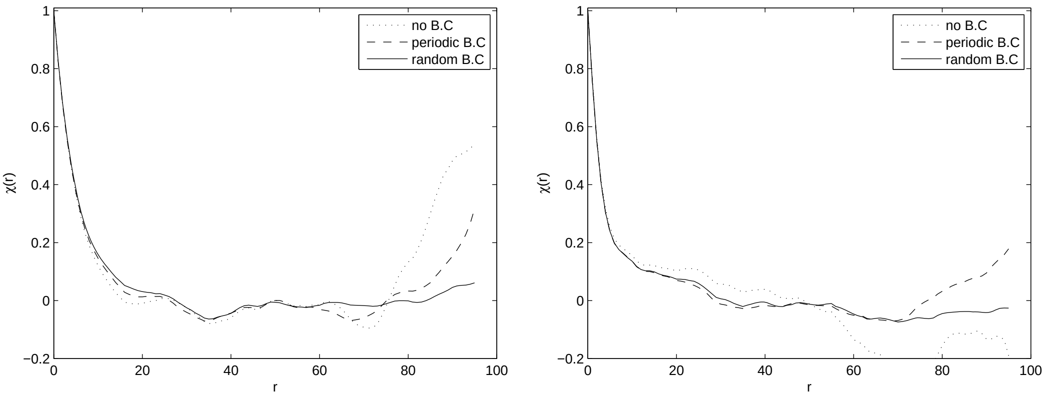

(a) (b)

Figure 2.3.1.1.2: Correlation functions extracted from binary map and its periodic and random representations. (a) Shows for scan 11 and (b) shows for scan 23.

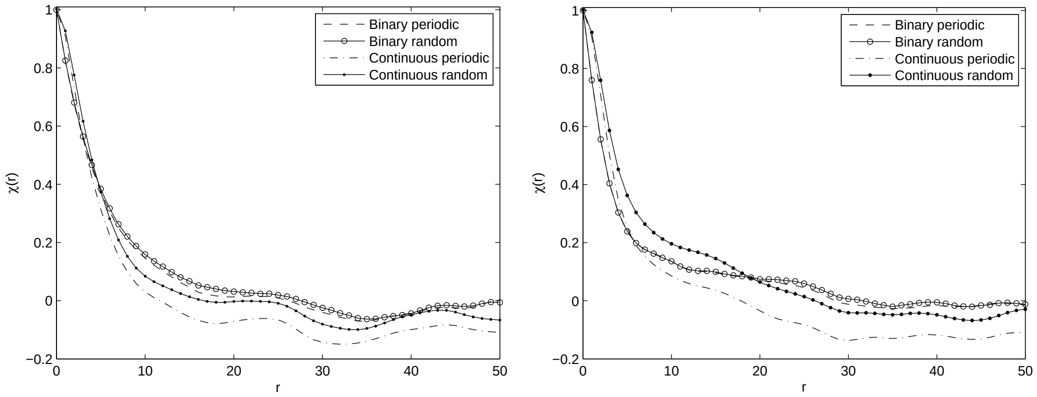

(a) (b)

Figure 2.3.1.1.3 Correlation functions extracted from random representations of binary and continuous media.

2.3.1.2 Correlation Function Testing for Anisotropy

Relations 2.3.1.1 and 2.3.2.2 are applicable for statistically homogeneous and isotropic materials. The first condition implies that the correlation function does not depend on the absolute positions of the points r_1 and r_2, but only on the distance separating the points dr. This is called translational invariance (Berryman 1987; Torquato 2002). See Fig 2.3.1.2.1 (a). The second condition implies that the correlation function does not depend on the orientation of the vector connecting r_1 and $r_2 = r_1 + dr$, relative to some fixed coordinate system. This is called rotational invariance; see Fig. 2.3.1.2.1 (b). Thus, correlation functions obtained by sampling the maps at 0, 45 and 90 degrees should be the same.

For anisotropic statistically homogeneous materials the correlation function is

$$\chi(\vec{r}_2) = \left\langle I^{(1)}(\vec{r}) - \varphi_1 \right\rangle \left\langle I^{(1)}(\vec{r} + \vec{r}_2) - \varphi_1 \right\rangle = \left\langle I^{(2)}(\vec{r}) - \varphi_2 \right\rangle \left\langle I^{(2)}(\vec{r} + \vec{r}_2) - \varphi_2 \right\rangle \qquad (2.3.1.2.1)$$

where $\vec{r}$ and $\vec{r}_2$ are vectors. It depends on the magnitude of vector $|\vec{r}_2|$ and its orientation. The two point probability function can also be modified appropriately for anisotropic media.

The correlation functions extracted in Section 2.3.1.1 are obtained by: (1) sampling the map in two orthogonal directions at orientations of 0 and 90 degrees relative to map edges, thus forming vertical (Ver) and horizontal (Hor) correlation functions. (2) By taking the average of both correlation functions. In Fig. 2.3.1.2.2 (a) the vertical and horizontal correlation functions are plotted for binary map (BM Scan 11) and for the periodic map (PM). There are significant differences between vertical and horizontal correlation functions of both maps. Furthermore, the anisotropy inherent in the binary map (differences in the vertical and horizontal correlation functions) is directly reflected in the correlation functions extracted from the periodic map. This is evident as correlation functions at the same orientation are in close correspondence for each map type.

On the other hand, in Fig. 2.3.1.2.2 (b) the vertical and horizontal correlation functions are plotted for periodic and random maps (Scan 11). Only small differences exist in the correlation functions (RM ver and RM hor) extracted from the random map. Thus anisotropy present in the single binary map is not reflected in its random map representation. Thus, small differences will exist in the average periodic and random correlation functions (PM/RM ver + PM/RM hor) when maps are anisotropic.

For the rest of the Section 2.3.1 statistics will be extracted from random map representations of the binary maps, as there is greater accuracy at longer offsets and anisotropy is reduced.

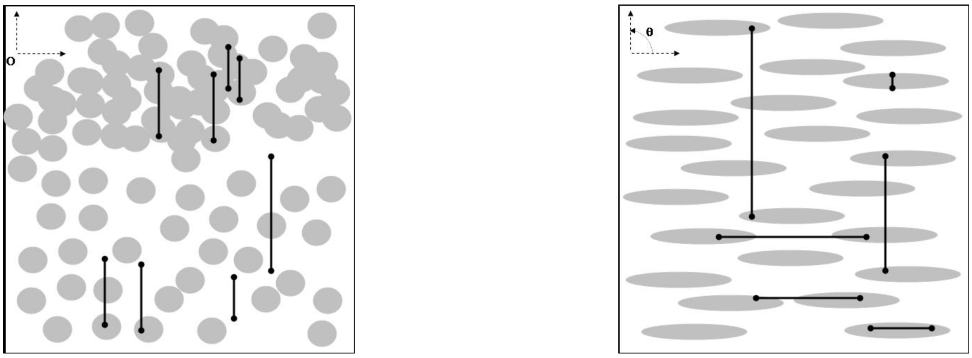

(a) (b)

Figure 2.3.1.2.1: Cartoon representations of statistically inhomogeneous and anisotropic media. (a) Statistically inhomogeneous media: $S_2(r_1,r_2)$ *will depend on the absolute positions of* r_1,r_2 *relative to the origin, as the top and bottom regions of the model are densely and sparsely populated by overlapping spheres. (b) Statistically anisotropic media:* $S_2(r_1,r_2)$ *will depend on the orientation of the vector connecting* r_1,r_2.

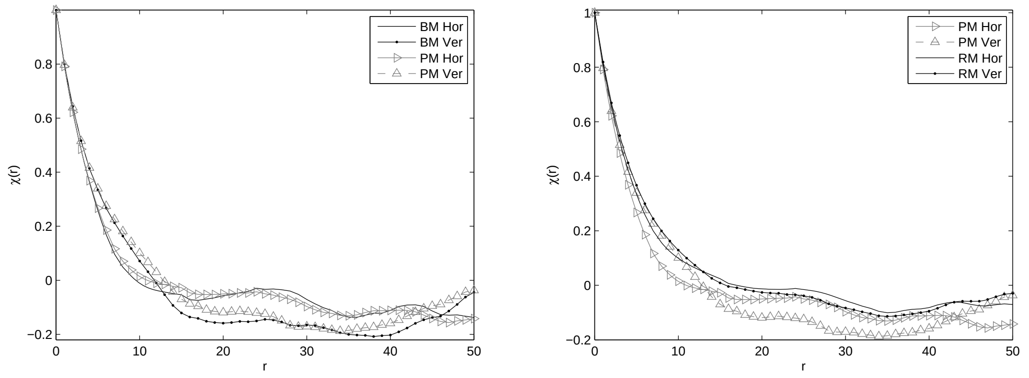

(a) (b)

Figure 2.3.1.2.2: Correlation functions extracted horizontally (Hor) and vertically (Ver) across different heterogeneity maps. (a) Shows the correlation functions extracted from the binary (BM) and periodic maps (PM). (b) Shows the correlation functions extracted from the periodic (PM) and random maps (RM). The application of random boundary conditions produces statistically isotropic media from anisotropic media.

2.3.1.3 Correlation Function versus Relative Percentage Fluid Saturation

The objective of this section is to access whether the correlation function is sensitive to changes in percentage fluid saturation. To this end, I extract correlation function from random map representations for the sample MGL2a. By visual inspection of the shape of the correlation functions two predominant sets are identified. The first set contains correlation functions which have an exponentially decreasing appearance, whilst the second set contains correlation functions of a different shape.

In Figure 2.3.1.3.1 (a) the first group of correlation functions are plotted. The relative percentage fluid saturation is shown in the legend. There are only small observable differences between each correlation function. Also plotted is the average of these correlation functions (thick dashed line) obtained by taking the mean of this group. The un-normalised variance is shown in Figure 2.3.1.3.2 (b) (dotted line with circles). In Figure 2.3.1.3.1 (b) the second group of correlation functions are plotted. There are no real observable differences between each correlation function. The average correlation function of this set (thick dashed line) is plotted and the variance between correlation functions at various saturations is shown in Figure 2.3.1.3.2 (b) (dotted line with crosses).

Note, the first set of correlation functions are obtained from random maps of low gas saturations (<23%), whilst the second set are obtained from random maps of higher gas saturations (>23%). Comparison of the average correlation functions for each group (Figure 2.3.1.3.2 (a)) shows that the shape of each curve is different.

On the basis of Figures 2.3.1.3.1 and 2.3.1.3.2, it appears that correlation functions are only sensitive to changes in fluid saturation below a critical percentage (here it is approximately 23%). Above this value there are only minor changes in the correlation function as gas saturation is increased (the variance shows that small changes occur around the Debye correlation length, Section 2.3.1.5). However, it must be noted that at greater X-ray tomographic resolutions the correlation functions may show an increased dependence on gas saturation (when percentages are high). That is, perhaps differences cannot be observed at mesoscale resolution.

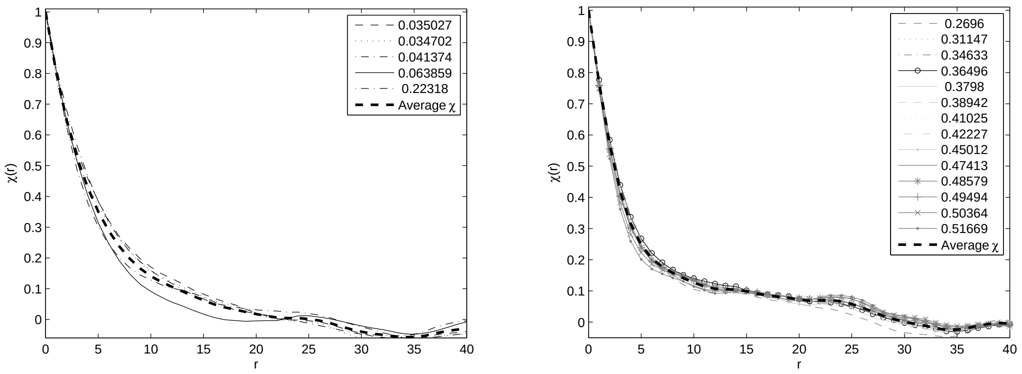

(a) (b)

Figure 2.3.1.3.1: Correlation functions extracted from random binary maps of MGL2a divided into saturation sets. (a) $\chi(r)$ small gas saturation and (b) $\chi(r)$ large gas saturation.

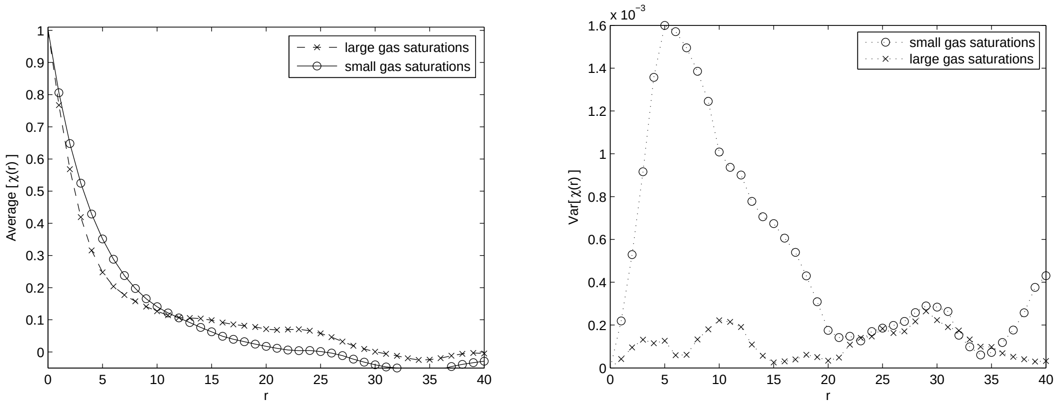

(a) (b)

Figure 2.3.1.3.2 Average correlation functions and variance of correlation functions. (a) Average of each set of correlation functions extracted from maps having small (line with circles) and large gas saturation (dashed line with crosses). (b) The variance of each set of small (dotted line with circles) and large gas saturation (dotted line with crosses).

2.3.1.4 Correlation Function versus Rock Type

Percentage fluid saturation influences the shape of the correlation function (as shown in Figures 2.3.1.3.1 and 2.3.1.3.2), but it is not the only influencing factor. In Fig. 2.3.1.4.1 (a) the average correlation function and (b) variances (for gas saturations greater than the critical percentage) are shown for three different types of rocks: MGL 8 (crosses), MGL 6 (circles) and MGL2a (triangles). The average correlation functions (in Fig 2.3.1.3.1 (a)) differ in shape.

As the average correlation function for each rock type is obtained from maps having gas saturations greater than the critical percentage, the shape differences are not caused by different percentages of gas. But rather it is a consequence of each rock having different fluid transport properties; that is porosity and permeability variations (wettability characteristics may not play a significant role here as all rock are of similar type, i.e. composed of the same mineral grains, etc). Unfortunately, experimental measurements of rock porosity and permeability are not known for these rock samples.

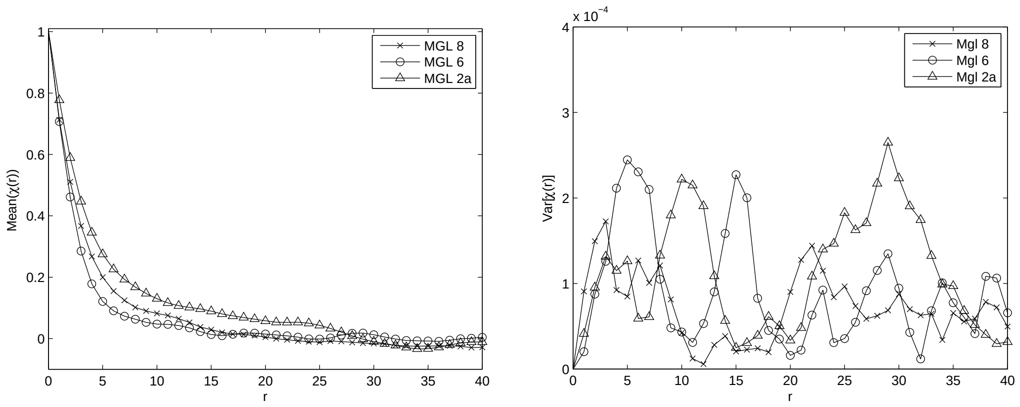

(a) (b)

Figure 2.3.1.4.1: Average correlation function and variance of correlation functions obtained from binary maps of MGL2a, MGL6 and MGL8 at large gas saturation. (a) Shows the average correlation functions for MGL2a (line with triangles), MGL6 (line with circles) and MGL8 (line with crosses). (b) Shows the variance in the set of correlation functions obtained from each rock sample.

2.3.1.5 Correlation Lengths

There are a host of different types of length scales which can be derived from a correlation function. Two common ones are the “Debye” and “mean” length scale. The first length scale can be derived from the correlation function by assuming that the binary map is a Debye random material (Debye & Bueche 1949). That is, for structures in which one phase consists of random shapes and sizes, the correlation function obeys

$$\chi(r) = \exp\left(\frac{-r}{a}\right). \tag{2.3.1.4.1}$$

Here a is the Debye correlation length which is defined as $\chi(a) = 1/e$ and e is Boltzman’s constant, see Fig 2.3.1.5.1.

The second length, termed here as the mean length is derived from the correlation function as

$$l_m = \left\{ \int_0^\infty r\chi(r)dr \right\}^{1/2} . \qquad (2.3.1.4.2)$$

This length scale arises in rigorous bounds on the fluid permeability and trapping constant of three dimensional isotropic random porous media (Berryman & Blair 1987, Torquato 2002). If the correlation function in Equation (2.3.1.5.2) is an exponentially decreasing function (Eq. 2.3.1.5.1), the mean length scale is equal to the Debye length scale $l_m = a$.

Any length scale derived from a correlation function will produce a length scale representative of the average spatial properties of the medium (a consequence of Eq. 2.3.1.2). That is, the Debye or permeability lengths are a measure of how coarse or fine the material is rather than indicating an average size of either phase. Thus, either length scale (2.3.1.4.1 or 2.3.1.4.2) derived from the correlation function will not indicate the size of the gas or water patches within the binary map.

Figure 2.3.1.5.2, shows the Debye correlation length extracted from the correlation functions of samples MGL 2a (circles), MGL 6 (asterixis) and MGL 8 (plus signs). It shows that the Debye length of MGL 2a decreases as gas saturation increases. The decrease is approximately linear. The Debye length of MGL 8 also decreases approximately linearly with saturation and a simular trend can be observed with MGL 6. Note that, the variances extracted in the previous section indicate that small changes in the correlation functions occur around the Debye correlation length. Thus these results are perfectly consistent with the conclusion that the correlation function is mostly insensitive to percentage fluid saturation at large gas saturations.

By analysing the mean correlation functions for MGL 2a at both low and high gas saturations, an interesting observation can be made. It appears that the mean correlation function for small gas saturations (solid line) is approximated well by a Debye correlation function (dotted line) with correlation length of $a = 3.5$; see Fig. 2.3.1.4.3. On the other hand, at high gas saturations there is only a good correspondence between the mean correlation function (dashed line) and the Debye correlation function (dashed-dotted line) at small offsets. This was also observed for MGL 6 (not shown here).

In Figure 2.3.1.4.4 the mean correlation function for large gas saturations (MGL 2a) is approximated well by two Debye correlation functions: one which models small offset behaviour χ_{Small} and one which models large offset behaviour $\chi_{L\arg e}$. That is,

$$\chi_2(r) = \chi_{Small} + \chi_{L\arg e} = b_S \exp\left(-\frac{r}{a_S}\right) + b_L \exp\left(-\frac{r}{a_L}\right) = b_S \exp\left(-\frac{r}{a_S}\right) + (1 - b_s)\exp\left(-\frac{r}{a_L}\right) \qquad (2.3.1.4.3)$$

where b_S, b_L are weighting coefficients of the correlation functions (with $1 > b_S > b_L > 0$), whilst a_S, a_L are the usual Debye correlation lengths (with $a_L > a_S > 0$). In Table 2.3.1.4.1, $\chi_2(r)$ is given for the mean correlation functions for large gas saturations of: MGL 2a, MGL 6, and MGL 8.

Table 2.3.1.4.1: Double Debye coefficients

Data	a_S	b_S	a_L	b_L	RMSE
MGL2a	2.30	0.73	12.28	0.27	0.02234
MGL 6	2.02	0.93	12.58	0.07	0.01357
MGL 8	2.77	0.85	9.11	0.15	0.01153

On the basis of this three conclusions could be made regarding fluid distribution versus saturation.

1) **Decrease the correlation length linearly as gas saturation is increased.**
2) **Small gas saturations $v_1 \leq 20\%$ can be approximated well by a single Debye correlation function.**
3) **Large gas saturations $v_1 \geq 20\%$ can be approximated reasonably well by two Debye correlation functions which are weighted.**

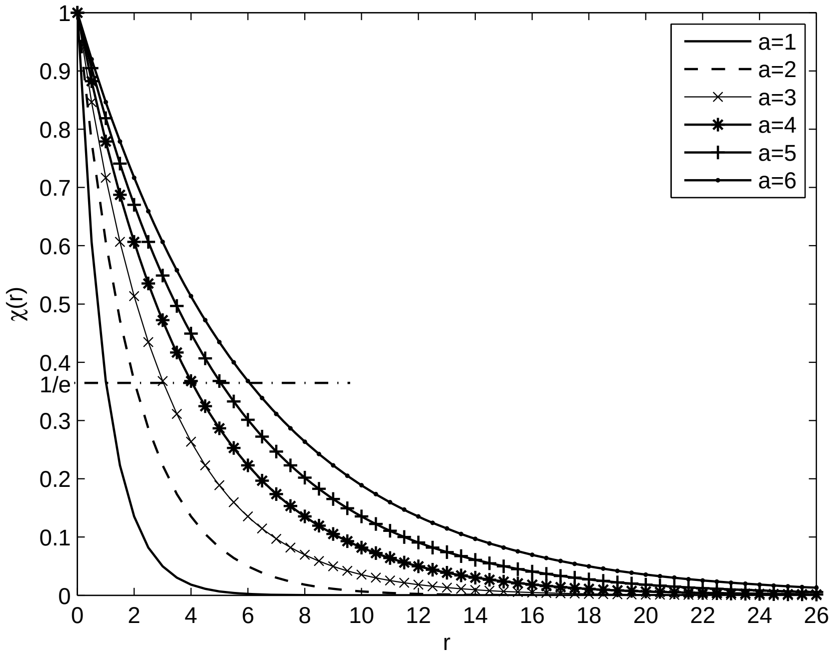

Figure 2.3.1.5.1: The Debye correlation function shown at different correlation lengths.

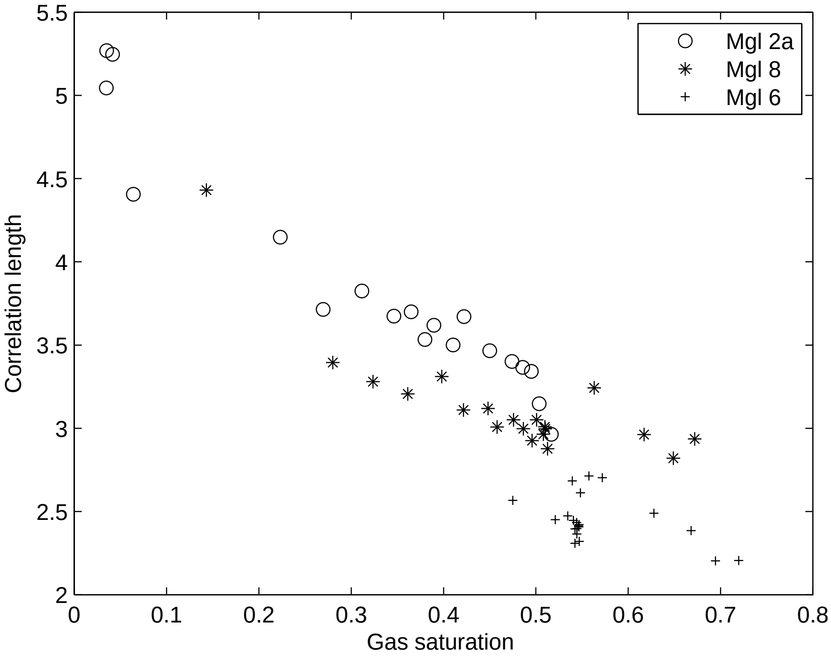

Figure 2.3.1.5.2: The Debye correlation lengths for different gas saturations for MGL 2a, MGL 6 and MGL 8.

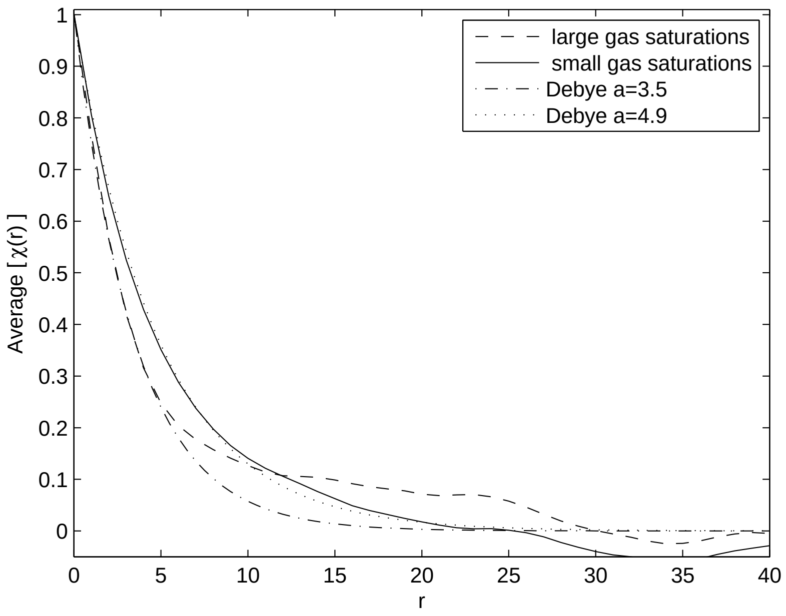

Figure 2.3.1.5.3: The Debye correlation function having different correlation lengths is compared against the average correlation functions of MGL2a.

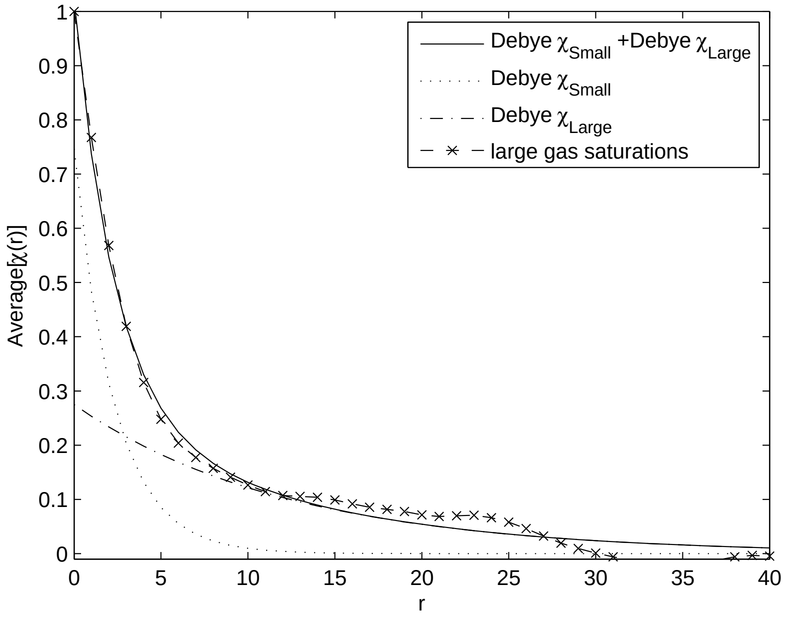

Figure 2.3.1.5.4: The average correlation function at large gas saturations is approximated by two Debye correlation functions χ_{Small} *and* $\chi_{L\arg e}$.

2.3.2 Linear Path Function

To shed light on what sort of spatial information is contained in different types of microstructural functions, such as the correlation function and the linear path function, it is useful to perform reconstruction studies. Such studies involve the following stages:

1. (1) a target model is sampled using the microstructural function of interest.
2. (2) An initial starting model is chosen and sampled using the microstructural function
3. (3) The initial starting model is perturbed (in some way) and sampled by the microstructural function. This is repeated until the microstructural function is the same as that of the target model (the real image).
4. (4) The final model is compared against the target model.

The reconstruction of 1-dimensional models of randomly positioned overlapping rods (Yeong & Torquato 1998a) and 2-dimensional models of randomly positioned overlapping discs (Yeong & Torquato 1998b) indicates what sort of descriptive information is contained in the correlation and linear path functions. It was found that reconstruction procedures which target only a correlation function produce models having the distribution characteristics of the original model, but not the clustering characteristics, whilst procedures which solely target the linear path function reproduce clustering characteristics, but not distribution characteristics. Moreover, optimum reconstruction strategies were ones which targeted both the correlation function and the linear path function simultaneously, thus generating models which “most closely” resembled the original models.

This suggests that the correlation function and volume concentration extracted together will contain necessary but not sufficient information to fully describe fluid saturation patterns. Furthermore, changes in fluid saturation patterns may not be quantifiable in terms of the correlation function as it may not be the most sensitive measure. Thus, in the following sections several other statistical measures will be extracted, such as the linear path function (this section), chord length density function (Section 2.3.3) and cluster statistics (Section 2.3.4). We would like to assess whether these other types of statistics are better suited to quantifying changes in fluid saturation patterns associated with changes in gas saturation.

The linear path function $L^{(i)}(dz)$ is defined for a statistically isotropic material as the probability that a line segment of length dr lies completely in either subdomain when randomly thrown into the sample (Torquato 2002), Fig. 2.3.2.1. That is, $L^{(1)}(dr)$ is the probability that a line segment of length dr lies entirely in the gas saturated domain, whilst $L^{(1)}(dr)$ is the probability that a line segment of length dr lies entirely in the water saturated domain. As the length of the line segment dr increases, the linear path functions $L^{(i)}(dz)$ will decrease monotonically, because the space available in either subdomain decreases with increasing dr. Thus, the limiting values for the linear path functions for small and large line segments are $\lim_{dz\to 0} L^{(i)}(dz) = \varphi_i$ and $\lim_{dz\to\infty} L^{(i)}(dz) = 0$. In particular, the linear path function contains some information on the connectivity $L^{(1)}(z) + L^{(2)}(z) + L^{(12)}(z) = 1$

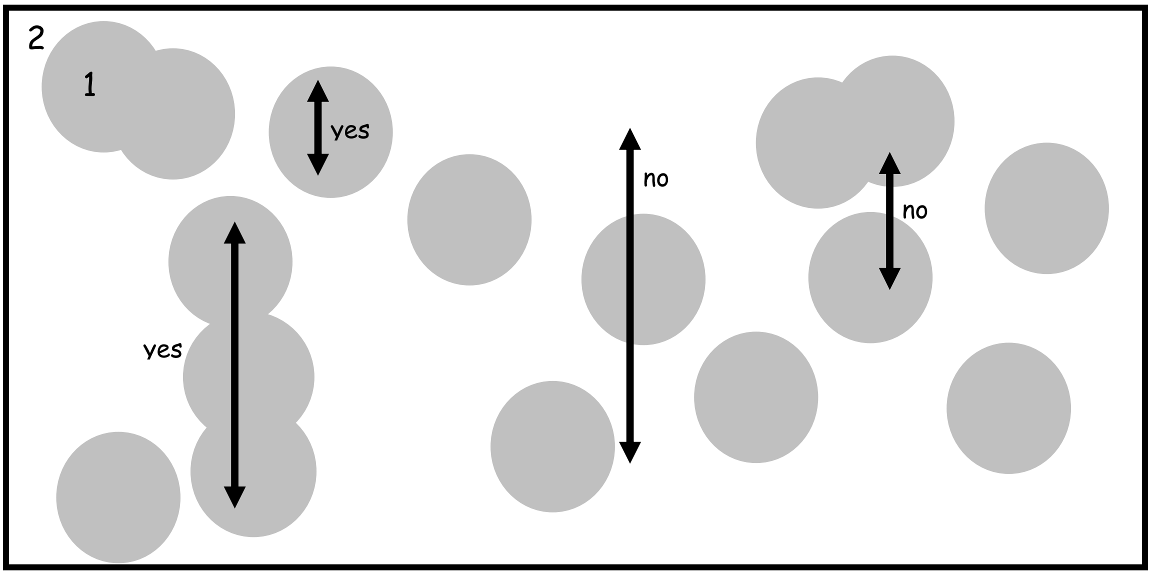

(a)

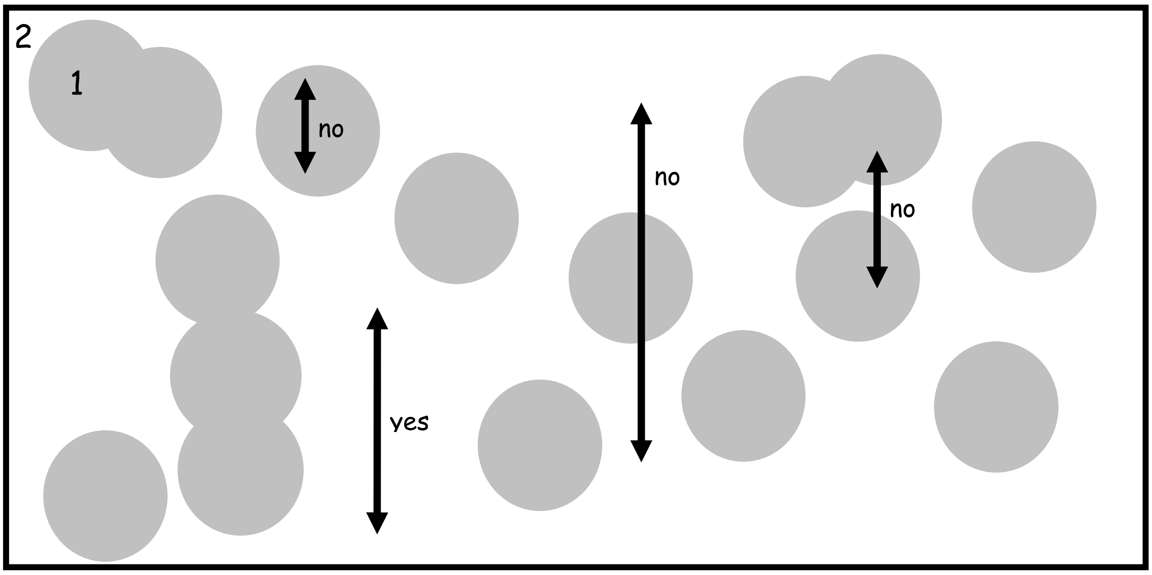

(b)

Figure 2.3.2.1: Cartoon representations of the linear paths. (a) Linear paths for phase 1 and (b) for phase 2.

Figure 2.3.2.2 shows the linear path function for the gas saturated and water saturated domains during the initial stages of the drainage experiment (i.e. small gas saturations). There initially is a clear separation in the linear paths of each domain. As gas saturation increases the linear path function of the gas saturated domain broadens and the linear path function of the water saturated domain sharpens. As gas saturation is increased further (Figure 2.3.2.3) the linear path functions for the gas saturated and water saturated domains converge. This suggests that linear paths of the two different domains are constant as saturation increases.

Analysis of the linear path function in addition to the correlation function indicates that:

1) The fluid saturation patterns during the later stages of the drainage experiment (i.e. high gas saturations) don’t change significantly. The correlation function which characterised the distribution of fluids and the linear path function which characterises connectedness (in a linear path) are both relatively constant.
2) The fluid pattern during the initial stages of the drainage experiment (i.e. small gas saturations) changes significantly with saturation.
3) During the initial stages of the drainage experiment there is a clear separation of length scales between the water saturated domain and the gas saturated domain. For the rest of the experiment there is not a clear separation between the length scales.

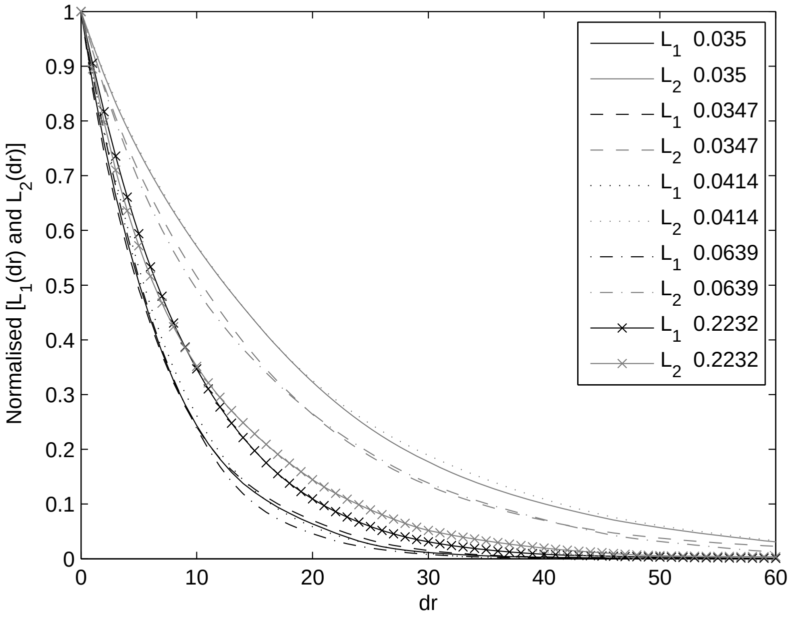

Figure 2.3.2.2 : The linear path function for the gas $L^{(1)}(dr)$ *and water* $L^{(2)}(dr)$ *saturated domain during the initial stages of the drainage experiment.*

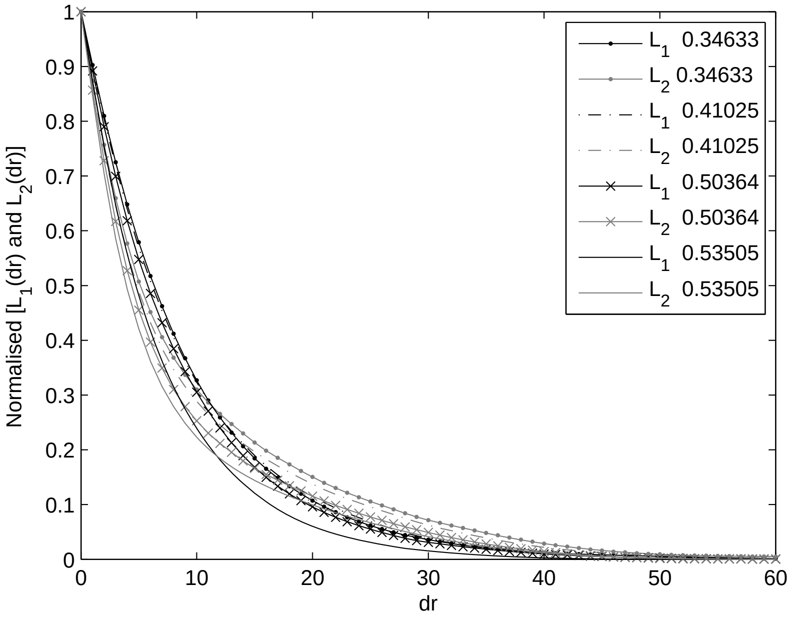

Figure 2.3.2.3: The linear path function for the gas $L^{(1)}(dr)$ *and water* $L^{(2)}(dr)$ *saturated domain during the final stages of the drainage experiment.*

2.3.3 Chord Length Density Function

The chord length density function $p^{(i)}(dr)$ is defined as the probability of finding a chord of length between r and $r+dr$ in subdomain i (Lu & Torquato 1992). It is related to the linear path function by

$$p^{(i)}(dr) = \frac{l_C^{(i)}}{\varphi_i}\frac{d^2 L^{(i)}(dr)}{dr^2} . \qquad (2.3.3.1)$$

Conceptually speaking chords are all of the line segments between the intersections of an infinitely long line with the subdomain interfaces, as shown in Figure 2.3.3.1. From the chord length density function the mean chord length can be derived by

$$l_C^{(i)} = \int_0^\infty r p^{(i)}(r) dr . \qquad (2.3.3.2)$$

The mean chord length is related to the specific surface area via

$$l_C^{(i)} = \begin{cases} \frac{2\varphi_i}{d}, & d = 1 \\ \frac{\pi\varphi_i}{s_v}, & d = 2 \\ \frac{4\varphi_i}{s_v}, & d = 3 \end{cases} . \qquad (2.3.3.3)$$

Figure 2.3.3.2 (a) shows the chord length density function for the gas saturated domain during the initial stages of the drainage experiment on MGL 2a. As gas saturation is increased, the probability of chords of width 2-3 pixels increases. For the smallest gas saturations the chord length density function has an exponential shape (solid line and dashed line). This is most likely a result of noise during the initial scans (which may be greater than the mean threshold of the map). As gas saturation increases further the shape of the probability density function becomes more bell like, with the most probable chord lengths having widths of 2 to 5 pixels. Similarly, the chord length density function of water (shown in (b)) has a bell like shape and peaks around 2 to 5 pixels with probabilities increasing as gas saturation increases.

Fig.2.3.3.2 (c) and (d) show the probability density function for the gas and water saturated domains during the later stages of the drainage experiment. As gas saturation increases there is very little change in the chord length density functions for either subdomain except within the 2-5 pixel range, where probabilities still increase with gas saturation.

Fig. 2.3.3.2 (e) shows the mean chord lengths for the gas (asterixis) and water (circles) saturated domains derived using Equation (2.3.3.2). As gas saturation increases, the mean chord length for the gas saturated domain decreases, whilst the mean chord length of the water saturated domain increases. (f) Shows the specific surface derived using the mean chord lengths (via Eq (2.3.3.3)) of (e). There is a large discrepancy between the specific surfaces obtained from the mean chord length of the gas saturated patches (asterixis) and from the mean chord lengths of the water saturated patches (circles). Certainly, the mean chord lengths for the gas saturated patches should be more accurate then the mean chord lengths of the water saturated patches for lower gas saturations, as the gas patches are distinct and isolated (keeping in mind that noise may be a factor at very small gas saturations). For lower gas saturations there are very few lengths which are counted as water saturated chords, because they may not intersect the gas water interface at the two end points (see Figure 2.3.3.1 (b)).

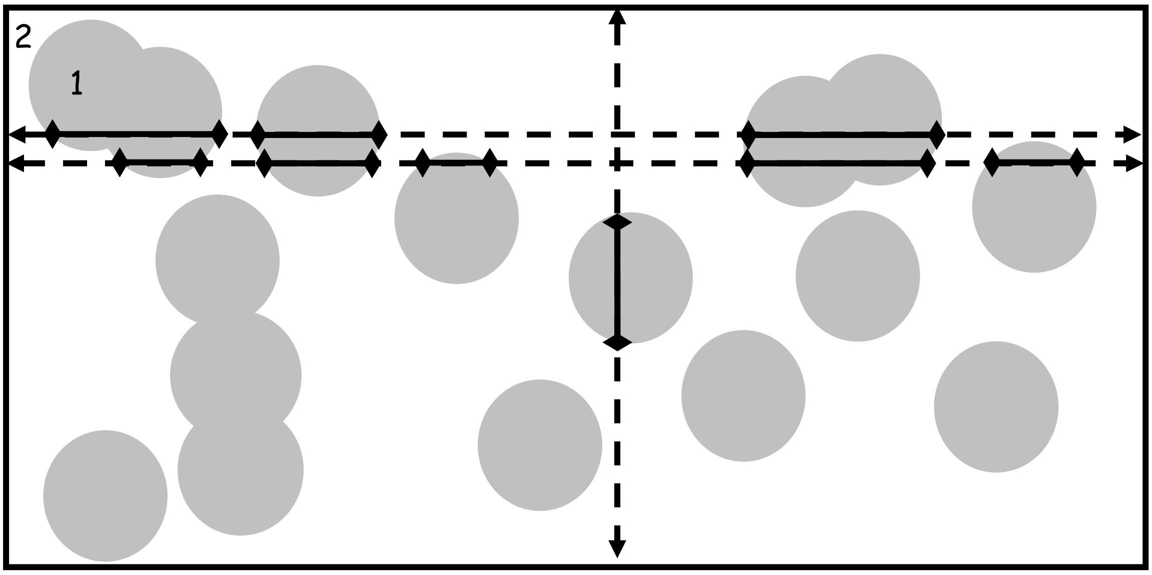

(a)

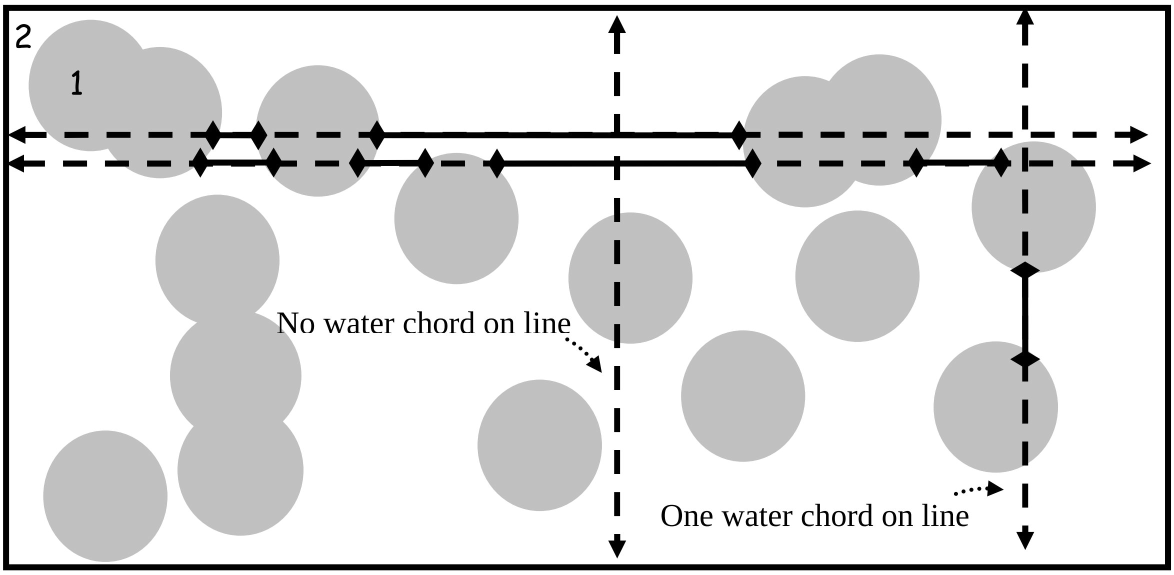

(b)

Figure 2.3.3.1: Cartoon representation of chord lengths. (a) Shows the chord lengths (solid line with bars situated on the domain interface) which contribute to the chord length density function for subdomain 1 and (b) subdomain . The dashed lines represent infinite lines laid down over the map.

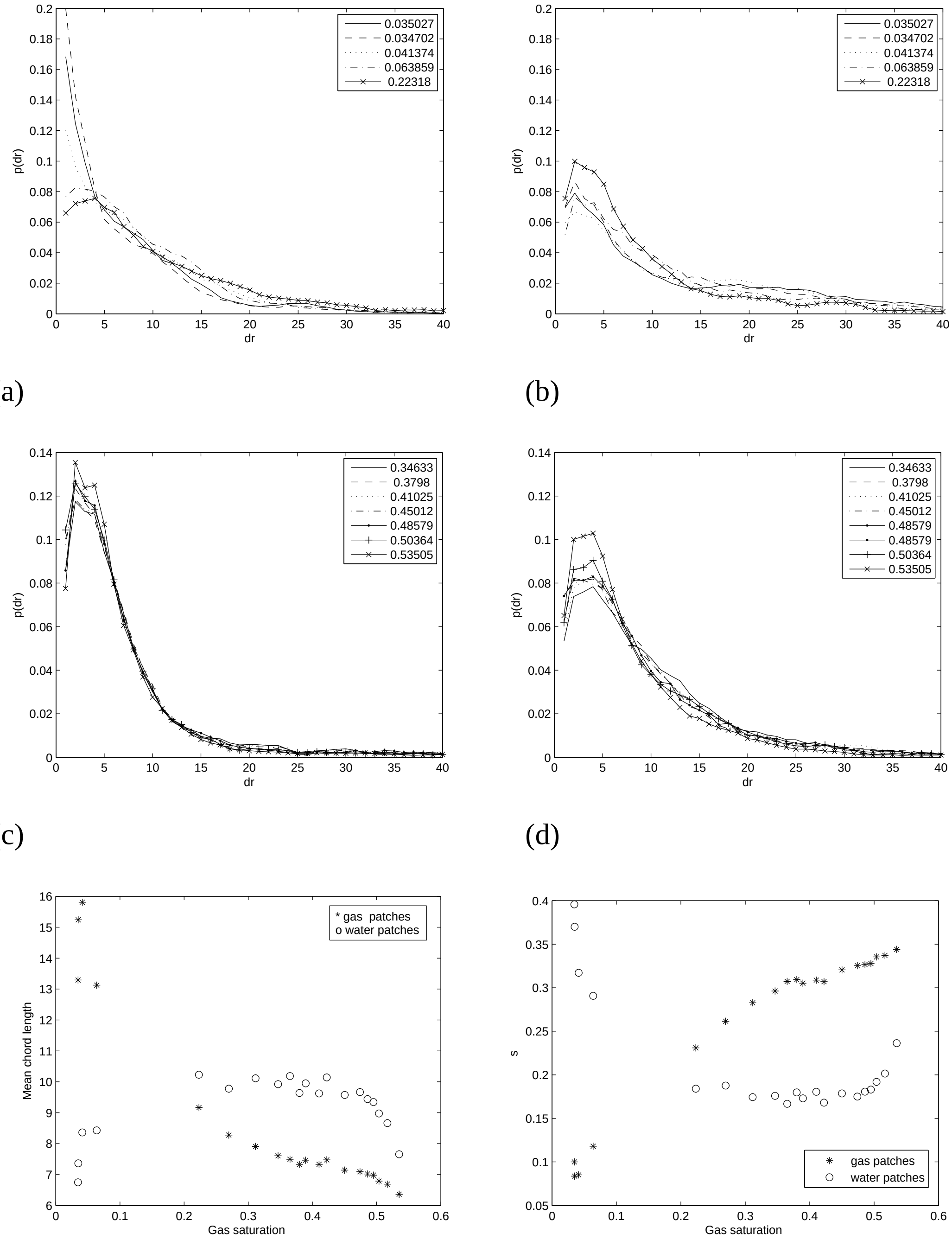

(a) (b)

(c) (d)

(e) (f)

Figure 2.3.3.2 Chord length density functions during the initial and final stages of the drainage experiment. (a) Shows gas and (b) water saturated domain during the initial stages (final (c) and (d)) of the drainage experiment. (e) Mean chord lengths for the gas and water saturated patches and (f) specific surface.

2.3.4 Cluster Statistics

A cluster of subdomain i refers to that region of subdomain i which can be reached from a point in subdomain i without passing through subdomain $j, (j \neq i)$ (Torquato et al. 1988). That is, a set of pixels which belong to the gas saturated subdomain will form a cluster when every member of that pixel set can be accessed via at least one pathway consisting entirely of pixels belonging to the gas saturated subdomain, see Figure 2.3.4.1.

To identify clusters within the gas saturated subdomain (or water saturated subdomain) the Hoshen and Kopelman (1976) cluster labelling algorithm was implemented. The output of this algorithm is cluster labels and cluster numbers for each separate cluster label.

In Figure 2.3.4.3 cluster labels are shown for (a) gas and (b) water saturated subdomains of Scan 8, respectively. The colour bar (in a and b) shows the number of different clusters in each map. In (a) there is over 60 different gas clusters, whilst in (b) there is only 14 different water clusters. In (c) gas and (d) water cluster numbers are shown for each different label. The colour bar (in c and d) shows the population of pixels in each cluster. The largest gas cluster in Scan 8 has a population of over 700 pixels, whilst the largest water cluster in Scan 8 has a population over 6000 pixels.

In Figure 2.3.4.4 cluster labels are shown for (a) gas and (b) water saturated subdomains of Scan 15, respectively. The colour bar shows the number of different clusters in each map. In (a) there are 14 different gas clusters, whilst in (b) there are 47 different water clusters. In (c) gas and (d) water cluster numbers are shown for each different label. The colour bar (in c and d) shows the population of pixels in each cluster The largest gas cluster in Scan 8 has a population of over 5000 pixels, whilst water cluster in Scan 8 has a population of approximately 2000 pixels.

Comparison of Figures 2.3.4.3 (a) and 2.3.4.4 (a) show that with increasing gas saturation the total number of gas clusters decreases from 60 to 14 clusters; whilst the average number of pixels belonging to a single cluster decreases (as seen in Figures 2.3.4.3 (c) and 2.3.4.4 (c)). This arises because the gas clusters within scan 8 join up to form one major cluster in scan 15. Conversely, when gas saturation increases the number of water clusters increases from 13 (in Figure 2.3.4.3 (b)) to 46 (in Figure 2.3.4.4 (b)); whilst comparison of Figure 2.3.4.3 (d) and 2.3.4.4 (d) show that there is one dominant water cluster at low gas saturation and an increasing number larger populated water clusters at larger gas saturations.

When all of the different clusters within the gas saturated subdomain (or water saturated subdomain) are identified, it is possible to decompose the two point probability function $S^{(i)}(r_1, r_2)$ into two different types of probability functions

$$S^{(i)}(r_1, r_2) = C^{(i)}(r_1, r_2) + E^{(i)}(r_1, r_2)\,. \tag{2.3.4.1}$$

Here $C^{(i)}(r_1, r_2)$ is the cluster function which is the probability of finding two points at positions r_1 and r_2 that belong to the same cluster of subdomain i, whilst $E^{(i)}(r_1, r_2)$ is the blocking function which is the probability of finding two points at positions r_1 and r_2 which belong to different clusters of subdomain i, refer to Figure 2.3.4.2.

Decomposition of the two point probability function $S^{(i)}(r_1, r_2)$ into $C^{(i)}(r_1, r_2)$ and $E^{(i)}(r_1, r_2)$ gives information on “connectedness” and “disconnectedness” within the map. The same basic algorithm which was employed in Section 2.3.1 to extract $S^{(i)}(r_1, r_2)$ can be employed to determine $C^{(i)}(r_1, r_2)$ and $E^{(i)}(r_1, r_2)$ from the cluster labelled maps (see Figure 2.3.4.3 (a) and (b) and 2.3.4.4 (a) and (b)).

Here no boundary conditions are added to extend the binary map domain (see Section 2.3.1.1) as this may create artificial cluster information. For instance, what may be labelled as two different gas saturated clusters in the single binary map could be labelled as one single cluster when boundary condition maps are added to single binary map. This would arise when the boundary maps provide a connecting path of pixels between the two different clusters within the binary map.

Figure 2.3.4.5 (a) shows three different probability functions for scan 8. They are the two point probability function $S^{(i)}(r_1, r_2)$ (solid line) which is decomposed into the cluster probability function $C^{(i)}(r_1, r_2)$ (dashed line with crosses) and the blocking probability function $E^{(i)}(r_1, r_2)$ (dashed-dotted line). The contribution made by the cluster function to the two point probability function decreases as the scalar distance between points increases; whilst the contribution made by the blocking function increases as the scalar distance between points increases. Evidently for scan 8, the two point probability function does not accurately convey information on gas patch connectedness throughout the binary map as there are significant differences between the two point probability function and connectedness function as offset increases.

Figure 2.3.4.5 (b) shows three different probability functions for scan 15. They are the two point probability function $S^{(i)}(r_1, r_2)$ (solid line) which is decomposed into the cluster probability function $C^{(i)}(r_1, r_2)$ (dashed line with crosses) and the blocking probability function $E^{(i)}(r_1, r_2)$ (dashed-dotted line). The contribution made by the blocking function to the two point probability function is insignificant, as there is close correspondence between the cluster function and the two point probability function. Evidently when there is one large gas cluster the two point probability function (for gas saturation) captures information on connectedness.

To summarise, the use of cluster statistics and decomposition of the two point probability function provides valuable insight into the spatial distribution of pore fluids. The cluster statistics are useful for assigning inclusion/host fluid relationships, when there are large differences between cluster numbers and cluster populations. Although only shown here for gas saturated domains, decomposition of the two point probability function into blocking and cluster functions provides a measure of connectedness and disconnectedness of fluid heterogeneities on the mesoscale.

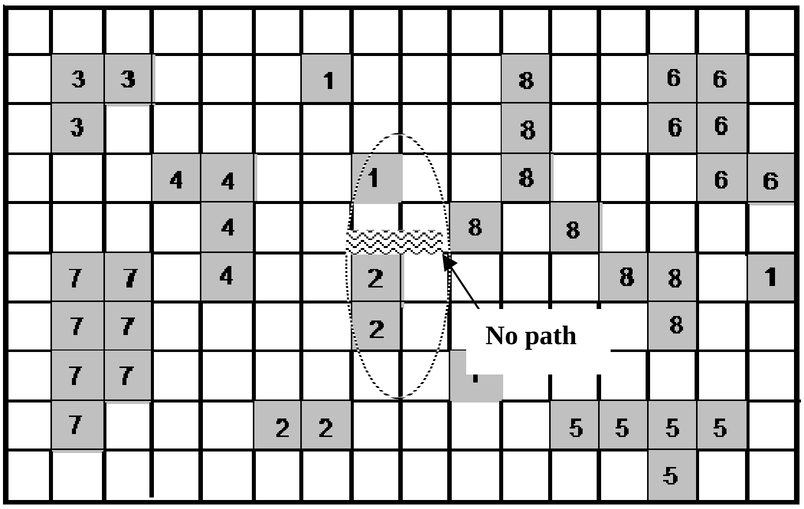

Figure 2.3.4.1: Clustering pixels. The grey and white pixels belong to different subdomains. There are four different clusters of size 1 and two different clusters of size 2 and one cluster of sizes 3, 4, 5, 6, 7, and 8. The grey pixels enclosed in the ellipse are not part of the same cluster as a path which connects the clusters that consists entirely of grey pixels doesn't exist.

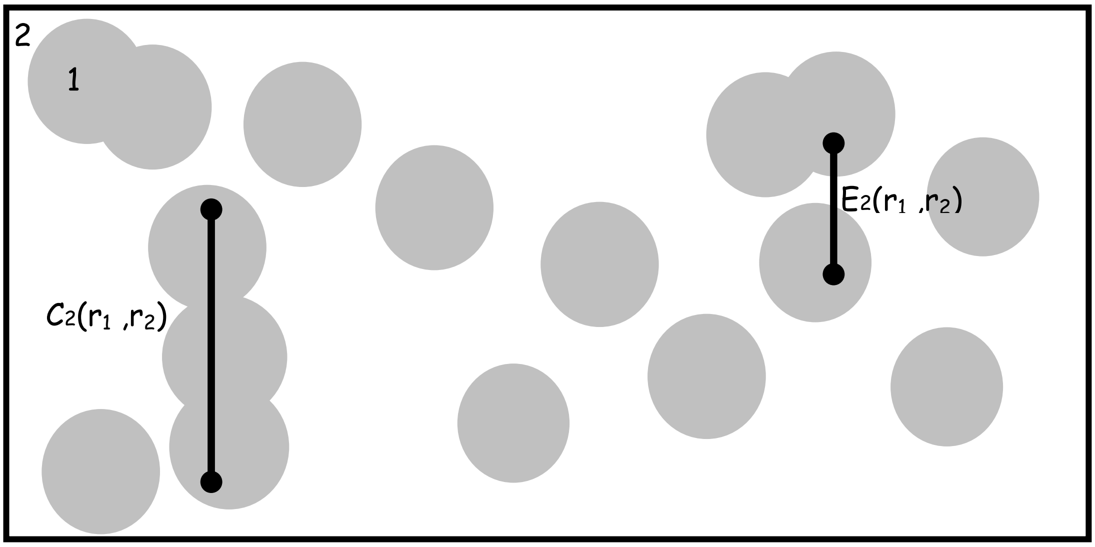

Figure 2.3.4.2: Cartoon representation of two point probability functions. The two point probability function $S^{(i)}(r_1,r_2)$ *can be decomposed into the cluster probability function* $C^{(i)}(r_1,r_2)$ *and the blocking probability function* $E^{(i)}(r_1,r_2)$.

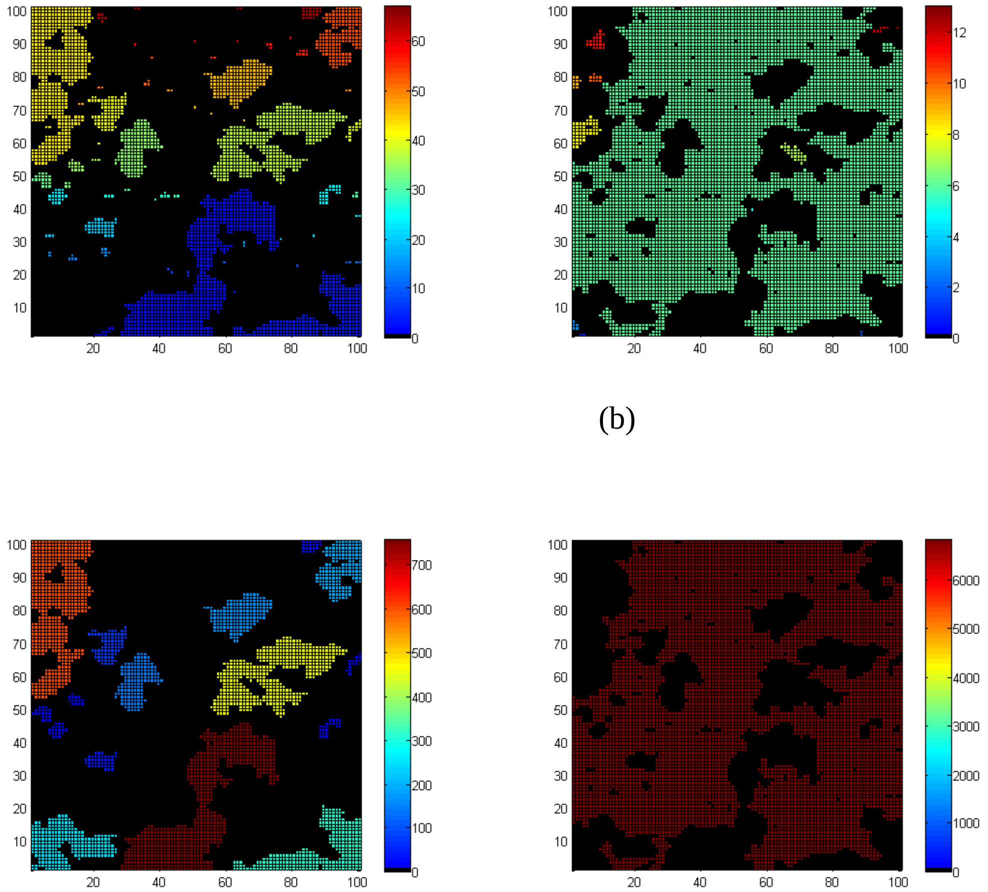

(a)

(b)

(c)

(d)

Figure 2.3.4.3: Cluster labels and cluster numbers for gas and water saturated subdomains of the binary map for scan 8. (a) Shows cluster labels for the gas saturated domain and (b) shows cluster labels for the water saturated domain. (c) Shows cluster numbers for the gas saturated domain and (d) shows cluster numbers for the water saturated domain.

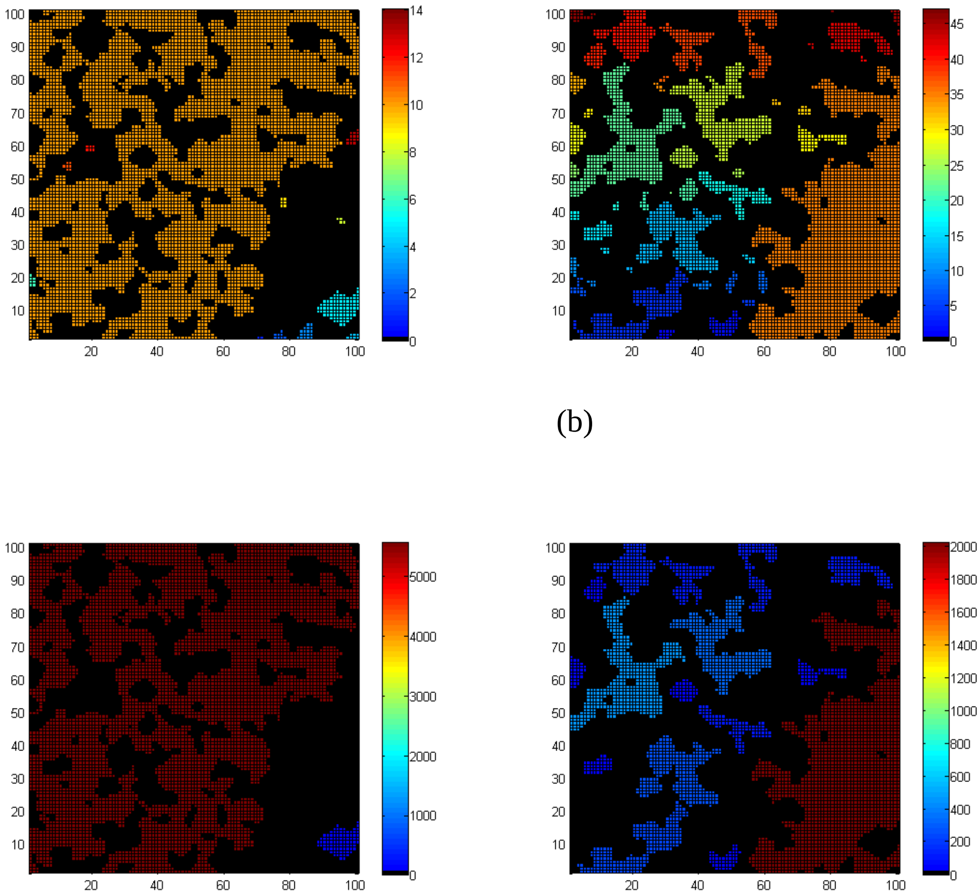

(a) (b)

(c) (d)

Figure 2.3.4.4 Cluster labels and cluster numbers for gas and water saturated subdomains of the binary map for scan 15. (a) Shows cluster labels for the gas saturated domain and (b) shows cluster labels for the water saturated domain. (c) Shows cluster numbers for the gas saturated domain and (d) shows cluster numbers for the water saturated domain.

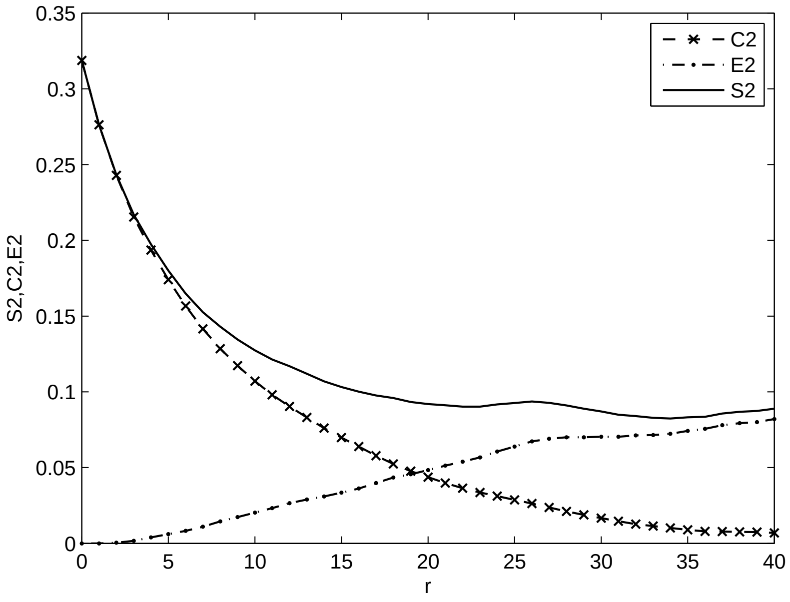

(a)

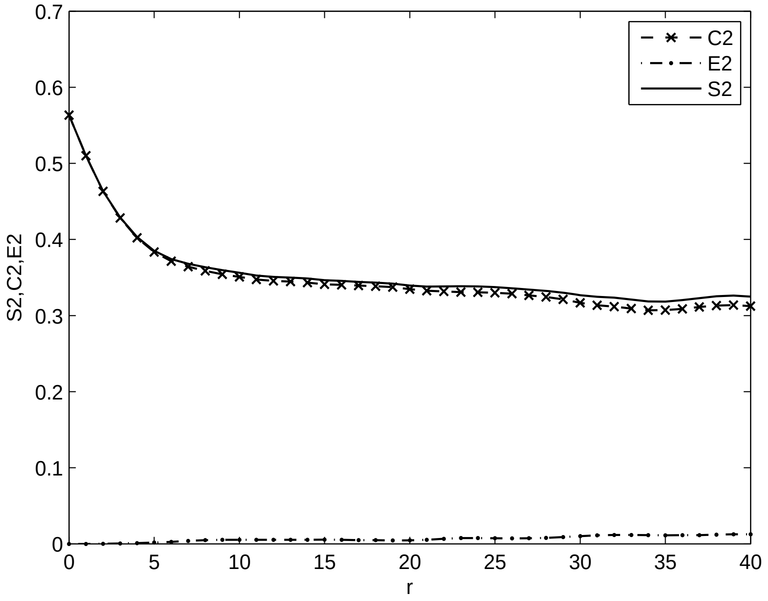

(b)

Figure 2.3.4.5: Two point probability function decomposition into cluster and blocking functions. (a) Shows $S^{(i)}(r_1, r_2)$ *(solid line),* $C^{(i)}(r_1, r_2)$ *(dashed line with crosses) and* $E^{(i)}(r_1, r_2)$ *(dotted line) for gas saturated domain extracted from the binary map of scan 8.(b) Shows the probability functions extracted from the binary map of scan 15.*

2.4 Summary of Results

Four different types of statistics were extracted from binary map representations of gas saturation maps. The first statistic was the normalised autocorrelation function $\chi(r)$. It was derived from the two point probability function $S^{(i)}(r_1, r_2)$ extracted from the binary maps using Monte Carlo methods. During the initial stages of the drainage experiment, the autocorrelation function changed significantly as gas saturation increased. Moreover, for small gas saturations $\chi(r)$ was approximated well by a single Debye correlation function. However, during the latter stages of the drainage experiment (i.e. for large gas saturation) $\chi(r)$ did not vary much as gas saturation increased. For those gas saturations $\chi(r)$ was approximated well by two Debye correlation functions: one which models short range behaviour and one which models long range behaviour.

In terms of length scales two different types of measures were considered, the Debye correlation length and the mean chord length. Of these two measures the Debye correlation length is considered more reliable. The reason is that the mean chord length derived from the water saturated subdomains may be erroneous if water has the role of host fluid. This occurs because the mean chord length for the water saturated domain needs to be extracted from the intersection of two endpoints lying on the gas/water interface, which doesn’t always arise when water is a host fluid with gas inclusions.

The Debye correlation length showed “almost” a linear decrease with percent gas saturation. In particular, the variance of the correlation functions obtained during the initial and latter stages of the drainage experiment showed that largest changes in correlation functions generally occur around the Debye correlation length. Here, double Debye correlation lengths were not examined for saturation dependence; this is a subject of future work.

The third statistical measure of use is the linear path function. It is useful for obtaining a thorough description of the fluid saturation pattern, in that the linear path function is a measure of connected linear paths within the binary maps. As a statistic in its own right, the linear path functions of the gas and water saturated domain were considerably different during the initial stages of the experiment. However, during the final stages of the experiment the shape of the linear path functions of both domains closely resembled one another. In conjunction with the correlation functions it indicates that the saturation patterns do not change significantly during the latter stages of the experiment.

The last statistics extracted from the binary maps were based on cluster analysis. That is, identifying how many gas and water saturated clusters were present in a particular binary map. Probability functions extracted from cluster labelled binary maps showed that connectedness and disconnectedness within an image can be identified using cluster and blocking functions.

It must be noted that these results are preliminary due to the limited number of samples analysed. Moreover further work needs to be conducted to characterise how binary mesoscale maps should be created from gas saturation mesoscale maps. Should we be seeking to identify “predominantly” or “average” gas/water saturated subdomains. In this study I used a simple thresholding technique about average gas saturation of a map. Hence the statistics extracted in this chapter are all relative to some average pixel which generally contains a percentage of both gas and water. One could possibly improve on this thresholding technique.

2.5 Chapter Conclusions

In this chapter statistics were extracted from X-ray tomographic images of partially saturated core samples so as to enable description of realistic fluid distributions. By analysing the saturation dependence of these statistics, it was shown how saturation patterns change as gas saturation is increased during drainage experiments on different types of limestone rocks. In particular, the correlation function and the correlation length are identified as being the most useful statistics for describing fluid saturation patterns and changes in fluid saturation patterns.

Chapter 3

Patchy Saturation Models for Complex and Irregular Fluid Distribution

3.0 Introduction

Maximising the recovery of known hydrocarbon reserves is one of the biggest challenges facing the petroleum industry today. One of the causes of low recovery rates is the creation of a production-induced transition zone, where the reservoir rock is saturated with a mixture of oil, gas, and/or water. In the transition zone the fluids form patches of various sizes, with the spatial distribution of patches largely controlled by the heterogeneity of the rock itself. Identification of this zone and determination of its properties (oil, water and gas saturations) is a key problem in the monitoring of petroleum production using time-lapse (4-D) seismic data (Calvert 2005). In order to solve this problem, it is necessary to know the relationship between fluid saturation and seismic characteristics (elastic moduli, velocity and attenuation).

Recent X-ray tomographic studies (Chapter 2; Monsen & Johnstadt 2004; Cadoret et al. 1995; Cadoret et al. 1998) of partially fluid saturated core samples show fluid saturation on the mesoscale that is complex and irregular. Acoustic measurements conducted concurrently (Cadoret et al. 1995; Cadoret et al. 1998) indicate that wave attenuation and velocity dispersion vary as fluid distribution changes. Most theoretical models (White 1975; Johnson 2001; Pride et al. 2004, see Chapter 1, Section 1.3) for attenuation and dispersion due to mesoscopic heterogeneities assume that fluid heterogeneities are distributed in a regular way. Although, these models allow us to calculate dynamic-equivalent elastic moduli as a function of percent fluid saturation and wave frequency, they do not enable us to take into account possible effects caused by complex and irregular distribution of pore fluids.

In order to evaluate how complex fluid distributions affect attenuation and dispersion, we require theoretical models which allow fluid heterogeneities to be distributed in less idealised ways. In this Chapter I introduce two such models. The first is the 1D continuous random media (1DCRM) model of Müller and Gurevich (2004), which utilizes a correlation function that can be changed to model different sequences of fluid layers. The second is the discrete random media (DRM) model of Ciz and Gurevich (2005) which assumes that fluid heterogeneities are randomly distributed spherical inclusions within an otherwise homogeneously saturated rock. I also derive a third patchy saturation model, which is a 3-dimensional analogue of 1DCRM (Müller & Gurevich 2004) called 3DCRM. It utilizes a correlation function to describe the three dimensional spatial variation of fluids within an otherwise homogeneous rock.

The Chapter is organised as follows. In Section 3.1 I introduce 1DCRM and derive different correlation functions which show how different layering sequences affect attenuation and dispersion. In Section 3.2 I introduce DRM and compare attenuation and dispersion estimates against White’s model for periodically distributed spherical inclusions. In Section 3.3 I derive 3DCRM and model attenuation and dispersion for different correlation functions, fluid contrasts, etc. In Section 3.4, I use 3DCRM to model attenuation and dispersion due to different types of randomly distributed fluid inclusions, such as spheres In Section 3.5, I show how to use 3DCRM to model attenuation and dispersion due to fluid heterogeneities observed in imaged saturation maps (Chapter 2).

3.1 1-Dimensional: 1DCRM Layering

It is important to study the effect that thin fluid saturated porous layering has on compressional wave propagation as layering is ubiquitous in nature and seismic exploration is routinely used to image the subsurface. White et al. (1975) were the first to illustrate that mesoscopic layering of different fluids could cause significant intrinsic attenuation of compressional waves at seismic frequencies, due to wave induced fluid flow. White and co-authors modelled periodically alternating gas and water layers within an otherwise homogeneous porous rock frame. The results of this study were later validated by Norris (1993) who recast the problem using Biot's equations of dynamic poroelasticity (Biot 1962).

Gurevich and Lopatnikov (1995) modelled attenuation and dispersion due to wave induced fluid flow also using dynamic poroelasticity (Biot 1962). Their approach is based on statistical wave theory. They assumed that Biot's poroelastic coefficients could be expressed as smoothly varying random functions of one spatial coordinate. Their study revealed that the low frequency asymptote for frequency-dependent attenuation due to random layering was proportional to $\omega^{1/2}$, whilst for periodic layering, it was proportional to ω. Müller and Gurevich (2004) specialised those results to the case of patchy saturation, where only heterogeneities in fluid properties exist (this model will be discussed next). Müller and Rothert (2006) provide a physical explanation for different low frequency asymptotic attenuation behaviour caused by periodic and random layering.

Gelinsky and Shapiro (1997) study attenuation and dispersion due to random layering of rock and fluid heterogeneities including (in addition to the wave induced fluid flow effects) attenuation and dispersion due to elastic scattering at high wave frequencies (see also Gurevich et al. 2007). Gelinsky and Shapiro (1997) show that gas saturation of more compliant layers and water saturation of less compliant layers reduces attenuation due to wave induced fluid flow, but increases attenuation due to scattering. The reverse was also shown, that gas saturation of less compliant layers and water saturation of more compliant layers cause wave induced fluid flow attenuation to increase and scattering attenuation to decrease. Gelinsky et al. (1998) verified these results numerically.

Pride et al. (2002) use a numerical approach (Kennett reflectivity code) to investigate attenuation due to different types of layer sequences. They model attenuation due to mesoscopic fluid flow, elastic scattering and global flow mechanisms. They show for layer sequences having large variation in layer widths that attenuation due to wave induced fluid flow is independent of frequency, whilst for small variations in layer widths that mesoscopic fluid flow attenuation is dependent on frequency.

My interest is in identifying attenuation effects due to different types of layered systems; however my approach is much simpler. I derive correlation functions which can be inserted into the random media model of Müller and Gurevich (2004) (explained below). In particular, I examine how periodicity and deviations from periodicity affect attenuation and dispersion.

The patchy saturation model of Müller and Gurevich (2004)

When pore fluid bulk modulus varies continuously in magnitude in one-spatial dimension according to some correlation function $\chi(r)$ within an otherwise homogeneous porous rock; attenuation and dispersion can be estimated using the patchy saturation model of Müller and Gurevich (2004). This model is a specialization of the results of Gurevich and Lopatnikov (1995), which model the effective P-wave number for fluctuations in both frame and fluid bulk modulus. The saturated P-wave modulus is

$$\tilde{H}_{1D}(\omega) = H_0\left[1 - isk_2\int_0^\infty \chi(r)\exp(ik_2 r)dr\right], \tag{3.1.1}$$

where

$$k_2 = \sqrt{i\omega}\,\frac{\left\langle \sqrt{\frac{\eta}{\kappa}N} \right\rangle}{\langle N \rangle}$$

is the effective slow P-wave number, which is rewritten in shorthand as

$$k_2 = \sqrt{\frac{i\omega}{D_0}} \text{ where } \sqrt{D_0} = \frac{\langle N \rangle}{\left\langle \sqrt{\frac{\eta}{\kappa}} N \right\rangle} .$$

Here D_0 is diffusivity defined in terms of averaged fluid viscosity η, permeability κ and by a combination of averaged poroelastic moduli $N = ML/H$, where M, L and H are given by Gassmann (1951) (defined in Chapter 1, Section 1.1.1). The angle brackets donate ensemble averaging and the normalised autocorrelation function is

$$\chi(r) = \frac{\langle \varepsilon(z)\varepsilon(z-r) \rangle}{\langle \varepsilon(z)^2 \rangle} , \tag{3.1.2}$$

where ε represents fluctuations in poroelastic parameters about the mean

$$\varepsilon(z) = \frac{\alpha(z)M(z)}{H(z)} - \left\langle \frac{\alpha(z)M(z)}{H(z)} \right\rangle , \tag{3.1.3}$$

and s is a dimensionless coefficient given by

$$s = \left\langle \frac{1}{H} \right\rangle^{-1} \left(\left\langle \frac{\alpha^2}{L^2} N \right\rangle - \left\langle \frac{\alpha}{L} \right\rangle^2 \left\langle \frac{1}{N} \right\rangle^{-1} \right) . \tag{3.1.4}$$

When there are only variations in fluid bulk modulus Equation (3.1.3) implies $\varepsilon(z) \approx \varepsilon_{MM}(z)$, as the variation in the saturated P-wave modulus H in Equation (3.1.3) due to variations in fluid modulus M are small, that is $H(z) \approx H$. As the statistical approach employed by Gurevich and Lopatnikov (1995) utilizes the so-called method of statistical smoothing (Karel & Keller 1964) widely used in the theory of waves in random media; the 1DCRM model (Equation 3.1.1) is accurate for small contrasts in fluid bulk modulus and approximate when fluid contrast increases.

By varying the correlation function different 1D fluid distributions can be considered. In particular, when it is assumed that the pore-space is saturated by only two fluids, attenuation and dispersion due to binary fluid distributions can be modelled. In the next three subsections, attenuation and dispersion is modelled due to different types of binary layered media.

3.1.1 Attenuation and Dispersion: Due to Periodic Layering

In the study of Gurevich and Lopatnikov (1995) and Gurevich et al. (1997) the random media approach was used to model effects due to periodic layering, even though the approach was not originally designed for this purpose. They modelled periodic layering using a saw tooth autocorrelation function, thus restricting analysis of attenuation and dispersion to periodic layering consisting of layers of equal thickness (i.e. 50% saturation). Here I derive a new correlation function, which is less restrictive. It will allow us to investigate whether the 1DCRM approach can be adapted to model attenuation and dispersion due to binary periodic layering having any relative layer widths (i.e. arbitrary percentage fluid saturation). Here we assume that rock saturated by fluid one and fluid two has layer widths L_1 and $L_2 = L_P - L_1$ where L_P is the spatial repetition width.

In order to use the 1DCRM it is necessary to derive a correlation function appropriate for periodic layering. The approach utilized here is to take a rectangular periodic function (see Figure 3.1.1.1) given by

$$rect(r) = \begin{cases} 1 & -L_1/2 \le r \le L_1/2 + nL_P \quad n = 0....\infty \\ 0 & otherwise \end{cases} \tag{3.1.1.1}$$

and explicitly perform the autocorrelation (thereby assuming a random shift). This produces an autocorrelation function which is a triangular periodic function given by

$$tri(r) = \begin{cases} 1 - 2r/L_1 & 0 \le r \le L_1/2 + nL_P & n = 0....\infty \\ 0 & L_1/2 + nL_P \le r \le -L_1/2 + (n+1)L_P & n = 0....\infty \\ 1 - 2L_P/L_1 + 2r/L_1 & -L_1/2 + (n+1)L_P \le (n+1)L_P & n = 0....\infty \end{cases} \tag{3.1.1.2}$$

Here no restrictions are placed on layer width, which means that any percentage fluid saturation can be considered with Equation (3.1.1.2).This is substituted into Equation (3.1.1) to obtain an effective saturated P-wave modulus of

$$\tilde{H}_{1D}(\omega) = H_{BGW}\left[1 - isk_2\tilde{B}(k_2)\right], \tag{3.1.1.3}$$

where

$$\widetilde{B}(k_2)=\frac{2L_P ik_2L_1+4L_P\left(1-\exp\left(\frac{ik_2L_1}{2}\right)+\exp(ik_2L_P)\left(\left(1-\frac{ik_2L_1}{2}\right)\right)-\exp\left(\frac{ik_2L_1}{2}\right)\right)+ik_2{L_1}^2(\exp(ik_2L_P)-1)}{2ik_2L_1L_P(\exp(ik_2L_P)-1)} \tag{3.1.1.4}$$

In Figure 3.1.1.2, attenuation and dispersion are modelled for periodic layering of light gas and water; the physical properties are shown in Tables 3.1.1.1 and 3.1.1.2. The gas layer width $L_1 = 6\text{ cm}$ and the water layer width is 14cm ($L_P = 20\text{ cm}$), this corresponds to 70% layering of water with another low contrasting fluid. Attenuation and dispersion are estimated using Johnson’s model (Equation 1.3.2.10 and Equation 1.3.2.5) (solid line) and 1DCRM with periodic correlation function (Equation 3.1.1.3 with Equation 3.1.1.4) (dashed line). The figure shows that (a) attenuation and (b) dispersion estimates obtained from both models correspond closely. Hence, the random media approach (1DCRM) accurately predicts for arbitrary saturation percentages the effect of periodic stratification, even though it was not originally designed for this purpose.

Table 3.1.1.1: Rock properties

K	7 GPa	K_g	35 GPa	ϕ	0.08
μ	9 GPa	ρ_g	2650 Kg/m^3	κ	1e-13 m^2

Table 3.1.1.2: Saturating fluid properties

K_{fw} Water	2.25 GPa	$K_{f\text{ -lc}}$ Low contrast with water	2.0 GPa	K_f Heavy gas	0.25 GPa	K_f Light gas	0.1 GPa
ρ_w	990 Kg/m^3	$\rho_{w\text{-lc}}$	990 Kg/m^3	ρ	400 Kg/m^3	ρ_g	100 Kg/m^3
η_w	1e-3 Pa s	$\eta_{w\text{-lc}}$	1e-3 Pa s	η	6e-5 Pa s	η_2	3e-5 Pa s

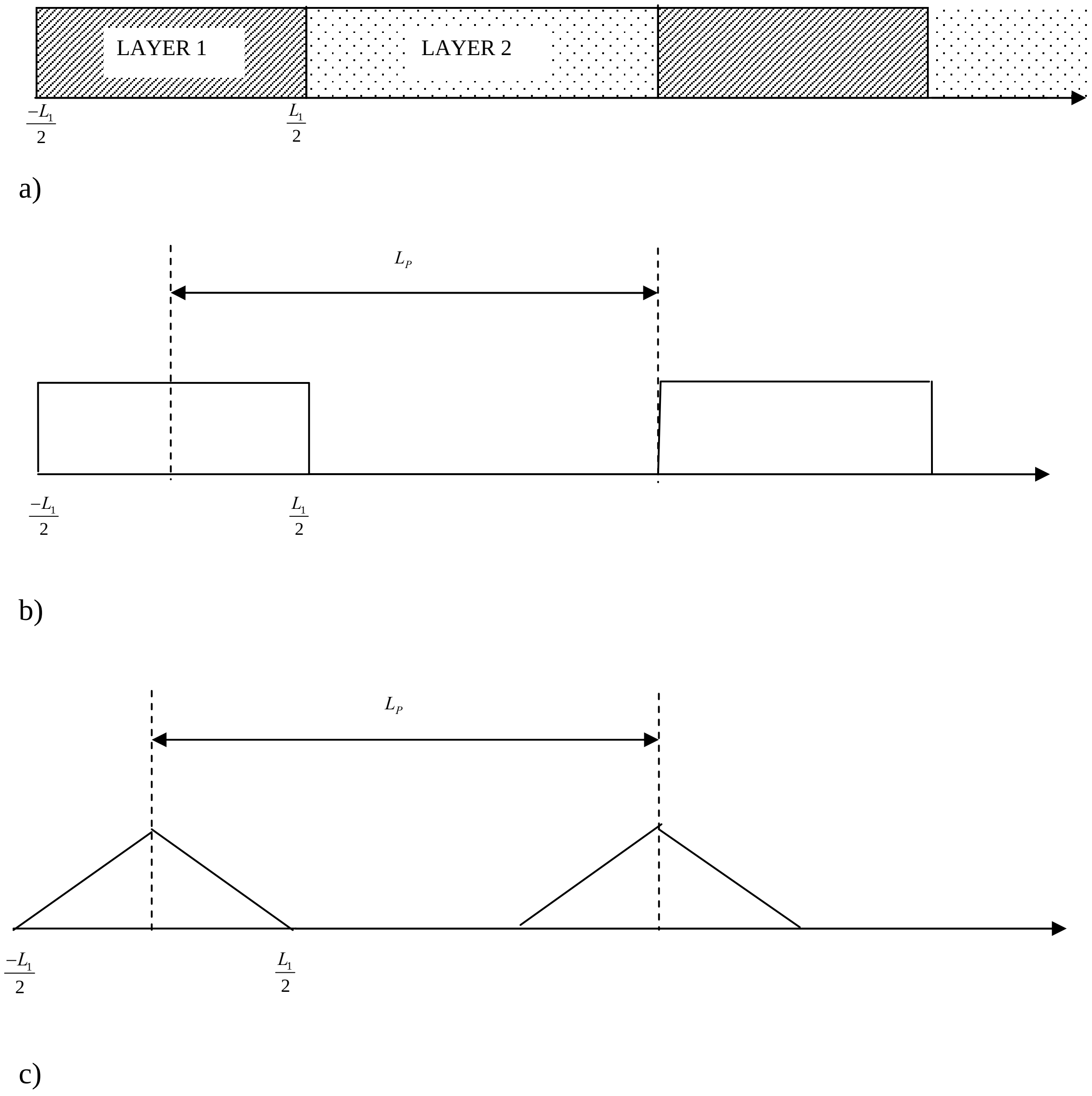

Figure 3.1.1.1: Construction of autocorrelation function for periodic layering. (a) Shows periodic layered media, (b) corresponding periodic pulse sequence and (c) autocorrelation of periodic pulse sequence as given by a triangular function.

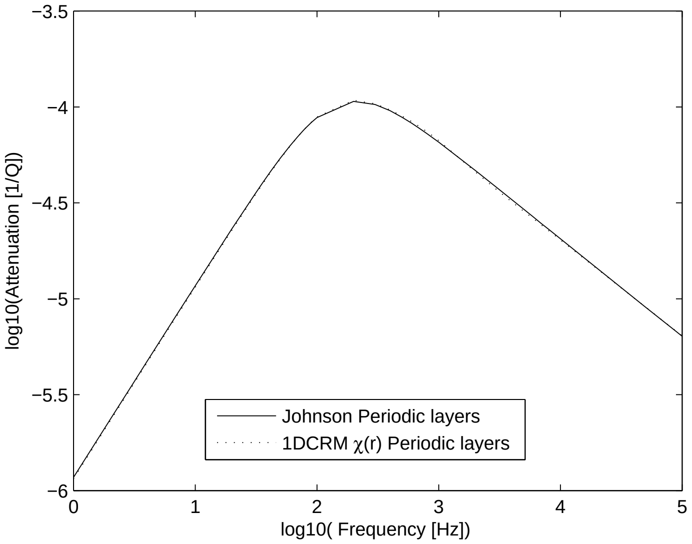

a)

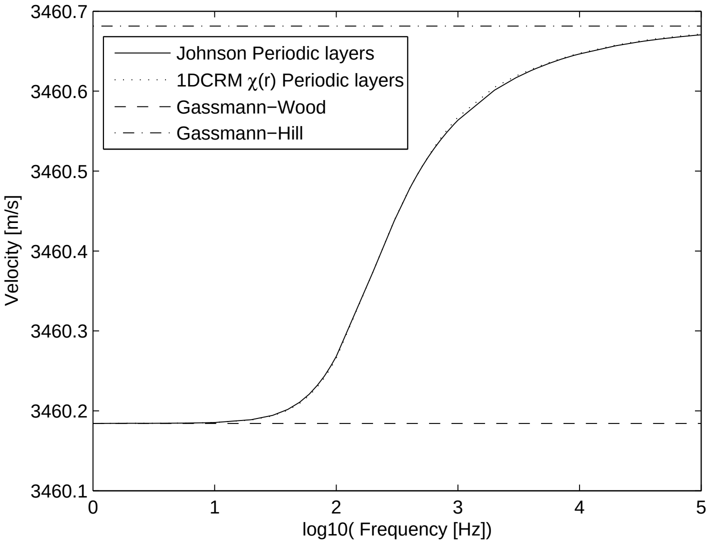

b)

Figure 3.1.1.2 Frequency-dependent attenuation and dispersion estimates from 1DCRM and Johnson (2001) for periodic layering. (a) Shows attenuation and (b) shows velocity predicted using 1DCRM (dotted line) and Johnson (solid line). Clearly there is good agreement between both approaches.

3.1.2 Attenuation and Dispersion: due to Quasi-Periodic Layering

Strictly periodic systems are unlikely to exist in the earth. I am therefore interested to explore deviations from periodicity on patchy saturation signatures. Specifically, layering which is almost spatially periodic is called quasi-periodic. One type of quasi-periodic layered media arises when a layer of fixed width P is repeated at a repetition period comprising of an average spatial period L_P plus a random spatial shift υ_k. See Figure 3.1.2.1 (a) where layer 1 (cross hatched) is of constant length, whilst layer 2 (dotted) is almost of constant length.

Layered systems of this kind stand in direct analogy to sequences of binary random pulses (Levin 1968, Franks 1969), which are characterised by a series of rectangular pulses of fixed amplitude one separated by periods of amplitude 0, see Figure 3.1.2.1 (b) and (c). Spectral densities and correlation functions derived for binary random pulse sequences can be suitably modified and incorporated into the 1DCRM (Equation 3.1.1). Here I derive a correlation function for quasi-periodic layering, which I substitute into Equation (3.1.1) to obtain the saturated P-wave modulus for quasi-periodic layered media.

Levin (1968) has derived the (power) spectral density corresponding to the quasi-periodic random pulse sequence (shown in Figure 3.1.2.1(c)) as

$$\tilde{B}(\omega)=\frac{P^2}{T_P}\operatorname{sinc}^2\left(\frac{\omega P}{2}\right)\left\{1-\left|R_\nu(\omega)\right|^2+\frac{2\pi}{T_P}\left|R_\nu(\omega)\right|^2\sum_{n=-\infty}^{\infty}\delta\left(\omega-\frac{2\pi n}{T_P}\right)\right\}. \qquad (3.1.2.1)$$

Here $\delta(x)$ is the Dirac delta function and $\operatorname{sinc}(x)=\frac{\sin(x)}{x}$, whilst $R_\nu(\omega)$ is the characteristic function of the probability density function w of the random variable ν, that is

$$R_\nu(\omega)=\int\exp(i\omega\upsilon)g(\upsilon)d\upsilon\,. \qquad (3.1.2.2)$$

To derive the correlation function, the inverse Fourier transform of Equation (3.1.2.1) is taken giving

$$B(t)=\frac{P^2}{T_P}\left[\frac{1}{P}\operatorname{tri}\left(\frac{t}{2P}\right)\right]*\left\{\delta(t)-G(t)+\frac{1}{T_P}G(t)*\sum_{n=-\infty}^{\infty}\exp\left(\frac{2\pi ni}{T_P}t\right)\right\}, \qquad (3.1.2.3)$$

where $*$ refers to convolution, $G(t)=g(t)*g(t)$ and $\mathrm{tri}(x)$ is a symmetric triangular function.

This expression (Equation 3.1.2.3) is manipulated further to give

$$B(t)=\frac{P}{T_P}\left(\mathrm{tri}\left(\frac{t}{2P}\right)*\left[\delta(t)-G(t)\right]+\sum_{n=-\infty}^{\infty}G(t)*\mathrm{tri}\left(\frac{t-nT_P}{2P}\right)\right). \tag{3.1.2.4}$$

As Equation (3.1.2.4) was obtained for a positive signal with unit amplitude, I need to subtract the squared mean of the signal to obtain a correlation function for a centred signal. I also need to normalise the correlation function, when both are done:

$$B(t)=\frac{T_P}{T_P-P}\left(\mathrm{tri}\left(\frac{t}{2P}\right)-\mathrm{tri}\left(\frac{t}{2P}\right)*G(t)-\frac{P}{T_P}+\sum_{n=-\infty}^{\infty}G(t)*\mathrm{tri}\left(\frac{t-nT_P}{2P}\right)\right)=B_a(t)+B_{const}(t)+B_P(t). \tag{3.1.2.5}$$

Hence the correlation function due to quasi periodic layering is composed of three different types of contributions:

(1) aperiodic component given by:

$$B_a(t)=\frac{T_P}{T_P-P}\left(\mathrm{tri}\left(\frac{t}{2P}\right)-\mathrm{tri}\left(\frac{t}{2P}\right)*G(t)\right), \tag{3.1.2.6}$$

(2) constant component given by:

$$B_{const}(t)=\frac{-P}{(T_P-P)}, \tag{3.1.2.7}$$

(3) periodic component given by:

$$B_P(t)=\frac{T_P}{T_P-P}\left(\sum_{n=-\infty}^{\infty}G(t)*\mathrm{tri}\left(\frac{t-nT_P}{2P}\right)\right). \tag{3.1.2.8}$$

To calculate wave attenuation and dispersion due to quasi periodic layering Equations (3.1.2.6)-(3.1.2.8) can be substituted into Equation (3.1.1).

For the aperiodic component:

$$\tilde{B}_a(\omega) = \int_0^\infty B_a(t)\exp(-i\omega t)dt = \frac{T_P}{T_P - P}\int_0^\infty \left[\mathrm{tri}\left(\frac{t}{2P}\right) - \mathrm{tri}\left(\frac{t}{2P}\right) * G(t)\right]\exp(-i\omega t)dt$$

$$= \frac{T_P}{T_P - P}\int_0^\infty \mathrm{tri}\left(\frac{t}{2P}\right)\exp(-i\omega t)dt - \int_0^\infty \mathrm{tri}\left(\frac{t}{2P}\right) * (g(t) * g(t))\exp(-i\omega t)dt$$

$$= \frac{T_P}{T_P - P}\left[1 - |R(\omega)|^2\right]\int_0^\infty \mathrm{tri}\left(\frac{t}{2P}\right)\exp(-i\omega t)dt = \frac{T_P}{T_P - P}\left[1 - |R(\omega)|^2\right]\int_0^P \left(1 - \frac{t}{P}\right)\exp(-i\omega t)dt$$

$$= \frac{T_P}{T_P - P}\left[1 - |R(\omega)|^2\right]\frac{1}{\omega}\left[i\,\mathrm{sinc}\left(\frac{\omega P}{2}\right)\exp\left(\frac{-iP\omega}{2}\right) - i\right]. \qquad (3.1.2.9)$$

For the constant component:

$$\tilde{B}_{const}(\omega) = \frac{-P}{T_P - P}\int_0^\infty \exp(-i\omega t)dt = \frac{iP}{\omega(T_P - P)}. \qquad (3.1.2.10)$$

For the periodic component:

$$\tilde{B}_P(\omega) = \int_0^\infty B_p(t)\exp(i\omega t)dt \int_0^\infty \frac{T_P}{T_P - P}\left(\sum_{n=-\infty}^{\infty} G(t) * \mathrm{tri}\left(\frac{t - nT_P}{2P}\right)\right)\exp(i\omega t)dt$$

$$= \int_0^{T_P} B_P(t)\exp(i\omega t)dt + \int_{T_P}^{2T_P} B_P(t - T_P)\exp(i\omega t)dt + \int_{2T_P}^{3T_P} B_P(t - 2T_P)\exp(i\omega t)dt + \ldots.$$

$$= \int_0^{T_P} B_P(t)\exp(i\omega t)dt + \exp(-i\omega T_P)\int_{T_P}^{2T_P} B_P(t - T_P)\exp(i\omega(t - T_P))dt +$$

$$+ \exp(-i\omega 2T_P)\int_{2T_P}^{3T_P} B_P(t - 2T_P)\exp(i\omega(t - 2T_P))dt + \ldots.$$

$$= \int_0^{T_P} B_P(t)\exp(i\omega t)dt[1 + \exp(-i\omega T_P) + \exp(-i\omega 2T_P) + \ldots] = \int_0^{T_P} B_P(t)\exp(i\omega t)dt\left[\sum_{m=0}^{\infty}\exp(i\omega m T_P)\right]$$

$$= \frac{\int_0^{T_P} B_P(t)\exp(-i\omega t)dt}{1 - \exp(-i\omega T_P)},$$

which simplifies after much algebra to

$$\tilde{B}_P(\omega) = \frac{iT_P}{T_P - P}R^2(\omega)\frac{T_P\,\mathrm{sinc}\left(\frac{\omega T_P}{2}\right) - (T_P - P)\mathrm{sinc}\left(\frac{\omega P}{2}\right)\mathrm{sinc}\left(\frac{\omega(T_P - P)}{2}\right)}{2\sin\left(\frac{\omega T_P}{2}\right)}. \qquad (3.1.2.11)$$

The addition of Equations (3.1.2.9) –(3.1.2.11) gives

$$\begin{aligned}\tilde{B}(\omega) &= \tilde{B}_a(\omega)+\tilde{B}_{const}(\omega)+\tilde{B}_P(\omega)\\ &= \frac{i}{\omega}\left[\frac{T_P}{T_P-P}\left[1-R^2(\omega)\right]\left[\operatorname{sinc}\left(\frac{\omega P}{2}\right)\exp\left(\frac{-iP\omega}{2}\right)\right]+\frac{R^2(\omega)\operatorname{sinc}\left(\frac{\omega P}{2}\right)\operatorname{sinc}\left(\frac{\omega(T_P-P)}{2}\right)}{\operatorname{sinc}\left(\frac{\omega T_P}{2}\right)}-1\right].\end{aligned}$$

This is further manipulated to

$$\begin{aligned}\tilde{B}(\omega) = \frac{2i}{\omega^2 P}\frac{T_P}{T_P-P}\Bigg[&\sin\left(\frac{\omega P}{2}\right)\exp\left(\frac{-iP\omega}{2}\right)-R^2(\omega)\exp\left(\frac{iP\omega}{2}\right)\\ &-\exp\left(\frac{-iP\omega}{2}\right)-\frac{\sin\left(\frac{\omega P}{2}\right)}{\sin\left(\frac{\omega T}{2}\right)}\exp\left(\frac{-iP\omega}{2}\right)\exp\left(\frac{-i\omega(T_P-P)}{2}\right)\Bigg]-\frac{i}{\omega}\end{aligned} \tag{3.1.2.12}$$

where $R(\omega)$ is defined for any $0<\upsilon_k\le T_P-P$ as

$$R(\omega)=\sin\left(\frac{\omega h}{2}\right)\Big/\left(\frac{\omega h}{2}\right).$$

Equation (3.1.2.12) can be substituted into Equation (3.1.1.3) to obtain the saturated P-wave modulus due to quasi-periodic layering, by setting $\omega=-ik_2$

In this example, I compare estimates from 1DCRM using the quasi-periodic correlation function against Johnson’s approach for periodic layering. I model 30% light gas layering which repeats quasi-periodically with water layers. Figure 3.1.2.2 shows (a) attenuation and (b) dispersion for each approach. The quasi-periodic attenuation curve (dotted line) is slightly broader than the periodic attenuation curve (solid line) and the quasi-periodic velocity curve has the same velocity as the periodic curve, at lower wave frequencies. Despite these observations, there is very little difference in the patchy saturation signatures of quasi-periodic and periodic layering, unlike the case of random layering which shall be discussed next.

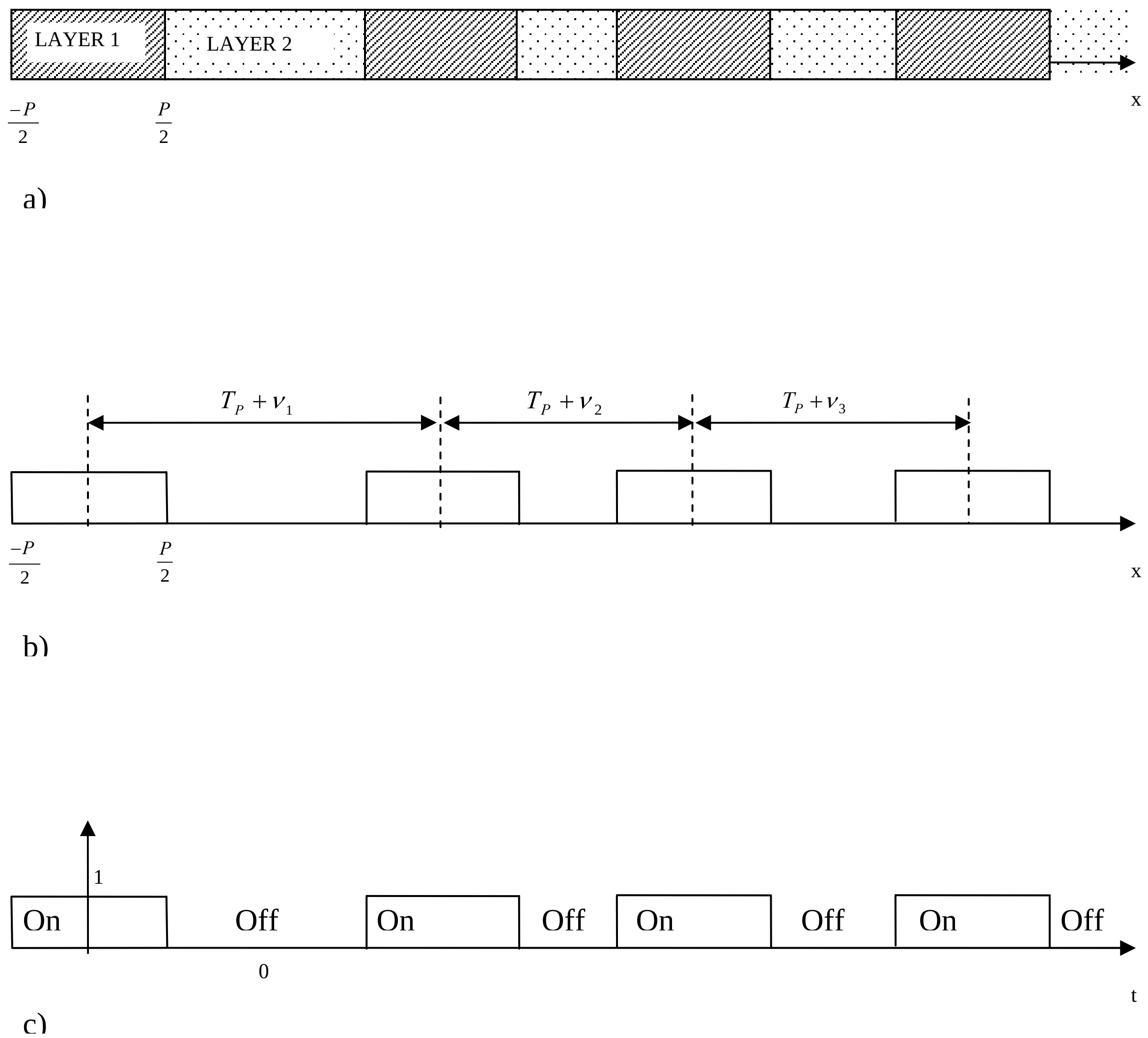

Figure 3.1.2.1: Quasi-periodic layers and pulses. (a) Shows quasi periodic repetition of more compressible fluid layers in terms of spatial layers, (b) shows the spatial repetition period and random shift, (c) Shows the random binary signal analogy from radio physics.

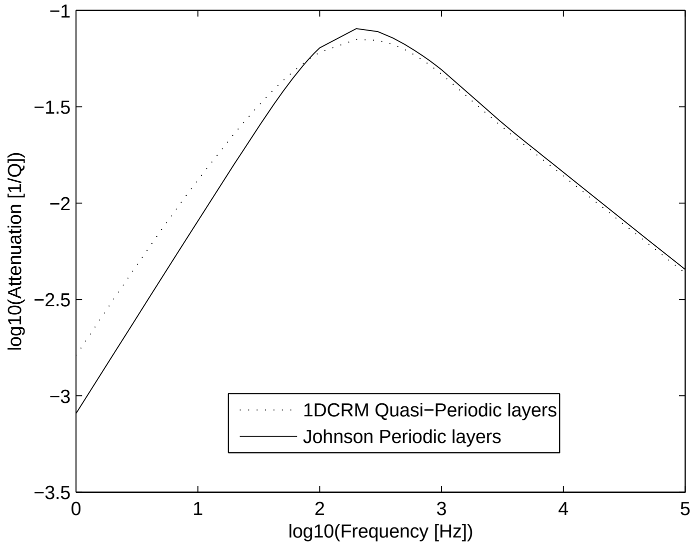

(a)

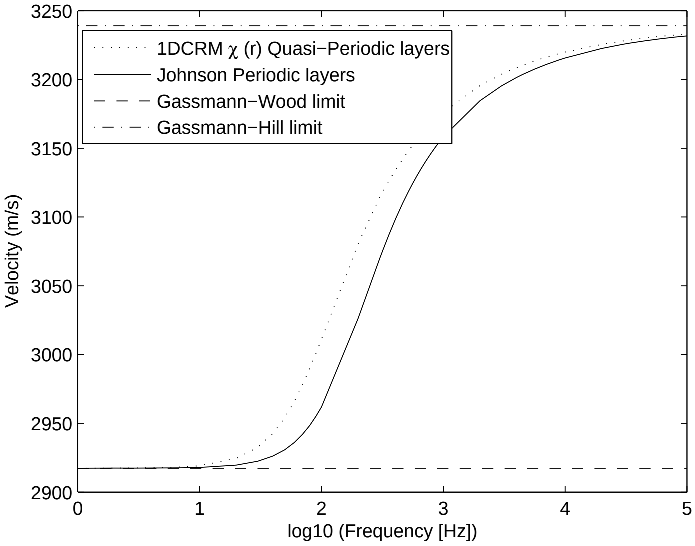

(b)

Figure 3.1.2.2: 1DCRM with quasi-periodic correlation function versus Johnson (2001) for periodic layering. (a) Shows attenuation and (b) dispersion due to 30 percent layering light gas within water. The quasi periodic attenuation curve (dotted line) is slightly broader than the periodic attenuation curve (solid line), whilst rapid velocity dispersion occurs at lower frequencies for the quasi periodic layering than for periodic layering.

3.1.3 Attenuation and Dispersion: due to Random Layering

Like periodic and quasi-periodic models, a randomly layered sequence of two different fluids will consist of individual layers which are fully saturated by only one type of fluid. However, unlike the preceding layered media models all layers are of variable width. That is, gas layers and water layers alternate at random spatial intervals. One way of interpreting such layered sequences is in terms of a random facsimile signal (Franks 1969). Here I modify Franks' terminology to suit the application of random layering of two fluids, hence showing what sort of correlation function can be utilized to model this type of layering.

One can define a random function $x(r)$ which has a binary output, such that $x(r)=0$ for gas saturated layers and $x(r)=1$ for water saturated layers where the probabilities of gas and water saturated layers are $P[x(r)=0]=v_1=1-v_2$ and $P[x(r)=1]=v_2$. The spatial length between successive gas to water and water to gas transitions is a random variable. This can be modelled by assuming that $\{r_k; k=0,\pm1,\pm2,\pm3,.....\}$ is an ordered sequence of random variables distributed over the entire real line according to a Poisson point process with rate parameter λ_p. The rate parameter λ_p is equivalent to the average number of transitions between gas and water in a unit interval. In the intervals defined by the random points r_k, $x(r)$ has a constant value of 0 or 1. Furthermore, the values of $x(r)$ in different intervals are statistically independent.

The layer sequence has a mean value of $\langle x(r)\rangle = \Pr[x(r)=1]=v_2$ which is equivalent to average water saturation. The autocorrelation function (un-normalised, un-centred) is

$$\chi(r+R)=\Pr[x(r+R)=1 \quad \& \quad x(r)=1], \tag{3.1.3.1}$$

where probabilities in Equation (3.1.3.1) depend on whether r and $r+R$ are in same or different spatial intervals defined by r_k. Let A refer to event $x(r+R)=1$ and B refer to the event $x(r)=1$. The probability of r and $r+R$ residing in the same interval is:

$$\Pr[x(r+R)=1 \quad \& \quad x(r)=1]=\Pr[A \,\&\, B]=\Pr(A)\Pr\left(B/A\right)=v_2, \tag{3.1.3.2}$$

as events A and B are statistically dependent. The probability that r and $r+R$ reside in different intervals is:

$$\Pr[x(r+R)=1 \quad \& \quad x(r)=1]=\Pr[A \,\&\, B]=\Pr(A)\Pr(B)=v_2^{\,2}, \tag{3.1.3.3}$$

as events A and B are statistically independent.

Moreover, the probability that r and $r+R$ reside in the same interval is $P_0(|R|) = \exp(-\lambda|R|)$ as it is a Poisson point process.

The correlation function is then

$$\chi(R) = v_2 \exp(-\lambda_p|R|) + v_2{}^2[1-\exp(-\lambda_p|R|)] = v_2(1-v_2)\exp(-\lambda_p|R|) + v_2{}^2 . \qquad (3.1.3.4)$$

Equation (3.1.3.4) is un-normalised and un-centred, hence it needs to be converted

$$\tilde{\chi} = \frac{\chi(R) - v_2^2}{v_2(1-v_2)} = \exp(-\lambda_p|R|) \qquad (3.1.3.5)$$

Equation (3.1.3.5) shows that the correlation function for random layering (described by a Poisson point process) is given by an exponential function. By comparing Equation (3.1.3.5) with

$$\chi(r) = \exp\left(\frac{-2|r|}{a}\right), \qquad (3.1.3.6)$$

we see that

$$\lambda_d = \frac{2}{a} .$$

This means that the correlation length a is an inverse of the rate parameter λ_p. That is, if there are lots of transitions between gas and water saturated layers occurring within the unit interval, than the correlation length is small. Thus, a small correlation length could be used to model finely distributed random layers. On the other hand, if fewer water gas transitions occur within the unit interval then the correlation length is large. This would produce random layering which is coarse. To model attenuation and dispersion Equation (3.1.3.6) is substituted into Equation (3.1.3) giving (Müller & Gurevich 2004)

$$\tilde{H}(\omega) = H_{BGW}\left[1 + \frac{s}{1 + \frac{2i}{k_2 a}}\right], \qquad (3.1.3.7)$$

where H_{BGW} is Woods limit on the saturated P-wave modulus and

$$s = \frac{(H_{BGH} - H_{BGW})}{H_{BGW}} .$$

In Figure 3.1.3, I compare attenuation and velocity dispersion for random layering and periodic layering. I use 1DCRM with an exponential correlation function (Equation 3.1.3.7) to model wave induced fluid flow arising between random layering; whilst Johnson’s approach is utilized to model wave induced fluid flow for periodic layering. For consistency, I assume that there is 30% light gas layers randomly or periodically distributed within water layers. The rock frame and fluid properties are the same as those listed in Tables 3.1.1.1 and 3.1.1.2.

Figure 3.1.3 (a) shows that attenuation due to random (dotted line) and periodic (solid line) layering exhibits different frequency dependency at low frequencies. Also, the attenuation curve is broader for random layering than for periodic layering. This means that attenuation due to random layering will be substantially greater at lower wave frequencies than attenuation due to periodic layering (providing of coarse scaling of correlation lengths and layer widths are comparable).

Figure 3.1.3 (b) shows velocity dispersion curves for random (dotted line) and periodic (solid line) stratification of light gas and water. Both models approach the theoretical limits on velocity given by Gassmann-Wood and Gassmann-Hill. The bandwidth over which velocity changes most rapidly is wider for random layering than for periodic layering.

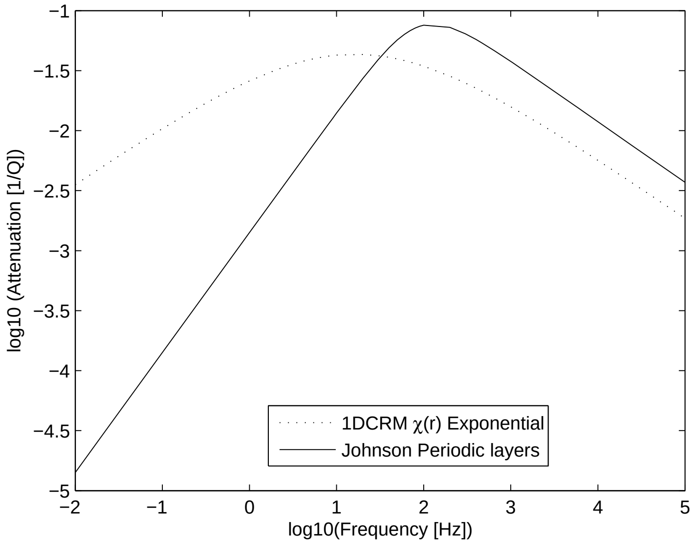

(a)

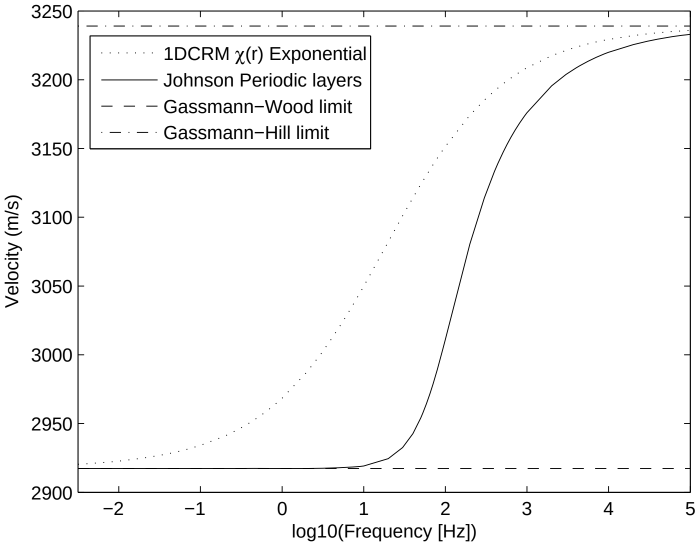

(b)

Figure 3.1.3.1: 1DCRM with exponential correlation function versus Johnson (2001) for periodic layering. (a) Shows attenuation and (b) dispersion due to 30 percent layering of light gas within water. The attenuation curve for random layering (dotted line) has different frequency dependence at low frequencies relative to the periodic attenuation curve (solid line). The velocity dispersion occurs across a wider bandwidth random layering than for periodic layering.

3.2 3-Dimensional: Random Distribution of Spherical Inclusions

Small gas bubbles in water and small liquid drops in gas are likely to assume a spherical shape because of surface tension. Surface tension is force acting tangential to the surface of an interface separating two dissimilar fluids (Bachelor 1967). Surface tension arises because different fluids have different intermolecular cohesive forces (Chang 1994). For instance, cohesive forces like dipole moments are responsible for attraction between neighbouring polar molecules within water. Water molecules away from the gas-water interface experience balanced cohesive forces, where as water molecules adjacent to the interface experience unbalanced cohesive forces (due to the presence of neighbouring gas molecules). The unbalanced forces cause water molecules to be drawn inwards and sideways along the interface, this minimizes the interfacial surface area. Hence, spherical shaped gas bubbles and liquid drops are formed (see Figure 3.2.1).

In porous media the physics which dictates the shape of heterogeneous fluid patches, such as minimization of interfacial surface area (between fluid-fluid and fluid-solid), the process and history of fluid saturation within rock, the shape of pore-spaces, fluid transport properties, rock wettability etc., is not fully understood. Hence, as a first start towards modelling attenuation/dispersion due to realistic three dimensional fluid distributions in porous rock, some studies (Ciz et al. 2005; 2006; Markov et al. 2007) have assumed in analogy to bubbly fluids, a random distribution of spherical shaped fluid inclusions. In this Section I outline the approach of Ciz et al. (2006) as it will be utilized extensively in Chapters Four and Five.

Ciz et al. (2005, 2006) have derived explicit expressions for attenuation and phase velocity dispersion due to a random distribution of spherical heterogeneities within porous rock. I call their model DRM, which stands for discrete random media. The derivation of their model, involves two main stages. In the first stage a problem of scattering by a single inclusion is analysed. Under the assumption of mesoscopic inclusion this analysis yields a closed-form solution for the scattering amplitude (Ciz & Gurevich 2005). The second stage utilizes the Waterman and Truell (1961) theorem of multiple scattering to approximate the scattered wave field of a system of randomly distributed poroelastic inclusions (Ciz & Gurevich 2005).

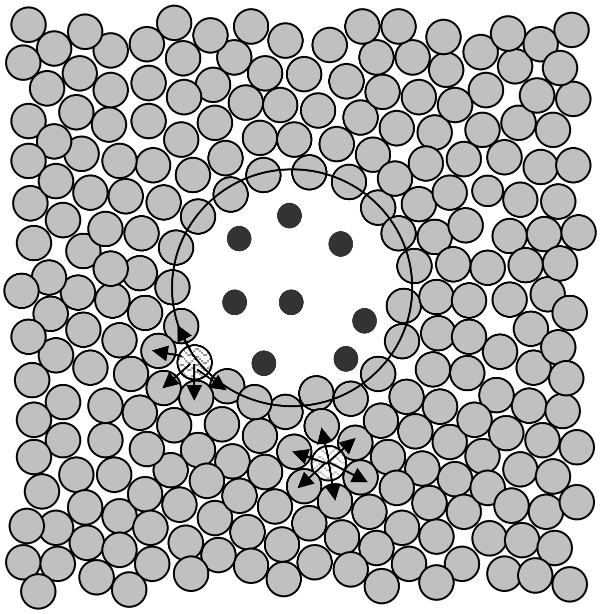

Figure 3.2.1: A spherical gas bubble in a liquid. The arrows denote intermolecular cohesive forces acting between molecules,

3.2.1 Single inclusion scattering

The problem of scattering of an elastic wave in a poroelastic material (host) by a spherical inclusion of another poroelastic material (inclusion) was first considered by Berryman (1985). When the incident wave interacts with the inclusion of radius a, it produces fast and slow compressional waves and a shear wave in the host (called scattered or reflected waves) and three of the same kinds of waves within the inclusion (called refracted waves), Figure 3.2.1.1.

Both the inclusion and host medium are described by Gassmann equations (1.1.7-1.1.9) and Biot's equations of poroelasticity (1.1.1-1.1.3). Standard boundary conditions (Dersiewicz & Shalak 1963) apply on the interface between the inclusion and host at $r = a$:

I. continuity of normal stress
II. continuity of tangential stress
III. continuity of normal average solid displacement
IV. continuity of tangential average solid displacement
V. continuity of fluid pressure
VI. continuity of average relative solid-fluid displacement

Similarly to the corresponding scattering problem in elasticity (Yamakawa 1962), the solution of poroelastic scattering problem is sought for by expanding the reflected and refracted waveforms in series of spherical harmonics (Berryman 1985):

$$
\begin{gathered}
u_{1r} = -\sum_{n=0}^{\infty}\left[\frac{B_n^+}{k_+^2}\frac{d}{dr}h_n^{(1)}(k_+ r) - \frac{B_n^-}{k_-^2}\frac{d}{dr}h_n^{(1)}(k_- r)\right]P_n(\cos\theta)\,, \\
u_{3r} = \sum_{n=0}^{\infty}\left[\frac{D_n^+}{\left(k_+^{'}\right)^2}\frac{d}{dr}j_n(k_+^{'} r) - \frac{D_n^-}{\left(k_-^{'}\right)^2}\frac{d}{dr}j_n(k_-^{'} r)\right]P_n(\cos\theta)\,,
\end{gathered}
\tag{3.2.1.1}
$$

where, u_{1r} and u_{3r} are normal displacements in the host and inclusion and B_n^+, B_n^-, D_n^+, D_n^- are coefficients corresponding to reflected and refracted fast and slow harmonics of order n, $j_n^{(1)}, h_n^{(1)}$, are spherical Bessel functions of the first and third kind, $P_n(\cos\theta)$ is the Legendre polynomial of the order n and k_+, k_- are wave numbers of the fast and slow waves. Similar representation is derived for the polar angle components of displacements, which involve scattering coefficients C_n and E_n corresponding to reflected and refracted shear wave.

Application of the standard boundary conditions yields a 6×6 system of linear equations in terms of six unknown wave field coefficients of each order $n \geq 1$. For order $n = 0$ a similar 4×4 system of linear equations in terms of 4 unknown wave field coefficients is obtained (Berryman 1985).

The general infinite series formulation of Berryman (1985) gives a complete solution of the single scattering problem for an inclusion of arbitrary size (larger than the pore size) and for any frequency. Ciz and Gurevich (2005) showed that this solution can be greatly simplified if the frequency is small compared to Biot's characteristic frequency, and the inclusion is mesoscopic. In particular, they showed that at most three first terms of the series are significant in this case, and gave explicit analytical expressions for these terms.

Furthermore, it was shown that the term with $n = 2$ is proportional to the difference in shear modulus between the inclusion and the host medium. Thus in the specific case where the inclusion differs from the host medium by the fluid properties only, this term can be neglected and the scattering coefficient of the fast compressional wave is given by the sum of the zero-order and first-order terms with coefficients (Ciz et al. 2005):

$$B_0^+ = \frac{i\xi_+^3\left(K - K^{'}\right)}{3H^{''}} + i\xi_+^3 H\left(\frac{C}{H} - \frac{C^{'}}{H^{''}}\right)^2 \Bigg/ \left[N^{'}\,\frac{j_0\left(\xi_-^{'}\right)}{j_1\left(\xi_-^{'}\right)}\xi_-^{'} - N\,\frac{h_0^{(1)}\left(\xi_-\right)}{h_1^{(1)}\left(\xi_-\right)}\xi_-\right], \tag{3.2.1.2}$$

$$B_1^+ = \frac{\xi_+^3}{3}\left(1 - \frac{\rho'}{\rho}\right). \tag{3.2.1.3}$$

In these expressions, $\xi_\pm = k_\pm a$, a prime (or no prime) above a parameter denotes within the inclusion (or host), whilst ρ refers to the effective density of the porous rock.

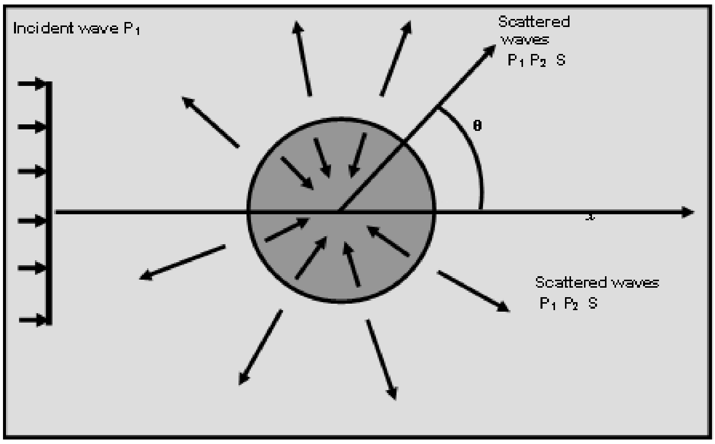

Figure 3.2.1.1: Shows the incident plane fast compressional wave and the reflected and refracted waves.

3.2.2 Random Distribution of Inclusions

Waterman and Truell (1961) showed that the velocity and attenuation of waves propagating in a medium containing a random distribution of identical inclusions can be related to the amplitude of the waves scattered from a single inclusion (Figure 3.2.2.1). According to their theory, the complex effective wave number is given by:

$$\left(\frac{k_{eff}}{k_+}\right)^2=\left[1+\frac{2\pi\upsilon f(0)}{k_+^2}\right]^2-\left[\frac{2\pi\upsilon f(\pi)}{k_+^2}\right]^2, \qquad (3.2.2.1)$$

where $k_+=\omega/v_+$ is the wave number of the fast *P*-wave in the host, υ is the density or number of scatterers per unit volume, and $f(0)$, $f(\pi)$ are forward and backward scattering amplitudes which are related to scattering coefficients by

$$f(0)=\frac{1}{ik_+}\sum_{n=0}^{\infty}i^n B_n^+, \quad f(\pi)=\frac{1}{ik_+}\sum_{n=0}^{\infty}(-i)^n B_n^+, \qquad (3.2.2.2)$$

For random distribution of mesoscopic fluid patches the scattering amplitudes are determined by substituting scattering coefficients (3.2.1.2) and (3.2.1.3) into (3.2.2.2). Incorporating a weak scattering approximation and neglecting quadratic terms in υ reduces the effective wave number (3.2.2.1) to

$$k_{eff}=k_+\left[1+\frac{4\pi\upsilon f(0)}{k_+^2}\right]^{1/2}\approx k_+\left[1+\frac{2\pi\upsilon f(0)}{k_+^2}\right]. \qquad (3.2.2.3)$$

Real and imaginary components of k_{eff}, yield the effective phase velocity v_{eff} and dimensionless attenuation (inverse quality factor) Q^{-1}

$$\frac{1}{v_{eff}}=\frac{1}{v_+}\left[1+\frac{3}{2}\frac{\delta}{\xi_+^3}\mathrm{Re}\left\{-iB_0^+ +B_1^+\right\}\right], \qquad (3.2.2.4)$$

$$Q^{-1} = 3S_1\Im\left\{\frac{\left(C_2H_1 - C_1H_2\right)^2}{H_2H_1^2}\frac{1}{N_1\dfrac{j_0\left(\xi_-^{(1)}\right)}{j_1\left(\xi_-^{(1)}\right)}\xi_-^{(1)} - N_2\dfrac{h_0^{(1)}\left(\xi_-^{(2)}\right)}{h_1^{(1)}\left(\xi_-^{(2)}\right)}\xi_-^{(2)}}\right\}, \tag{3.2.2.5}$$

where $\delta = \upsilon\big/\left(4/3\pi a^3\right)$ is the fractional volume concentration of the inclusions.

The discrete random media model discussed here models fluid patches of spherical shape, and in this respect it is similar to the regular cell models (White 1975; Johnson 2001; Pride et al. 2004). However, unlike these models, DRM is based on scattering theory and thus implies that fluid inclusions are distributed randomly through out the rock, which is more realistic. On the other hand, since phase velocity and attenuation estimates (3.2.2.4) and (3.2.2.5) are based on applying the single scattering approximation of Waterman and Truell, DRM is limited to small concentrations of inclusions. The range of admissible concentrations depends on contrasts in fluid properties between the inclusion and the host medium.

The next example models attenuation and phase velocity due to a random distribution of spherical inclusions (using the DRM model above) and a periodic distribution of spherical inclusions (using White's model (1975) as the reference model). In Figure 3.2.2.1, attenuation and phase velocity are shown when there are small contrasts in saturating fluids (a) 0.1% heavy gas and (b) 10% heavy gas within an otherwise water saturated rock. In both cases, the more compressible fluids are modelled as inclusions. In (c) the more compressible fluid is modelled as the host saturating fluid for the situation of large contrasts between fluids. Figure 3.2.2.1, top row (a) shows good agreement between attenuation and phase velocity estimates for small contrasts in fluid properties when the volume concentration of the included phase is small. Figure 3.2.2.1, middle row (b) shows a larger volume concentration of the included fluid results in different attenuation and phase velocity estimates. In particular, the phase velocity estimate of the DRM does not converge to the low frequency Gassmann-Wood limit. This is a consequence of the weak scattering approximation employed in the models derivation.

When the more compressible fluid is modelled as the host saturating fluid, the DRM can handle larger contrasts in fluid properties. In (c), attenuation and phase velocity dispersion is modelled for 50% water inclusions within an otherwise air saturated host rock of porosity 0.08. There is very good agreement between attenuation and phase velocity estimates. Figure 3.2.2.1, shows that the attenuation behaviour of periodic and random distributions of fluid inclusions is proportional to ω for low frequencies and proportional to $\omega^{-1/2}$ for high frequencies. Providing the weak scattering conditions are met, there is good agreement between attenuation and phase velocity estimates for periodic and random distributions of fluid inclusions.

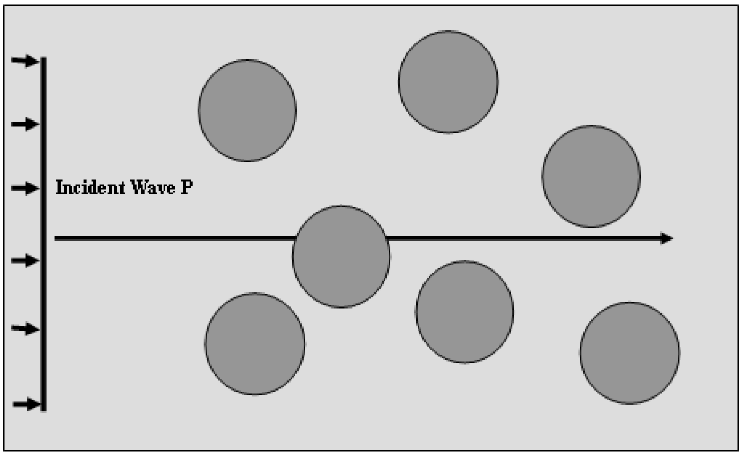

Figure 3.2.2.1: Showing a compressional wave incident on a random distribution of spherical inclusions of another poroelastic material.

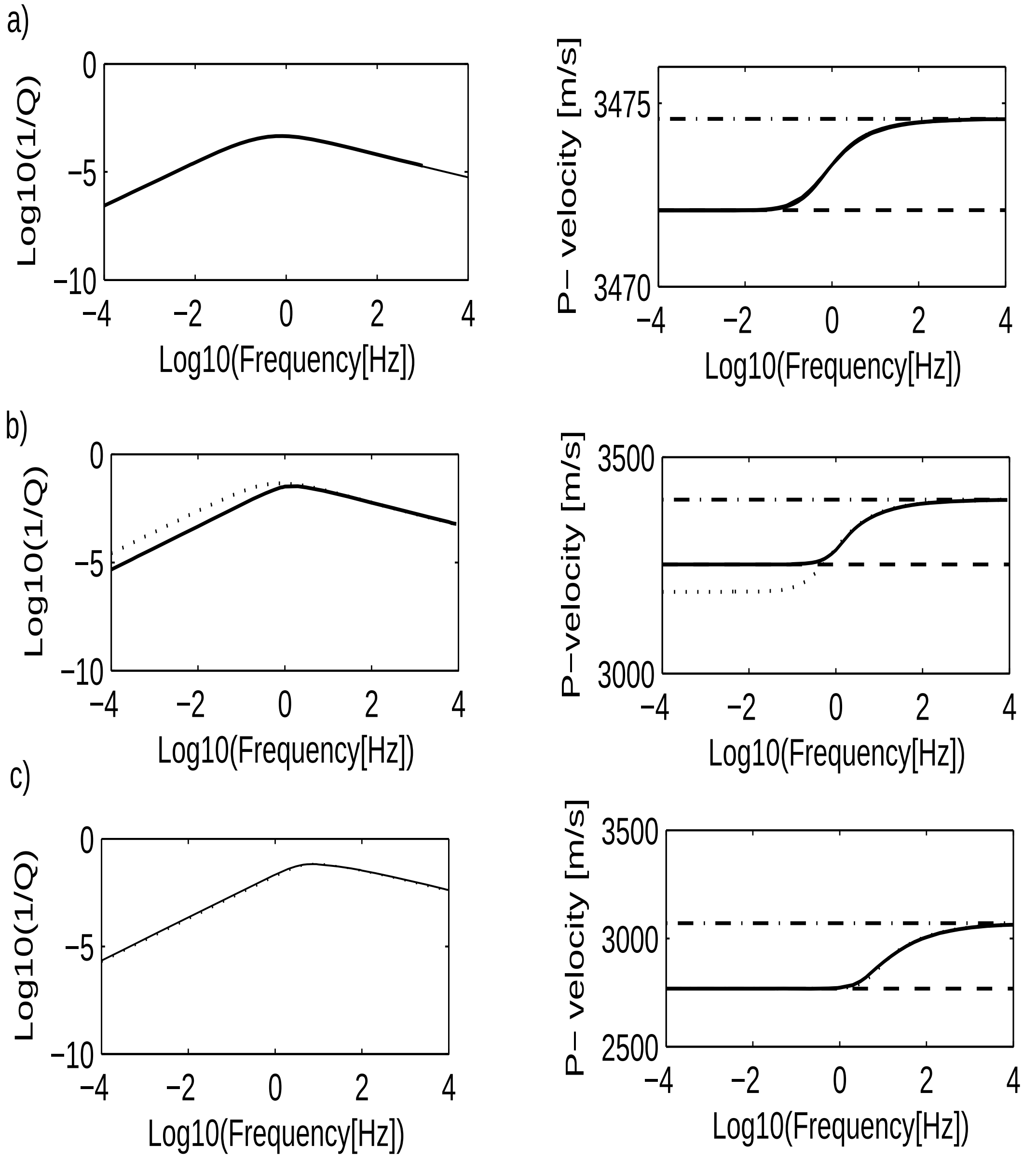

Figure 3.2.2.2: Attenuation and dispersion estimates from heavy gas inclusions within an otherwise water saturated porous rock of porosity 0.08. White's model (solid line)), Ciz and Gurevich (dotted line)) (a) has an inclusion concentration of 0.1 % (b) has an inclusion concentration of 10%, (c) attenuation and dispersion when the more compressible fluid is modelled as the host saturating fluid. In this case, water inclusions are modelled within an air saturated host rock. Good agreement is seen between periodic and random estimates.

3.3 3-Dimensional-Continuous Random Media (3DCRM)

Both of the partial saturation models (1DCRM) and (DRM) outlined above allow attenuation and dispersion to be estimated due to fluid geometries that are more realistic than the idealised geometries assumed by White's periodic approach (Section 1.3.1). However, they are still not suitable for modelling attenuation and dispersion due to fluid distributions obtained from saturation maps (Chapter Two). As the first model assumes complex layering and the second model assumes fluid inclusions are fixed in size and shape, whilst Chapter 2 fluid distributions were shown to be described well by correlation functions, like an exponential function (Debye correlation function).

In this section I develop a patchy saturation model, which allows greater versatility and flexibility in the distribution of pore fluids. Thus, it is more suited to the problem of modelling attenuation and dispersion due to realistic fluid distributions. The basis of this model is the generalised 3-dimensional poroelastic model of Müller and Gurevich (2005a, 2005b). Their model allows attenuation and dispersion to be predicted due to mesoscale heterogeneities in the bulk and shear modulus of the porous rock frame, in addition to heterogeneous fluid saturation. Such a medium is described by Biot's equations of poroelasticity with poroelastic coefficients that are continuous random functions of position. The Müller and Gurevich (2005a,b) approach is the same as that utilized by Gurevich and Lopatnikov (1995). Hence statistical smoothing is applied, which limits the precision of the model to small contrast in the physical properties of the heterogeneities.

According to Müller and Gurevich (2005a,b), the complex effective P-wave number in a 3-dimensional heterogeneous porous solid is

$$\bar{k}_{eff} = k_+\left(1 + \Delta_2 + \Delta_1 k_-^2 \int_0^\infty r\chi(r)\exp(ik_- r)dr\right), \tag{3.3.1}$$

with dimensionless coefficients given by,

$$\Delta_1 = \frac{\alpha^2 ML}{2H^2}\left(\sigma_{LL}^2 - 2\sigma_{LM}^2 + \sigma_{MM}^2\right),\ \Delta_2 = \frac{L}{2H}\sigma_{LL}^2 + \frac{\alpha^2 M}{2H}\sigma_{MM}^2, \tag{3.3.2}$$

where $k_+ = \omega\sqrt{\rho/H}$, $k_- = \sqrt{i\omega\eta/\kappa N}$,are the fast and slow P-wave numbers for the background medium, $\chi(r)$ is the normalised spatial correlation function which describes the spatial variation in rock/fluid properties (see Figure 3.3.1) and σ_{xx}'s are normalised variances of the different elastic moduli and L, M, N, H are poroelastic moduli given by Gassmann (see Chapter 1, Section 1.1.1).

For partial fluid saturation, only variances in fluid modulus M exist, so that $\sigma_{LL} = \sigma_{LM} = 0$, This reduces the complexity of the dimensionless coefficients in Equation (3.3.2) to $\Delta_2 = \alpha^2 M \sigma_{MM}^2 / 2H$ and $\Delta_1 = \left(L/H \right) \Delta_2$. To obtain the fast and slow *P-wave* numbers for the average background media, it is necessary to calculate the average properties of the fluid modulus *M*, saturated P-wave modulus H and fluid viscosity *η*. This is accomplished by taking the saturation-weighted average of each property: $\langle X \rangle = X_1 v_1 + X_2 v_2$, where v_1, v_2 are percent saturation of each fluid and $v_1 + v_2 = 1$. Thus the average fluid modulus is $M_0 = M_1 v_1 + M_2 v_2$; the average viscosity is $\eta_0 = \eta_1 v_1 + \eta_2 v_2$ and the average saturated P-wave modulus is $H_0 = L + \alpha^2 M_0$.

By using

$$v_{eff} = \omega / \mathrm{Re}\{\bar{k}_{eff}\} = \sqrt{H_{eff} / \rho_{tot}} \,,$$

Equation (3.3.1) can be transformed into an effective complex saturated *P*-wave modulus given by:

$$H_{eff}(\omega) = H_0 \left(1 - \Delta_2 - \Delta_1 k_-^2 \int_0^\infty r \chi(r) \exp(ik\_r) dr \right)^2 , \qquad (3.3.3)$$

where H_0 is the average background *P*-wave modulus determined from Gassmann's equation using the average fluid modulus M. Real and imaginary components of (3.3.3) yield the effective phase velocity $v_{eff} = \sqrt{\mathrm{Re}\{H_{eff}\} / \rho}$ and specific attenuation (inverse quality factor) $Q_{eff}^{-1} = \mathrm{Im}\{H_{eff}\} / \mathrm{Re}\{H_{eff}\}$ respectively.

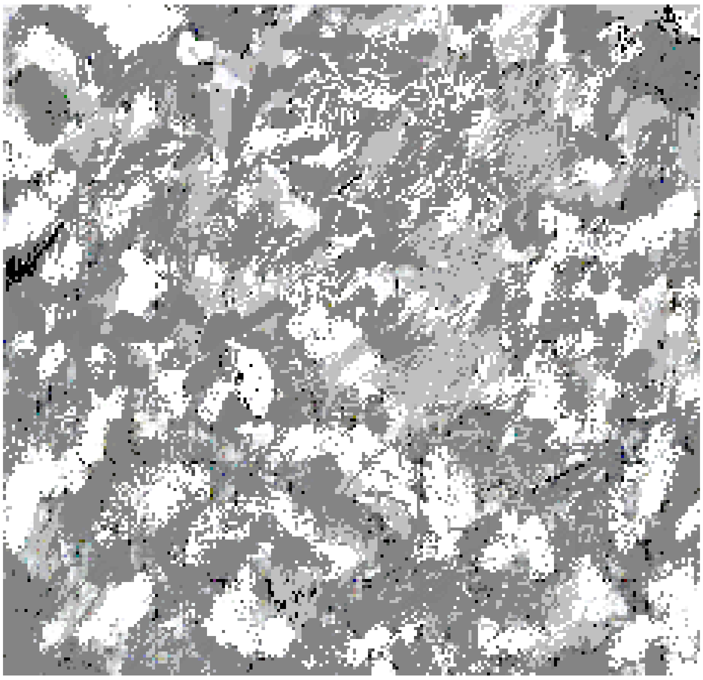

Figure 3.3.1: An idealized representation of a random medium described by some correlation function $\chi(r)$

3.3.1 Low and high frequency limits

Application of statistical smoothing in the inception of the generalised framework of Müller and Gurevich (2005a) limits the accuracy of Equation (3.3.3) to pore fluids having small contrast in fluid bulk moduli $\sigma_{MM} << 1$. This can be seen by studying the theoretical low- and high frequency limits on the P-wave moduli obtained from Equation (3.3.3). They are:

$$H_{low} = H_0 \left(1 - \Delta_2\right)^2, \tag{3.3.1.1}$$

and

$$H_{high} = H_0 \left(1 - \Delta_2 + \Delta_1\right)^2, \tag{3.3.1.2}$$

respectively. For small contrast in fluid properties $\sigma_{MM} << 1$ these moduli approach theoretical Gassmann-Wood H_W and Gassmann-Hill H_H limits as given by equations (1.1.7)-(1.1.9) and (1.2.2.1), and (1.2.2.2) respectively.

I will now show that the model does converge to Gassmann-Wood and Gassmann-Hill limits for small contrasting fluids. Let the fluid moduli for fluid 1 and fluid 2 be

$$M_1 = M_0 - \delta_1 \text{ and } M_2 = M_0 + \delta_2 , \tag{3.3.1.3}$$

where δ_1 and δ_2 are displacement fluid moduli for each respective fluid. By taking the average $M_1 v_1 + M_2 v_2 = M_0$; the second fluid displacement modulus can be formulated in terms of the first fluid displacement modulus $\delta_2 = \frac{\delta_1 v_1}{v_2}$, this gives a normalised variance of $\sigma_{MM}^2 = \frac{\langle M^2 \rangle}{\langle M \rangle^2} - 1 = \frac{v_1}{v_2} \frac{\delta_1^2}{M_0^2}$.

Firstly, consider the effective fluid modulus M_W obtained using Wood law

$$\frac{1}{M_W} = \frac{(v_1 + v_2)(\alpha - \phi)}{K_S} + \phi \left[\frac{v_1}{K_{f1}} + \frac{v_2}{K_{f2}} \right] = v_1 \left[\frac{(\alpha - \phi)}{K_S} + \frac{\phi}{K_{f1}} \right] + v_2 \left[\frac{(\alpha - \phi)}{K_S} + \frac{\phi}{K_{f2}} \right] = \frac{v_1}{M_1} + \frac{v_2}{M_2} = \left\langle \frac{1}{M} \right\rangle . \tag{3.3.1.4}$$

This shows that effective fluid modulus for Wood's limit is equal to the harmonic average of both fluid moduli. Substitution of Equations (3.3.1.3) into (3.3.1.4) gives

$$M_W = \frac{(M_0 - \delta_1)\left(M_0 + \delta_1 \frac{v_1}{v_2} \right)}{v_1 (M_0 - \delta_1) + v_2 \left(M_0 + \delta_1 \frac{v_1}{v_2} \right)} = M_0 - \delta_1 \left(1 - \frac{v_1}{v_2} \right) - \frac{\delta_1^2}{M_0} \frac{v_1}{v_2} . \tag{3.3.1.5}$$

The saturated P-wave modulus at Woods limit is then

$$H_W = L + \alpha^2 M_W = H_0 - \alpha^2 \left(\frac{\delta_1^2}{M_0} \frac{v_1}{v_2} \right) - \alpha^2 \delta_1 \left(1 - \frac{v_1}{v_2} \right) . \tag{3.3.1.6}$$

Now consider (3.3.1.1)

$$H_{low} = H_0 (1 - \Delta_2)^2 \approx H_0 (1 - 2\Delta_2) = H_0 - \alpha^2 M_0 \sigma_{MM}^2 = H_0 - \alpha^2 \left(\frac{\delta_1^2}{M_0} \frac{v_1}{v_2} \right) \approx H_W + \alpha^2 \delta_1 \left(1 - \frac{v_1}{v_2} \right) \tag{3.3.1.7}$$

where the last term in (3.3.1.7) is small when contrast is small.

Consider high frequencies, using Gassmann (Eq. (1.1.7)-(1.1.9)) the saturated P-wave modulus for the regions of the rock saturated by fluid 1 and fluid 2 are

$$H_1 = L + \alpha^2 M_1 \text{ and } H_2 = L + \alpha^2 M_2 . \tag{3.3.1.8}$$

Substitution of (3.3.1.8) into Hills limit (1.2.2.2) gives

$$H_{BGH} = \frac{H_1 H_2}{v_1 H_1 + v_2 H_2} = \frac{\left(H_0 - \alpha^2 \delta_1\right)\left(H_0 - \frac{\alpha^2 \delta_1 v_1}{v_2}\right)}{H_0 + \frac{\delta_1 \alpha^2}{v_2}\left(v_1^2 - v_2^2\right)} = H_0 - \frac{v_1}{v_2} \frac{\alpha^4 \delta_1^2}{\left(H_0 - \delta_1 \alpha^2 \left(1 - \frac{v_1}{v_2}\right)\right)} . \qquad (3.3.1.9)$$

Now consider the high frequency limit of the model (Equation 3.3.1.2)

$$H_{HIGH} = H_0 \left(1 + \Delta_1 - \Delta_2\right)^2 \approx H_0 \left(1 + 2\left(\Delta_1 - \Delta_2\right)\right) = H_0 + \frac{\alpha^2 M_0 L}{H_0} \sigma_{MM}^2 - \alpha^2 M_0 \sigma_{MM}^2 = H_0 - \frac{v_1}{v_2} \frac{\alpha^4 \delta_1^2}{H_0} . \qquad (3.3.1.10)$$

Thus as contrast becomes small Equations (3.3.1.9) and (3.3.1.10) will converge.

In other words, the moduli given by Equations (3.3.1.1) and (3.3.1.2) are asymptotically consistent with Gassmann-Wood and Gassmann-Hill limits for small contrast in fluid modulus. However, in partially saturated rocks the variation in fluid properties is often large, resulting in significant deviation of predicted low- and high-frequency moduli from the theoretical limits.

To make the model consistent with the theoretical limits of Gassmann-Wood equations and Gassmann-Hill equations, I introduce a scaling function:

$$H_{SC}\left(\omega\right) = H_W \left(1 + \frac{H_H - H_W}{H_{high} - H_{low}} \times \frac{H_{eff}\left(\omega\right) - H_{low}}{H_W}\right). \qquad (3.3.1.11)$$

The new complex modulus $H_{SC}\left(\omega\right)$ predicted by Equation (3.3.1.11) behaves similarly to that predicted by Equation (3.3.3) but is consistent with the theoretical limits when contrast in fluid bulk moduli is large. This scaled model is called the 3D continuous random media (3DCRM) of patchy saturation.

The scaling function approximation (3.3.1.11) can be understood as taking the exact frequency dependence of the saturated P-wave modulus (at low fluid contrast) and supposing that for high fluid contrast the frequency-dependent characteristics (in Equation (3.3.1.11)) are the same. That is, the only factor considered to effect the frequency-dependent characteristics of the saturated P-wave modulus is fluid distribution, which is described by a correlation function.

3.3.2 Different Fluid Distributions: Exponential and Gaussian Correlation Functions

Dispersion and attenuation in CRM depends on the correlation function $\chi(r)$, which in turn is determined by the spatial distribution of saturating fluids. To obtain closed-form expressions for Equation (3.3.3) one needs to specify the correlation function.

In particular, for an exponential correlation function (Debye random media)

$$\chi(r) = \exp(-|r|/a) \ , \tag{3.3.2.1}$$

the effective complex *P*-wave modulus is

$$H_{eff}(\omega) = H_0 \left(1 - \Delta_2 - \frac{\Delta_1 k_-^2 a^2}{(ik_- a - 1)^2}\right)^2 , \tag{3.3.2.2}$$

where *b* is the correlation length, which characterizes a characteristic length of the inhomogeneities.

For a double Debye correlation function of:

$$\chi_2(r) = \chi_{Small} + \chi_{L\arg e} = b_S \exp\left(-\frac{r}{a_S}\right) + b_L \exp\left(-\frac{r}{a_L}\right) = b_S \exp\left(-\frac{r}{a_S}\right) + (1 - b_s)\exp\left(-\frac{r}{a_L}\right), \tag{3.3.2.3}$$

the effective complex P-wave modulus is

$$H_{eff}(\omega) = H_0 \left(1 - \Delta_2 - \Delta_1 k_-^2 \left(\frac{b_S {a_S}^2}{(ik_- a_S - 1)^2} + \frac{(1 - b_S) {a_L}^2}{(ik_- a_L - 1)^2}\right)\right)^2 . \tag{3.3.2.4}$$

For a Gaussian correlation function

$$\chi(r) = \exp(-r^2/b^2), \tag{3.3.2.5}$$

equation (3.3.3) yields:

$$H_{eff}(\omega) = H_0 \left(1 - \Delta_2 - 2\Delta_1 y^2 \left[1 - y\sqrt{\pi}\exp(y^2)\mathrm{erfc}(y)\right]\right)^2 , \tag{3.3.2.6}$$

where *erfc* denotes the complementary error function and $y = -ik\_b/2$.

I note that for a large class of correlation functions explicit expressions for the effective *P*-wave modulus can be obtained, such as for a fractal distribution of fluids (Müller et al. 2008). In the next couple of examples, I will illustrate some general properties of 3DCRM.

I. Shape of attenuation and dispersion curves

The physical properties used in this example correspond to 30% light gas saturation in an otherwise water saturated rock (as shown in Tables (3.1.1.1) and (3.1.1.2)). Figure 3.3.2.1 shows (a) attenuation and (b) velocity estimates obtained using exponential and Gaussian correlation functions. Both attenuation curves have the same frequency dependence at low frequencies, being proportional to ω. However at high frequency the attenuation curves display different frequency dependencies, with the exponential being proportional to $\omega^{-1/2}$, whilst the Gaussian is proportional to ω^{-1}. (b) Shows the frequency bandwidth for which velocity changes rapidly is wider for exponentially correlated fluid distributions than for the Gaussian correlated fluid distributions.

II. Peak frequency of attenuation

The rock properties used in this example are for the same rock as above, the fluid properties are 30% heavy gas saturation in an otherwise water saturated rock (as given in Table 3.1.1.2). Figure 3.3.2.2 shows frequency-dependent (a) attenuation and (b) velocity estimates obtained using an exponential correlation function with different correlation lengths ranging from *a=0.5m to a=0.0625m* . As the correlation length decreases the frequency at which attenuation is maximum shifts towards higher frequencies. Similarly the frequency bandwidth over which velocity changes most rapidly, also shifts to higher frequencies. Although not shown here a similar effect has been observed by having a fixed correlation length and varying the permeability of the rock. Namely, as permeability decreases the peak frequency of attenuation will shift to higher frequencies, whilst for lower permeability the peak frequency of attenuation will shift to lower frequencies (Müller et al. 2007).

Figure 3.3.2.3 shows the peak frequency of attenuation for a range of rock permeabilities (~1 to 0.001 Darcy) having fluid heterogeneities of different correlation lengths (50cm to 0.25 cm). As the permeability decreases so does the frequency at which attenuation peaks for each correlation length. This occurs as fluid pressure equilibration in less permeable rocks, requires more time than in highly permeable rocks, for a fixed patch size. As the patch size (in terms of correlation length) increases, more time is required for fluid pressure equilibration as the diffusion length (refer to Chapter 1, Section 1.2.2) is less than the patch size.

I freely acknowledge that certain regions of the permeability-frequency space (within Figure 3.3.2.3) may be dominated by elastic scattering and other mechanisms, etc. and that the assumptions of low frequency Biot theory underpinning 3DCRM will be invalid. Hence, mesoscopic fluid flow will not be controlling factor on the acoustic response of partially saturated rock for these frequencies and permeability. Nevertheless, Figure 3.3.2.3 illustrates nicely that attenuation will peak in the seismic bandwidth for a range of rock permeabilities and saturation correlation lengths.

III. Magnitude of attenuation

Figure 3.3.2.4 shows maximum attenuation (at peak frequency) as a function of Biot's coefficient (see Chapter 1, Section 1.1). The shear wave modulus of the dry frame is altered as to satisfy Poisson ratio v=0.2. Fluid distribution is assumed to be exponential and there is 90 % water saturation with 10 % saturation by another fluid having moduli of K_{fi} *=0.01, 0.1, 1 GPa*. The figure highlights two points: 1) as the Biot coefficient decreases the magnitude of attenuation deceases. This occurs because fluid flow effects are diminished for stiff rocks because the fluid pressure induced by rock frame compression is reduced. 2) When the difference in fluid bulk moduli decreases, the magnitude of attenuation decreases. This occurs as the rock frame will induce similar fluid pressure in fluids of similar compressibility, hence reducing the gradient in fluid pressure between heterogeneities and thus wave induced fluid flow is diminished.

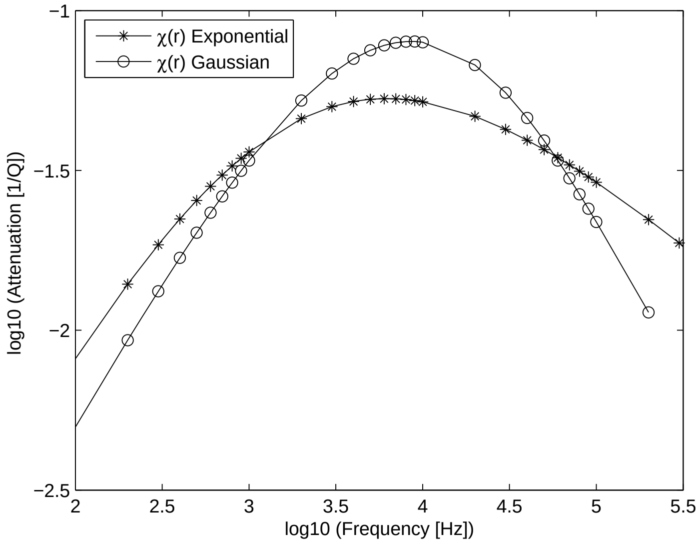

(a)

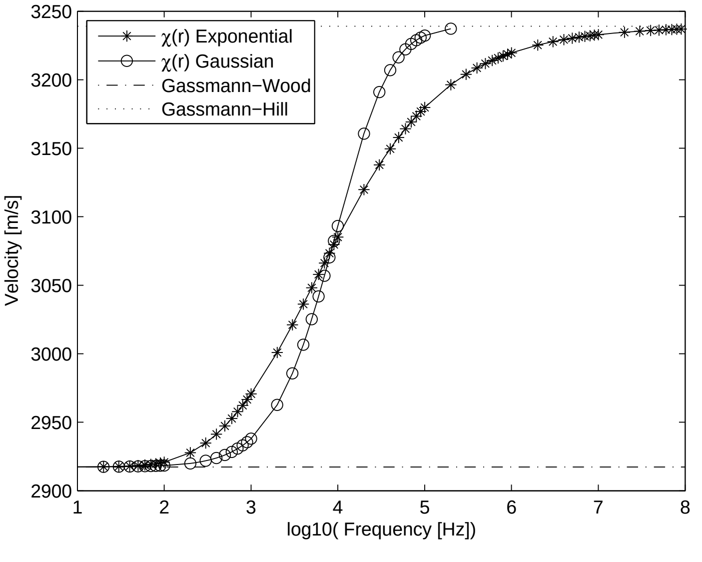

(b)

Figure 3.3.2.1: Frequency-dependent attenuation and dispersion from 3DCRM with different correlation functions. (a) Shows attenuation and (b) velocity when correlation functions are exponential and Gaussian, the correlation lengths are the same. The frequency-dependent shapes of the attenuation and dispersion curves are different.

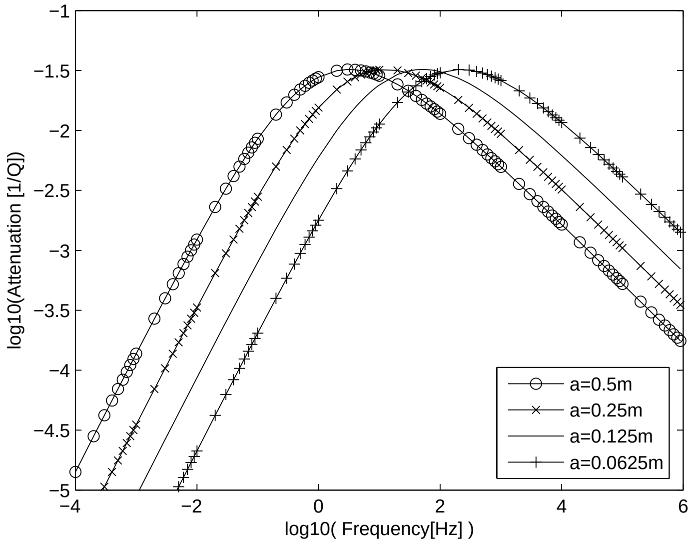

(a)

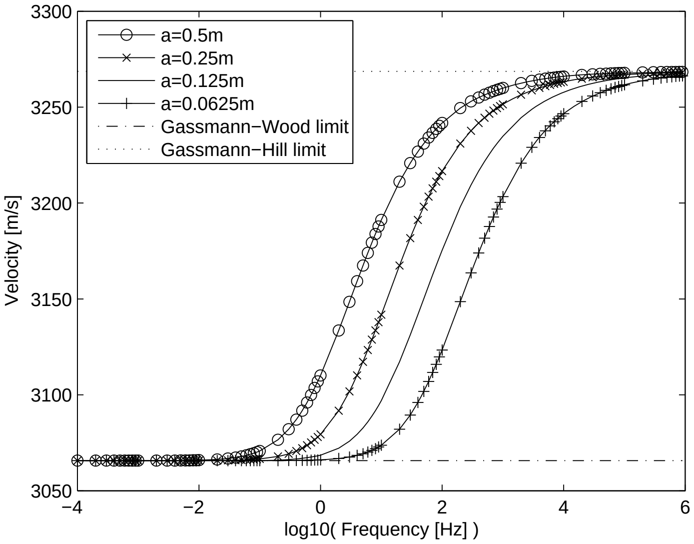

(b)

Figure 3.3.2.2: The influence of correlation length on attenuation and dispersion. (a) Shows attenuation and (b) velocity curves. As the correlation length is reduced, the frequency-dependent curves are shifted to higher frequencies.

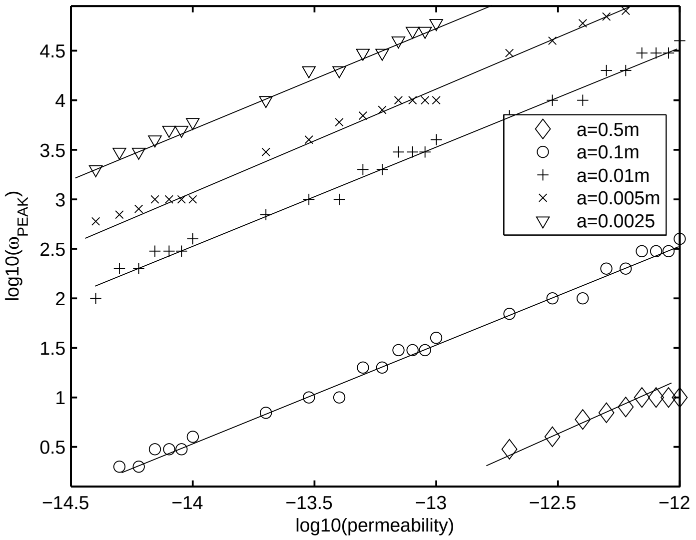

Figure 3.3.2.3: Peak attenuation frequency for rocks of different permeabilities having different characteristic fluid heterogeneity length scales (correlation lengths).

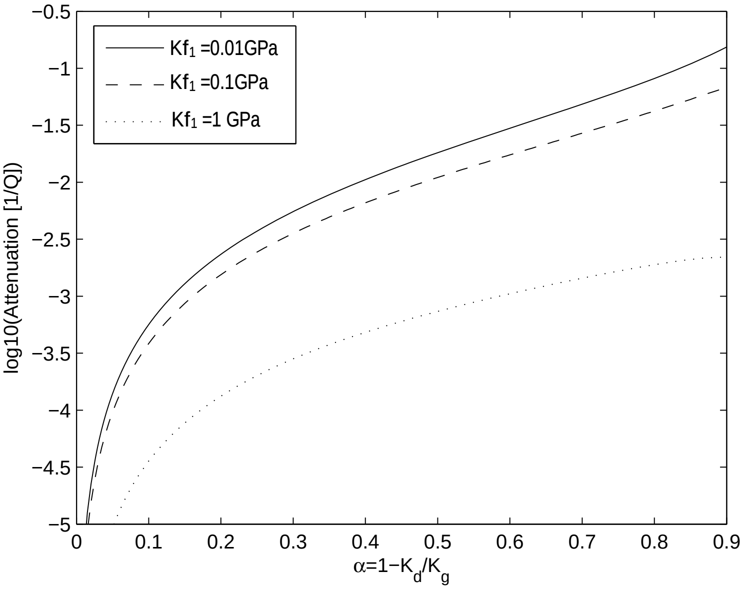

Figure 3.3.2.4: Peak attenuation value as a function of frame stiffness (Biot coefficient) for 90% water saturated rock having fluid heterogeneities of different compressibility.

3.4 Application of 3DCRM to Special Fluid Distributions

In the previous section, 3DCRM was used to model attenuation/dispersion due to fluid heterogeneities characterised by specific correlation functions, such as exponential and Gaussian. These correlation functions typically arise from random media having complex and irregular variations in material properties (Klimes 2002). When fluid heterogeneities are distributed using such correlation functions, it is not always possible to distinguish an “included” fluid from a “host” fluid. Moreover, in some applications we actually want to model fluid inclusions of regular or fixed shape. For these situations exponential and Gaussian correlation functions are not really suitable.

If we wish to use 3DCRM to model attenuation and dispersion due to a random distribution of fluid inclusions (having regular shape), then we need to search for appropriate correlation functions. An obvious correlation function to look for is one which describes a 3D distribution of randomly positioned spheres. This correlation function would allow us to use 3DCRM to model attenuation and dispersion due fluid bubbles distributed randomly thorough a rock saturated by another fluid. Luckily, I have found such a correlation function (Torquato & Stell 1985); amongst two others which are both interesting and relevant: the overlapping spheres (Weissberg 1963,Torquato 2002) and random checkerboard (Lu & Torquato 1992). In this section, I will model attenuation and dispersion using these three correlation functions.

3.4.1 3DCRM for Non-overlapping Spherical Inclusions

The DRM model outlined in Section 3.2 implicitly assumes that fluid heterogeneities are present as randomly distributed spheres and thus it assumes a geometry enabling us to model attenuation and dispersion due to bubbles. However, DRM is only accurate for certain inclusion concentrations and certain fluid contrasts. As such, my motivation for using 3DCRM is to find a less restrictive approach to model attenuation and dispersion, due to bubble like fluid distributions.

The key to using 3DCRM to model attenuation and dispersion due to bubble like fluid distributions is knowing the right correlation function to substitute into Equation (3.3.3). The correlation function I use was derived by Torquato and Stell (1985). It describes the two point probability function of a random distribution of non-overlapping spheres in equilibrium (see also Section 5.4). As the evaluation of the Torquato and Stell analytical correlation function requires the inverse Fourier transform of a complicated function, I use their tabulated results (given in Table 3.4.1.1) for illustration. Noting that in principle, one could perform the necessary computations to evaluate their correlation function for any inclusion concentrations which are physically realisable.

To use the results presented in Table 3.4.1.1, one must convert them to a correlation function. To do this I use Equation (2.3.1.2), which shows that the two point probability function for the inclusion phase can be derived from the host phase and vice versa. In Figure 3.4.1.1 the correlation function is shown for 10%, 20% and 30 % spherical inclusions. As the inclusion concentration increases, oscillatory correlations become more pronounced as there is a higher probability that the two offset points are more likely to sample spherical inclusions.

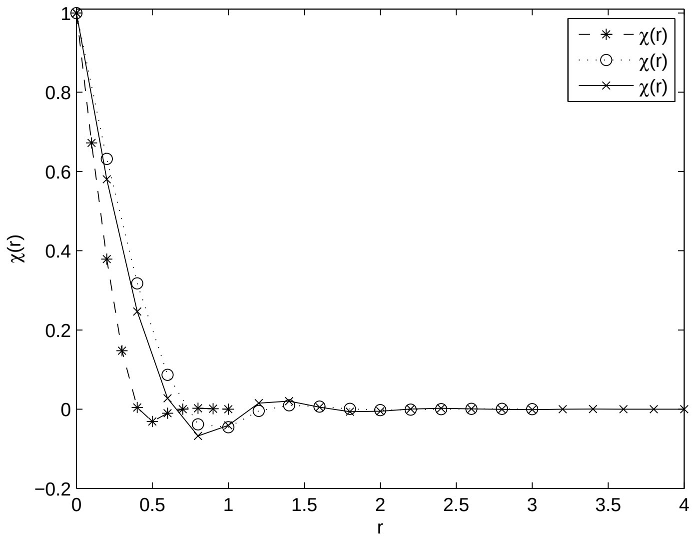

*Figure: 3.4.1.1: Correlation functions for a 3D random distribution of spherical inclusions. The correlation functions for 10%, 20% and 30% saturations are given by symbols *, o, x, respectively. The correlation functions for higher inclusion saturations have more pronounced oscillations.*

Table 3.4.1.1: Two point probability function values for the host medium of randomly distributed non-overlapping spherical inclusions.

	$S_2(r)$	$S_2(r)$	$S_2(r)$
r	$v_i = 0.1$	$v_i = 0.2$	$v_i = 0.3$
0.0	0.9000	0.8000	0.7000
0.2	0.8705	0.7411	0.6119
0.4	0.8441	0.6908	0.5418
0.6	0.8233	0.6539	0.4958
0.8	0.8104	0.6339	0.4758
1.0	0.8072	0.6327	0.4814
1.2	0.8091	0.6393	0.4932
1.4	0.8100	0.6416	0.4943
1.6	0.8102	0.6411	0.4911
1.8	0.8101	0.6401	0.4887
2.0	0.8100	0.6396	0.4889
2.2		0.6398	0.4901
2.4		0.6400	0.4905
2.6		0.6401	0.4902
2.8		0.6401	0.4899
3.0		0.6400	0.4898
3.2			0.4900
3.4			0.4901
3.6			0.4900
3.8			0.4900
4.0			0.4900

To examine the accuracy of the 3DCRM I make comparisons with DRM. In order to utilize the DRM model (Equations 3.2.2.4 and 3.2.2.5) accurately at inclusion concentrations of 10% or more, I need to assume that the less compressible fluid is in the inclusion, whilst the more compressible fluid is the host. Otherwise, the DRM model does not converge to Gassmann-Wood limits. Hence, I model 10 % water inclusions in an otherwise gas saturated host rock.

Figure 3.4.1.2 shows DRM and 3DCRM (with Torquato and Stell (1985) correlation function) estimates of (a) attenuation and (b) dispersion due to 10 % randomly distributed water inclusions within an otherwise air saturated rock. The attenuation and velocity curve for 3DCRM (dashed solid dotted line) are in good agreement with DRM (solid line) over the entire frequency range. This indicates that 3DCRM can be used to model attenuation and dispersion due to randomly distributed non-overlapping spherical inclusions.

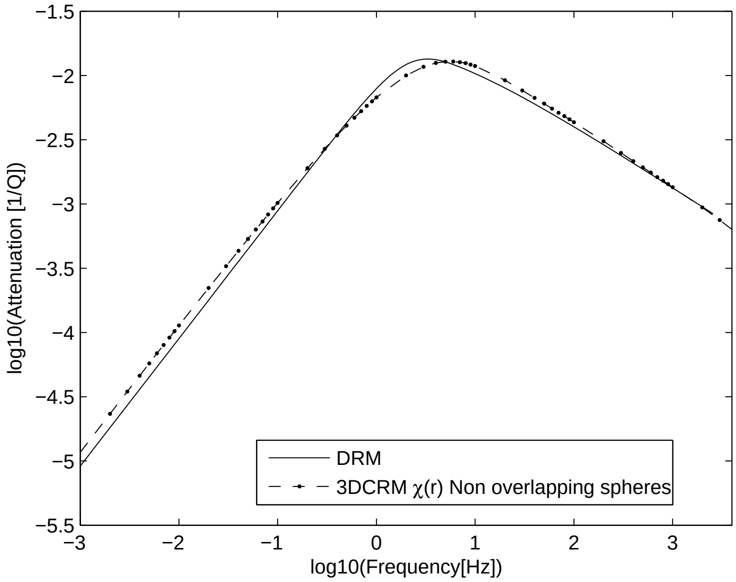

(a)

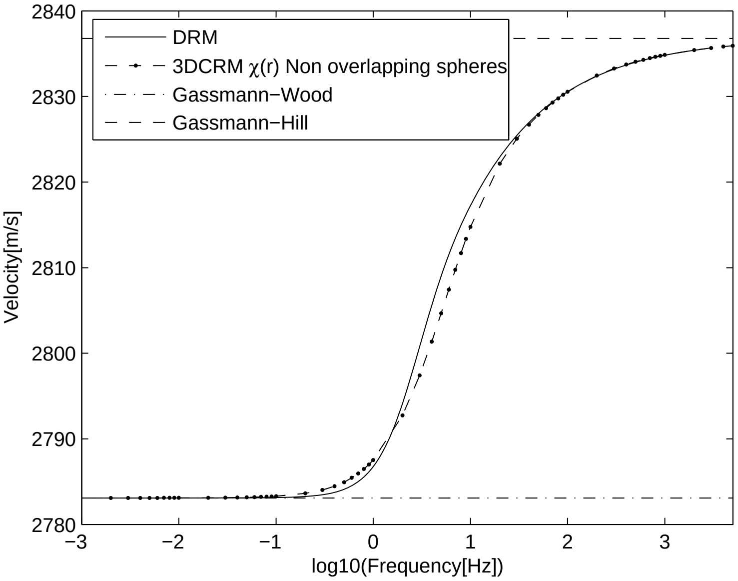

(b)

Figure 3.4.1.2: Comparison of DRM and 3DCRM attenuation and dispersion estimates for randomly distributed spheres. (a) Shows attenuation and (b) dispersion estimates. The frequency-dependent curves are in good agreement.

To compare attenuation and dispersion estimates obtained using 3DCRM with (1) exponential (Equation 3.3.2.1) and (2) random sphere (Table 3.4.1.1) correlation functions, it is necessary to relate key parameters which characterize each type of media. The first is characterized by a correlation function and correlation length; whilst second (the discrete media) is characterized by a correlation function defined in terms of inclusion radius, volume concentration, etc. Below I derive an approximate relationship that links the key parameters of each media. The approach utilized is to equate the power expansion of the exponential correlation function, to the correlation function defined by Torquato (2002) for a random distribution of non-overlapping spherical inclusions.

For a random array of identical three-dimensional non-overlapping spheres of diameter D, an approximate two point probability function valid for small offset *r* is

$$S_2(r) = v_1 - \frac{s_v}{4} r + \frac{Z v_1}{4}\left(\frac{r}{D}\right)^2 + O\left(r^3\right), \qquad (3.4.1.1)$$

where s_v is the specific surface, defined to be the interface area per unit volume and Z is the mean coordination number defined to be the average number of contacts a given sphere has with its neighbour (Frisch & Stillinger 1963). By assuming that the spheres are isolated (i.e. not in contact) the coordination number becomes zero. Furthermore, by considering small offsets and using relation Equation 3.1.2.1 the correlation function becomes

$$X(r) \approx \frac{v_1 - \frac{s_v}{4} r - v_1^2}{v_1 v_2} = 1 - \frac{s_v}{4 v_1 v_2} r\,. \qquad (3.4.1.2)$$

Setting this equal to the exponential correlation function (assuming small offsets) gives

$$X(r) = 1 - \frac{s_v}{4 v_1 v_2} r = \exp\left(\frac{-r}{a}\right) \approx 1 - \frac{r}{a},$$

thus

$$a = \frac{4 v_1 v_2}{s_v} = \frac{v_1 v_2}{\pi \rho_{sp} R^2}\,, \qquad (3.4.1.3)$$

where $\rho_{sp} = n_{sp} / L_B^3$ is the number of spheres per unit volume. Equation (3.4.1.3) allows us to choose the correlation length (Debye) of the exponential correlation function, such that attenuation and dispersion curves have similar frequency scaling to the attenuation and dispersion curves estimated from the DRM. This relation can also be modified to enable comparison of 3DCRM with periodically distributed spheres (i.e. White's model)

$$a = \frac{4v_1 v_2}{s_v} = \frac{4v_1 v_2 R_C^3}{3R_i^{\ 2}}, \tag{3.4.1.4}$$

where R_C is the composite volume radius (see Chapter 1, Section 1.3).

In the next example I model a rock which is saturated by 10% gas bubbles (fluid bulk modulus $K_{f1} = 1\mathbf{GPa}$) in an otherwise water saturated rock. Hence, the more compressible fluid is modelled as spherical inclusions, whilst the less compressible fluid is the host. The spherical inclusions have a radius of r=0.5m and all other rock properties are as Table 3.1.1.1. Figure 3.4.1.3 shows (a) attenuation and (b) dispersion as predicted by 3DCRM with exponential correlation function (dotted line) and with non-overlapping sphere correlation function (dashed and dotted line), and DRM (solid line). The first aspect to note is that DRM does not satisfy the lower limit on velocity given by Gassmann-Wood equations and hence the approach is inaccurate for this modelling scenario. Secondly, the 3DCRM attenuation curve is broader when the correlation function is exponential. Thirdly, by setting the correlation length according to Equation (3.4.1.3) the frequency at which both 3DCRM curves peak are in reasonable agreement.

The broadness of the 3DCRM attenuation with exponential correlation function relative to the DRM attenuation is not surprising, as the correlation length (given by Equation 3.4.1.3) is an average length scale, whilst DRM has only one length scale being the inclusion radius. Hence there will be fluid patches (within an exponentially correlated media) persisting on length scales less than and greater than the correlation length. This means that when wave frequency increases, patches that are smaller than the average patch size will remain relaxed, whilst others which are larger than the average patch size will become unrelaxed. This has the effect of broadening the attenuation curve of the 3DCRM and extending the frequency band width for which velocity changes most rapidly.

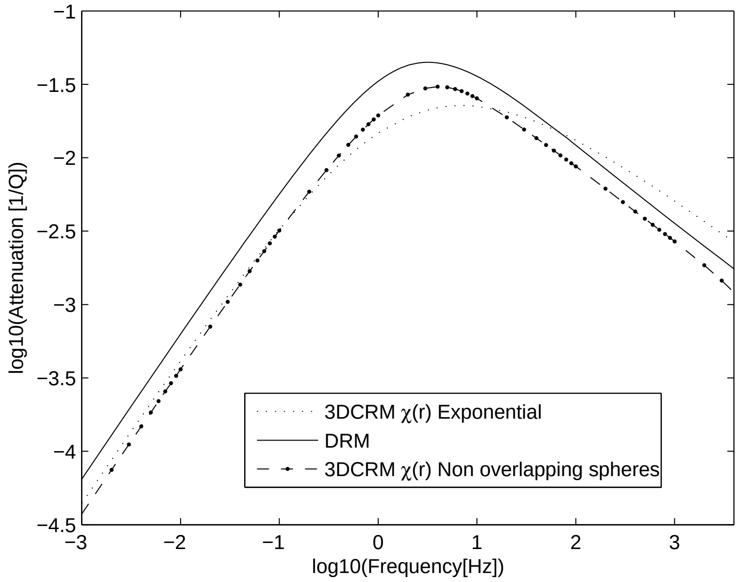

(a)

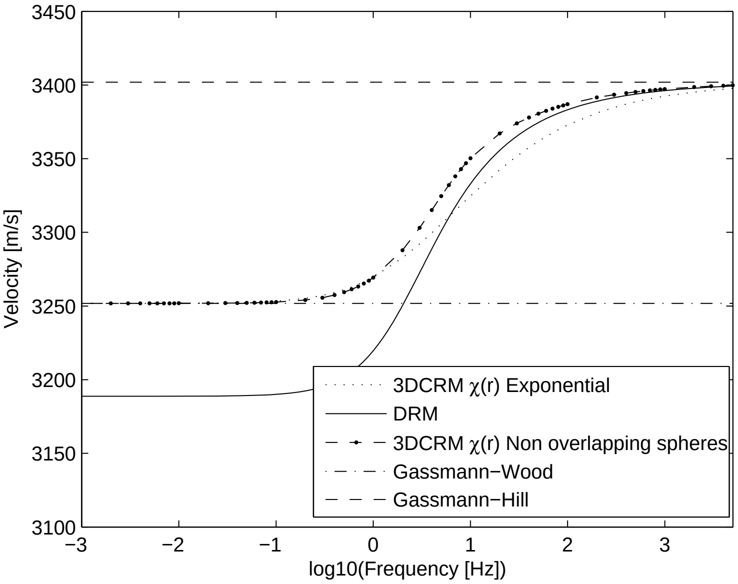

(b)

Figure 3.4.1.3: Comparison of DRM and 3DCRM attenuation and dispersion estimates for randomly distributed spheres of heavy gas. (a) Shows attenuation and (b) dispersion estimates. The DRM approach does not converge to Gassmann-Wood limits and hence the attenuation estimates are erroneous.

3.4.2 3DCRM Overlapping Sphere Correlation Function

In the previous section, 3DCRM was compared against DRM when fluid heterogeneities were randomly distributed non-overlapping spherical inclusions. That is, there were randomly distributed spherical fluid inclusions (existing on a lengthscale greater than pore scale, but less than wavelength scale) within an otherwise homogeneously fluid saturated rock. It was found that 3DCRM and DRM were in good agreement for cases where DRM satisfies the Gassmann-Wood limit. Another fluid heterogeneity/geometry which is very similar and also of interest is randomly distributed overlapping spherical inclusions (i.e. inclusions may have non zero intersection volume). This type of fluid distribution may arise when the discrete spherical fluid patches join together to form larger patches, which could occur when the included fluid concentration increases. Here I show by choosing an appropriate correlation function that 3DCRM can be used to model attenuation and dispersion due to more complicated spherical shapes.

The two point probability function of randomly distributed overlapping spheres having sphere radius R (Torquato 2002) is :

$$S_2(r) = \exp\left[-\eta^* \frac{v_2(r;R)}{v_1(R)}\right]. \tag{3.4.2.1}$$

Here η^* is the reduced density given by

$$S_1 = v_2 = \exp(-\eta^*), \tag{3.4.2.2}$$

where v_2 is the volume fraction of the host fluid. For overlapping spheres there is reduced density, because the union volume of a system of overlapping spheres is less than the union volume of a system of non-overlapping spheres (refer to Figure 3.4.2.1 a). Specifically, the union volume of two overlapping spheres (Figure 3.4.2.1 (b)) is

$$\frac{v_2(r;R)}{v_1(R)} = 2\Theta(r-2R) + \left[1 + \frac{3}{4}\frac{r}{R} - \frac{1}{16}\left(\frac{r}{R}\right)^3\right]\Theta(2R-r), \tag{3.4.2.3}$$

where

$$\frac{v_2(r;R)}{v_1(R)} = \left[1 + \frac{3}{4}\frac{r}{R} - \frac{1}{16}\left(\frac{r}{R}\right)^3\right], \qquad (r \le 2R), \tag{3.4.2.4}$$

and

$$v_2(r;R)/v_1(R) = 2 \qquad (r \geq 2R) \qquad (3.4.2.5)$$

Hence the two point probability function is:

$$S_2(r) = v_2 \exp\left(-\eta^*\left[\frac{3}{4}\frac{r}{R} - \frac{1}{16}\left(\frac{r}{R}\right)^3\right]\right) \qquad (r \leq 2R) \qquad (3.4.2.6)$$

and

$$S_2(r) = v_2^2 \,. \qquad (r \geq 2R) \qquad (3.4.2.7)$$

Substitution of Equations (3.4.2.6) and (3.4.2.7) into the normalised correlation function gives

$$\chi(r) = \frac{S_2(r) - v_2^2}{v_1 v_2} = \frac{\exp\left(-\eta^*\left[\frac{3}{4}\frac{r}{R} - \frac{1}{16}\left(\frac{r}{R}\right)^3\right]\right) - v_2}{v_1} \qquad (r \leq 2R) \qquad (3.4.2.8)$$

and

$$\chi(r) = 0 \qquad (r \geq 2R) \qquad (3.4.2.9)$$

Unfortunately, substitution of Equation (3.4.2.8) into the saturated P-wave modulus Equation (3.3.3) results in an integral that I was not able to solve or find an analytical solution for. Hence to use this particular correlation function in 3DCRM will require numerical integration of Equation (3.3.3) or simplification of the correlation function (Equation (3.4.2.8)) to allow analytical integration. In the following examples, I shall numerically estimate the integral within Equation (3.3.3) (Section 3.3 page 110).

In the first example, I model attenuation/dispersion due to spherical inclusions of heavy gas having total volume concentration of 0.1% within an otherwise water saturated rock. Figure 3.4.2.2 shows (a) attenuation and (b) velocity as predicted by DRM and 3DCRM with overlapping sphere correlation function (Equation 3.4.2.8). Clearly, both curves are in excellent agreement. This is expected as DRM satisfies the lower limit on velocities given by Gassmann-Wood; whilst a medium described by correlation function (3.4.2.8) at such small volume fractions is representative of a system of non-overlapping spheres. That is, at such low volume fractions of inclusions there will be little overlap and hence the overlapping sphere correlation function can be utilized to model a system of non-overlapping spheres. Thus both DRM and 3DCRM curves should be in agreement.

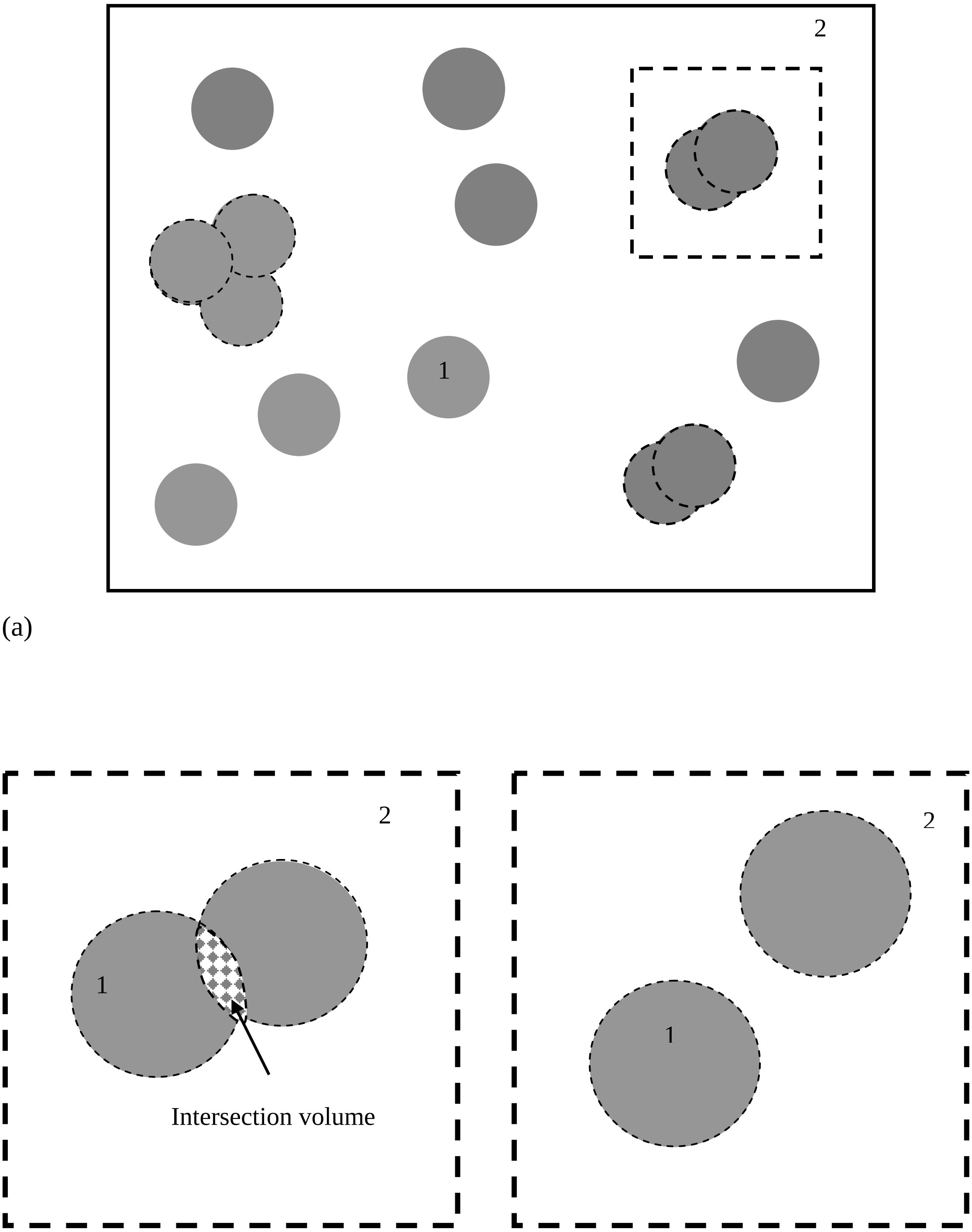

(a)

(b)

(c)

Figure 3.4.2.1: Cartoon representation of overlapping sphere fluid distribution. (a) Shows a random distribution of spherical inclusions which are permitted to overlap. This can create very complicated bubble like shapes. (b) The intersection of the overlapping spheres is cross-hatched, this causes reduced density relative to two non-overlapping spheres as shown in (c).

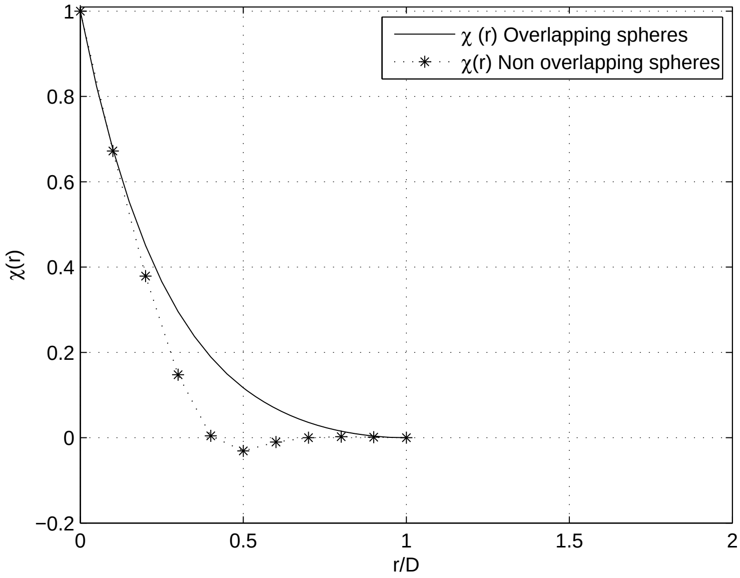

(a)

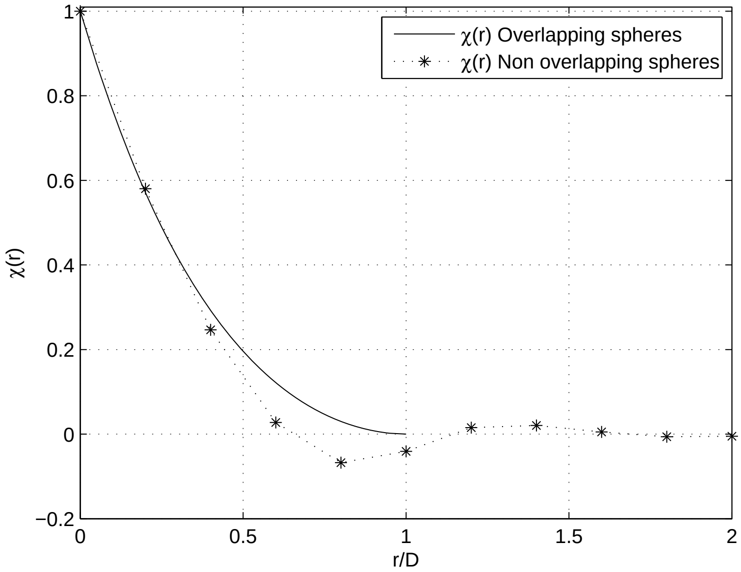

(b)

Figure 3.4.2.2: 3DCRM overlapping and non-overlapping correlation functions. (a) Shows correlation functions for 10 % spherical inclusions and (b) for 30% spherical inclusions.

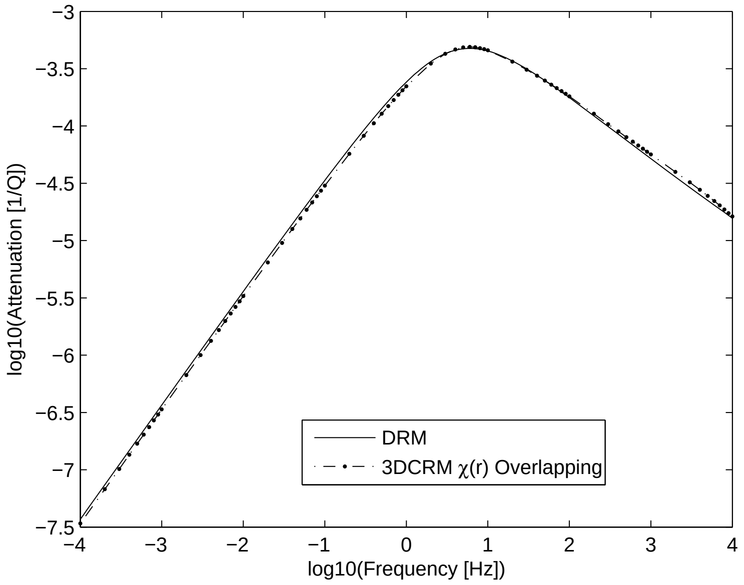

(a)

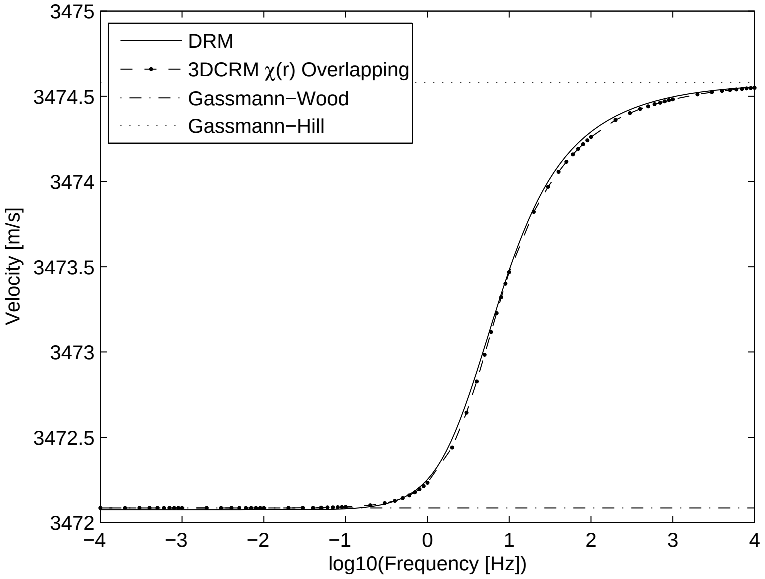

(b)

Figure 3.4.2.3: Frequency-dependent attenuation and dispersion estimates obtained from randomly distributed non-overlapping (DRM) and overlapping spheres (3DCRM) for very small inclusion concentrations. (a) Shows attenuation and (b) velocity dispersion. There is good agreement between the models because the inclusion concentration is very small and hence there is minimal sphere overlap.

In the next example, I model attenuation and dispersion due to spherical inclusions of heavy gas having total volume concentration of 30 % within an otherwise water saturated rock. Figure 3.4.2.3 shows (a) attenuation and (b) velocity as predicted by DRM, 3DCRM with overlapping sphere correlation function (Eq 3.4.2.8) and 3DCRM with non-overlapping sphere correlation function. At volume concentrations equal to 30% DRM does not converge to the Gassmann-Wood limit, hence the velocity and attenuation estimates of this model are not reliable at this inclusion concentration. The 3DCRM with overlapping and non-overlapping correlation functions produce attenuation and velocity curves which differ. The high frequency asymptotes do not correspond as the volume to surface ratio of the two models is different.

The attenuation curve predicted from the overlapping sphere fluid distribution is broader than the attenuation curve predicted from the non-overlapping sphere approach. The reason for this is that the overlapping sphere distribution creates patch sizes which are greater than the diameter of a single sphere when spheres overlap. Hence, patches of this width (relative to the inclusion radius) require wave frequencies to be lower in order to achieve fluid pressure equilibration. This has the effect of broadening the attenuation curve and also increases the frequency bandwidth of dispersion.

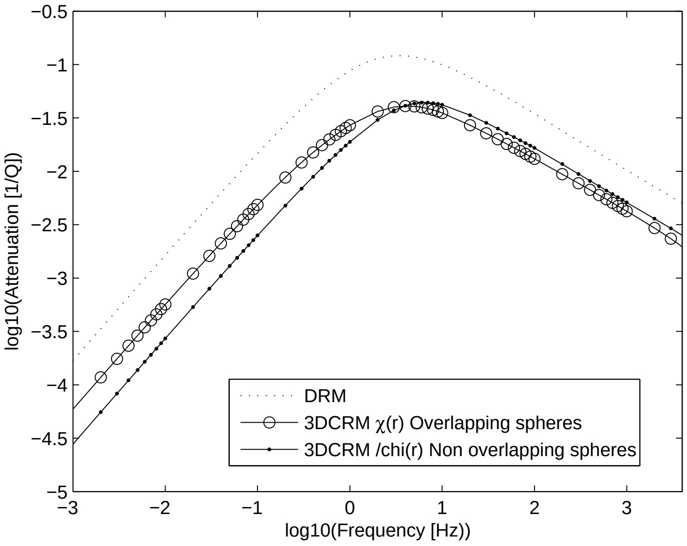

(a)

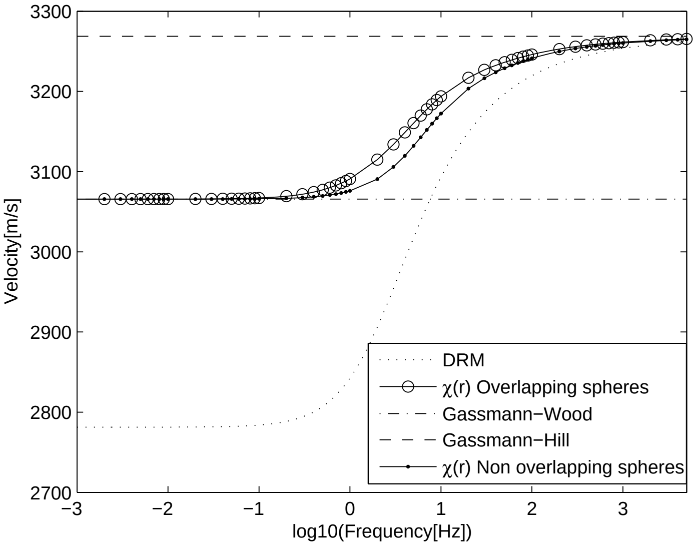

(b)

Figure 3.4.2.4: Frequency-dependent attenuation and dispersion estimates obtained from randomly distributed non-overlapping (DRM) and overlapping spheres (3DCRM) for 30% inclusion concentrations. (a) Shows attenuation and (b) shows dispersion. The DRM (dotted line) does not converge to Gassmann-Wood limits and 3DCRM with overlapping (circles) and non-overlapping (solid dots) correlation functions produces slightly different attenuation and dispersion curves, indicating the presence of overlapping inclusions.

3.4.3 Random Checkerboard Correlation Function

Let’s suppose that two pore fluids are distributed randomly throughout the rock, but that we do not know, or wish to assume, how they are spatially correlated. This scenario can be modelled by partitioning the rock into symmetric cells of some size and shape, with cells being randomly assigned as fluid 1 or fluid 2 by probabilities of v_1 and $v_2 = 1 - v_1$, respectively. This is called a symmetric cell material.

One manifestation of a symmetric cell material is when 3d space is tessellated into cubes of equal width L_C. This type of tessellation produces what is known as the random checkerboard (see Figure 3.4.3.1). Lu and Torquato (1992) have derived the two point probability function $S_2(\boldsymbol{r})$ corresponding to this type of material. It depends on the orientation of vector $\boldsymbol{r}$ and its magnitude (Torquato 2002). However, it can be converted to a rotationally invariant two point probability function by averaging over spherical polar and azimuthal angles (Mecke 1998). For this case

$$S_2(r) = W_2^1(r)v_1v_2 + v_1^2 \tag{3.4.3.1}$$

where $W_2^1(r)$ is a rotationally averaged weighting function, it sums to one and is independent of the percent fluid saturation. Note that, one-point weighting functions in general depend on the cell shape and size, hence for other types of cell shapes (octahedrons etc) the weighting function will be different. Torquato (2002) give the analytical and tabulated rotationally averaged $W_2^1(r)$ (see Table 3.4.3.1).

From Equation (3.4.3.1), the normalised and centred correlation function corresponding to a 3D checkerboard is determined as

$$\chi(r) = \frac{S_2(r) - v_1^2}{v_1v_2} = W_2^1(r). \tag{3.4.3.2}$$

Hence the correlation function (Equation 3.4.3.2) depends only on the weighting function and thus is independent of percent saturation of the two pore fluids, see Figure 3.4.3.1(a).

Figure 3.4.3.2 (b) shows attenuation and (c) velocity calculated using Equations (3.3.3 and 3.3.1.11) for two different cube widths. By reducing the cube width the curves are shifted to higher frequencies. These curves represent attenuation and dispersion when spatial correlation in pore fluid distribution does not exist. In reality, it is highly unlikely that correlation in fluid heterogeneities will be absent because of the influence of rock permeability etc. Hence, we would not expect frequency-dependent curves like this. Nevertheless, this example shows by tessellating space up into cubes and randomly assigning fluids, the attenuation and dispersion estimates are dominated by the dimensions of the cube length, and are in fact independent of percentage saturation of the pore fluids.

Table 3.4.3.1: Weights for 3D random checkerboard

r	$W_2^{(1)}(r)$	r	$W_2^{(1)}(r)$	r	$W_2^{(1)}(r)$
0.0	1.0	0.6	0.31199	1.2	0.00857
0.1	0.85629	0.7	0.23465	1.3	0.00229
0.2	0.72483	0.8	0.16669	$\sqrt{2}$	0.00032
0.3	0.60515	0.9	0.10765	1.5	0.00005
0.4	0.49677	1.0	0.05704	1.6	0.00000
0.5	0.39921	1.1	0.02404	$\sqrt{3}$	0.0

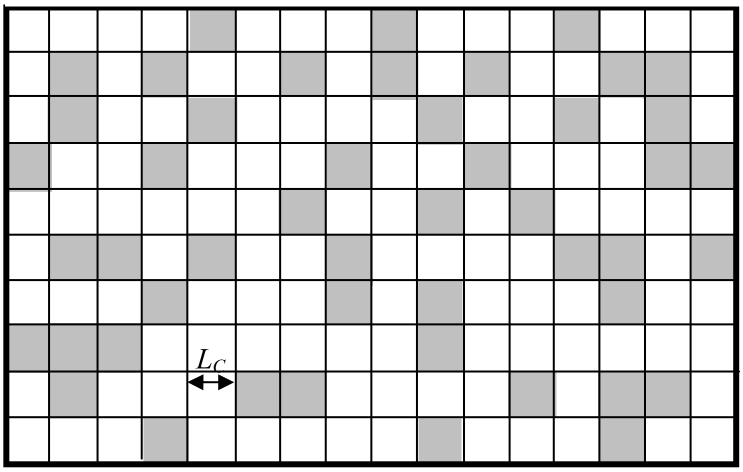

a)

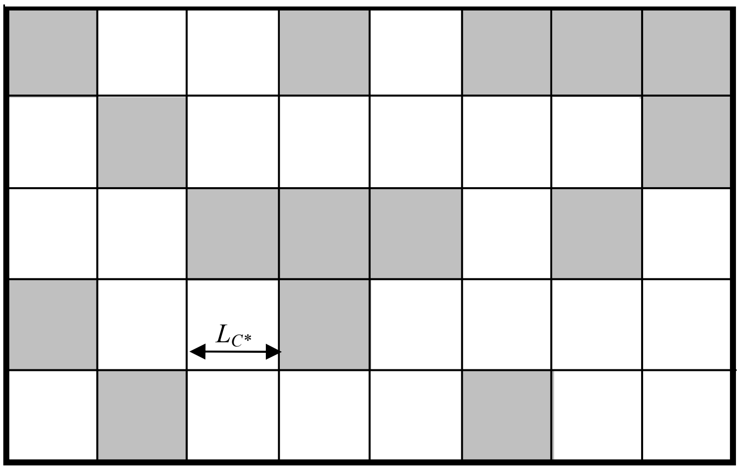

b)

Figure 3.4.3.1: Cartoon representation of random checkerboard materials. There are random checkerboards having cell widths of (a) L_C *and (b)* L_{C*} *where* $L_C < L_{C*}$*. The two point probability density function of checkerboards (a) and (b) are the same when the volume fraction of grey to white cells is equivalent.*

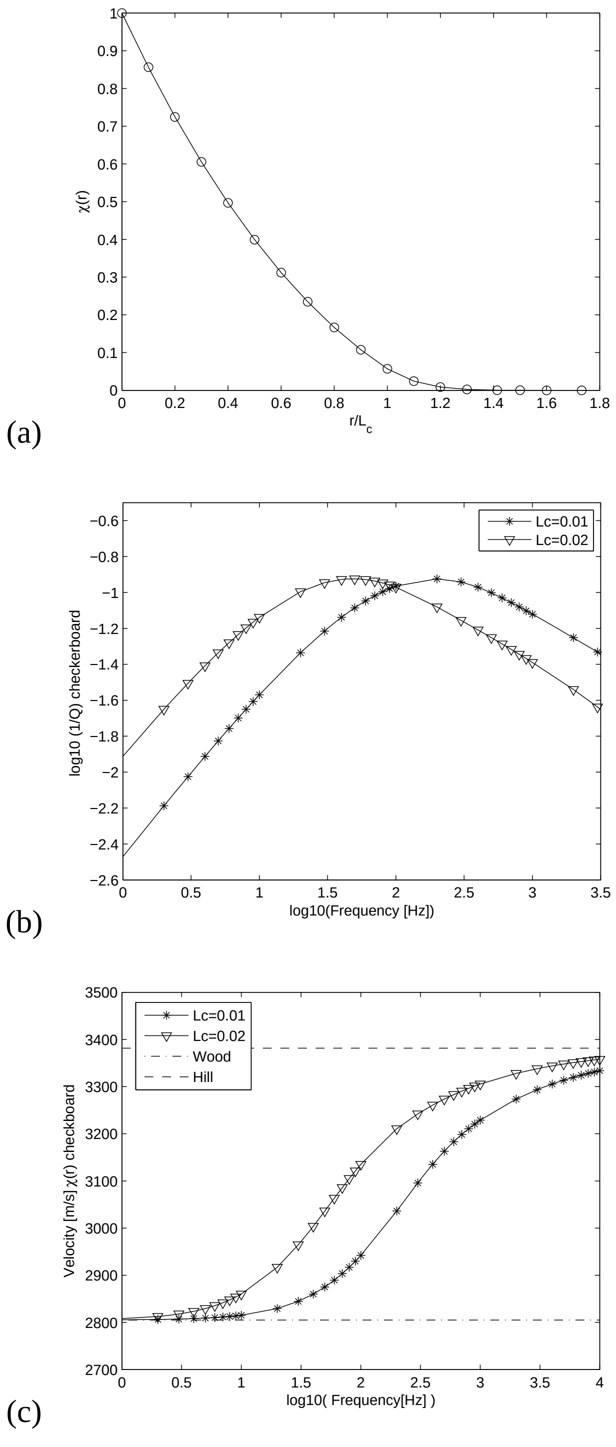

Figure 3.4.3.2 Correlation functions, attenuation and dispersion for random checkerboard materials (a) Correlation function for checkerboard material normalised by cube length. (b) Attenuation and (c) velocity for checkerboard correlation function for different cube lengths.

3.5 Modelling Attenuation and Dispersion from Gas Saturation Maps

A significant advantage of using 3DCRM is that it can be utilized to model attenuation and dispersion due to any correlation function. In the above section, I provided formulas for frequency-dependent P-wave modulus for several well known correlation functions. In this section, I show one particular way in which 3DCRM can be related to correlation functions extracted from processed X-ray tomographic images (Chapter 2). The 3DCRM is the only patchy saturation modelling approach capable of taking into account this type of realistic spatial information. For the modelling examples below I assume the following rock and fluid properties.

Table 3.5.1: Rock properties for MGL2a modelling

K	26 GPa	K_g	74 GPa	ϕ	0.25
μ	15 GPa	ρ_g	2650 Kg/m^3	κ	5e-12 m^2

Table 3.5.2: Fluid Properties for MGL2a modelling

K_{fw} Water	2.25 GPa	K_f Heavy gas	0.25 GPa	K_f Light gas	0.1 GPa
ρ_w	990 Kg/m^3	ρ	400 Kg/m^3	ρ_g	100 Kg/m^3
η_w	1e-3 Pa s	η	6e-5 Pa s	η_2	3e-5 Pa s

3.5.1 Continuous Random Media

The correlation function utilized in the 3DCRM model describes mesoscopic spatial variation of fluid modulus M about an average value M_0, as a result of spatial variations in fluid bulk modulus K_F. In general, fluid heterogeneities may exhibit either discrete or continuous spatial variation on the mesoscale. Discrete variation occurs when the fluid bulk modulus varies spatially as a piecewise constant function (see Figure 3.5.1.2 (a)). That is, regions of rock are 100% saturated by either fluid one or fluid two. This is usually what we think of when we imagine fluid heterogeneities, be it on the porescale or mesoscale.

On the other hand, continuous variation arises when the fluid bulk modulus varies as a smooth spatial function about an average fluid bulk modulus (see Figure 3.5.1.1 (b)). On the pore scale, we wouldn’t normally expect the fluid bulk modulus to show this type of spatial variation because distinct fluid-fluid interfaces exist. However, on the mesoscale it may be possible, as more than one fluid type may share the pore-space within a mesoscopic patch (say for instance of cm length). Hence, the fluid bulk modulus of the mesoscopic patch will likely assume an effective value due to the presence of multiple fluids. Moreover, if there is continuous variation in the relative percentage of saturating fluids over mesoscale resolution, the effective fluid bulk modulus on the mesoscale will vary continually.

In Chapter Two, when I examined gas saturation maps of MGL2a (Figure 2.2.2 (a)-(m)), I found evidence for the second type of fluid heterogeneity (continuous variation). For instance, in the early stages of the drainage experiment (gas saturations less than 23%) there were distinct mesoscopic patches having gas saturations of 10-30%, within an otherwise 100% water saturated rock. Moreover, in the later stages of the drainage experiment (gas saturations greater than 23%) most of the pore-space was affected by the presence of gas, this created many different mesoscopic patches having gas saturations ranging from 10% to 90%.

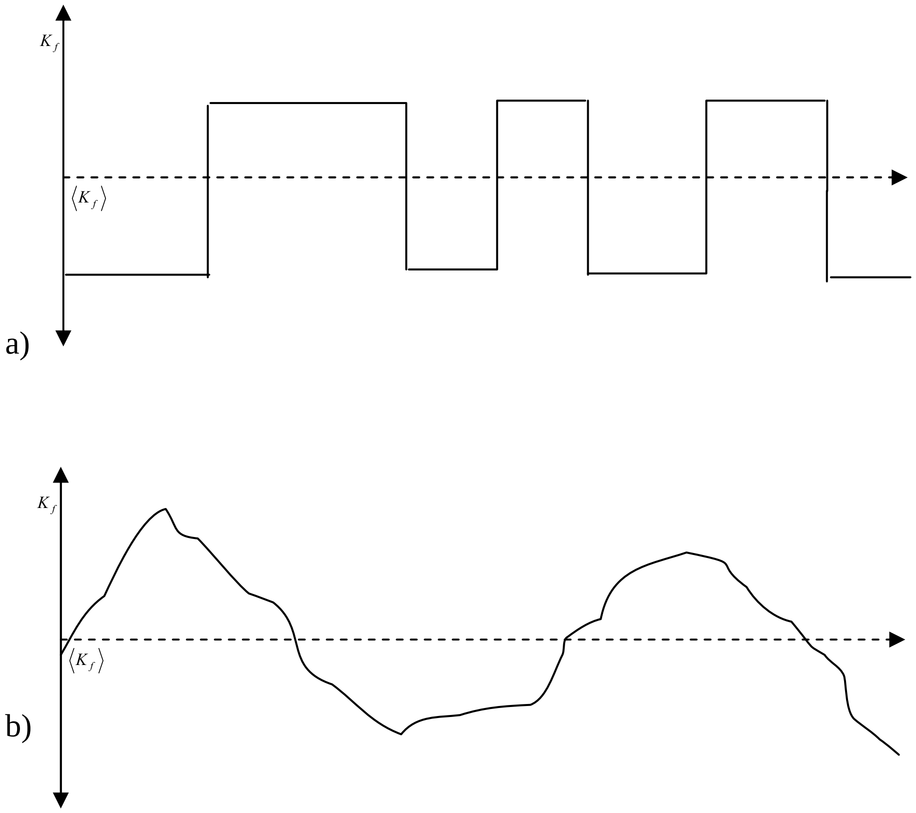

Figure 3.5.1.1 Mesoscopic fluid heterogeneities fluctuating about the average fluid bulk modulus. (a) Shows discrete spatial variation in fluid bulk modulus and (b) shows continuous spatial variation in fluid bulk modulus.

3.5.2 Gas Saturation Maps

The gas saturation maps (Figure 2.2.2 (a)-(m))) show for a particular rock where gas bearing pores exist. Specifically, the CT value of a pixel indicates the percentage of gas saturation in the pore-space covered by that pixel (via Equation 2.2.6). That is, pixel values range from zero to one, where zero and one indicate 0% and 100% gas saturation, respectively; though intermediate values indicate pore-space of mixed gas-water composition. Spatial statistics like the correlation function or correlation length can be extracted from these maps. However, this information describes spatial characteristics of percent gas variation on mesoscale, and not spatial information on the variation of fluid modulus M. Hence, it cannot be utilized directly in CRM theory.

I can however use information on percent gas saturation to construct a new map which represents fluid bulk modulus variation on the mesoscale. This can be used to construct a fluid modulus map from which a correlation function consistent with CRM requirements can be extracted. In transforming the gas saturation map into an effective fluid bulk modulus map, I assume that fluid pressures of gas and water within the pore-space of each pixel are equal, then Wood's fluid mixing equation (Equation 1.2.2.1) is used to construct an effective fluid bulk modulus for each pixel. However, in principle, it is also possible to utilize other fluid mixing equations, such as Brie et al. (1995) or Voigt (Mavko & Mukerji 1998) averages to create an effective fluid bulk modulus. Below I propose a procedure to model attenuation/dispersion using 3DCRM.

3.5.3 The Methodology

Step 1: Convert the saturation map into an effective fluid bulk moduli map using Woods fluid mixing equation. This can be achieved by

$$KWoodMap^{-1} = \left[\frac{1 - GasSatMap}{K_{fw}} + \frac{GasSatMap}{K_{fg}} \right], \qquad (3.5.3.1)$$

where $GasSatMap$ is a particular gas saturation map (Figure 2.2.2 (a)-(m)), K_{fw} is the fluid bulk modulus of water and K_{fg} is the fluid bulk modulus of gas.

Step 2: Convert the fluid bulk moduli map ($KWoodMap$) to fluid moduli map M using

$$M^{-1} = \left[\frac{(\alpha - \phi)}{K_g} + \frac{\phi}{KWoodMap} \right]. \qquad (3.5.3.2)$$

Step 3: Calculate mean M_{i0} of the fluid moduli map:

$$M_{i0} = \text{mean}(M) = \frac{1}{N_P} \sum_{i=1}^{N_p} M(i), \qquad (3.5.3.3)$$

where N_P is the total number of pixels in the fluid moduli map. Also calculate the mean M_{j0} of the fluid moduli map using

$$M_{j0} = \text{mean}(M) = \sum_{j=1}^{Nj} v(j)(M(j)), \qquad (3.5.3.4)$$

where M is the fluid moduli map divided into N_j partitions of width ΔM. That is, if $M_1 = \min(M_i)$ and $M_2 = \max(M_i)$ then $M_2 - M_1 = N_j \Delta M$. Here $v(j)$ is the fraction of pixels having fluid moduli $M(j)$. The partitioning of the fluid moduli is acceptable when $M_{i0} = M_{j0}$. This partitioning step is necessary to calculate the variance.

Step 4: Calculate normalised variance of the fluid moduli map using

$$\sigma_{MM}^2 = \mathrm{var}(M_{j0}) = \frac{\sum_{j=1}^{npart} v(j)(M(j))^2}{M_{j0}{}^2} - 1, \tag{3.5.3.5}$$

Step 5: Calculate normalised centred autocorrelation function of fluid moduli map

Step 6: Calculate Woods limit

$$\frac{1}{M_W} = \sum_{j=1}^{Nj} \frac{v(j)}{M(j)} \text{ and } H_{BGW} = L + \alpha^2 M_W, \tag{3.5.3.6}$$

Step 7: Calculate Hills limit

$$\frac{1}{H_{BGH}} = \sum_{j=1}^{Nj} \frac{v(j)}{L + \alpha^2 M(j)}. \tag{3.5.3.7}$$

Computation of Equations (3.5.3.1-7) together with Equation 3.3.1 yields for a particular saturation map the frequency dependent saturated P-wave modulus, from which attenuation/dispersion is computed. Below I perform this analysis for gas saturation maps (from MGL2a) having average gas saturations of 4.6% and 34.4%.

3.5.4 The Examples

Figure 3.5.4.1 shows (a) the gas saturation map having average gas saturation 4.6 %. The colour bar indicates the percentage of gas within the pore-space covered by each pixel, blue refers to 0% gas saturation, whilst red refers to 100% gas saturation. (b) Shows the effective fluid bulk modulus map derived from the gas saturation map having assumed Wood’s fluid mixing equation with water and light gas fluids. The colour bar shows effective fluid bulk modulus; dark red indicates an effective fluid bulk modulus close to water; whilst blue an effective fluid bulk modulus influenced by gas. Note that a small percentage of gas greatly influences the fluid bulk moduli of an effective fluid. (c) Displays the fluid moduli map calculated using Equation (3.5.3.2). The fluid moduli map has a variance of $\sigma_{MM}^2 = 0.1663$; red and blue areas highlight fluid moduli least and most affected by gas, respectively. (d) Compares correlation functions extracted from gas saturation and fluid moduli maps. An important point is shown, that correlation functions extracted from gas saturation maps (solid line) are generally not equivalent to correlation functions extracted from fluid moduli maps (dashed line).

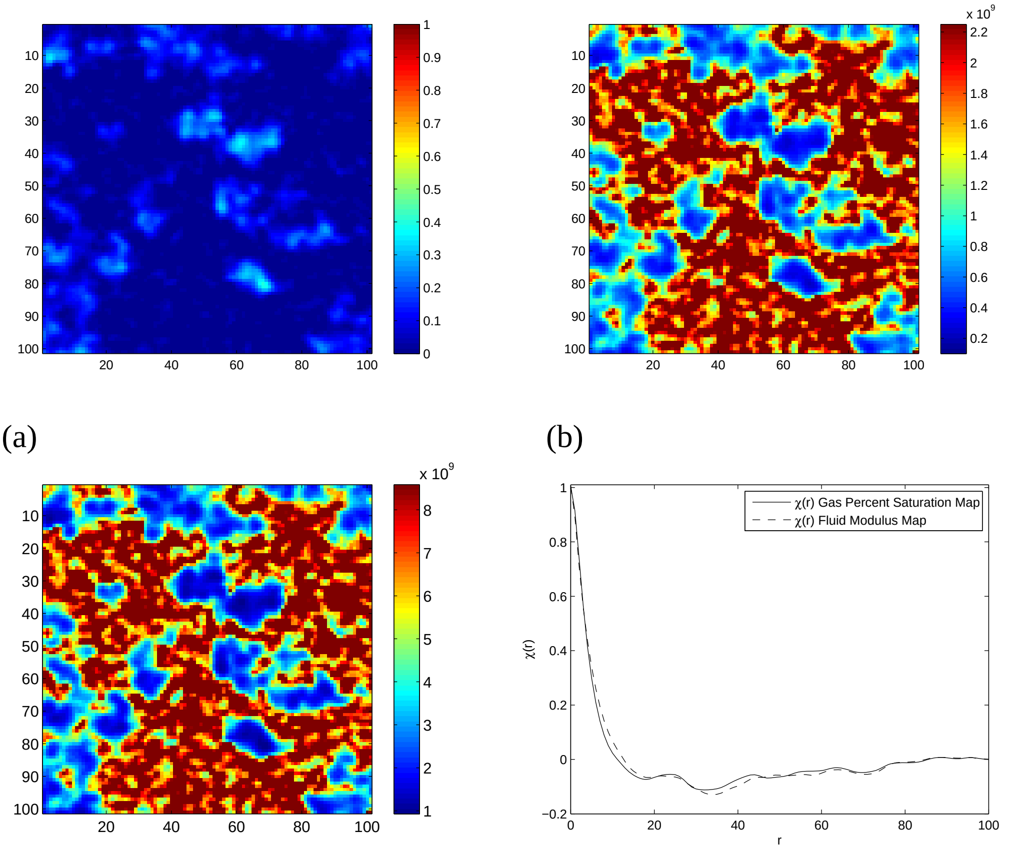

(a) (b)

(c) (d)

Figure 3.5.4.1: Scan 10 fluid heterogeneity maps and correlation functions. (a) Gas percent fluid saturation map (b) Effective fluid bulk modulus map (c) Fluid modulus map (d) Correlation functions extracted from the gas percent fluid saturation map (solid line) and from fluid modulus map (dashed line).

There is one instance in which the correlation functions are equivalent. That is, when fluid contrast is small. Figure 3.5.4.2(a) shows the fluid moduli map (average gas saturation 4.6%) assuming water and heavy gas pore-fluids. This map has a variance of $\sigma_{MM}^{2} = 0.0038$. Figure 3.5.4.2 (b) shows the correlation function extracted from the fluid moduli map saturated by heavy gas (Figure 3.5.4.2(b)) (dashed line) and the correlation function extracted from the gas saturation map (Figure 3.5.4.1(a)) (solid line). The two correlation functions are in good correspondence. This indicates that when fluid contrast is small, such as with water and heavy gas, one may extract the correlation function directly from the gas saturation map. However, when fluid contrast is large, such as with water and light gas (or air), one needs to extract the correlation function from the fluid moduli map.

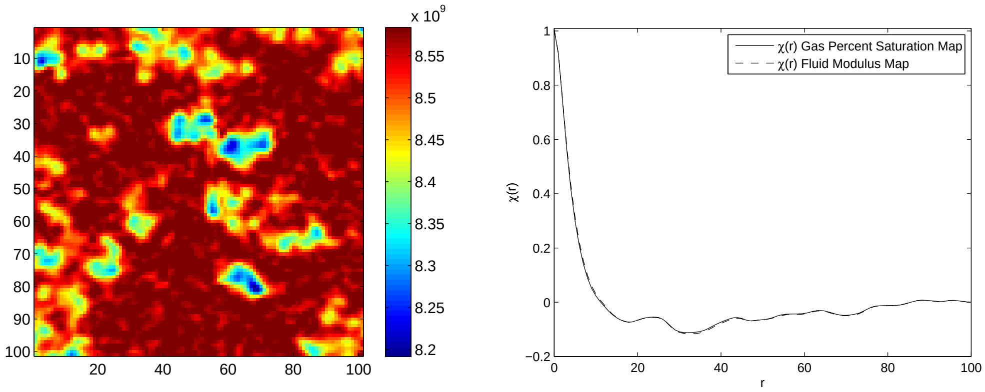

(a) (b)

Figure 3.5.4.2: Scan 10 fluid heterogeneity maps and correlation functions when fluid contrast is small (a) Fluid modulus map assuming heavy gas and (b) correlation function extracted from fluid modulus map is compared against correlation function extracted from the gas saturation map.

I now suggest two ways in which spatial statistics extracted from a fluid moduli map (ie like Figure 3.5.4.1 (c)) can be utilized in 3DCRM to estimate attenuation and velocity. The first approach centres on incorporating the correlation function directly into Equation (3.3.3). Clearly this approach requires numerical integration to determine the saturated P-wave modulus from which attenuation/velocity can be estimated. The second approach centres on approximating the correlation function (in Figure 3.5.4.1(d)) by an exponential correlation function with Debye correlation length derived from the correlation function (Figure 3.5.4.1(d)). By making this approximation, I can use a closed form expression for the saturated P-wave modulus (Equation 3.3.2.2) to determine attenuation and velocity.

Figure 3.5.4.3 shows frequency-dependent (a) attenuation and (b) velocity due to fluid modulus variation for Scan 10 (Figure 3.5.4.1 (c)). The first approach to estimating attenuation/velocity via numerical integration (dotted line with solid points) is compared against the second closed form approach (solid line). There is reasonable correspondence between attenuation and velocity estimated from both approaches at low frequencies. The peak magnitude of attenuation is also similar. For a small percentage of gas saturation (4.6%), attenuation is of the order $Q^{-1} = 0.1$, which is significant. Unfortunately, at high frequencies the numerical integration of Equation (3.3.3) central to the first approach was found to break down. This caused significant errors in the attenuation and velocity estimates at high frequencies. The same type of error was observed in Section 3.4, where it was necessary to numerically integrate Equation 3.3.3 for different correlation functions. In that study, I minimized the error by interpolating the correlation function to finer spacings. The same approach could also be adopted here to minimize the numerical integration error observed in the first approach.

Although not shown here, I use steps 1-2 to construct a fluid moduli map for the gas saturation map Scan 15, having average gas saturation of 34.4%. From this map I derive the correlation function and follow the procedure (steps (3-7)) to calculate attenuation and dispersion. Figure 3.5.4.4 shows frequency-dependent (a) attenuation and (b) velocity calculated using spatial statistics extracted from the fluid modulus map using the same two approaches. Relative to Figure 3.5.4.3, the peak magnitude of attenuation and degree of velocity dispersion is reduced significantly, attenuation is now of the order $Q^{-1} = 0.001$. That is, by increasing gas saturation from 4.6 % to 34.4% the frequency-dependent effects due to wave induced fluid flow are estimated to decrease.

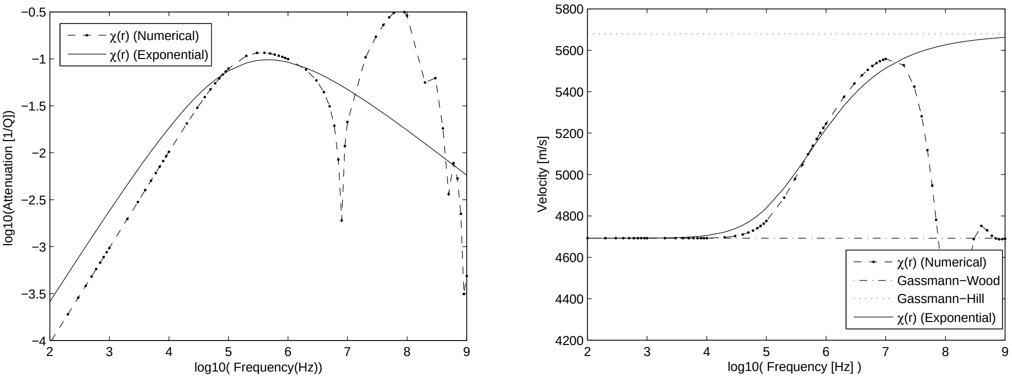

(a) (b)

Figure 3.5.4.3 Frequency-dependent attenuation and dispersion modelled using statistics extracted from fluid heterogeneity maps. (a) Attenuation and (b) velocity due to correlation functions extracted from fluid modulus map of Scan 10(average gas saturation 4.6%)

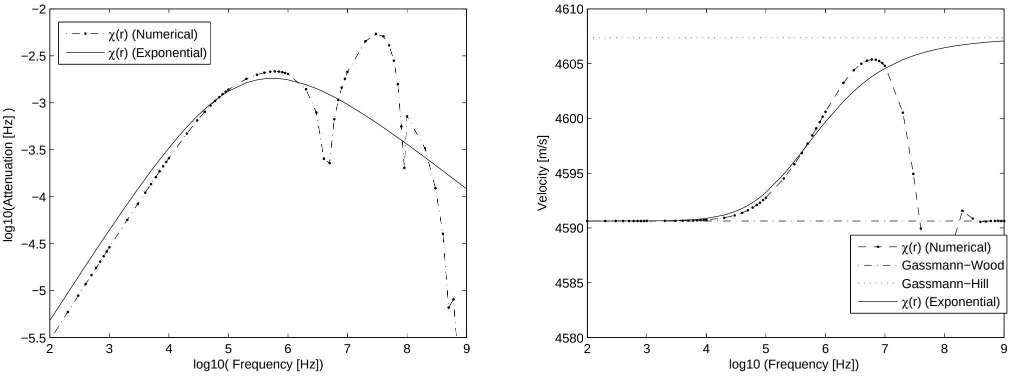

(a) (b)

Figure 3.5.4.4 Frequency-dependent attenuation and dispersion modelled using statistics extracted from fluid heterogeneity maps. (a) Attenuation and (b) velocity due to correlation functions extracted from fluid modulus map of Scan 15 (average gas saturation 34.4%).

3.6 Conclusions

Reservoir rocks are often saturated by two or more fluid phases forming complex patterns on all length scales. In this Chapter I have shown how the 1DCRM model of Müller and Gurevich (2004) can be utilized with a variety of different correlation functions to model attenuation/dispersion due to complicated 1D fluid heterogeneities. In particular, I showed by introducing a quasi-periodic correlation function that small uncertainties in the repetition period of layered media has little effect on the attenuation and dispersion signatures. Hence, quasi-periodic and periodic layering produce almost equivalent attenuation and dispersion of P-waves.

Providing the weak scattering conditions for the DRM (Ciz et al. 2006) model are met, I found that there is good agreement between attenuation and phase velocity estimates for random and periodic distributions of spherical fluid inclusions. This was somewhat surprising as 1D random and periodic structures produced very different low frequency attenuation behaviour.

In order to model attenuation and dispersion due to complicated fluid distributions, such as those found in X-ray tomographic images of partially saturated rock, I developed the 3DCRM model. My patchy saturation model shows greatest versatility in modelling attenuation and dispersion due to different types of fluid distributions. In particular, I derived close form expressions for the frequency-dependent saturated P-wave modulus due to fluid distributions given by exponential and Gaussian correlation functions. I also showed that 3DCRM could be used to model fluid distributions given by random distributions of regular shaped heterogeneities, such as spherical inclusions. Moreover, I found that 3DCRM could be used to model attenuation/dispersion due to higher concentrations of fluid inclusions than the DRM model.

In my final section of this Chapter, I developed a strategy for modelling attenuation and dispersion due to correlation functions extracted from gas saturation maps. I illustrated this process for continuous fluid distribution maps. The 3DCRM model is the only patchy saturation model capable of taking into account such realistic spatial information.

Chapter 4

Extension of the APS framework

4.0 Introduction

The key difference between the regular cell models (Chapter 1) and the random media models (Chapter 3) rests in how fluid distribution is accounted for. The regular cell models, such as APS (Johnson 2001) utilize periodic layering or concentric sphere fluid distributions, whilst the random media models (1DCRM, 3DCRM) utilize a correlation function to describe fluid distribution. As was shown in the previous chapter, the advantage of utilizing a correlation function is flexibility. That is, one can model attenuation and dispersion due to different fluid distributions by simply changing the correlation function. Moreover, for certain geometries like periodic layering and randomly distributed spheres, CRM was shown to be in good agreement with patchy saturation approaches, such as APS and DRM. Hence, CRM can model effects due to different fluid distributions, but is the reverse true: *can the regular cell models be extended in some way to take into account effects due to more complicated fluid distributions*?

The driving impetus behind this question is the need to remove (or access) restrictions on fluid contrast which may affect the precision of the CRM models. That is, the CRM models are precise for low contrasting pore fluids, but are approximate for high contrasting pore fluids. On the other hand, the regular cell models are precise for any fluid contrast, but are formulated for specific fluid distributions. Hence, if the restriction on fluid distribution can be removed from the regular cell approaches, perhaps they may be utilized to model attenuation and dispersion due to complicated fluid distributions at any fluid contrast.

In this Chapter, I show how the regular cell approach of Johnson (2001) called APS can be extended to model attenuation and dispersion due to complicated fluid distributions. This regular cell model was chosen for extension because of its simple and generalized framework. My approach is to modify two special parameters within this framework called "shape" and "frequency scaling" parameters. Specifically, I derive new equations for these parameters, which allow other pore fluid distributions to be modelled. By substitution of the new shape and frequency scaling parameters into the APS framework, I am able to model attenuation and dispersion due to different fluid distributions.

The Chapter is organised as follows. In Section 1, I analyse the frequency-dependent characteristics of the Johnson model. In Section 2, shape and frequency scaling parameters are derived for layered media; whilst in Section 3 they are derived for different types of three dimensional fluid distributions.

4.1 The Johnson APS model

4.1.1 APS Framework Specified in terms of Saturated P-wave Moduli

The APS framework of Johnson (2001) discussed in Section 1.3.2 is formulated in terms of bulk moduli. As I am interested in P-wave attenuation and dispersion, it is convenient to specify the framework in terms of saturated P-wave moduli.

According to APS theory (Equation 1.3.2.10), the dynamic saturated P-wave modulus can be written as

$$\tilde{H}_J(\omega) = H_{BGH}\left(1 - \delta bf(\omega)\right), \tag{4.1.1.1}$$

where

$$bf(\omega) = \frac{1}{1 - \zeta + \zeta\sqrt{1 - \frac{i\omega\tau}{\zeta^2}}}. \tag{4.1.1.2}$$

Equation (4.1.1.2) defines a branching function (see Section 4.1.1.2). All of the frequency dependence in the APS framework is contained within this function. It is defined in terms of a fluid contrast factor (difference between Wood and Hill bounds):

$$\delta = \frac{H_{BGH} - H_{BGW}}{H_{BGH}}; \tag{4.1.1.3}$$

the so-called shape parameter:

$$\zeta = \frac{(\delta H_{BGH})^3}{2K_{BGW}K_{BGH}^2 TG^2}, \tag{4.1.1.4}$$

and frequency scaling parameter:

$$\tau = \left[\frac{\delta H_{BGH}}{K_{BGH}G}\right]^2. \tag{4.1.1.5}$$

In Equations (4.1.1.4) and (4.1.1.5), parameters T and G define the low and high frequency asymptotes. In particular, the low frequency asymptote of the saturated P-wave modulus is

$$\lim_{\omega \to 0} \tilde{H}(\omega) = H_{BGW} - K_{BGW}Ti\omega, \tag{4.1.1.6}$$

where the frequency coefficient T is defined by Equation (1.3.2.2). The high frequency asymptote is

$$\lim_{\omega \to \infty} \tilde{H}(\omega) = H_{BGH} - K_{BGH}G(-i\omega)^{-1/2}, \tag{4.1.1.7}$$

where the frequency coefficient G is defined by Equation (1.3.2.9).

The low and high frequency asymptotes (Equations (4.1.1.6 - 4.1.1.7)) will be utilized extensively in Sections 4.2 and 4.3 where new T and G coefficients will be derived by equating these asymptotes with frequency asymptotes derived from other 1D and 3D models (Chapter 3). Once new T and G coefficients are determined, shape and frequency scaling parameters can be obtained using Equations (4.1.1.4 - 4.1.1.5). These can be substituted into Equation (4.1.1.2) to model attenuation and dispersion using Equation (4.1.1.1).

4.1.2 The Logic behind using a Branching Function

In many problems of wave phenomena in dissipative media it is often difficult or impossible to express the complex and frequency-dependent parameter of interest in closed form, but may be possible to obtain simple asymptotic solutions in both low and high frequency limits. A good example is the problem of dynamic permeability in a porous medium, where an explicit analytical solution is only known for very restricted geometries of parallel circular or flat cylindrical channels (Biot 1956b), but asymptotic expressions can be derived for much more general cases (Johnson et al. 1987). In such situations it is logical to approximate the solution at intermediate frequencies by a simple function which would obey the physical constraints, such as energy conservation and causality conditions, and converge to the asymptotic solutions in the low and high frequency limits. Such connecting functions are sometimes called branching functions.

The APS theory of Johnson (2001) utilizes such a function (Equation 4.1.1.2) to describe the frequency-dependent behaviour of the saturated bulk modulus, because analytical solutions are hard to obtain over the entire frequency range. In other contexts, such as dynamic permeability, a branching function approximation was developed by Johnson et al.. (1987) who showed that for the known cases of circular and flat channels it gives a very precise approximation of the exact solutions, see also Pride et al. (1993); Zhou and Sheng (1989). Branching functions have also been used to approximate the frequency-dependent moduli of porous media with mesoscopic inhomogeneities (Pride et al. 2003; Galvin et al. (2007)).

The branching function utilized in any given dynamic problem is in general non unique. That is, one could substitute another kind of branching function, which serves the same purpose. For instance, Pride et al. (1993) list five different branching functions which could replace the branching function utilized in the dynamic permeability model of Johnson et al. (1987). However, each function postulated is more complicated then the simple function first implemented in the original model and produce very similar results.

The frequency dependency of the dynamic saturated P-wave modulus in the APS framework is embedded within the branching function given by Equation (4.1.1.2). Hence, to determine possible frequency-dependent behaviour of the saturated P-wave modulus (Equation 4.1.1.1), it is sufficient to analyse the frequency-dependent characteristics of this function. This can be done by analysing asymptotic behaviour at low and high frequencies.

4.1.3 Frequency-dependent Behaviour of the Branching Function

Here I study the frequency-dependent behaviour of APS by extracting frequency asymptotes from the branching function (Equation 4.1.1.2).

Low Frequency: Relaxed fluid pressure

Two different frequency asymptotes are present for wave frequencies $\omega \to 0$. First note that energy conservation requires that $\zeta \geq 0$ (otherwise attenuation would be negative).

1) If the shape parameter is finite and $\zeta >> 0$, in the low frequency limit we can assume

$$\frac{i\omega\tau}{\zeta^2} << 1. \qquad (4.1.3.1)$$

Applying the binomial theorem on Equation (4.1.1.2) gives

$$\lim_{\omega \to 0} bf\left(\omega\right) = 1 + \frac{i\omega\tau}{2\zeta}. \qquad (4.1.3.2)$$

In this case wave attenuation is proportional to wave frequency.

2) The case $\zeta = 0$ can be considered by rearranging (4.1.1.2),

$$bf\left(\omega\right) = \frac{1}{1 - \zeta + \sqrt{\zeta^2 - i\omega\tau}} \qquad (4.1.3.3)$$

and taking the limit at $\zeta \to 0$. For sufficiently low frequencies such that $\omega\tau << 1$, Equation (4.1.3.3) becomes

$$\lim_{\omega \to 0} bf\left(\omega\right) = 1 - \sqrt{-i\omega\tau}\ . \qquad (4.1.3.4)$$

In this case wave attenuation is proportional to the square root of frequency.

3) When wave frequency is low and the shape parameter is $0<\zeta^2<<\omega\tau<1$, Equation (4.1.3.3) becomes

$$\lim_{\zeta\to 0} bf(\omega)=\frac{1}{1-\zeta+\sqrt{-i\omega\tau}},$$

applying binomial theorem gives an asymptote of

$$\lim_{\omega\to 0} bf(\omega)=1+\zeta-\sqrt{-i\omega\tau}\,. \tag{4.1.3.5}$$

In this case wave attenuation is proportional to the square root of frequency.

High Frequency: Unrelaxed fluid pressure

For wave frequencies $\omega\to\infty$, two different frequency asymptotes are present.

1) The first can be derived directly from Equation (4.1.1.2), where the branching function becomes

$$\lim_{\omega\to\infty} bf(\omega)=\frac{1}{\sqrt{-i\omega\tau}}\,. \tag{4.1.3.6}$$

In this case wave attenuation is inversely proportional to the square root of frequency.

2) When the shape parameter satisfies

$$\frac{2}{\zeta}<\frac{\omega\tau}{\zeta^2}<1,$$

the branching function becomes

$$\lim_{\omega\to\infty} bf(\omega)=\frac{2\zeta}{-i\omega\tau}\,. \tag{4.1.3.7}$$

In this case wave attenuation is inversely proportional to frequency.

4.1.4 Varying the Shape Parameter of the Branching Function

In Chapter 3 it was observed that changing the fluid distribution will alter the frequency-dependent behaviour of attenuation and dispersion. Hence, if APS has the capacity to estimate attenuation and dispersion when fluid distribution is random and irregular then APS must be able to exhibit a broad range of frequency-dependent behaviour. Here I show by changing the shape parameter within the branching function, different types of frequency-dependent behaviour will result. Thus, APS has the potential to be utilized to model effects due to complicated fluid distributions.

The imaginary component of the branching function is related to attenuation, whilst the real component is related to phase velocity. Figure 4.1.4.1 shows (a) imaginary and (b) real components of the branching function as frequency changes. In (a) and (b) each curve has a shape parameter value ranging from 0 to 100. As the shape parameter alters different frequency-dependent curves are observed, hence there is different frequency-dependent velocity and attenuation. In fact, there appears to be four different shaped frequency-dependent curves, this is most easily observed by examining the imaginary component of the branching function. Each curve is described by different frequency asymptotes (Equations 4.1.3.2, 4.1.3.4- 4.1.3.7). Next I define each curve category.

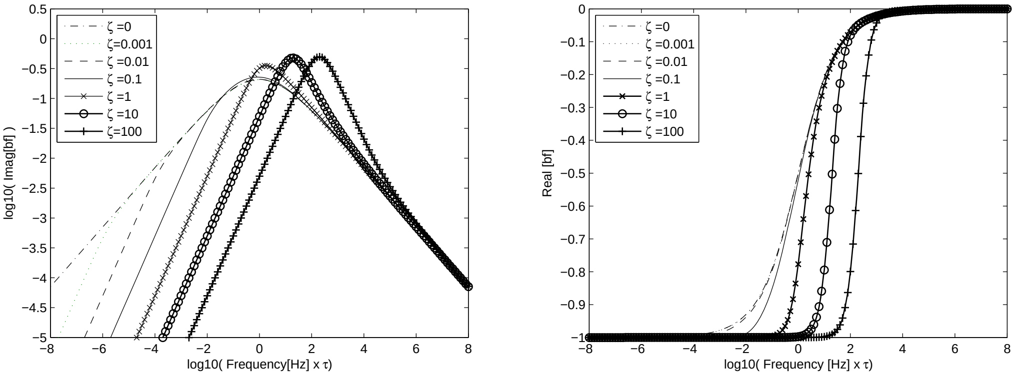

(a) (b)

Figure 4.1.4.1: Frequency dependence of branching function components. (a) Real and (b) imaginary components of the branching function for different values of the shape parameter. There appears to be 4 different types of frequency-dependent curves.

Category 1 (see Figure 4.1.4.2) arises when the shape parameter $\zeta = 0$. For this type of attenuation curve, the branching function in the low frequency limit scales with the square root of frequency,

$$\lim_{\omega \to 0} bf(\omega) = 1 - \sqrt{-i\omega\tau} ,$$

whilst the high frequency asymptote is inversely proportional to the square root of frequency

$$\lim_{\omega \to \infty} bf(\omega) = \frac{1}{\sqrt{-i\omega\tau}} .$$

This type of frequency-dependent behaviour was observed in Section 3.1.3 for randomly distributed layers of water and gas.

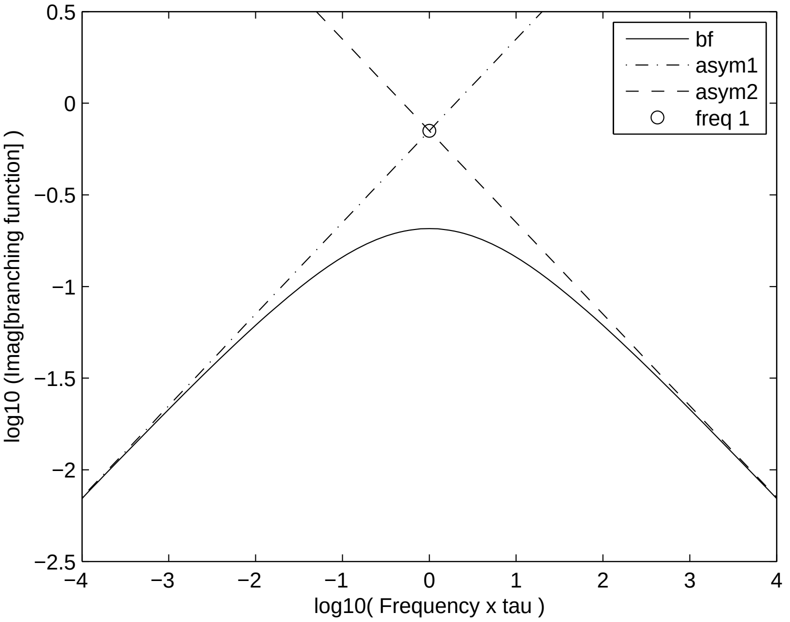

Figure 4.1.4.2: Category 1 attenuation curve. The imaginary component of the branching function with $\zeta = 0$ *(solid line) is defined by one low frequency (asym1) and one high frequency asymptote (asym2). The crossover frequency (freq 1) is shown by the circle.*

Category 2 (see Figure 4.1.4.3) arises when the shape parameter $\zeta \to 0$. For this type of curve there are three dominant frequency regimes. The low frequency dependence is proportional to frequency

$$\lim_{\omega\to 0} bf\left(\omega\right) = 1 + \frac{i\omega\tau}{2\zeta} ,$$

the intermediate frequency dependence $\omega_1 < \omega < \omega_2$ (ω_1, ω_2 defined in Table 4.1.4.1) is proportional to the square root of frequency,

$$\lim_{\omega\to\omega_1} bf\left(\omega\right) = 1 + \zeta - \sqrt{-i\omega\tau}$$

whilst the high frequency dependence is inversely proportional the square root of frequency.

$$\lim_{\omega\to\infty} bf\left(\omega\right) = \frac{1}{\sqrt{-i\omega\tau}}$$

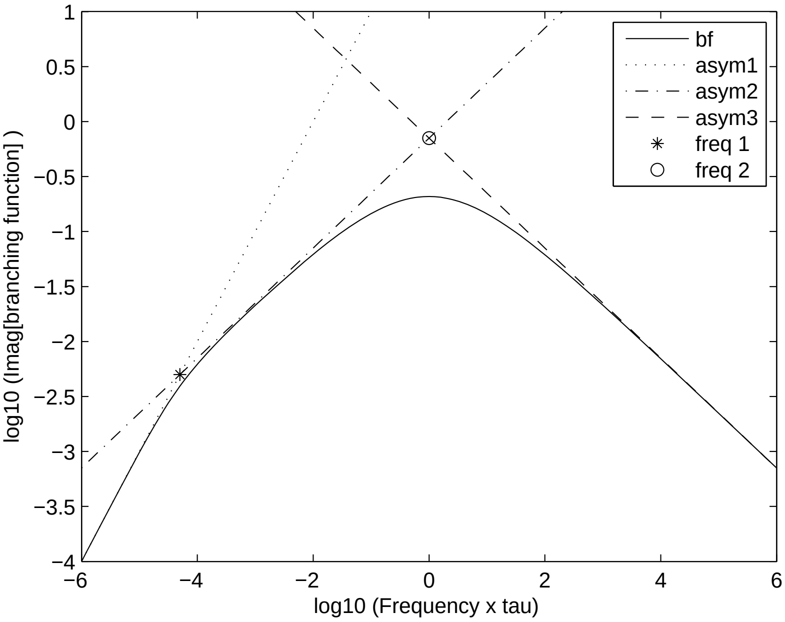

Figure 4.1.4.3: Category 2 attenuation curve. The imaginary component of the branching function with $\zeta = 0.005$ *(solid line) is defined by two low frequency asymptotes (asym1 (dotted) and asym2 (dashed-dotted)) and one high frequency asymptote (asym3 (dashed)). There are two cross over frequencies shown by an asterisk (freq1) and circle (freq2) .*

Category 3 (see Figure 4.1.4.4) arises when there is only one crossover frequency, giving a shape parameter of $\sqrt{\frac{(\omega_1\tau)^3}{2}}$. For this type of curve there are 2 dominant frequency regimes. The low frequency dependence is proportional to frequency

$$\lim_{\omega\to 0} bf(\omega) = 1 + \frac{i\omega\tau}{2\zeta},$$

whilst the high frequency dependence is inversely proportional to the square root of frequency

$$\lim_{\omega\to\infty} bf(\omega) = \frac{1}{\sqrt{-i\omega\tau}}.$$

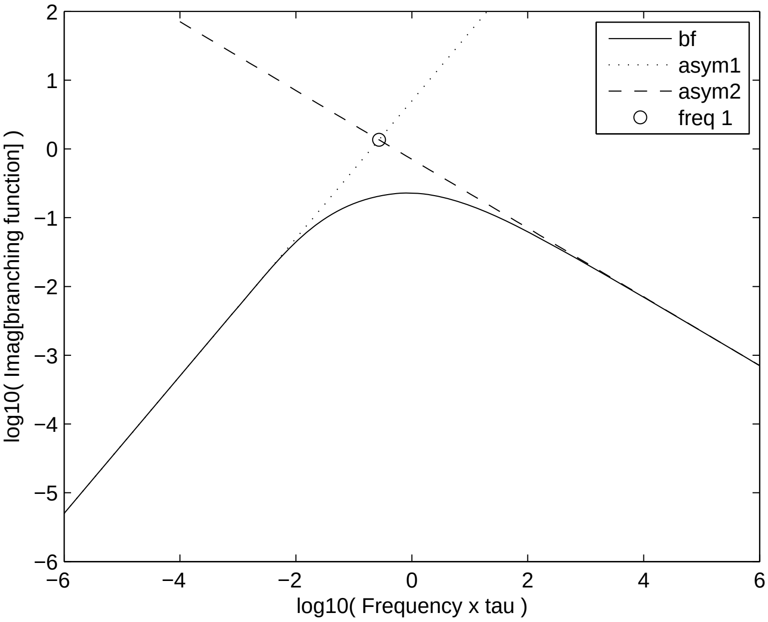

Figure 4.1.4.4: Category 3 attenuation curve. The imaginary component of the branching function with $\zeta = 0.1$ *(solid line) is defined by one low frequency asymptote (asym1 (dotted)) and one high frequency asymptote (asym2 (dashed)). The crossover frequency (freq1) is shown by a circle.*

Category 4 (see Figure 4.1.4.5) arises when the shape parameter satisfies

$$\frac{2}{\zeta} < \frac{\omega\tau}{\zeta^2} < 1$$

For this type of curve there are three dominant frequency regimes. The low frequency dependence is proportional to frequency

$$\lim_{\omega\to 0} bf\left(\omega\right) = 1 + \frac{i\omega\tau}{2\zeta},$$

whilst the intermediate frequency dependence $\omega_1 < \omega < \omega_2$ (ω_1, ω_2 defined in Table 4.1.4.1) is inversely proportional to frequency

$$\lim_{\omega\to\omega_2} bf\left(\omega\right) = \frac{2\zeta}{-i\omega\tau}$$

and inversely proportional to the square root of frequency.

$$\lim_{\omega\to\infty} bf\left(\omega\right) = \frac{1}{\sqrt{-i\omega\tau}}$$

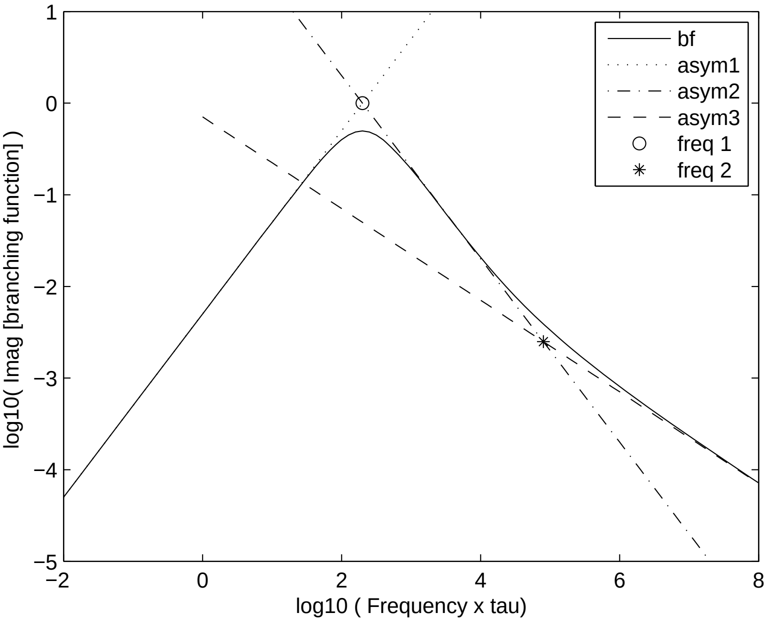

Figure 4.1.4.5 Category 4 attenuation curve. The imaginary component of the branching function with $\zeta = 100$ *(solid line) is defined by one low frequency asymptote (asym1 (dotted)) and two high frequency asymptotes (asym2 (dashed dotted) and asym1 (dashed)). There are two crossover frequencies freq1 (circle) and freq2 (asterisk).*

Figures 4.1.4.1-4.1.4.5 show for different values of the shape parameter, the APS framework will exhibit different frequency-dependent behaviour. In particular, I have identified four possible categories of frequency-dependent behaviour; refer to Table 4.1.4.1 for a summary. The next step is to determine how the shape parameter relates to spatial characteristics which describe different fluid distributions, i.e. like correlation functions. By establishing this type of relationship we can modify the shape parameter appropriately for different fluid distributions and substitute into the APS framework to calculate attenuation and dispersion.

Table 4.1.4.1: Different categories of frequency-dependent attenuation curves

Category	Number of asymptotes	Number of crossover frequencies	ω_1 (Hz)	ω_2 (Hz)	ζ
1	2	1	$\frac{1}{\tau}$	~	0
2	3	2	$\frac{2\zeta^2}{\tau}$	$\frac{1}{\tau}$	$\sqrt{\frac{\omega_1}{2\omega_2}}$
3	2	1	$\frac{(2\zeta^2)^{1/3}}{\tau}$	~	$\sqrt{\frac{(\omega_1\tau)^3}{2}}$
4	3	2	$\frac{2\zeta}{\tau}$	$\frac{8\zeta^2}{\tau}$	$\frac{\omega_2^2}{32\omega_1^2}$

4.2 1-Dimensional Media: Layering

The intrinsic attenuation of compressional waves due to wave induced fluid flow between layers of porous rock containing different pore fluids is well studied for the extremes of periodic layering (White 1979; Norris 1993; Johnson 2001) and random layering (Gurevich & Lopatnikov 1995; Gelinsky & Shapiro 1997; Gelinsky et al. 1998; Müller & Gurevich 2004). Here I show that the APS framework can be utilized to model both periodic and random layering by simply changing the shape and frequency scaling parameters appropriately.

The technique (Toms et al. 2006; Toms et al. 2007) used is to derive low and high frequency asymptotes from different types of layered media modelled using 1DCRM (such as periodic, quasi-periodic, and random). From these asymptotes, I can extract the T and G coefficients to form new shape and frequency scaling parameters, which are substituted into the APS framework to model attenuation and dispersion. I start with periodic layering, in order to access the accuracy of my approach and then proceed to more complicated layering systems.

4.2.1 Layering with Periodic Repetition

Although periodic functions are not random, they can be considered as a realisation of a random function with periodic autocorrelation function. Thus attenuation and dispersion of waves in a system of periodic layers can be modelled by substituting a periodic correlation function into 1DCRM model. Then we can use low and high frequency asymptotes of the solution for the saturated P-wave modulus to derive T and G, as well as shape ζ and frequency scaling τ parameters (using Equations (4.1.1.4) and (4.1.1.5)). Using these parameters I can construct the branching function solution. A comparison of such a solution (or its parameters) to either an exact solution (Norris, 1993) or the APS solution for periodic flat slab geometry can be a good test of the applicability of the branching function solutions based on asymptotes derived from CRM.

In the limit of low frequencies, the saturated P-wave modulus (Equation 3.1.1.3 and Equation 3.1.1.4) now expressed in terms of layer saturations S_1 , S_2 is

$$\lim_{\omega \to 0} H(\omega) = H_W \left(1 - \frac{si\omega}{D_0} \frac{S_1 S_2 h^2}{12} \right),$$

comparison with Equation (4.1.1.6) gives

$$T = \frac{sH_{BGW} S_1 S_2 h^2}{12 K_{BGW} D_0} . \tag{4.2.1.1}$$

where s is a non dimensional coefficient given by Equation 3.1.4. In the limit of high frequencies, the saturated P-wave modulus (Equation 3.1.1.3 and Equation 3.1.1.4) now expressed in terms of layer saturations S_1 , S_2 is

$$\lim_{\omega \to \infty} H(\omega) = H_{BGH} \left(1 - \frac{\delta \sqrt{D_0}}{S_1 S_2 h \sqrt{-i\omega}} \right),$$

comparison with Equation (4.1.1.7) gives

$$G = \frac{sH_{BGW} \sqrt{D_0}}{S_1 S_2 K_{BGH} h} . \tag{4.2.1.2}$$

Substitution of Equations (4.2.1.1-2) into Equation (4.1.4.2) and Equation (4.1.4.3) gives shape and frequency scaling parameters:

$$\zeta = 6 S_1 S_2 , \tag{4.2.1.3}$$

and

$$\tau = \frac{S_1{}^2 S_2{}^2 h^2}{D_0} . \tag{4.2.1.4}$$

An important feature of the shape and frequency scaling parameters is saturation dependence. In Figure 4.2.1.1 the shape parameter (Eq. (4.2.1.3)) is compared against the shape parameter computed using Johnson's T coefficient (applicable for periodic layering having any fluid contrast (Equation 1.3.2.1)). There is 100% correspondence between the two shape parameters when fluid contrast is low.

Figure 4.2.1.2 shows frequency-dependent (a) attenuation and (b) velocity calculated using three approaches: APS with T coefficient for periodic layering (Equation 1.3.2.5) (solid black line with filled circles), APS with shape and frequency scaling parameters derived above (Equation 4.2.1.3 and Equation 4.2.1.4) (solid grey line with unfilled circles) and 1DCRM with periodic correlation function (solid black line with crosses). Attenuation and velocity are calculated for periodic layering of water

($Kf = 2.25GPa$) with another fluid having slightly greater compressibility $Kf = 2GPa$, water saturation is 70 %. There is good correspondence between all three frequency-dependent attenuation and velocity estimates over the entire frequency range, which indicates that the branching function approximation central to APS theory is reasonably accurate at intermediate frequencies.

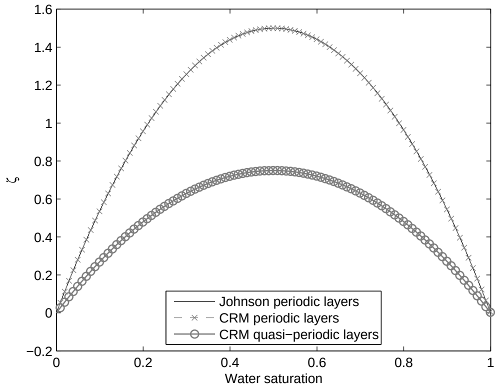

Figure 4.2.1.1: Shape parameter versus water saturation for low fluid contrast periodic and quasi-periodic layering

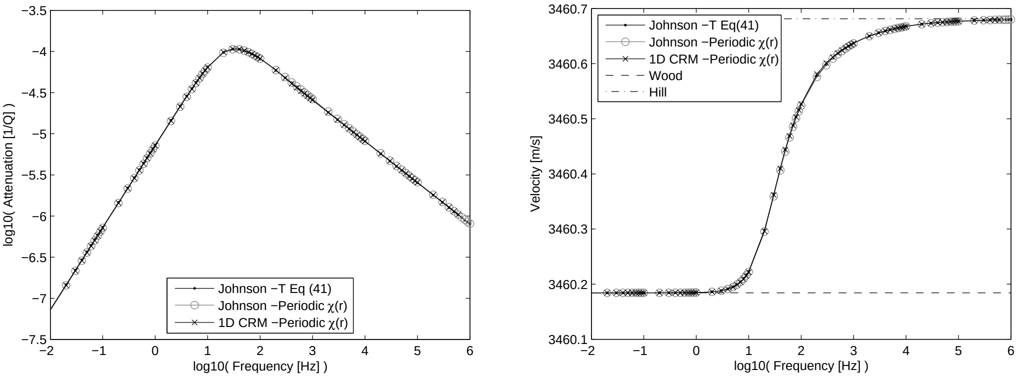

Figure 4.2.1.2: Frequency-dependent attenuation and dispersion due to low fluid contrast periodic layers. (a) Attenuation and (b) velocity for periodic layering of water with another fluid having slightly greater compressibility, water saturation is 70 percent.

Figure 4.2.1.3 shows shape parameter versus water saturation calculated using Johnson's T coefficient (Equation 1.3.2.5) for layering of water with more compressible fluids (bulk moduli ranging from $Kf = 2GPa$ to $Kf = 0.1MPa$). The shape parameter is no longer symmetric about 50 % water saturation. Moreover, the shape parameter dependence on percent water saturation changes significantly as the difference in fluid bulk moduli between the layers increases. That is, for low fluid contrast $Kf = 2GPa$, the shape parameter curve is symmetric about percent water saturation where as for large fluid contrast $Kf = 0.1MPa$ the shape parameter shows very different dependence on percent water saturation. Hence, the shape parameter for periodic layers exhibits dependency upon both fluid contrast and percent water saturation.

Figure 4.2.1.4 shows frequency-dependent (a) attenuation and (b) velocity calculated using three approaches: APS with T coefficient for periodic layering (Equation 1.3.2.5) (solid black line with filled circles), APS with shape ζ and frequency scaling τ parameters derived above (Equation 4.2.1.3 and Equation 4.2.1.4) (solid grey line with unfilled circles) and 1DCRM with periodic correlation function (solid black line with crosses). Attenuation and velocity are calculated for periodic layering of water ($Kf = 2.25GPa$) with another fluid of greater compressibility $Kf = 100MPa$, water saturation is 70 %. The magnitude of attenuation predicted using all three approaches is similar. However, the peak frequency of attenuation predicted using the Johnson model (APS with T coefficient given by Equation 1.3.25) is somewhat shifted, also the shape of the attenuation and dispersion curves are slightly different than the attenuation and dispersion curves predicted using 1DCRM and APS with Equation 4.2.1.3.

The discrepancy between attenuation/dispersion (Figure 4.2.1.4 a,b) arises because the shape parameter predicted using Johnson's T coefficient (Equation 1.3.2.5) accounts for fluid contrast, whilst the shape parameter given by Equation 4.2.1.3 is independent of fluid contrast. As the shape parameter (Equation. 4.2.1.3) was derived from 1DCRM theory which is precise at low fluid contrast, substitution of the new shape parameter into the APS framework will affect the accuracy of the APS approach. That is, APS becomes precise (approximate) for low (high) fluid contrast.

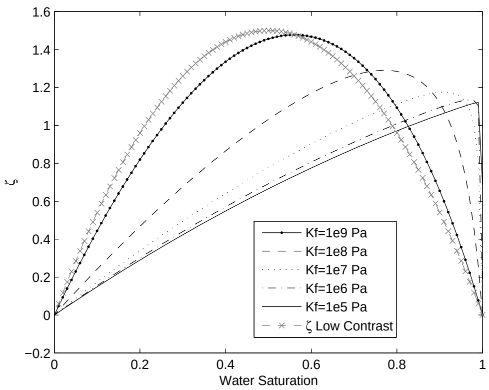

Figure 4.2.1.3: Shape parameter versus water saturation for periodically layered media having a range of fluid contrasts

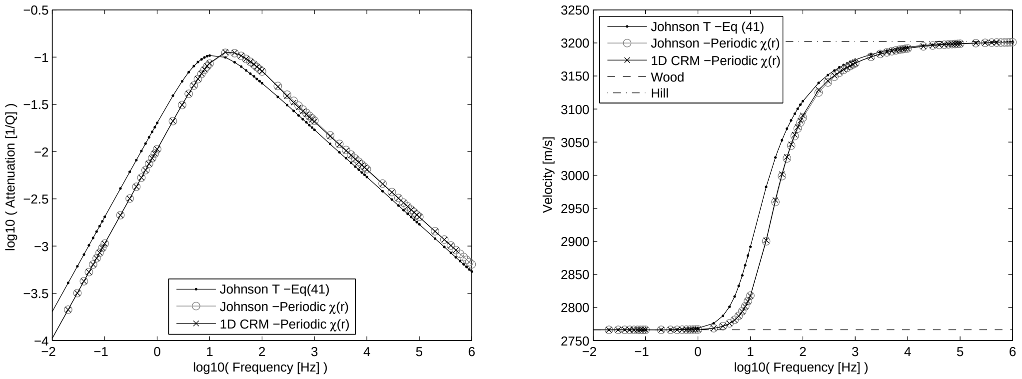

Figure 4.2.1.4: Frequency-dependent attenuation and dispersion due to high fluid contrast periodic layers. (a) Attenuation and (b) velocity for periodic layering of water with another fluid having greater compressibility $Kf = 100MPa$*, water saturation is 70%.*

4.2.2 Layering with Quasi-Periodic Repetition

Shape and frequency scaling parameters can also be derived for quasi-periodic layering of fluid heterogeneities by using 1DCRM results obtained in Section 3.1.2. At low frequencies the saturated P-wave modulus is

$$\lim_{\omega\to 0} H(\omega) = H_{BGW}\left(1 - \frac{si\omega}{D_0}\frac{S_1S_2h^2}{6}\right),$$

comparison with Equation (4.1.1.6) gives

$$T = \frac{sH_{BGW}S_1S_2h^2}{6K_{BGW}D_0}\,. \tag{4.2.2.1}$$

At high frequencies the saturated P-wave modulus is

$$\lim_{\omega\to\infty} H(\omega) = H_{BGH}\left(1 - \frac{\delta\sqrt{D_0}}{S_1S_2h\sqrt{-i\omega}}\right),$$

comparison with Equation (4.1.1.7) gives

$$G = \frac{\delta\sqrt{D_0}}{S_1S_2K_{BGH}h}\,. \tag{4.2.2.2}$$

Substitution of Equations (4.2.2.1) and (4.2.2.2) into Equations (4.1.1.4) and (4.1.1.5) gives shape and frequency scaling parameters of

$$\zeta = 3S_1S_2\,, \tag{4.2.2.3}$$

and

$$\tau = \frac{S_1{}^2S_2{}^2h^2}{D_0}\,. \tag{4.2.2.4}$$

In Figure 4.2.1.1, the shape parameter for quasi periodic layering (solid line with grey circles) is compared against the shape parameter for periodic layering. The shape parameter for quasi periodic layering never exceeds the value of 1, hence certain frequency-dependent attenuation and velocity will not occur for this type of layered system (at least at low contrast).

Figure 4.2.2.1 shows (a) attenuation and (b) velocity for quasi periodic layering of low fluid contrast, as predicted using Johnson’s framework with shape and frequency scaling parameters derived above. This is compared against 1DCRM with quasi periodic correlation function (Equation 3.1.2.12 and Equation 3.1.1.3) and Johnson’s framework with periodic shape and frequency scaling parameters. The attenuation curve is broader for quasi-periodic layering than for periodic layering. At intermediate frequencies, there are discrepancies between the estimates of the 1DCRM and Johnson’s framework (with Equations 4.2.2.3-4). This again is a small error which can be attributed to the branching function approximation.

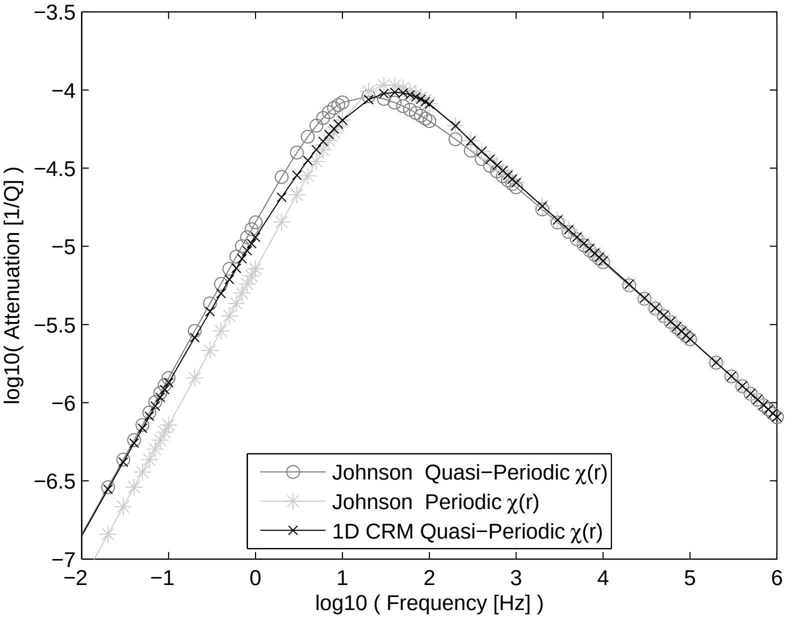

(a)

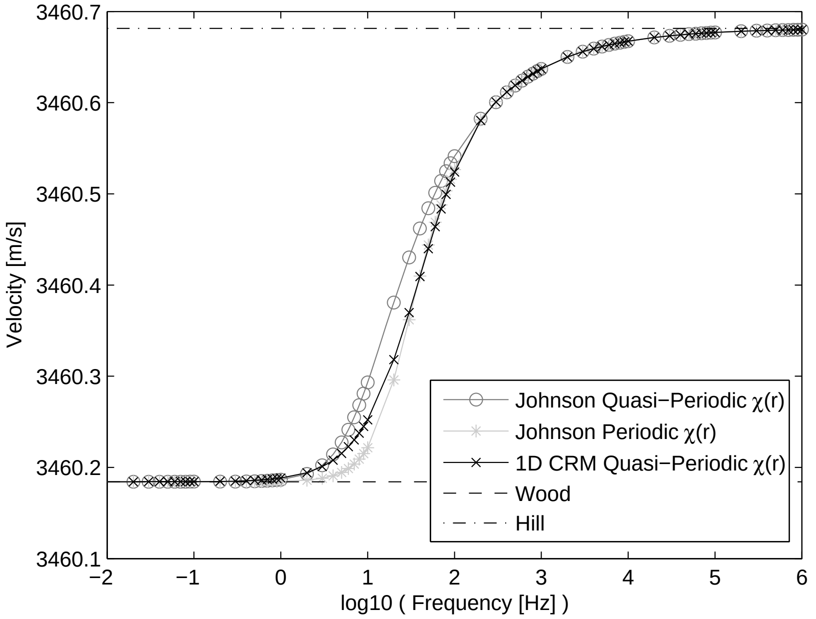

(b)

Figure 4.2.2.1: Frequency-dependent attenuation and dispersion due to low fluid contrast quasi-periodic layers. (a) Attenuation and (b) velocity, there are small differences between the branching function solution and the 1DCRM estimate at intermediate frequencies.

4.2.3 Random Layering

When rock/fluid heterogeneities are randomly layered, it is well known that the low frequency asymptote of the saturated P-wave modulus is proportional to the square root of frequency. In order for the Johnson framework to exhibit the same type of low frequency behaviour, the shape parameter must be set to zero (as per Section 4.1.1).

In this section, I show that the Johnson framework (with shape parameter equal to zero) can be utilized to model the effects of random layering as described by an exponential correlation function. My approach is to equate the high frequency asymptote of the 1DCRM model with the high frequency asymptote of the Johnson framework, so as to derive a G coefficient. I then show that if the G coefficient is set according to the CRM model, the low frequency asymptotes of both models coincide.

Firstly, consider the saturated P-wave modulus for exponentially correlated layering as given by the 1D CRM

$$\tilde{H}(\omega) = H_{BGW}\left[1 + \frac{s}{1 + \frac{2i}{k_2 d_L}}\right]. \qquad (4.2.3.1)$$

It has a high frequency asymptote of

$$\lim_{\omega\to\infty} \tilde{H}(\omega) \approx H_{BGH}\left(1 + \frac{\delta\sqrt{D_0}}{d_L}\frac{1}{\sqrt{-i\omega}}\right). \qquad (4.2.3.2)$$

Comparison of asymptote (Equation 4.2.3.2) with the high frequency asymptote of Johnson's framework ($\lim_{\omega\to\infty} \tilde{H}(\omega) = H_{BGH} - K_{BGH} G(-i\omega)^{-1/2}$) gives

$$G = \frac{\delta\sqrt{D_0}H_{BGH}}{d_L K_{BGH}}. \qquad (4.2.3.3)$$

At low frequencies the asymptote of the 1DCRM (Eq. 4.2.3.1) is

$$\lim_{\omega\to 0} \tilde{H}(\omega) = H_{BGW}\left[1 - ik_2 d_L \frac{s}{1 - ik_2 d}\right] \approx H_{BGW}\left[1 - ik_2 ds(1 - ik_2 d)\right] \approx H_{BGW}\left[1 + s\frac{d_L}{\sqrt{D_0}}\sqrt{-i\omega}\right]. \qquad (4.2.3.4)$$

When the shape parameter in Johnson’s framework is set to zero, the saturated P-wave modulus (Equation (4.2.0.1)) becomes

$$\tilde{H}_J(\omega) = H_{BGH}\left(1-\frac{\delta}{1+\sqrt{-i\omega\tau}}\right). \qquad (4.2.3.5)$$

It has a low frequency asymptote of

$$\lim_{\omega\to 0}\tilde{H}_J(\omega) = H_{BGH}\left(1-\delta\left(1-\sqrt{-i\omega\tau}\right)\right).$$

Substitution of the G coefficient into τ (Equation 4.1.1.5) reduces the low frequency asymptote of Johnson’s framework to

$$\lim_{\omega\to 0}\tilde{H}_J(\omega) = H_{BGH} - \left(H_{BGH} - H_{BGW}\right)\sqrt{-i\omega}\,\frac{\delta H_{BGH}}{K_{BGH}G} = H_{BGW}\left(1+s\frac{d_L}{\sqrt{D_0}}\sqrt{-i\omega}\right). \qquad (4.2.3.6)$$

Hence, Equations (4.2.3.4) and (4.2.3.6) show that the low frequency asymptotes of both models coincide when the G coefficient of Johnson’s framework is interpreted in terms of Equation (4.2.3.3). Moreover, with a little bit of algebra it can be shown that both models coincide over the entire frequency range.

That is, the 1DCRM saturated P-wave modulus (Equation 4.2.3.1) can be rearranged to:

$$\tilde{H}(\omega) = H_{BGH} - sH_{BGW} + \frac{sH_{BGW}}{1+\dfrac{2i}{k_2 d_L}}, \qquad (4.2.3.7)$$

where $H_{BGW} = H_{BGH} - sH_{BGW}$ is utilized. Equation (4.2.3.7) simplifies to

$$\lim_{\omega\to 0}\tilde{H}_J(\omega) = H_{BGH} - \left(H_{BGH} - H_{BGW}\right)\sqrt{-i\omega}\,\frac{\delta H_{BGH}}{K_{BGH}G} = H_{BGW}\left(1-s\sqrt{-i\omega}\,\frac{d_L}{\sqrt{D_0}}\right). \qquad (4.2.3.8)$$

Hence, when G is given by Equation (4.2.3.3) and $\zeta = 0$, the Johnson framework is directly equivalent to CRM with exponential correlation function. In Figure 4.2.3.1, (a) attenuation and (b) velocity are compared using both approaches, as expected from the above analysis, there is exact correspondence between the results. Thus the branching function approximation is shown to be accurate for random layering.

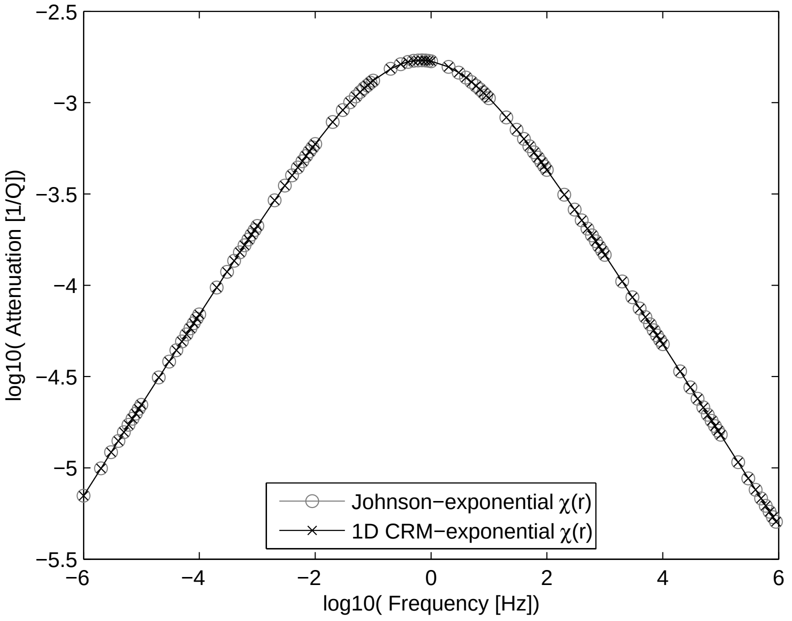

(a)

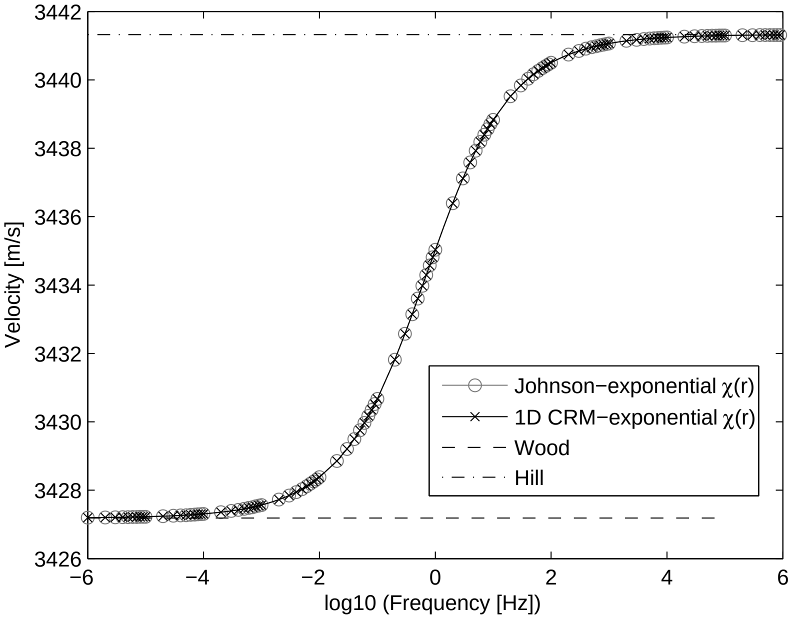

(b)

Figure 4.2.3.1: Frequency-dependent attenuation and dispersion due to low fluid contrast randomly distributed layers of moderate fluid contrast. (a) Attenuation and (b) dispersion curves for the Johnson model with $\zeta = 0$ *(grey line with circles) versus the 1DCRM with exponential correlation function.*

4.2.4 Generalised Correlation Function

Generalised shape and frequency scaling parameters can be determined for layered media having an unspecified correlation function of $\chi(r)$. At low frequencies, Equation (3.1.1) reduces to

$$\lim_{\omega\to 0} H \approx H_{BGW}\left[1 - sik_2\int_0^\infty \chi(r)(1+ik_2 r)dr\right] = H_{BGW}\left[1 - sik_2\int_0^\infty \chi(r)dr - s(ik_2)^2\int_0^\infty r\chi(r)dr\right]$$

(4.2.4.1)

where $\exp(ik_2 r)$ is replaced by its Taylor's series expansion. Substitution of the wave number $k_2 = \sqrt{\frac{i\omega}{D_0}}$ into Equation (4.2.4.1) gives

$$\lim_{\omega\to 0} H = H_{BGW}\left[1 - s\frac{\sqrt{-i\omega}}{\sqrt{D_0}}\int_0^\infty \chi(r)dr + s\frac{i\omega}{D_0}\int_0^\infty r\chi(r)dr\right]. \qquad (4.2.4.2)$$

This equation reveals that the saturated P-wave modulus has two dependencies at low frequency. The first scales with the square root of frequency, which arises when fluid stratification is random (as shown in Section 4.2.3), whilst the second is proportional to frequency, which is associated with periodic stratification of pore fluids (Section 4.2.1).

If $\int_0^\infty \chi(r)dr = 0$, which arises when pore fluid stratification is periodic, one can determine the T coefficient of Johnson's framework by comparing Equations (4.2.4.2) and (4.1.1.6). This gives

$$T = \frac{s}{D_0}\frac{H_{BGW}}{K_{BGW}}\int_0^\infty r\chi(r)dr\ . \qquad (4.2.4.3)$$

For high frequencies, it is only important to consider the correlation function at small offsets. Hence $\chi(r)$ can be expanded in a Taylor series

$$\chi(r) = \chi_0 + \chi_1 r + O(r^2),$$

where $\chi_0 = \chi(0) = 1$ and $\chi_1 = \frac{d\chi(0)}{dr}$.

The saturated P-wave modulus is

$$\lim_{\omega\to\infty} H \approx H_{BGW}\left[1 - sik_2\int_0^\infty (1+\chi_1 r)\exp(ik_2 r)dr\right] = H_{BGW}\left[1+s-\frac{s\chi_1}{ik_2}\right] = H_{BGH}\left[1-\frac{\delta\chi_1\sqrt{D_0}}{\sqrt{-i\omega}}\right], \tag{4.2.4.4}$$

where $\delta = \frac{(H_{BGH} - H_{BGW})}{H_{BGH}}$. Comparison with Equation (4.1.1.7) yields a G coefficient of

$$G = \frac{\delta\chi_1\sqrt{D_0}H_{BGH}}{K_{BGH}}. \tag{4.2.4.5}$$

Substitution of the T and G coefficients into Equation (4.1.1.4) gives a shape parameter of

$$\zeta = \frac{1}{2\left(\frac{d\chi(0)}{dr}\right)^2\int_0^\infty r\chi(r)dr}; \tag{4.2.4.6}$$

whilst substitution of Equation (4.2.4.5) into (4.1.1.5) gives a frequency scaling parameter of

$$\tau = \frac{1}{\left(\frac{d\chi(0)}{dr}\right)^2 D_0}. \tag{4.2.4.7}$$

It must be stressed that the shape parameter formula (Eq. (4.2.4.6)) is only valid if $\int_0^\infty \chi(r)dr = 0$. When $\int_0^\infty \chi(r)dr \neq 0$ which is the case for most correlation functions (such as exponential or Gaussian etc), the second term in Equation (4.2.4.2) dominates, that is

$$\frac{\sqrt{-i\omega}}{\sqrt{D_0}}\int_0^\infty \chi(r)dr >> s\frac{i\omega}{D_0}\int_0^\infty r\chi(r)dr.$$

When the second term in Equation (4.2.4.2) dominates, the saturated P-wave modulus at low frequencies is proportional to the square root of frequency. To enable the APS framework to be utilized to model this type of frequency behaviour, the shape parameter must be set to zero.

4.3 Three-dimensional Media

One motivation behind the development of the 3D patchy saturation models (given in Chapter 3) was to investigate whether 3D random and periodic poroelastic structures exhibit similar difference in the low frequency asymptotic behaviour as observed in 1D random and periodic structures. In Chapter 1 and 3, I showed that the frequency-dependent asymptotic behaviour is in general similar between periodic and most 3D random structures. In Sections 4.3.1-4.3.3, shape and frequency scaling parameters are derived for different 3D random structures. One question addressed will be whether 3D random and periodic structures are identifiable in terms of different shape and frequency scaling parameters, even though the low and high frequency asymptotic behaviour has similar frequency dependencies.

4.3.1 3D Discrete Random Media

Shape and frequency scaling parameters for a random distribution of non-overlapping spherical inclusions (of a different pore fluid) can be determined by deriving low and high frequency attenuation asymptotes from the discrete random media model (Section 3.2). The attenuation described by DRM (Equation (3.2.2.5)) can be rewritten as

$$Q^{-1} = 3v_1\Im\left\{\frac{P^*}{\left[N_1\dfrac{j_0(z_1)z_1}{j_1(z_1)} - N_2\dfrac{h_0^{(1)}(z_2)z_2}{h_1^{(1)}(z_2)}\right]}\right\}, \qquad (4.3.1.1)$$

where $P^* = \dfrac{(C_2H_1 - C_1H_2)}{H_2H_1^2}$ and $z_1 = k_1R$ and $z_2 = k_2R$.

Derivation of low and high frequency asymptotes from Equation 4.3.1.1 requires analysing the low and high frequency behaviour of the Bessel functions (i.e. $z_{1,2} \to 0$ and $z_{1,2} \to \infty$). For low frequencies $z_{1,2} \to 0$, the Bessel functions of the first kind reduce to

$$j_0(z) = 1 - \frac{z^2}{6}, \quad j_1(z) = \frac{z}{3}\left[1 - \frac{z^2}{10}\right]$$

and the ratio becomes $\frac{j_0(z)}{j_1(z)} \approx \frac{3}{z}\left(1-\frac{z^2}{6}\right)\left(1+\frac{z^2}{10}\right) \approx \frac{1}{z}\left(3-\frac{z^2}{5}+O(z^4)\right)$. The Bessel functions of the second kind reduce to

$$h_0^{(1)} = \frac{-i\exp(iz)}{z},\ h_1^{(1)} = -\exp(iz)\left(\frac{z+i}{z^2}\right)$$

and the ratio becomes $\frac{h_0^{(1)}}{h_1^{(1)}} = \frac{iz}{z+i} \approx z(1+iz)$. Substitution of these results into Equation (4.3.1.1) gives

$$\lim_{\omega\to 0} Q^{-1} = 3v_1\Im\left\{\frac{P^*}{\left[N_1\frac{j_0(z_1)z_1}{j_1(z_1)} - N_2\frac{h_0^{(1)}(z_2)z_2}{h_1^{(1)}(z_2)}\right]}\right\} \approx 3v_1\Im\left\{\frac{1}{3N_1}\left(1+\frac{{z_1}^2}{15}+\frac{N_2{z_2}^2}{3N_1}\right)\right\},$$

which simplifies to

$$\lim_{\omega\to 0} Q^{-1} = \frac{v_1P^*R^2\omega}{\kappa{N_1}^2}\left(\frac{\eta_1}{15}+\frac{\eta_2}{3}\right). \qquad (4.3.1.2)$$

Equation (4.3.1.2) shows that the low frequency asymptote of attenuation is directly proportional to frequency. This means that the T coefficient of Johnson's framework can be determined for a random distribution of spherical inclusions. By taking the real and imaginary components of the low frequency asymptote of the saturated P-wave modulus $\lim_{\omega\to 0}\tilde{H}(\omega) = H_{BGW} + K_{BGW}Ti\omega$, attenuation is derived as

$$\lim_{\omega\to 0} Q^{-1} = \frac{\Im\{\tilde{H}\}}{\Re\{\tilde{H}\}} = \omega\frac{K_{BGW}T}{H_{BGW}}. \qquad (4.3.1.3)$$

Comparison of Equation (4.3.1.2) and Equation (4.3.1.3) gives a T coefficient of

$$T = \frac{v_1H_{BGW}}{K_{BGW}}\frac{P^*R^2}{\kappa{N_1}^2}\left(\frac{\eta_1}{15}+\frac{\eta_2}{3}\right). \qquad (4.3.1.4)$$

At high frequencies, the ratios of the Bessel functions are

$$\lim_{z\to\infty}\frac{j_0(z)}{j_1(z)} = \frac{\frac{\sin z}{z}}{\frac{\sin z}{z^2}-\frac{\cos z}{z}} \approx \frac{\sin z}{\cos z} = \frac{\exp(iz)-\exp(-iz)}{i(\exp(iz)+\exp(-iz))} = -i \text{ and}$$

$$\lim_{z\to\infty}\frac{h_0^{(1)}}{h_1^{(1)}} = \frac{iz}{z+i} = \frac{i}{1+\frac{i}{z}} \approx i\left(1-\frac{i}{z}\right) \approx i.$$

Substitution of these results into (4.3.1.1) gives

$$\lim_{\omega\to\infty} Q^{-1} = 3S_1\Im\left(\frac{S_1P^*}{\left(-i(1+i)N_1\sqrt{\frac{\omega\eta_1}{2N_1\kappa}}-i(1+i)N_2\sqrt{\frac{\omega\eta_2}{2N_2\kappa}}\right)}\right)=\frac{3}{2}\frac{S_1P^*}{\left(N_1\sqrt{\frac{\omega\eta_1}{2N_1\kappa}}+N_2\sqrt{\frac{\omega\eta_2}{2N_2\kappa}}\right)R_1}. \qquad (4.3.1.5)$$

Equation (4.3.1.5) shows that the high frequency asymptote of attenuation is inversely proportional to the square root of frequency. Thus, the G coefficient of Johnson's framework can be determined. By taking the real and imaginary components of the high frequency asymptote of the saturated P-wave modulus $\lim_{\omega\to\infty}\tilde{H}(\omega)=H_{BGH}+K_{BGH}G(-i\omega)^{-1/2}$, attenuation is derived as

$$\lim_{\omega\to\infty} Q^{-1} = \frac{\Im\{\tilde{H}\}}{\Re\{\tilde{H}\}}=\frac{\frac{K_{BGH}G}{\sqrt{2\omega}}}{H_{BGH}+\frac{K_{BGH}}{\sqrt{2\omega}}G}\approx\frac{K_{BGH}G}{\sqrt{2\omega}H_{BGH}}. \qquad (4.3.1.6)$$

Comparison of Equation (4.3.1.5) and Equation (4.3.1.6) gives

$$G=\frac{3H_{BGH}S_1P^*}{K_{BGH}\left(\sqrt{\frac{N_1\eta_1}{\kappa}}+\sqrt{\frac{N_2\eta_2}{\kappa}}\right)R_1}. \qquad (4.3.1.7)$$

Substitution of the T (Equation 4.3.1.4) and G (Equation 4.3.1.7) coefficients into Equation (4.1.1.4) gives a shape parameter of

$$\zeta=\frac{(H_{BGH}-H_{BGW})^3}{18H_{BGW}H_{BGH}^2\left(\frac{P^{83}}{\kappa^3N_1^2}\right)\left(\frac{\eta_1}{15}+\frac{\eta_2}{3}\right)S_1^3\left(N_1\eta_1+2\sqrt{N_1N_2\eta_1\eta_2}+N_2\eta_2\right)}, \qquad (4.3.1.8)$$

and a frequency scaling parameter of

$$\tau=\frac{\delta^2R_i^2}{9S_1^2P^{*2}\kappa}\left(\sqrt{N_1\eta_1}+\sqrt{N_2\eta_2}\right)^2. \qquad (4.3.1.9)$$

These expressions for the shape and frequency scaling parameters are only valid for fluid contrasts and fluid percentages which don't violate DRM limitations. For instance, Equation (4.3.1.1) is valid for high contrasting pore fluids, but only for small inclusion concentrations of the more compressible fluid (see Section 3.2). Hence, in order to model shape and frequency scaling parameters at larger inclusion concentrations, a low contrast approximation is made. That is, I assume that the bulk modulus of the included fluid is comparable to the bulk modulus of the host fluid. When this is done, the shape parameter (Equation 4.3.1.8) reduces to

$$\zeta = \frac{5}{6}\frac{S_2^3\left(\sqrt{\eta_1}+\sqrt{\eta_2}\right)^2}{\left(\eta_1 + 5\eta_2\right)}, \qquad (4.3.1.10)$$

with frequency scaling parameter of

$$\tau = \frac{{S_2}^2 R_i^2 H_2}{9\kappa L M_2}\left(\sqrt{\eta_1}+\sqrt{\eta_2}\right)^2. \qquad (4.3.1.11)$$

In Figures 4.3.1.1-3 the shape parameter computed using Johnson's T coefficient for concentric spheres (Equation 1.3.2.7) (dashed black line) is compared against shape parameters computed using Equations (4.3.1.8) (solid black line) and (4.3.1.10) (dotted black line). Shown are shape parameters when one fluid is water and the other fluid has (a) low contrast ($K_f = 2\mathbf{GPa}$) (b) moderate contrast $K_f = 1\mathbf{GPa}$ and (c) large contrast $K_f = 0.01\mathbf{GPa}$ in fluid bulk moduli, respectively.

When fluid contrast is (a) small, the shape parameters calculated using Equations (4.3.1.8) and (4.3.1.10) are identical. The shape parameter for the periodic distribution of spheres differs from the shape parameter for a random distribution. All shape parameters are dependent on percentage saturation and approach the limiting value of $\zeta = 5/9$ at small inclusion saturations.

When fluid contrast is (b) moderate, the shape parameters for periodic and random distributions of spheres (Equation 4.3.1.8) are no longer symmetric in saturation. That is, the shape parameter value for a rock which is 20 percent saturated by gas and 80 percent saturated by water is not the same as the shape parameter for a rock which is 80 percent saturated by gas and 20 percent saturated by water. There are also discrepancies between the shape parameter values calculated using Equations (4.3.1.8) and (4.1.3.10). This is expected as the first equation takes into account fluid contrast, whilst the second equation doesn't. In Chapter 5, these Equations (4.3.1.8) and (4.1.3.10) will be studied to identify which is representative at what fluid contrast and inclusion saturation.

When fluid contrast is (c) large, the shape parameters for periodic and random distributions of spheres (Equations 4.3.1.8) depend heavily on percent fluid saturation. A rock which is less then 10 percent saturated by gas will have a shape parameter (for both periodic and random distributions of spheres) that suggests entirely different frequency-dependent attenuation behaviour, than a rock which is saturated by more then 10 percent gas.

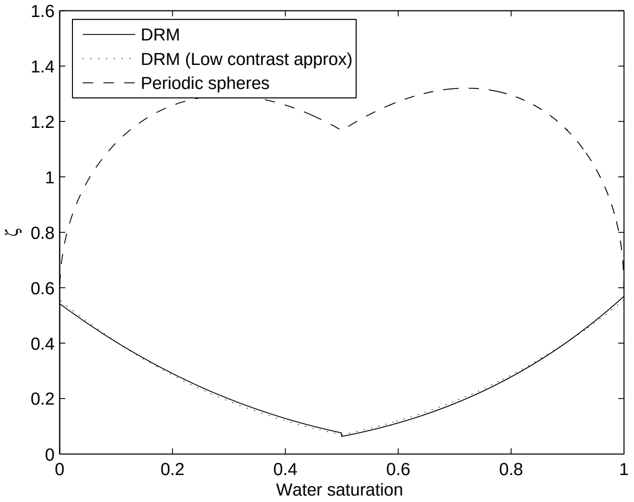

Figure 4.3.1.1: Shape parameters for low fluid contrast spherical inclusions as a function of water saturation. Shape parameters for periodic spheres (dashed line) are different from shape parameters of randomly distributed spheres (DRM Equation (4.3.1.8) solid line) and randomly distributed spheres of low contrast (DRM Equation (4.3.1.10)). Fluid contrast was small, so there is good correspondence between the DRM shape parameters.

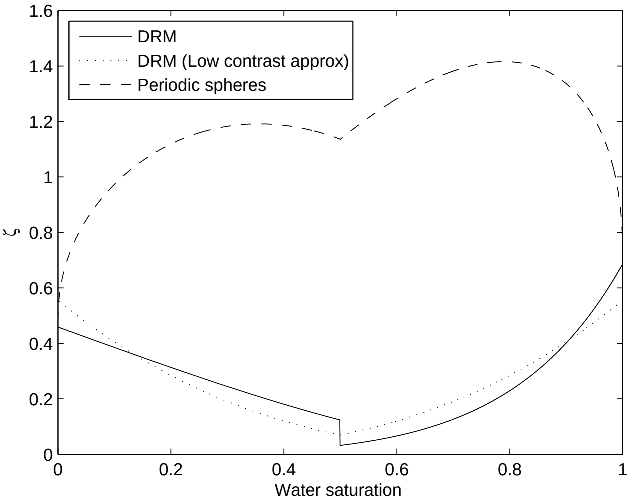

Figure 4.3.1.2: Shape parameters for moderate fluid contrast spherical inclusions as a function of water saturation. Shape parameters for periodic spheres (dashed line) are different from shape parameters of randomly distributed spheres (DRM Equation (4.3.1.8) solid line) and randomly distributed spheres of low contrast (DRM Equation (4.3.1.10)). Fluid contrast was moderate; hence the DRM shape parameters are differing

.

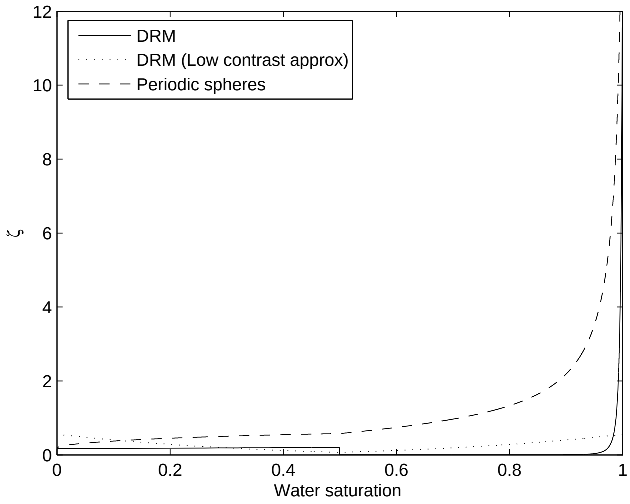

Figure 4.3.1.3: Shape parameters for high fluid contrast spherical inclusions as a function of water saturation. Shape parameters for periodic spheres (dashed line) differ from shape parameters for randomly distributed spheres (DRM Equation (4.3.1.8) solid line) and randomly distributed spheres of low contrast (DRM Equation (4.3.1.10)).

4.3.2 3D Continuous Random Media

If some particular normalised autocorrelation function $\chi(r)$ describes the spatial distribution of pore fluids in three spatial dimensions; shape and frequency scaling parameters may be derived from the 3DCRM model (Section 3.3), providing that the low and high frequency dependence of the saturated P-wave modulus is proportional to ω and $1/\sqrt{\omega}$, respectively. This is not always the case for certain types of correlation functions, such as Gaussian, fractal etc., see Discussion 4.3.2.3.

First, I simplify the 3DCRM framework to

$$\tilde{H}(\omega) = H_{BGW}\left(1 - s\left(\frac{i\omega}{D_0}\right)\int_0^\infty r\chi(r)\exp\left(\sqrt{-i\omega/D_0}\,r\right)dr\right), \qquad (4.3.2.1)$$

where

$$s = \frac{H_{BGH} - H_{BGW}}{H_{BGW}}. \qquad (4.3.2.2)$$

In the limit of low frequencies the saturated P-wave modulus (Equation 4.3.2.1) reduces to

$$\lim_{\omega\to 0}\tilde{H}(\omega) = H_{BGW}\left(1 - \frac{i\omega s}{D_0}\int_0^\infty r\chi(r)dr\right). \qquad (4.3.2.3)$$

Comparing Equation (4.3.2.3) with Equation (4.1.1.6) yields a T coefficient of

$$T = \frac{H_{BGW}\,s}{K_{BGW}\,D_0}\int_0^\infty r\chi(r)dr \;. \qquad (4.3.2.4)$$

At high frequencies only behaviour at small offsets is important. Assume that the normalised autocorrelation function can be expanded in a power series

$$\chi(r) = \chi_0 + \chi_1 r + O\left(r^2\right),$$

where $\chi_0 = \chi(0) = 1$ and $\chi_1 = \frac{\partial\chi(0)}{\partial r}$.

Then, the integral in Equation (4.3.2.1) is reduced to

$$\int_0^\infty r\chi(r)\exp(ik_2 r)dr \approx \int_0^\infty r(1+\chi_1 r)\exp(ik_2 r)dr = \left[\frac{1}{(ik_2)^2}\right] + \frac{2\chi_1}{(ik_2)^3}\,, \tag{4.3.2.5}$$

Substitution of Equation (4.3.2.5) into Equation (4.3.2.1) gives a high frequency saturated P-wave modulus of

$$\lim_{\omega\to\infty} \tilde{H}(\omega) = H_W\left(1 + s + \frac{2\chi_1 s\sqrt{D_0}}{\sqrt{-i\omega}}\right), \tag{4.3.2.6}$$

comparison with Equation (4.1.1.7) gives a G coefficient of

$$G = \frac{2H_{BGW}\chi_1\delta\sqrt{D_0}}{K_{BGH}}\,. \tag{4.3.2.7}$$

By substituting the T and G coefficients derived above into Equations (4.1.1.4) and (4.1.1.5), the shape parameter corresponding to a generalised correlation function is obtained

$$\frac{1}{\zeta} = 8\left(\frac{d\chi(0)}{dr}\right)^2 \int_0^\infty r\chi(r)dr\,, \tag{4.3.2.8}$$

with a frequency scaling parameter of

$$\frac{1}{\tau} = 4D_0\left(\frac{d\chi(0)}{dr}\right)^2. \tag{4.3.2.9}$$

Below I use Equations (4.3.2.8) and (4.3.2.9) to derive shape and frequency scaling parameters for different three dimensional fluid distributions described by specific correlation functions. However, it must be stressed that Equations (4.3.2.8) and (4.3.2.9) and hence, the results derived below are only precise for low contrast in fluid properties due to approximations made within the 3DCRM approach.

4.3.2.1 Relationship to Statistics from Gas Saturation Maps

Further analysis of Equations (4.3.2.8) and (4.3.2.9) reveal that the shape and frequency scaling parameters can be directly related to statistical measures (aside from the correlation function $\chi(r)$) extracted from tomographic images. By recognizing that the derivative of the correlation function $\chi(r)$ is related to the surface to volume ratio of fluid heterogeneities by

$$\frac{\partial\chi(0)}{\partial r} = -\frac{S}{4V},$$

the shape parameter can be written as

$$\frac{1}{\zeta} = \frac{1}{2}\left(\frac{S}{V}\right)^2 a_M{}^2, \tag{4.3.2.1.1}$$

and the frequency scaling parameter as

$$\frac{1}{\tau} = \frac{D_0}{4}\left(\frac{S}{V}\right)^2, \tag{4.3.2.1.2}$$

where $\frac{S}{V}$ is the surface to volume ratio of the fluid patches and a_M is the mean correlation length defined by Equation (2.3.1.5.2) as

$$a_M = \left(\int_0^\infty r\chi(r)dr\right)^{1/2}.$$

Equations (4.3.2.1.1) and (4.3.2.1.2) show how to determine the shape and frequency scaling parameters directly from characteristics of the tomographic images.

4.3.2.2 Debye Random Media

For a Debye random distribution of fluids which can be modelled using an exponential correlation function given by $\chi(r) = \exp\left(\frac{-r}{a}\right)$, the shape parameter derived using Equation (4.3.2.8) is $\zeta_E = 1/8$. It is a constant value independent of correlation length, percent fluid saturation and fluid contrast. This means that the shape of the attenuation and velocity curves will not change as the correlation length, percent fluid saturation and fluid contrast is altered. The corresponding frequency scaling parameter is $\tau_E = a^2/(4D_0)$, which is proportional to the square of the correlation length. Thus changing the correlation length will shift the curve in frequency.

Figure 4.3.2.2.1 shows (a) attenuation and (b) velocity obtained from Johnson's model with shape and frequency scaling parameters ζ_E and τ_E (obtained above). This is compared against the CRM model having an exponential correlation function. The contrast between pore-fluid bulk moduli is kept small, with an included fluid of bulk moduli $K_{f1} = 2\text{GPa}$ within a rock 90% saturated by water ($K_{f2} = 2.25\text{GPa}$). For this scenario, the CRM model is precise. Thus the shape of attenuation and velocity curves predicted via CRM are accurate over the entire frequency range. Only small differences are observed between the Johnson model and CRM at intermediate frequencies. This means that the branching function is reasonably accurate at intermediate frequencies and thus the dynamic behaviour is well approximated using Johnson's model with shape and frequency scaling parameters of ζ_E and τ_E.

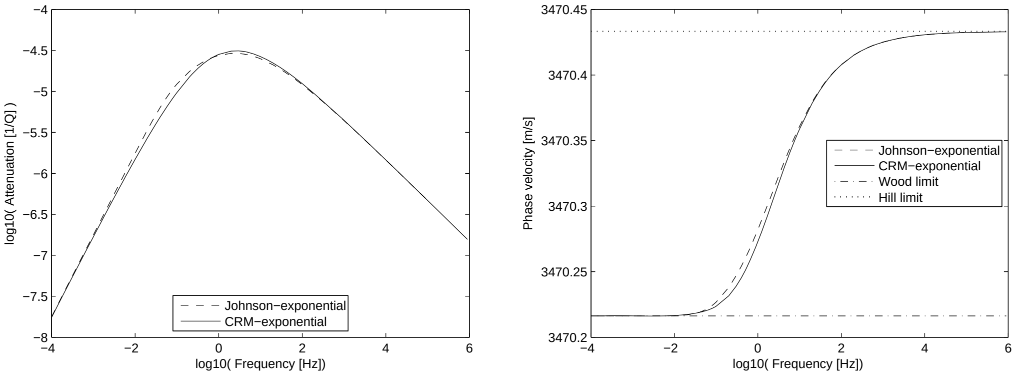

(a) (b)

Figure 4.3.2.2.1: Frequency-dependent attenuation and dispersion due to 3D exponential fluid distribution. (a) Attenuation and (b) velocity estimates using Johnson's model (dashed line) with shape and frequency scaling parameters appropriate for an exponential correlation function and for CRM with exponential correlation function (solid line). The theoretical bounds on velocity are given by Wood (dashed–dotted line) and Hill (dotted line).

When the distribution of fluids can be modelled using a double Debye correlation function

$$\chi_2(r) = \chi_{Small} + \chi_{L\arg e} = b_S \exp\left(-\frac{r}{a_S}\right) + b_L \exp\left(-\frac{r}{a_L}\right),$$

which may be appropriate for modelling the fluid distribution towards the end of a drainage experiment (see Section 2.3.1.5), the shape parameter and frequency scaling parameters are

$$\zeta = \frac{1}{8\left(b_S a_S^2 + b_L a_L^2\right)\left(\frac{b_S}{a_S} + \frac{b_L}{a_L}\right)^2}, \qquad \tau = \frac{1}{4D_0\left(\frac{b_S}{a_S} + \frac{b_L}{a_L}\right)^2}.$$

For instance, the shape parameter of the average correlation function of MGL2a (during the latter stages of the drainage experiment) is $\zeta = \mathbf{0.0243}$. In general, if the distribution of fluids can be modelled using many different Debye correlation functions

$$\chi_N(r) = \sum_{i=1}^{N} b_i \exp\left(-\frac{r}{a_i}\right),$$

then the shape parameter and frequency scaling parameters are

$$\zeta = \frac{1}{8\left(\sum_i b_i a_i^2\right)\left(\sum_i \frac{b_i}{a_i}\right)^2}, \ \tau = \frac{1}{4D_0\left(\sum_i \frac{b_i}{a_i}\right)^2}.$$

4.3.2.3 Overlapping Sphere Models

When the fluid distribution is described by an overlapping sphere model having autocorrelation function:

$$\chi(r) = \frac{\exp\left(-\gamma\left(1 + \frac{3}{4}\frac{r}{R} + \frac{1}{16}\left(\frac{r}{R}\right)^3\right)\right) - v_1^2}{v_1 v_2},$$

the shape parameter needs to be determined via numerical integration as an analytical solution to the integral (in Equation (4.3.2.8)) was not found. In Figure 4.3.2.2 (dotted line) the shape parameter is shown for the overlapping sphere distribution; it depends on the relative percentage of two pore fluids but is independent of the sphere radius. The frequency scaling parameter is

$$\tau = \frac{9D_0(\log v_1)^2}{4R^2 v_2^2},$$

which depends on both relative percentage of pore fluids and the square of the inclusion radius. Figure 4.3.2.3.1 shows that the shape parameters for random distributions of spherical inclusions (both non-overlapping-DRM and overlapping) differ from periodic distributions of spherical inclusions.

However, one can make a linear approximation to the non-overlapping sphere correlation function; this serves to preserve some of the spatial characteristics of the original function, whilst allowing (Equation 4.3.2.1) to be solved analytically. The approximation used is $\chi(r) = 1 - \frac{r}{2R}$ for $r \le 2R$ and $\chi(r) = 0$ for $r > 2R$. The corresponding shape parameter is a constant $\zeta = \frac{3}{4}$ and the frequency scaling parameter is $\tau = \frac{R^2}{D_0}$.

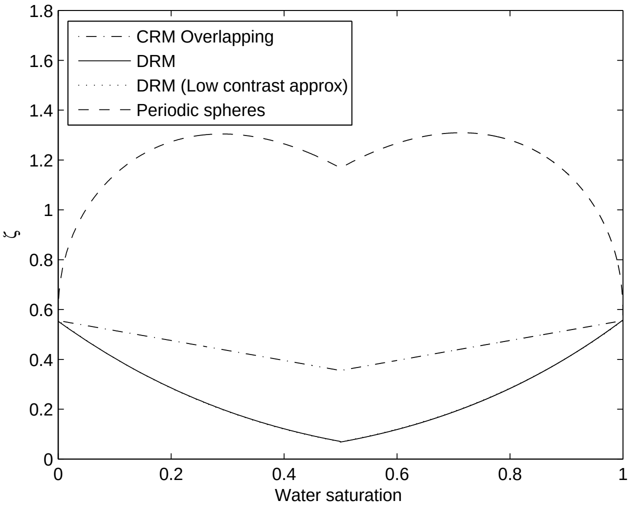

Figure 4.3.2.3.1: Shape parameters for different 3D distributions of spherical inclusions of low fluid contrast. Periodic (dashed line), random (DRM Equations (4.3.1.8) and (4.3.1.10)) and overlapping sphere distributions (numerically calculated using Eq. (4.3.2.1)) shape parameters all depend differently on water saturation.

4.3.2.3 Discussion

For the Gaussian correlation function $\chi(r) = \exp\left(\frac{-r^2}{a^2}\right)$ utilized in Section 3.3.2 for which attenuation doesn't have the required frequency dependence, the shape parameter is infinite. This can be seen by taking the derivative of the frequency scaling parameter $\frac{d\chi(r)}{dr} = \frac{-2r}{a^2}\exp\left(\frac{-r^2}{a^2}\right)$ which is equal to zero at the origin ($r = 0$). Thus, the G coefficient is zero and the shape parameter and frequency scaling parameter are infinite.

This can be taken one step further by considering a fractal distribution of pore fluids. Müller and Toms (2007) have shown that the high frequency asymptote of attenuation for a fractal distribution of pore fluid is $Q^{-1} \propto \omega^{-\upsilon}$, where υ is the Hurst exponent. For $\upsilon = 1/2$, the fractal medium is exponential and thus the shape and frequency scaling parameters are given as above. However, when the Hurst exponent $\upsilon < 1/2$, the $S/V \to \infty$ as the ratio of the surface area of the patches increases, which means the G coefficient approaches zero and the shape and frequency scaling parameters are infinite.

This shows that shape and frequency scaling parameters (for the Johnson framework) do not have finite values for all correlation functions. The only model having the flexibility to estimate attenuation and dispersion due to *any* 3D fluid distribution is the 3DCRM modelling approach. However, it is precise for low fluid contrast and *only* approximate at large fluid contrast.

4.4 Chapter Summary

The main results of this Chapter are given in the Tables. They show T and G coefficients along with shape and frequency scaling parameters for different types of fluid distributions. Note that, outside the validity of the original models (please refer to the discussions in Chapter 3), the shape and frequency scaling parameters should only be taken as a rough guide.

Table: 4.4.1: T and G coefficients for 1D fluid stratifications.

Layered media	Correlation function	T coefficient	G coefficient
Periodic	see Section 3.1.1	$\frac{sS_1S_2H_{BGW}h^2}{12K_{BGW}D_0}$	$\frac{sH_{BGW}\sqrt{D_0}}{S_1S_2K_{BGH}h}$
Quasi-periodic	see Section 3.1.2	$\frac{sS_1S_2H_{BGW}h^2}{6K_{BGW}D_0}$	$\frac{sH_{BGW}\sqrt{D_0}}{S_1S_2K_{BGH}h}$
Exponential	$\exp\left(\frac{-2\lvert r\rvert}{d_L}\right)$	∞	$\frac{\delta\sqrt{D_0}H_{BGH}}{d_LK_{BGH}}$
Generalised	$\chi(r)$	$\frac{s}{D_0}\frac{H_{BGW}}{K_{BGW}}\int_0^\infty r\chi(r)dr$	$\frac{\delta\chi_1\sqrt{D_0}H_{BGH}}{K_{BGH}}$

Table: 4.4.2: Shape and frequency scaling parameters for 1D fluid stratifications.

Layered media	Shape parameter ζ	Frequency scaling τ parameter
Periodic	$6S_1S_2$	$\frac{S_1{}^2S_2{}^2h^2}{D_0}$
Quasi-periodic	$3S_1S_2$	$\frac{S_1{}^2S_2{}^2h^2}{D_0}$
Exponential	0	$d_L{}^2/D_0$
Generalised	$\left(2\left(\frac{d\chi(0)}{dr}\right)^2\int_0^\infty r\chi(r)dr\right)^{-1}$	$\left(\left(\frac{d\chi(0)}{dr}\right)^2D_0\right)^{-1}$

Table: 4.4.3: T and G coefficients for 3D fluid distributions.

Media	Correlation function	T coefficient	G coefficient
Exponential	$\exp\left(\frac{-r}{a}\right)$	$\frac{a^2 H_{BGW} s}{K_{BGW} D_0}$	$\frac{-2\sqrt{D_0} H_{BGW} \delta}{K_{BGH} a}$
Linear approximation	$1-\frac{r}{2R_i}$	$\frac{2R_i^2 H_{BGW} s}{3K_{BGW} D_0}$	$\frac{-\sqrt{D_0} H_{BGW} \delta}{K_{BGH} R_i}$
Non-Overlapping Spheres	DRM approach	$\frac{R_i^2 P^*}{\kappa N_1^2}\left(\frac{\eta_1}{15}+\frac{\eta_2}{3}\right) H_{BGW} S_1$	$\frac{3H_{BGH} P^* S_1}{R_i K_{BGH}\left(\frac{N_1}{\sqrt{D_1}}+\frac{N_2}{\sqrt{D_2}}\right)}$
Generalised	$\chi(r)$	$\frac{H_{BGW} s}{K_{BGW} D_0}\int_0^\infty r\chi(r)dr$	$\frac{2H_{BGW}\chi_1\delta\sqrt{D_0}}{K_{BGH}}$

Table: 4.4.4: Shape and frequency scaling parameters for 3D fluid distributions.

Media	Shape ζ parameter	Frequency scaling τ parameter
Exponential	$1/8$	$a^2/(4D_0)$
Linear approximation	$3/4$	R^2/D_0
Non-Overlapping Spheres	$\frac{5S_2^3\left(\sqrt{\eta_1^2}+\sqrt{\eta_2^2}\right)^2}{6(\eta_1+5\eta_2)}$	$\frac{{S_2}^2 R_i^2 H_2}{9\kappa L M_2}\left(\sqrt{\eta_1}+\sqrt{\eta_2}\right)^2$
Generalised	$\left(8\left(\frac{d\chi(0)}{dr}\right)^2\int_0^\infty r\chi(r)dr\right)^{-1}$	$\left(4D_0\left(\frac{d\chi(0)}{dr}\right)^2\right)^{-1}$

4.5 Chapter Conclusions

In this Chapter I have shown that shape and frequency scaling parameters depend upon fluid distribution. The substitution of shape and frequency scaling parameters (given in the tables) into Johnson’s framework provides a simple means to model attenuation and dispersion due to many different types of pore fluid distributions. That is, both fluid layering and 3D spatial distributions can be easily modelled. However, there are still limitations on the use of the tabulated shape and frequency scaling parameters, as the accuracy of the models used to derive the parameters are limited to certain scenarios, such as low fluid contrast.

The comparison of Johnson’s framework with modified shape and frequency scaling parameters against modelling approaches which are explicit over the entire frequency range (DRM, 1DCRM, 3DCRM, etc) provides a method of testing the accuracy of the branching function at intermediate frequencies. Throughout the Chapter it has been shown that the branching function (via comparison) is reasonably accurate at intermediate frequencies for many different fluid distributions.

An issue which has not really been addressed in this Chapter, is, how the shape and frequency scaling parameters vary with fluid contrast. For a periodic and random distribution of spherical inclusions, initial modelling suggests that fluid contrast will have a large effect upon shape and frequency scaling parameters at small inclusion concentrations. In the next Chapter, I will investigate this issue further.

Chapter 5

Numerical Analysis of APS Shape Parameter

5.0 Introduction

All attenuation/dispersion models discussed in Chapters 1 and 3 of this thesis have advantages and disadvantages. The regular cell models (Chapter 1) are analytically limited to simplistic fluid distribution geometries (such as concentric spheres) but capable of modelling any fluid contrast. The random media models of Chapter 3 are mostly limited to low contrast pore fluids, but are capable of modelling complex and irregular distributions of fluids. In order to model compressional wave attenuation and dispersion when porous rock is saturated by “realistic fluids” in a “realistic way”, both fluid contrast and fluid distribution effects need to be understood and addressed in unison.

My motivation behind creating a synergy between the Chapter 1 and Chapter 3 modelling approaches is aimed at addressing this need, through combining the strengths of each type of approach. In Chapter 4, I have demonstrated that the APS framework (Johnson 2001) can be exploited to consider effects due to complicated fluid distributions. Prior to this, usage of the APS framework was restricted to simple fluid distributions, such as periodic layering, concentric circles (Krzikalla et al. 2006) and concentric spheres

Specifically, I show how two special parameters within the APS framework (called shape and frequency scaling parameters) can be suitably modified to account for effects due to: random layering, randomly distributed spheres and random fluid distributions given by a variety of correlation functions. However, the usage of the new shape and frequency scaling parameters, maybe constrained to certain fluid contrasts and fluid saturations.

The possible restrictions on the use of the new shape and frequency scaling parameters are a consequence of models which underpin their derivation, such as 1DCRM, DRM and 3DCRM. These models are precise for only certain fluid contrasts and fluid saturations. Hence, it is necessary to demarcate the range of volume concentrations and fluid contrasts for which my derived parameters (see Table 4.4.2 & Table 4.4.4) can be accurately utilized. In this Chapter, I investigate this issue when the fluid distribution is given by a 3D random distribution of spherical inclusions.

There are two possible ways one could investigate the applicability of the shape and frequency scaling parameters. Both approaches are based on numerical computation and require generating the appropriate synthetic models of interest (such as a 3D random distribution of spheres). The first approach is to use finite-difference approximations to forward model either the equations of poroelasticity (Dai et al. 1995; Ozdenvar & McMechan 1997; Helle et al. 2003) or the elastic wave equation with a Navier-Stokes equation for viscous fluid flow (Saenger et al. 2007). Once the synthetic wave field has passed through the synthetic model, wave attenuation and dispersion can be estimated. This allows shape and frequency scaling parameters to be determined using Equations (4.1.1.4) and (4.1.1.5). When simulations are run over models of different fluid contrast and volume concentrations, changes in shape and frequency scaling parameters can be related to changes in fluid contrast and volume concentration.

However, there are several drawbacks to using this approach. Firstly, it is computationally expensive to perform the necessary calculations for 3D distributions of fluids. Secondly, there are numerical issues with approximating wave equations, such as numerical stability and numerical dispersion (Trefethen 1982) which need to be handled with care, when the equations to be approximated are highly attenuative and dispersive, although, as illustrated by Saengar et al. (2007) numerical accuracy issues can be resolved and minimized by judicious choice of parameters. Thirdly, in the frequency range where attenuation is a maximum and P-wave velocity changes most rapidly, it may not be possible to estimate from the synthetic wave field the shape and frequency scaling parameters accurately.

The second approach to calculating shape and frequency scaling parameters for complicated fluid distributions having any fluid contrast, involves determining the shape parameter from direct numerical computation of the T coefficient (see Equation 4.1.1.6). The T coefficient governs the low frequency approach of the frequency-dependent saturated bulk modulus to the static limit given by Gassmann-Wood equations. Although, the Gassmann-Wood limit depends only on fluid volume fraction and fluid bulk moduli, the T coefficient also depends on fluid distribution via an auxiliary function Φ (and partial differential equation) defined within the APS framework.

The APS auxiliary function Φ is a solution of a potential equation that is related to the final stages of fluid pressure equilibration. It can be likened to a steady state diffusion equation for fluid pressure equilibration. In practice, the potential equation can only be solved analytically for very simple fluid geometries, such as periodic layering, concentric spheres etc. Hence determination of shape and frequency scaling parameters using the APS auxiliary function Φ has until now been restricted to simple regular geometries. However, in principle, the APS auxiliary function Φ can be solved for numerically (using finite-differences or finite elements) in cases where the fluid distribution is complicated, such as with randomly distributed spheres.

There are several advantages of numerically approximating the potential equation, over numerically approximating the analogous system of wave equations (the previous approach) in order to study shape and frequency scaling parameters. Firstly, it is computationally less expensive, especially in three spatial dimensions (as only one computation is required to obtain the solution for all frequencies). Secondly, the mathematical behaviour of the potential equation is far simpler, and hence the approach is easier to implement accurately. Thirdly, the approach is direct, enabling computation of the shape parameter (via the T coefficient defined in terns of the auxiliary function Φ) without having to process synthetic seismograms, etc.

In this Chapter, the latter approach is trialled. I compute the shape parameter ζ for a random distribution of spherical inclusions, in particular studying how ζ varies when spherical inclusion concentration and contrast is altered. The numerical estimates of the shape parameter are then compared against the analogous analytical shape parameters derived in Chapter 4 (Equations (4.3.1.8) and Equations (4.3.1.10)). This type of analysis could also be performed for other types of fluid distributions and their analytical shape parameters (Table 4.4.2 and Table 4.4.4). Hence, enabling demarcation of volume concentrations and fluid contrasts, for which, the analytical shape parameters could be used to extend the analytical capacity of APS to realistic fluid distributions.

The Chapter is organised as follows. In Section 1 the potential equations are defined. In Section 2, finite-difference theory is introduced and finite-difference approximations are made for the derivatives in the potential equations. Section 3 covers testing aspects of the algorithm. Section 4, includes a discussion on the synthetic media and presents the results of comparing numerical shape parameters versus theoretical shape parameters at different fluid contrasts.

5.1 The Physics

5.1.1 The APS Potential Equation

The potential equation for the auxiliary function Φ plays an important role in determining the shape parameter, as it affects the T coefficient governing the low frequency approach of the dynamic saturated bulk modulus to the static limit given by Gassmann-Wood equations. In this section, I explain the technique and physical considerations employed by Johnson (2001), when he derives the T coefficient and potential equation central to APS theory.

Johnson (2001) states that the macroscopic expression for energy dissipation per wave cycle expressed in terms of the dynamic saturated bulk modulus $\widetilde{K}(\omega)$ of an elementary volume V must be equivalent to the same quantity expressed as a volume integral of the appropriate combination of microscopically varying field variables. In other words, Johnson’s technique centres on equating: 1) the power per wave cycle (i.e. energy loss) caused by an oscillatory external stress applied to the surface of a partially saturated volume V with 2) the power per wave cycle of relative fluid-solid displacement averaged over the volume of the sample. Relative fluid-solid displacements occur because of fluid pressure equilibration. See Figure (5.1.1.1)

The same technique has subsequently been utilized by Tserkovynak and Johnson (2002) to study the effect capillary forces have on compressional wave attenuation. More recently, Müller and Rothert (2006) have applied a similar recipe to explain why there is a difference in frequency-dependent attenuation when heterogeneities are randomly and periodically layered.

The Johnson Approach:

(1) The power per wave cycle on the mesoscale is

$$\overline{P}_{MES} = \frac{1}{2}\,\mathrm{Real}\int \frac{\partial u^*}{\partial t}\cdot \tau.\hat{n}\,\mathrm{dS} \equiv -\frac{1}{2}\,\mathrm{Real}\left[i\omega V\,\frac{\left|P_e\right|^2}{\widetilde{K}(\omega)}\right], \qquad (5.1.1.1)$$

where V is the composite volume, P_e is the effective pressure and $\widetilde{K}(\omega)$ is the frequency-dependent saturated bulk modulus (at the low frequency limit) given by

$$\lim_{\omega \to 0} \widetilde{K}(\omega) = K_{BGW}(1 - i\omega T). \qquad (5.1.1.2)$$

Here K_{BGW} is the Gassmann-Wood static limit. Substitution of Equation (5.1.1.2) into Equation (5.1.1.1) gives

$$\overline{P}_{MES} = \frac{1}{2K_{BGW}}\,\frac{\omega^2 VT\left|P_e\right|^2}{1+\omega^2 T^2}. \qquad (5.1.1.3)$$

Hence, mesoscale power per wave cycle is expressed in terms of the parameter of interest, the low frequency T coefficient.

(2) Power per wave cycle from microscale consideration is

$$\overline{P}_{MIC} = -\frac{1}{2}\,\mathrm{Real}\int \phi\left(\frac{\partial U^*}{\partial t} - \frac{\partial u^*}{\partial t}\right)\cdot \nabla p_f \;\mathrm{d}V, \qquad (5.1.1.4)$$

where u, U are solid and fluid displacements, respectively and * refers to complex conjugation.

The spatial gradient in fluid pressure ∇p_f can be related to relative fluid-solid displacement through Darcy's law given by

$$\nabla p_f = \frac{i\omega\phi\eta}{k}\left(U - u\right).$$

Here it is assumed that the displacements $\left(u, U\right)$ have time variations of the form: $\exp\left(i\omega t\right)$. Substitution of Darcy's law into Equation (5.1.1.4) gives

$$\overline{P}_{MIC} = -\frac{1}{2}\,\mathrm{Real}\int \phi\left(\frac{\partial U^*}{\partial t} - \frac{\partial u^*}{\partial t}\right)\cdot\left(\frac{i\omega\phi\eta}{\kappa}\left(U - u\right)\right)\mathrm{d}V = \frac{\omega^2\phi^2}{2\kappa}\int \eta\left(r\right)\left|U\left(r\right) - u\left(r\right)\right|^2\,\mathrm{d}V\,. \quad (5.1.1.5)$$

(3) The mesoscale power $\overline{P}_{MES}$ (Eq. (5.1.1.3)) is equated with the microscale power $\overline{P}_{MIC}$ (Eq. (5.1.1.5)) and rearranged so as to obtain the T coefficient:

$$T = \frac{\phi^2 K_{BGW}}{\kappa V\left|P_e\right|^2}\int dV \eta\left(r\right)\left[U^{(0)}\left(r\right) - u^{(0)}\left(r\right)\right]^2. \qquad (5.1.1.6)$$

Here Johnson defines an auxiliary function Φ by

$$\nabla\Phi = \frac{-\eta\left(r\right)\left(U^{(0)}\left(r\right) - u^{(0)}\left(r\right)\right)}{P_e}. \qquad (5.1.1.7)$$

(4) Upon taking the divergence of both sides of Equation (5.1.1.7) the potential equation central to APS theory is formed:

$$\nabla\cdot\left[\frac{-1}{\eta\left(r\right)}\nabla\Phi\right] = \frac{\left(\nabla\cdot U^{(0)}\left(r\right) - \nabla\cdot u^{(0)}\left(r\right)\right)}{P_e} = \frac{\left(E^{(0)}\left(r\right) - \varepsilon^{(0)}\left(r\right)\right)}{P_e} = g\left(r\right). \qquad (5.1.1.8)$$

Here the auxiliary function Φ is related to difference in solid and fluid static strains and

$$g\left(r\right) = \frac{\alpha\left({}^{1}\!/\!{}_{K_W} - {}^{1}\!/\!{}_{K_f\left(r\right)}\right)}{\alpha - \phi K_d\left({}^{1}\!/\!{}_{K_g} + {}^{1}\!/\!{}_{K_W}\right)}\,.$$

Numerical determination of the T coefficient and shape parameter

In this Chapter, I shall approximate Equation (5.1.8) by finite-differences. Once Φ has been approximated, it can be integrated with weight $g(r)$ to yield the low frequency coefficient of the saturated bulk modulus. That is

$$T = \frac{\phi^2 K_{BGW}}{\kappa V} \int g(r) \Phi(r) dV \, . \qquad (5.1.1.9)$$

To determine the shape parameter ζ, I substitute the numerically determined T coefficient into

$$\zeta = \frac{(\delta H_{BGH})^3}{2 K_{BGW} K_{BGH}^2 T G^2} \, , \qquad (5.1.1.10)$$

where

$$\delta = \frac{H_{BGH} - H_{BGW}}{H_{BGH}} \, .$$

By determining the surface to volume ratio of the fluid patches and substituting it into

$$G = \frac{\kappa K_{BGH}}{\eta_1 \sqrt{D_1} + \eta_2 \sqrt{D_2}} \frac{\int \left| \Delta p_f \right|^2 dS}{\left| P_e \right|^2 V} \, ,$$

the G coefficient can be obtained.

For the case of randomly distributed spheres, the surface to volume ratio is known exactly. However, when fluid distributions are more complicated it can be numerically extracted from the synthetic model of interest using Monte Carlo methods, or obtained from the derivative of the correlation function describing the fluid distribution.

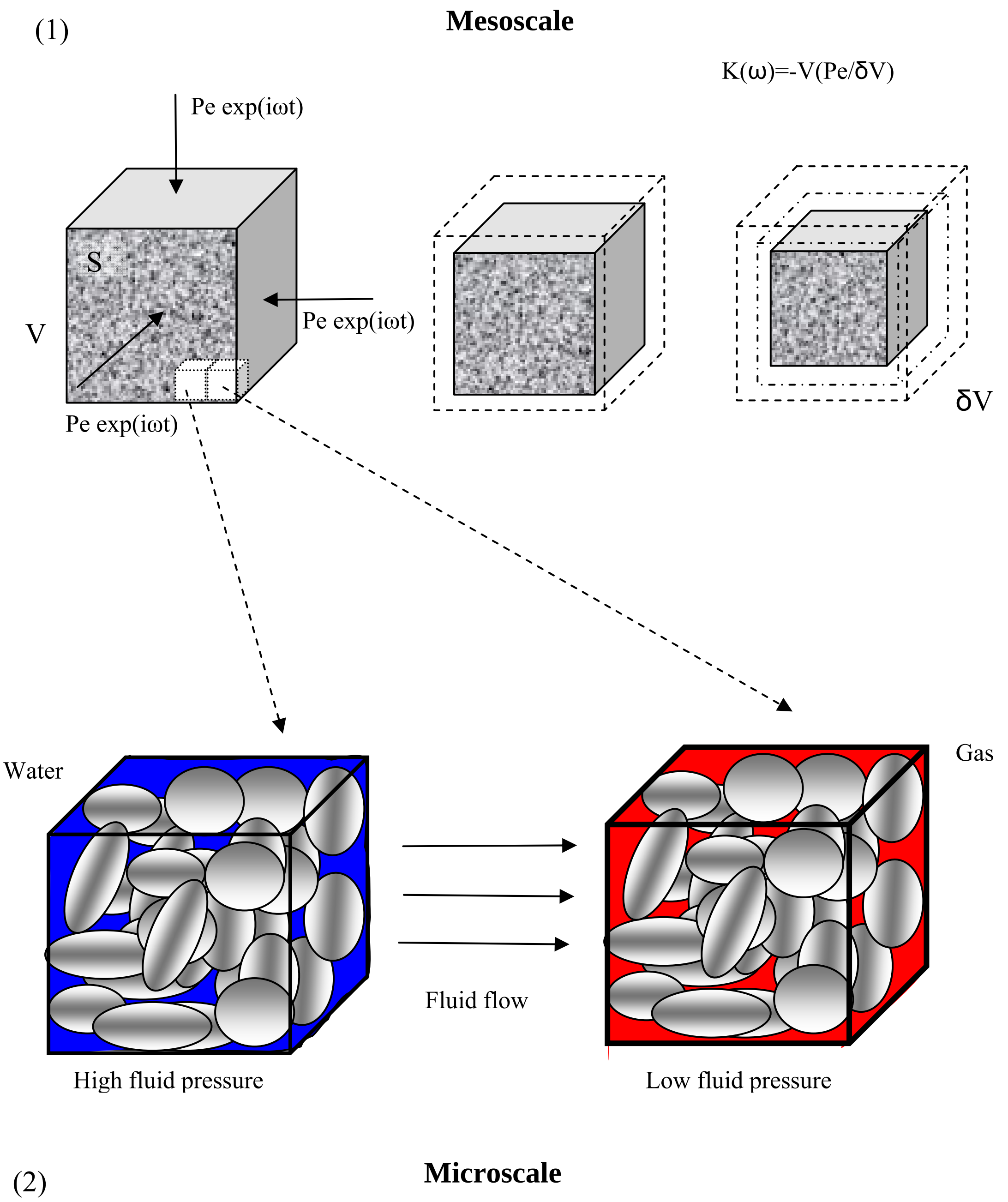

Figure 5.1.1.1: Schematic of the Johnson (2001) approach. Energy loss on the macroscale is equated with the volume average of losses due to fluid flow relative to the rock frame.

5.1.2 APS Potential Equations in 1, 2 and 3 Spatial Dimensions

The potential equation embedded in the APS framework (Equation 5.1.1.8) can be expanded to reveal spatial derivatives in viscosity and potential. For 1-dimensional fluid distributions:

$$-\frac{1}{\eta(x)}\left[\frac{d^2\Phi}{dx^2}\right]+\frac{1}{\eta(x)^2}\left[\frac{d\eta}{dx}\frac{d\Phi}{dx}\right]=g(x). \tag{5.1.2.1}$$

For 2-dimensional fluid distributions:

$$-\frac{1}{\eta(x,y)}\left[\frac{\partial^2\Phi}{\partial x^2}+\frac{\partial^2\Phi}{\partial y^2}\right]+\frac{1}{\eta(x,y)^2}\left[\frac{\partial\eta}{\partial x}\frac{\partial\Phi}{\partial x}+\frac{\partial\eta}{\partial y}\frac{\partial\Phi}{\partial y}\right]=g(x,y), \tag{5.1.2.2}$$

and 3-dimensional fluid distributions:

$$-\frac{1}{\eta(x,y,z)}\left[\frac{\partial^2\Phi}{\partial x^2}+\frac{\partial^2\Phi}{\partial y^2}+\frac{\partial^2\Phi}{\partial z^2}\right]+\frac{1}{\eta(x,y,z)^2}\left[\frac{\partial\eta}{\partial x}\frac{\partial\Phi}{\partial x}+\frac{\partial\eta}{\partial y}\frac{\partial\Phi}{\partial y}+\frac{\partial\eta}{\partial z}\frac{\partial\Phi}{\partial z}\right]=g(x,y,z). \tag{5.1.2.3}$$

As fluid viscosity can vary between the saturating fluids (often by several orders of magnitude), the spatial derivatives of viscosity specified in Equations (5.1.2.1-5.1.2.3) may not exist, because in general the viscosity variation is not a smooth function across the interface of two pore fluids. Hence, some sort of smoothing of the fluid viscosity is required along the fluid-fluid interface to make viscosity a smoothly varying function. However, when viscosity contrast is small, a simplified system of Equations detailed in the Section 5.1.3 can be useful.

5.1.3 APS Potential Equations with Small Fluid Viscosity Contrast

When contrast in fluid viscosity is small and thus can be considered negligible, spatial derivatives in viscosity are zero or small; thus $\eta(x,y,z)=\eta^*$ where η^* is an average viscosity. In these circumstances, Equations (5.1.2.1-5.1.2.3) reduce to Poisson's equations of the general form

$$\nabla^2\Phi=-\eta^* g(r) \tag{5.1.3.1}$$

where $r=r(x),r(x,y),r(x,y,z)$.

For 1-dimensional fluid distributions having only variations in fluid bulk moduli

$$\left[\frac{d^2\Phi}{dx^2}\right] = -\eta^* g(x). \tag{5.1.3.2}$$

For 2-dimensional fluid distributions

$$\left[\frac{\partial^2\Phi}{\partial x^2} + \frac{\partial^2\Phi}{\partial y^2}\right] = -\eta^* g(x,y), \tag{5.1.3.3}$$

and 3-dimensional fluid distributions

$$\left[\frac{\partial^2\Phi}{\partial x^2} + \frac{\partial^2\Phi}{\partial y^2} + \frac{\partial^2\Phi}{\partial z^2}\right] = -\eta^* g(x,y,z). \tag{5.1.3.4}$$

5.1.4 Boundary Conditions

The boundary conditions existing on Equations (5.1.2.1)-(5.1.2.3) are:

(1) Continuity of the potential across the interface between two media in contact. That is,

$$\Phi_1 = \Phi_2, \tag{5.1.4.1}$$

where 1 and 2 designate the potential within the porous rock saturated by fluid 1 and fluid 2, respectively.

(2) Continuity of relative flux of the potential across the boundary. That is,

$$\frac{1}{\eta_1}\frac{\partial\Phi_1}{\partial n} = \frac{1}{\eta_2}\frac{\partial\Phi_2}{\partial n}, \tag{5.1.4.2}$$

where *n* refers to the normal to the surface, whilst η_1, η_2 refer to viscosities of fluid 1 and fluid 2.

(3) As the medium is enclosed, there is a zero flux across the outer boundary

$$\frac{\partial\Phi}{\partial n} = 0 \text{ at } \Omega S. \tag{5.1.4.3}$$

The potential problem (Equations 5.1.2.1-5.1.2.3 with Equations 5.1.4.1-5.1.4.3) stands in direct analogy to a well known electrostatics problem of determining the electric field vector E in a material having varying dielectric constant κ and varying electric charge density ρ. The electric field E is expressible in terms of the electrostatic potential Θ as $E = -\nabla\Theta$ where the electrostatic potential satisfies the elliptical P.D.E given by $\nabla\cdot(-\kappa\nabla\Theta) = 4\pi\rho$ (Sneddon 1957; Johnson 2001).

In practice analytical solutions to the system of Equations (5.1.2.1-5.1.2.3 and 5.1.4.1-5.1.4.3) are obtainable for only the most simple geometries, such as periodic layering in 1D, concentric circles in 2D and concentric spheres in 3D (see Chapter 1, Section 1.4). I shall use the derived solutions to these simple idealised geometries to check the accuracy of my finite-difference solutions (refer to Section 5.3). Once the potential Φ is approximated, the T coefficient is determined by integration (Equation 5.1.1.9).

5.2 Basic Finite-difference Theory

In this section, I briefly introduce the theory utilized to develop the finite-difference solution of the APS potential equation. If further theoretical explanations are required, a good source of information can be found in Thomas (1990), Morten and Mayers (1988) and Ames (1977)

5.2.1 Finite-difference Approximations

To approximate the spatial derivatives in Equation (5.1.1.8), second order accurate centred finite-difference approximations are employed. The centred-difference approximation for the first spatial derivative of Φ with respect to the x direction is

$$\delta_0^{x_0}\Phi = \frac{\partial\Phi(x_0, y_0, z_0)}{\partial x_0} = \frac{\Phi(x_0+\Delta x, y_0, z_0) - \Phi(x_0-\Delta x, y_0, z_0)}{2\Delta x} + \mathrm{O}(\Delta x^2), \quad (5.2.1.1)$$

and the second derivative is

$$\delta_0^{2x_0}\Phi = \frac{\partial^2\Phi(x_0, y_0, z_0)}{\partial x_0^2} = \frac{\Phi(x_0+\Delta x, y_0, z_0) - 2\Phi(x_0, y_0, z_0) + \Phi(x_0-\Delta x, y_0, z_0)}{\Delta x^2} + O(\Delta x^2), \quad (5.2.1.2)$$

where x_0, y_0, z_0 are grid point locations and Δx is the grid size in the x direction. Here $\mathrm{O}(\Delta x^2)$ refers to the order of accuracy of the difference approximation, which is second order accurate. Similar approximations are employed for spatial derivatives in the y and z directions.

In effect, the application of finite-difference approximations to Equation (5.1.1.8) can be understood as taking a continuous spatial equation and converting it to a discrete spatial equation. Furthermore, it should be noted that approximations are made for each equation. Hence, finite-differences operate by approximating how the rate of change of the potential in one particular direction will vary with respect to the rate of change of the potential in another direction. This is in contrast with other numerical techniques, such as finite elements which seek to approximate the solution Φ directly.

5.2.2 Forming Difference Equations

In this section, I give the difference equations for 1D and 2D potential problems. They are formed by replacing the continuous spatial derivatives in Equations (5.1.2.1) and (5.1.2.3) with their discrete analogues given by Equations (5.2.1.1) and (5.2.1.2). The difference equation for the 3D potential problem will not be listed here, as it is very cumbersome to express.

When there are 1D heterogeneities in fluid bulk moduli and viscosity, the difference equation is:

$$\frac{-1}{\eta(x_0)}\left(\frac{\Phi(x_0+\Delta x)-2\Phi(x_0)+\Phi(x_0-\Delta x)}{\Delta x^2}\right)+\frac{1}{\eta^2(x_0)}\left(\frac{\eta(x_0+\Delta x)-\eta(x_0-\Delta x)}{2\Delta x}\right)\left(\frac{\Phi(x_0+\Delta x)-\Phi(x_0-\Delta x)}{2\Delta x}\right)=g(x)$$

(5.2.2.1)

The first bracketed term represents the second spatial derivative in potential, whilst the second bracketed term represents the first spatial derivative in viscosity, and the last bracketed term represents the first spatial derivative in potential. Hence, the second and third bracketed terms only contribute to the difference equation when neighbouring nodal points have different viscosities. Equation (5.2.2.1) can be rearranged to give

$$\Phi(x_0)=\frac{1}{2}(\Phi(x_0+\Delta x)+\Phi(x_0-\Delta x))+\frac{1}{8\eta(x_0)}(\eta(x_0+\Delta x)-\eta(x_0-\Delta x))(\Phi(x_0+\Delta x)-\Phi(x_0-\Delta x))+\frac{\eta(x_0)\Delta x^2 g(x_0)}{2},$$

(5.2.2.2)

Equation (5.2.2.2) shows that in the absence of viscosity gradients, the potential at some point x_0 depends only upon the average of the potentials at neighbouring points $x_0 - \Delta x$ and $x_0 + \Delta x$ and on the fluid properties of that point x_0. A quick inspection of this equation also shows that the boundary condition that the potential must be continuous across the interface separating the two different types of fluid can be satisfied when Δx approaches zero.

When there are two-dimensional heterogeneities in fluid bulk modulus and fluid viscosity, the difference equation is:

$$
\begin{aligned}
&\frac{-1}{\eta(x_0,y_0)}\left(\frac{\Phi(x_0+\Delta x,y_0)-2\Phi(x_0,y_0)+\Phi(x_0-\Delta x,y_0)}{\Delta x^2}+\frac{\Phi(x_0,y_0+\Delta y)-2\Phi(x_0,y_0)+\Phi(x_0,y_0-\Delta y)}{\Delta y^2}\right)\\
&+\frac{1}{\eta^2(x_0,y_0)}\left(\frac{\eta(x_0+\Delta x,y_0)-\eta(x_0-\Delta x,y_0)}{2\Delta x}\right)\left(\frac{\Phi(x_0+\Delta x,y_0)-\Phi(x_0-\Delta x,y_0)}{2\Delta x}\right)\\
&+\frac{1}{\eta^2(x_0,y_0)}\left(\frac{\eta(x_0,y_0+\Delta y)-\eta(x_0,y_0-\Delta y)}{2\Delta y}\right)\left(\frac{\Phi(x_0,y_0+\Delta y)-\Phi(x_0,y_0-\Delta y)}{2\Delta y}\right)=g(x_0,y_0). \qquad (5.2.2.3)
\end{aligned}
$$

Refer to Figure 5.2.2.1 for the geometrical layout of spatial derivatives of potential and viscosity. If the nodal points in the finite-difference grid are separated, such that $\Delta x = \Delta y = \Delta l$; Equation (5.2.2.3) can be rearranged to form:

$$
\begin{aligned}
\Phi(x_0,y_0)=&\ \frac{-1}{4}\left(\Phi(x_0+\Delta l,y_0)+\Phi(x_0-\Delta l,y_0)+\Phi(x_0,y_0+\Delta l)+\Phi(x_0,y_0-\Delta l)\right)\\
&+\frac{1}{16\eta(x_0,y_0)}\left(\eta(x_0+\Delta l,y_0)-\eta(x_0-\Delta l,y_0)\right)\left(\Phi(x_0+\Delta l,y_0)-\Phi(x_0-\Delta l,y_0)\right)\\
&+\frac{1}{16\eta(x_0,y_0)}\left(\eta(x_0,y_0+\Delta l)-\eta(x_0,y_0-\Delta l)\right)\left(\Phi(x_0,y_0+\Delta l)-\Phi(x_0,y_0-\Delta l)\right)-\frac{\eta(x_0,y_0)g(x_0,y_0)\Delta l^2}{4} \qquad (5.2.2.4)
\end{aligned}
$$

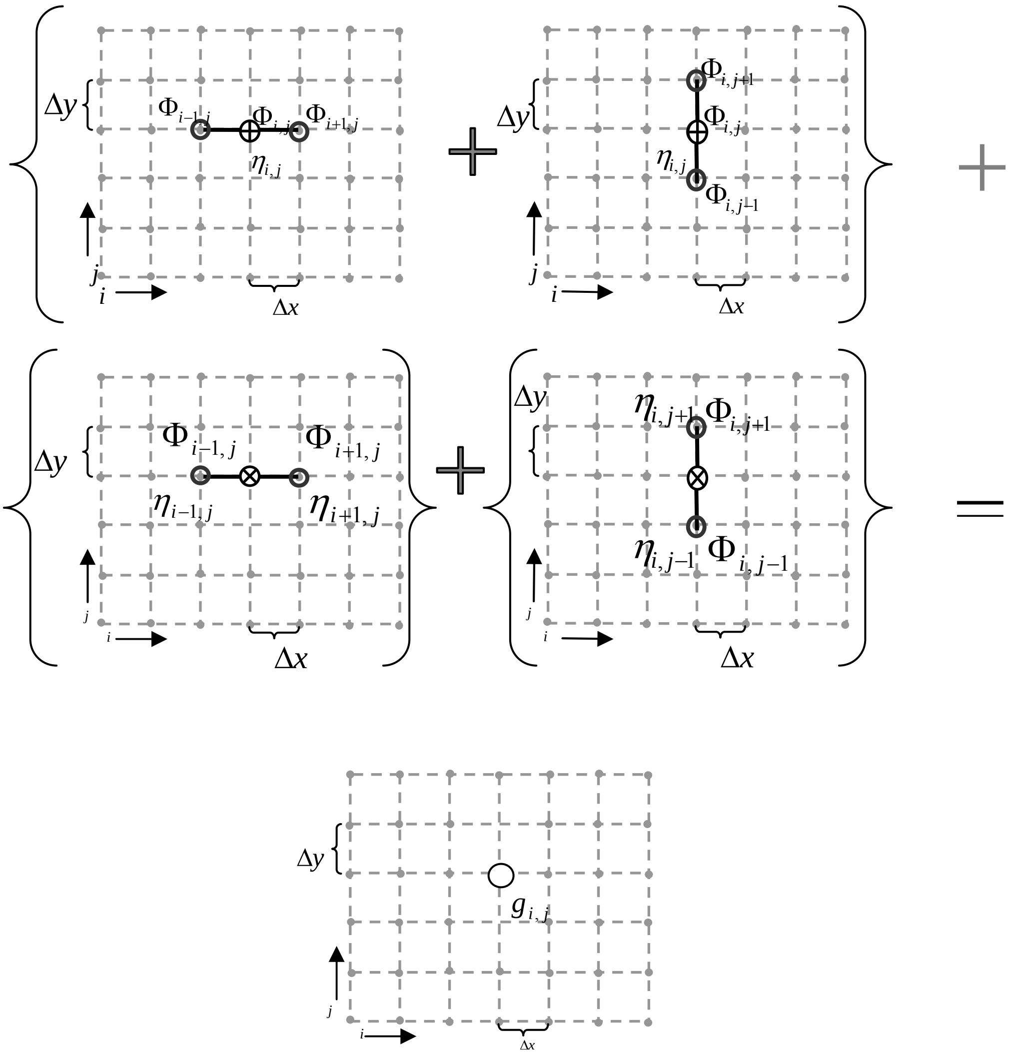

Figure 5.2.2.1: Showing the spatial location of the bracketed terms involved in the 2D difference equation (Equation 5.2.2.3). The first bracketed terms is the second spatial derivative in potential, we see that 5 potential values are utilized. The second bracket term represents the first spatial derivation in potential and viscosity in the x*-direction. The third bracketed term shows the first spatial derivation in potential and viscosity in the* y*-direction. The bottom grid shows where the location of the* g *coefficient is for this calculation.*

5.2.3 Implementing Boundary Conditions

The difference equations equivalent to no net-fluid flow boundary conditions (Equation 5.1.4.3) have the form:

$$\frac{\partial\Phi(x_1, y_1, z_1)}{\partial x} = \frac{\Phi(x_1 + \Delta l, y_1, z_1) - \Phi(x_1 - \Delta l, y_1, z_1)}{2\Delta l} = 0\,, \tag{5.2.3.1}$$

$$\frac{\partial\Phi(x_2, y_2, z_2)}{\partial y} = \frac{\Phi(x_2, y_2 + \Delta l, z_2) - \Phi(x_2, y_2 - \Delta l, z_2)}{2\Delta l} = 0\,, \tag{5.2.3.2}$$

where points (x_1, y_1, z_1) and (x_2, y_2, z_2) lie on boundaries parallel to the x and y axes, respectively. A similar difference equation can be formed for points lying on the boundary parallel to the z axes for 3-dimensional problems.

The easiest way of incorporating Equations (5.2.3.1 and 5.2.3.2) into the finite-difference schema is to align the boundary of the computational domain with the sample boundary (see Figure 5.2.3.1). When this is done, a series of “pseudo nodes” can be positioned outside the computational domain. These nodes assume values which enable Equations (5.2.3.1 and 5.2.3.2) to be satisfied. That is,

$$\Phi_P(x_1 + \Delta l, y_1, z_1) = \Phi(x_1 - \Delta l, y_1, z_1), \tag{5.2.3.3}$$

$$\Phi_P(x_2, y_2 + \Delta l, z_2) = \Phi(x_2, y_2 - \Delta l, z_2), \tag{5.2.3.4}$$

where Φ_P are pseudo nodes for boundary points (x_1, y_1, z_1) and (x_2, y_2, z_2).

Equations (5.2.3.3) and (5.2.3.4) indicate that the value taken by a pseudo node is the same as the value of the node nearest to the boundary, see Figure 5.2.3.1. The value of the potential $\Phi(x_1, y_1, z_1)$ at the boundary node can then be calculated using Equation (5.2.2.4) with one true (interior) node and one pseudo node.

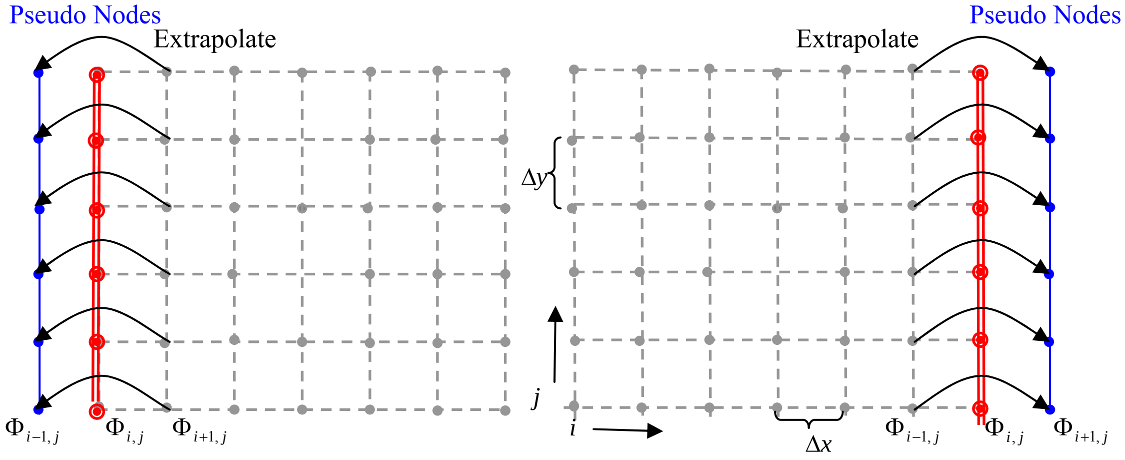

Figure 5.2.3.1: Application of no-net flow boundary conditions in the finite-difference schema. The no-net flow boundary conditions (red) are implemented on the edge of the inner computational domain, whilst pseudo nodes (blue) are placed outside the computational domain. The pseudo nodes assume the value of the potential immediately before the boundary.

5.2.4 Solution of Difference Equations

When centred-difference operators are substituted into the APS potential equation, the resulting finite-difference schema will be implicit. This means that the potential at points interior to the boundary can only be determined by solving a simultaneous set of linear algebraic equations, given by

$$Cu = v \,. \tag{5.2.4.1}$$

Here C is a square matrix of known coefficients, u is a column vector of unknown potential values and v is a column vector of known values. This type of schema is in contrast to schemas generated from hyperbolic (wave) and parabolic (diffusion) partial differential equations, which can take an explicit form for a particular choice of difference operators. That is, for wave equation schemas, its variables (particle displacements, particle velocities or stresses etc) at the newest time level can be solved for directly from previous values, at earlier time levels.

The implication of having an implicit finite-difference schema is that an extra step is generally required in order to obtain a solution. That is, for most practical problems the automatic solution to an implicit difference schema is not feasible, as it will require the inversion of a massive sparse tri-diagonal matrix, which certainly is the case for my APS application.

To circumvent this problem, I use successive over relaxation (SOR). This technique was developed by Frankel (1950) and Young (1954). To apply this technique, the order in which computations are performed through out the computation domain must be defined (using Equations 5.2.2.2 and 5.2.2.4). It is necessary to define an order because newly calculated nodes are used to update surrounding nodal points during future computations. I choose to perform computations throughout the grid along all columns of a particular row going from left to right. I start at the bottom-most row first and finish at the top row last. See Figure 5.2.4.1. A similar idea is applied for the 3D mesh.

Like the Gauss-Seidel method (Seidel 1874), SOR is an iteration technique that immediately utilizes the latest value of the iterant potential to calculate future values of the other potentials. The difference between the two approaches is that SOR includes a damping step. This step takes the new value of the potential Φ_{NEW} to be a weighted average of the old potential Φ_O and the latest calculated potential Φ_U according to

$$\Phi_{NEW} = \lambda_{dc}\Phi_U + (1 - \lambda_{dc})\Phi_{OLD}\,, \qquad (5.2.4.2)$$

here λ_{dc} is the damping coefficient.

This step is incorporated to reduce the number of iterations required for convergence to the solution. When $\lambda_{dc} = 1.0$ the method reduces to being Gauss-Seidel, when $\lambda_{dc} < 1.0$ it is termed under relaxation and when $\lambda_{dc} > 1$ the method is over-relaxed. SOR is convergent for $0 < \lambda_{dc} < 2$ (Morten & Mayers 1995). I generally use the value $\lambda_{dc} = 1.6$. Further experiments may be useful to determine the value of the damping coefficient that will optimise the rate of convergence.

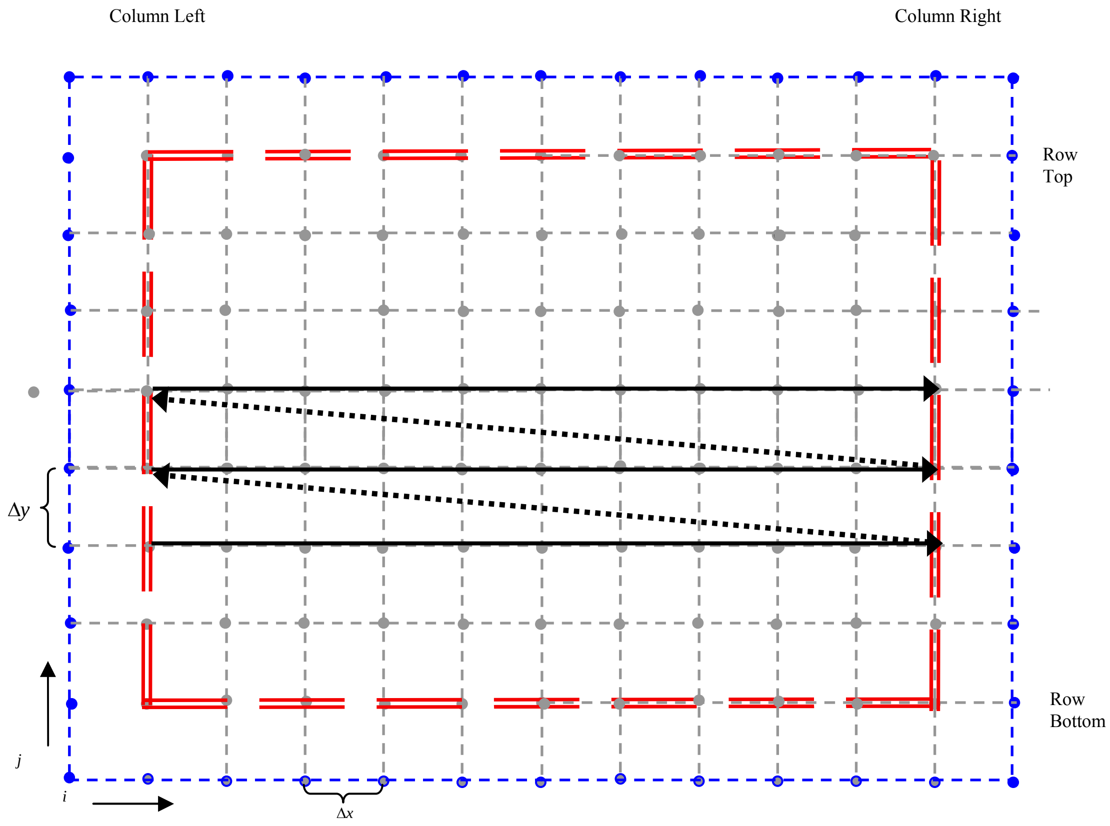

Figure 5.2.4.1: The order in which finite-difference computations are performed over the 2D grid. The computation starts at (bottom row-column left) and continues across the row until column right. Then computations start at row immediately above and continue across the row until column right etc.

5.2.5 Errors

In theory, any discrepancy existing between the finite-difference solution and the analytical solution arises because of error accumulation. For the finite-difference solution, the main sources of error can be categorized as:

(1) Differentiation errors: those arising because spatial approximations have been made to the spatial derivatives in potential and viscosity.
(2) Boundary errors: those arising because of inaccurate implementation of Neumann boundary conditions on the edge of the cell.
(3) Medium errors: those arising because of the discretisation of the synthetic model.
(4) Iteration errors: those arising because not enough SOR iterations are performed.

Clearly, it is of interest to develop the most accurate finite-difference solution possible; however it is also important to be pragmatic.

For instance, differentiation errors (1) can be minimized by utilizing higher order finite-difference operators, such as 4th or 8th order etc; however implementation of 4th or 8th order operators requires the potential to be calculated from a greater number of surrounding nodal point potentials. This in itself is not difficult to implement, however one must be consistent and also implement 4th order no net fluid flow conditions. Otherwise, there are no accuracy gains from using higher order finite-difference operators, as the accuracy of the schema is determined by the lowest accuracy of any component, such as a boundary condition (Thomas 1995). This occurs because the solution obtained from the boundary is propagated back into the interior computational domain by the finite-difference schema.

So, if I choose 4th order accurate finite-difference operators in the interior computational domain, then I am committed to also choosing 4th order accurate no net fluid flow boundary conditions. In order to implement the boundary conditions having 4th order accuracy, more pseudo nodes are required external to the interior computational domain.

The issue with introducing more pseudo nodes is that for a fixed number of possible computational points, which is 300x300x300 (system restriction) less computational points become available to the interior computational domain. Consequently, coarser finite-difference grids are required, thus the grid spacing increases, which decreases the accuracy of the difference operator and also causes discretisation errors of the synthetic model. Hence, in trying to fix one sort of error, other errors may be introduced.

My finite-difference schema has:

(1) Second order accurate finite-difference operators
(2) Second order accurate implementation of the boundary conditions.
(3) Smallest feasible grid spacing

5.3 Testing of the Algorithm

In this section I test the accuracy of the finite-difference algorithm against known analytical results. The input to the finite-difference algorithm is different 1D, 2D and 3D synthetic models; they digitally represent viscosity and fluid bulk modulus spatial variation. In 1D, the synthetic models generated are layered with periodic repetition. In 2D, models are generated consisting of circular inclusions (of uniform radius) that are distributed periodically and randomly (with and without overlap). In 3D, the algorithm is tested against the concentric sphere model of White (1975).

By testing the finite-difference algorithm like this, the strengths and weaknesses of the approach can be identified. This enables the algorithm to be applied accurately in Section 5.5, when the shape parameter is determined for a 3D random distribution of spherical inclusions.

5.3.1 1-Dimensional: Periodic Layering

Potential

In this section, I compare an analytical solution derived to the potential equations (Equations (5.1.3.2) and (5.1.2.1)) against the solution from the finite-different schema (incorporating difference Equation (5.2.2.2), boundary conditions (B.C) and SOR). The schema has a grid spacing of $\Delta x = 0.01m$. Layer properties are given in Table 5.3.1.1. The effect that viscosity variation has on the finite-difference schema is examined by trialling different layer viscosities.

Table 5.3.1.1: Parameters for FD computation of auxiliary function

	Properties	Layer 1	Layer 2
	Layer thickness (L_i)	3	4
	$g(r)$	1e1	$\frac{-g_1 L_1}{L_2}$
Case One	$\eta(r)$	1e-3	1e-3
Case Two	$\eta(r)$	1e-3	0.4e-4
Case Three	$\eta(r)$	1e-3	1e-5

Case One: there is no variation in fluid viscosity between the layers. Figure 5.3.1.1 shows that the finite-difference solution Φ_{FD} corresponds exactly with the analytical solutions given by Φ_1 and Φ_2 (in Layers One and Two), respectively. This shows that in the absence of fluid viscosity contrast, the 1D finite-difference schema is very accurate.

Case Two: Both layers have different viscosities; all other properties are the same as Case One. Figure 5.3.1.2 shows discrepancies between the finite-difference solutions Φ_{FD} and the analytical solutions Φ_1 and Φ_2 (in Layers One and Two). These discrepancies occur because Equation (5.1.2.1) requires viscosity to be smooth spatial function, and hence when the value in the viscosity jumps, the viscosity derivative does not exist. Thus the finite-difference solution $\Phi_{FD}(noSmoothing)$ becomes very inaccurate. Moreover, as the magnitude of the viscosity jump increases, the finite-difference solution $\Phi_{FD}(noSmoothing)$ became non-convergent. This source of error can be reduced by averaging the viscosity over a few nodal points which has the effect of making the viscosity a smooth spatial function. When the viscosity is smoothed across the interface, the finite-difference solution $\Phi_{FD}(Smoothing)$ corresponds reasonably well to the analytical solutions.

Case Three: The viscosity variation across the layer interface is increased, whilst all other properties are kept the same. In this example, I study different ways of averaging the viscosity across the interface in order to see what works best. Two different methods are tried. The first method utilizes the same type of smoothing applied to the layer interface as in the previous example. It is simple logarithmic averaging over a number of nodal points. That is, I take the logarithm of the viscosity values and then average these values over a certain number of nodal points. I then take the exponential of the averaged nodal values to obtain the viscosity smoothing. The other approach trialled is to convert the viscosity to a smoothly varying function, such as a $\tanh$ function. Figure 5.3.1.2 (a) shows the viscosity smoothing (of both approaches) as a function of position. Clearly fitting a smoothly varying function like the $\tanh$ function to the viscosity will provide the smoothest spatial variation.

Figure 5.3.1.2 (b) shows the finite-difference solutions for both types of viscosity smoothed media. The finite-difference computation obtained by using the log smoothing method $\Phi_{FD}(\log smoothing)$ follows the analytical solutions Φ_1 and Φ_2, closely. The finite-difference solution $\Phi_{FD}(\tanh smoothing)$ of the $\tanh$ smoothed viscosity medium does not follow the exact solutions as closely.

The above examples indicate that the 1D version of the finite-difference schema can provide an accurate approximation for the potential of layered media, providing that fluid viscosity contrast is treated carefully.

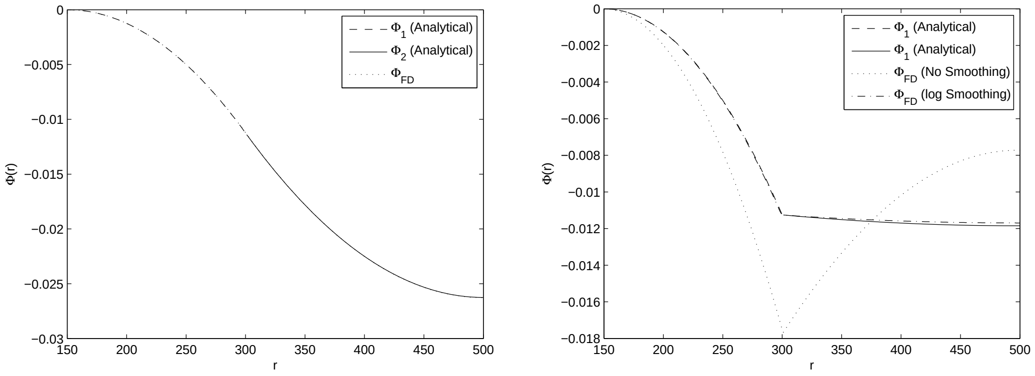

(a) (b)

Figure 5.3.1.1: Analytically and numerically determined potentials for periodic layering. (a) no viscosity variation and (b) with viscosity variation.

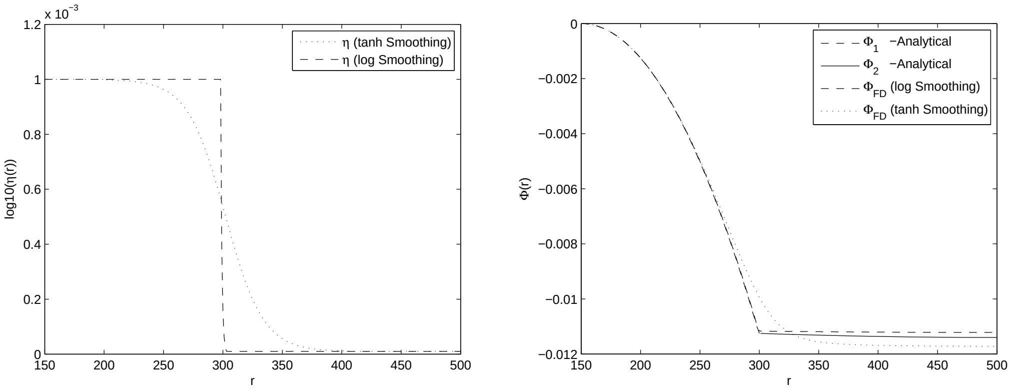

(a) (b)

Figure 5.3.1.2: The influence of viscosity variation on the potential derived from analytical and finite-difference solutions. (a) Shows two different techniques used to smooth viscosity in the vicinity of the layer interface. Here viscosity variation between layer one and layer two differ by two orders of magnitude. (b) Shows the potential determined from the exact solution and the finite-difference solution.

Shape Parameter-Low Fluid Contrast

According to Equation (5.1.1.9) the shape parameter can be determined by numerically integrating the potential with weight g. For periodic layering, I compare the numerical estimate of the shape parameter against both the exact analytical shape parameter (determined by substituting Equation 1.3.2.5 into Equation 1.3.2.13), and against the low contrast approximate shape parameter (Equation 4.2.1.3). The rock and fluid properties are shown in Tables 5.3.1.2 and 5.3.1.3. The focus of this series of tests is to examine how grid spacing affects the convergence of the finite-difference solution to the exact solution. The damping coefficient was set at 1.6 for this series of tests.

Table 5.3.1.2: Rock properties for finite-difference models

K	7 GPa	K_g	35 GPa	ϕ	0.08
μ	9 GPa	ρ_g	2650 kg/m^3	κ	1e-13 m^2

Table 5.3.1.3: Fluid properties for low contrast finite-difference models

K_{fw} Water	2.25 GPa	K_f Low Contrast	2.0 GPa
ρ_w	990 kg/m^3	ρ	990 kg/m^3
η_w	1e-3 Pa s	η	1e-3 Pa s

In Figure 5.3.1.3 the shape parameter constructed using the analytical solution is compared against the shape parameter constructed using the finite-difference solution. The model assumes that there is periodic layering of water and another slightly more compressible fluid, such that fluid bulk moduli contrast between the layering is small. In (a) the grid spacing was set at $\Delta x = 0.01m$ and the maximum number of iterations was $\max N = 50k$. The shape parameter constructed from the finite-difference solution (solid line with dots) at low water saturations scatters around the exact solution (solid line with plus signs). However at large water saturations the finite-difference solution has converged to the exact solution.

In Figure 5.3.1.3 (b) the grid spacing was reduced to $\Delta x = 0.001m$ and the maximum number of iterations was kept at $\max N = 50k$. Clearly, the finite-difference solution (solid line with dots) at low water saturations has converged to the exact solution (solid line with plus signs), but at larger water saturations (>30%) it is not converging to the exact solution. This indicates that when the grid spacing is fine more iterations are required for the finite-difference solution to converge to exact solution at large water saturations.

In Figure 5.3.1.3 (c) the grid spacing was kept at $\Delta x = 0.001m$ and the maximum number of iterations was increased to $\max N = 350k$. The figure shows that the finite-difference solution has now converged to the exact solution for all water saturations less than 83%.

These tests indicate that rapidity at which the finite-difference solution converges to the exact solution depends on the grid spacing. Moreover, a coarse grid will require fewer iterations to converge to the solution for large water saturations, whereas at low water saturations fewer iterations of a finer grid are required for convergence. Perhaps by altering the damping coefficient, the efficiency of the convergence of the finite- difference solution to the exact solution can be improved (although this was not tested here). In the next section I will show that the speed of convergence also depends on fluid contrast.

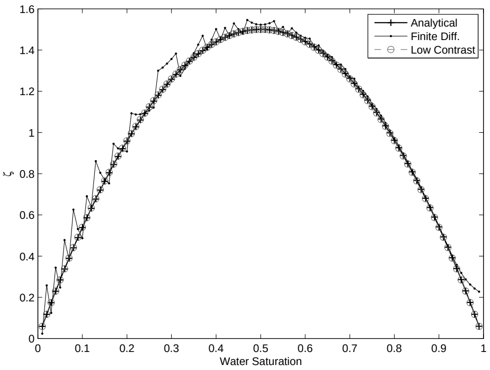

(a)

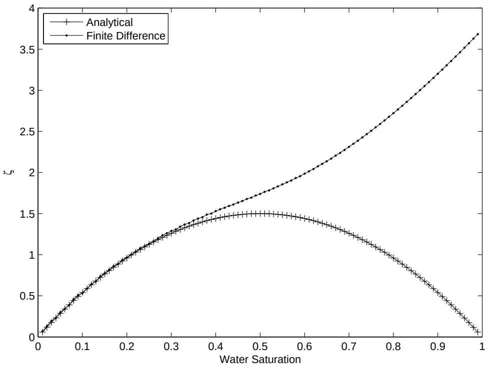

(b)

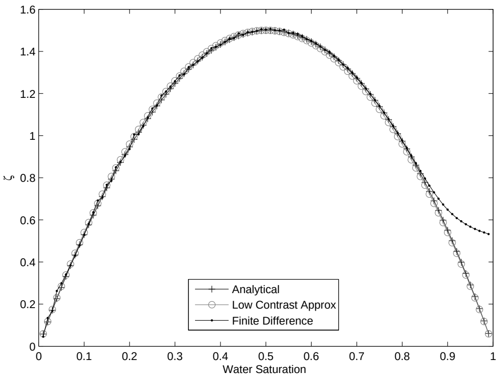

(c)

Figure 5.3.1.3: Shape parameters (analytical and numerical) for periodic layered media of low fluid contrast at different water saturations. (a) Shows coarse grid and (b) fine grid, both with a maximum number of iterations of $\max N = 50k$ *. (c) Shows fine grid* $\Delta x = 0.001m$ *with max number of iterations* $\max N = 350k$ *.*

5.3.2 Two-dimensional: Circular inclusions

In this section, the numerical shape parameter calculated using the 2D finite-difference schema is compared against an analytical shape parameter over analogous 2D models (see Figure 5.3.2.1). Specifically, the numerical shape parameter is calculated for a circular inclusion centred within a square, whilst the analytical shape parameter is calculated for a circular inclusion centred within a circle. The rock properties are given in Table 5.3.1.2 and the host fluid has the properties of water listed in Table 5.3.1.3. For this set of tests, two aspects are examined for water saturations greater then 50%:

(1) whether no net fluid flow boundary conditions imposed on the outer boundary of the square and circle will have a significant effect on the shape parameter.
(2) supposing that the solutions in (1) are in reasonable agreement; whether contrast in fluid bulk moduli and viscosity will affect the finite-difference accuracy.

Figure 5.3.2.2 shows the numerical shape parameter (asterisks) obtained from solving the finite-difference problem over a square grid containing a circular inclusion of a different fluid. The fluid inside the circular inclusion is more compressible than the fluid external to the inclusion; however there is not a large difference between fluid compressibilities (nor viscosities). This problem is solved at different water saturations, by varying the size of the square. The resolution of the grid spacing was $\Delta x = 0.01\mathbf{m}$ and the maximum number of iterations was $\max N = 50k$. Also shown is the exact analytical shape parameter (dashed line) for the concentric circle fluid distribution model of Krzikalla et al. (2006). Over a very wide range of water saturations, the two solutions are in good agreement. This indicates that although the no-net fluid flow boundary condition is applied to straight and circular boundaries, it has little effect on the 2D solutions.

Figure 5.3.2.3 (a) shows the numerical shape parameter and the analytical shape parameter as discussed in the previous example. However, the fluid properties of the inclusion change to a two order of magnitude difference in the bulk modulus of the inclusion relative to water (ie the inclusion becomes more compressible $Kf_i = 0.01GPa$) and a one order of magnitude difference in viscosity relative to water ($\eta_i = 0.1\mathbf{mPa\,s}$). There are large differences between the numerical and analytical shape parameters for water saturations greater than five percent.

In Figure 5.3.2.3 (b) the resolution of the grid spacing increases $\Delta x = 0.002\mathbf{m}$ and the max number of iterations increased ($\max N = 90k$), good agreement between the shape parameters was achieved over a wide range of water saturations. This indicates that the discrepancies in shape parameter estimates observed in Figure 5.3.2.3 (a) can be attributed to finite-difference resolution and convergence errors, rather then boundary effects. Moreover, it is important increase resolution and maximum number of iterations when modeling significant contrasts in fluid properties.

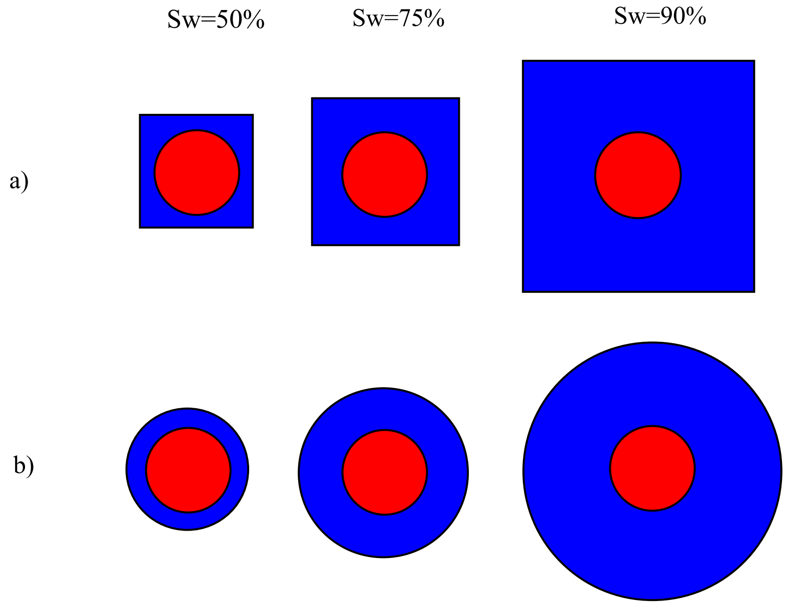

Figure 5.3.2.1: Analogous 2D models for different water saturations. (a) Shows circular inclusions of gas within an otherwise water saturated square. (b) Shows the concentric circle model.

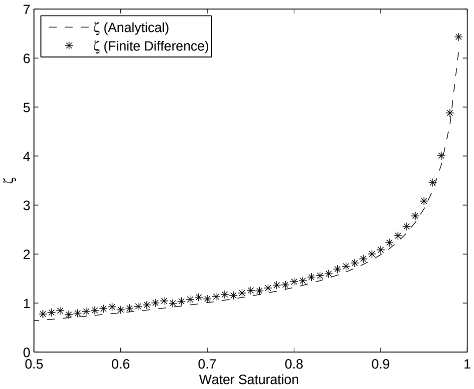

Figure 5.3.2.2: Numerical and analytical shape parameters for low contrast 2D model analogues. The numerical and analytical shape parameters are in good agreement at low fluid contrast even though the shape of each boundary (upon which B.C are applied) are different. Computations were performed with grid resolution $\Delta x = 0.01\mathbf{m}$ *and maximum number of iterations* $\max N = 50k$ *.*

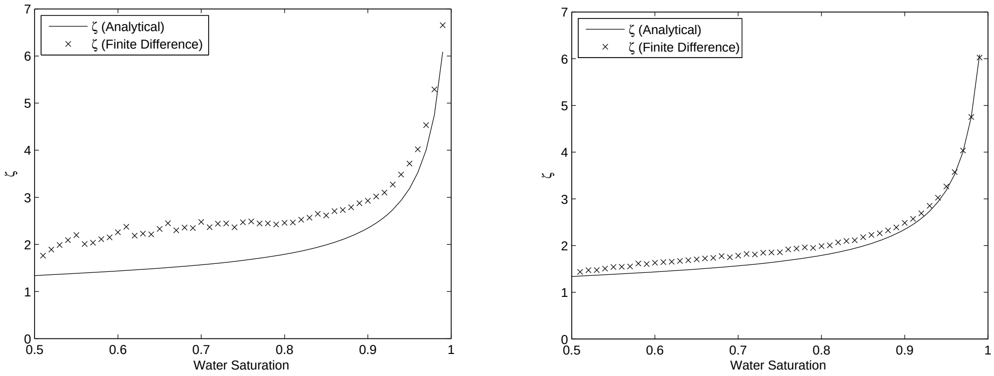

(a) (b)

Figure 5.3.2.3: High fluid contrast with one order of magnitude difference in viscosity. (a)The numerical and exact shape parameters differ significantly at water saturations greater than 10 percent, with grid resolution $\Delta x = 0.01\mathbf{m}$ *and maximum number of iterations* $\max N = 50k$ *. (b) Analytical and numerical shape parameters at increased resolution* $\Delta x = 0.002\mathbf{m}$ *and maximum number of iterations* $\max N = 90k$ *. There is good agreement between the shape parameters curves.*

5.3.3 Three-dimensional: Spherical inclusions

> “*You boil it in sawdust; you salt it in glue;*
> *You condense it with locusts and tape;*
> *Still keeping one principal object in view*
> *To preserve its symmetrical shape*”
>
> Lewis Carroll

White’s concentric sphere model is a geometry which has been utilized extensively in the literature to approximate the geometry of a sphere centred within a cube, see Figure 5.3.3.1. The reason for this is that partial differential equations etc usually have an analytical solution for the concentric sphere model, but not for a sphere centred within a cube. Recently in the literature (e.g like Vogelaar & Smeulders 2007) there has been some debate regarding the validity of making a concentric sphere approximation for wave induced fluid flow problems. Of which two concerns are raised. The first being that the concentric sphere model is a poor approximation to a “sphere within a cube” due to the different shaped boundaries, and secondly, that the no net fluid flow boundary condition imposed on the outer surface of the sphere is too restrictive.

In this section, I shall address the first concern. That is, I will test the analytical solution for the concentric sphere shape parameter, against a numerically estimated shape parameter for an equivalent sphere within a cube model.

The spatial resolution of the finite-difference grid is $\Delta x = 0.005m$ and the max number of iterations is $\max N = 50k$. A fluid of compressibility of $Kf_i = 0.01GPa$ saturates the spherical inclusion, whilst the host fluid has the compressibility of water. As significant viscosity variations can affect the accuracy of the finite-difference solution, I remove this possible source of error, by assuming that both fluids have the viscosity of water. The rock parameters are given in Table 5.3.1.3.

Figure 5.3.3.1 shows that the analytical solution (solid line) for the concentric sphere shape parameter is in good agreement with the numerical shape parameter (asterisks) for an equivalent sphere within a cube model. This favourable agreement extends over a wide range of water saturations and hence models configurations. Although not shown here, similar agreement was observed for a variety of inclusion-host fluid contrasts. Also shown are the shape parameter bounds for randomly distributed overlapping (see Section 4.3.2.2) and non-overlapping spheres (Equation 4.3.1.8). Finite-difference analysis of the randomly distributed non-overlapping spheres model will be delayed till Section 5.3.5.

This study indicates that the concentric sphere approximation utilized by White (1975) to simplify the mathematics and adopted widely (Johnson 2001; Pride et al. 2004) will provide a good approximation to the sphere within a cube for patchy fluid saturation problems.

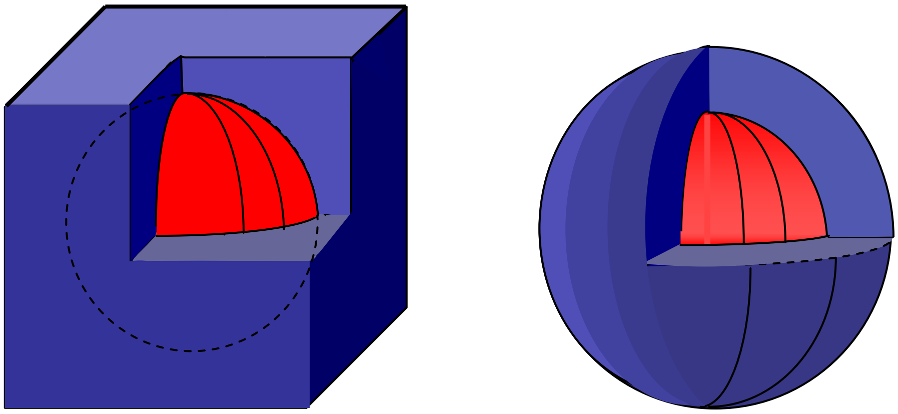

(a) (b)

Figure 5.3.3.1: Analogous 3D models: sphere within a cube and concentric spheres. (a) Spherical gas inclusion (red) situated in the centre of a cubical volume containing water (blue). (b) The concentric sphere approximation, which assumes that the cubical volume of water can be replaced by a spherical volume of water. This geometrical approximation was first utilized by White (1977).

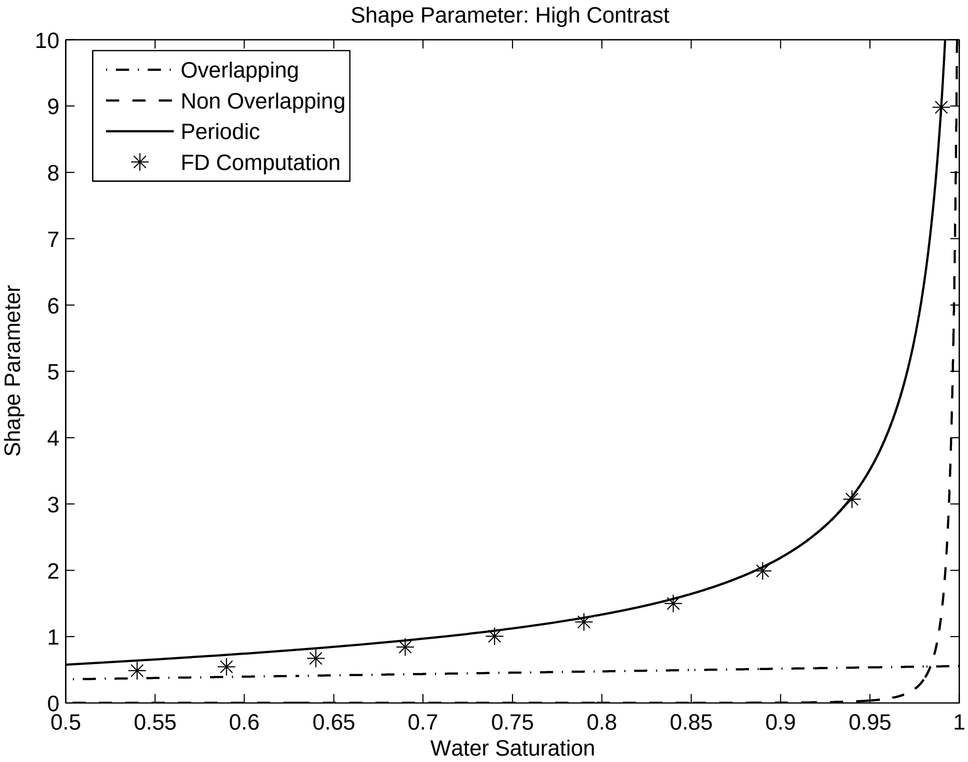

Figure 5.3.3.2: Comparison of shape parameters for the analytical concentric sphere model and the sphere with a cube geometry.

5.4 3D: Random Distribution of Non-overlapping Spheres

Three-dimensional synthetic models of randomly positioned non-overlapping spheres have been generated using the Random Sequential Addition (R.S.A) process (Torquato 2002). I extract statistical measures, such as the correlation function and correlation length from the synthetic models, using algorithms similar to those developed in Chapter 2, but extended appropriately for 3D analysis. My reason for doing this is to access whether the synthetic models generated provide an accurate statistical representation of randomly positioned spheres. By doing this, I can access whether any discrepancies between the numerically determined shape parameters and the analytical shape parameters can be attributed to the synthetic media utilized as input to the finite-difference code.

5.4.1 Random Sequential Addition

The non-overlapping sphere models have been generated using the random sequential addition process (R.S.A). A random distribution of spheres is created by randomly inserting a sphere into the volume, such that the sphere doesn't overlap with any previous spheres already inserted. As the process of sequentially adding spheres continues, the volume fraction of inclusions increases until no further spheres can be added to the volume without causing overlap. Numerical experiments have shown that for two-dimensional media the largest volume fraction of inserted disks is approximately 0.547 (Feder 1980), whilst in three dimensions the largest volume fraction of spheres is approximately 0.38 (Cooper 1988). Here I generate volume fractions of spherical inclusions much less than this limit, restricting computations to volume fractions of 31% or less.

In general, random distributions of disks or spheres generated using the RSA process produce configurations which are not in "equilibrium". That is, the spheres do not sample the configuration space uniformly, thus resulting in smaller maximum inclusion fractions and possible anisotropy (Torquato 2002).

5.4.2 The Synthetic Models

It is necessary to build models having different volume concentrations of inclusions v_1. The fraction of the volume occupied by the spheres is given by

$$v_1 = \frac{4}{3} n_{sp} \pi \left(\frac{R_1}{L_B} \right)^3$$

where n_{sp} is the total number of spheres of radius R_1 added to a cubic volume of side length L_B. There are a number of different methods of applying RSA such that different volume fractions of inclusions can be generated. Two approaches are explored here. In the first approach a fixed number of spheres n_{sp} is added to cubic volumes of different sizes. That is, higher volume concentrations of inclusions are generated by reducing the length size L_B (unit of Δx) of the cubic volume, whilst smaller volume concentrations of inclusions are generated by increasing the length size of the cubic volume.

Figure 5.4.2.1 and 5.4.2.2 show typical RSA configurations of non-overlapping spherical inclusions at volume fractions of 0.11 and 0.21. Both models have 50 spheres of radius 0.1. The volume fraction of each model is obtained by randomly adding 50 spheres to different sized cubes, thus larger volume fractions are achieved by using smaller and smaller cubes.

The second approach of generating different volume fractions of inclusions fixes the length size L_B (unit of Δx) of the cubic volume, but varies the number of spheres added. That is, small volume concentrations of inclusions are achieved by adding fewer spheres to the cubic volume than for larger volume fractions (see Figure 5.4.2.3). This approach was found to generate synthetic models which are better statistical representations of randomly positioned non-overlapping spheres.

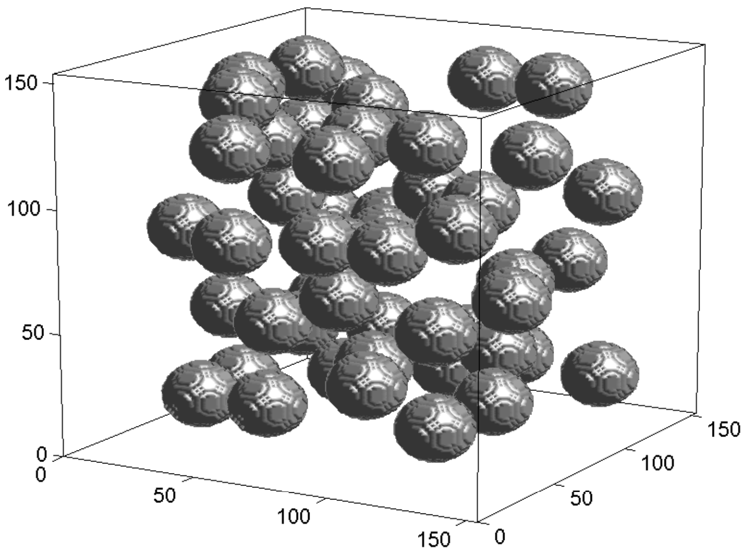

Figure 5.4.2.1: Fifty randomly positioned non-overlapping spheres of radius =0.1, inclusion concentration is 11 %. The cube has a side length of $L_B = 1.234\,\mathrm{m}$ *and the discretisation is* $\Delta x = 0.008$

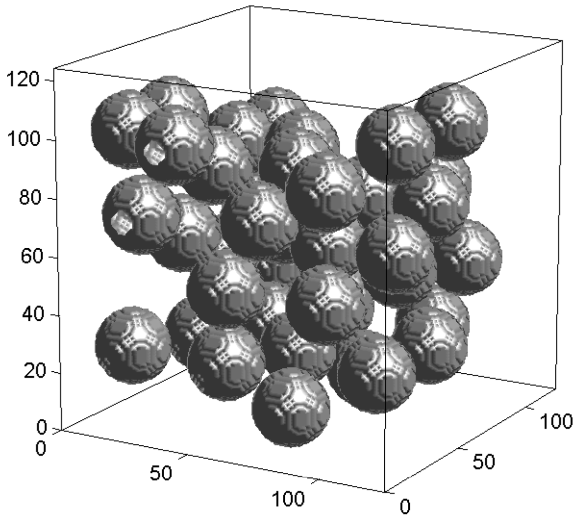

Figure 5.4.2.2: Fifty randomly positioned non-overlapping spheres of radius =0.1, inclusion concentration is 21%. The cube has a side length of $L_B = 0.999\,\mathrm{m}$ *and the discretisation is* $\Delta x = 0.008$

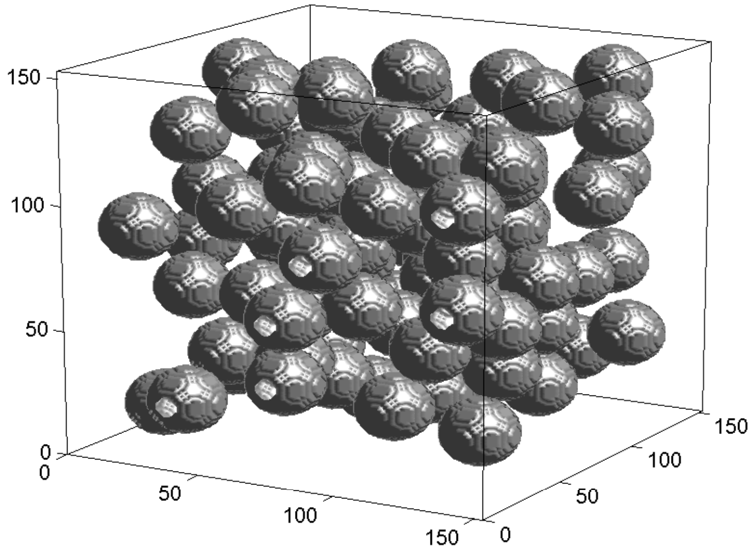

Figure 5.4.2.3: Ninety-four randomly positioned non-overlapping spheres of radius =0.1, inclusion concentration is 21%. The cube has a side length of $L_B = 1.234\,\mathrm{m}$ *and the discretisation is* $\Delta x = 0.008$

5.4.3 Statistical Properties

The two point probability density function is extracted from the models using the process detailed in Section 2.3.1. Each model is sampled in three orthogonal directions with the resulting two point probability density function given by the average of each orthogonal contribution. The normalised correlation function is derived from the two point probability function using

$$X(r)=\frac{S_2(r)-v_1^2}{v_1 v_2}.$$

As finite-dimensional models are used, periodic boundary conditions are applied to each surface of the cube. This has the affect of reducing probability errors, which affect the accuracy of the two point probability density function at long offsets. The addition of periodic boundary conditions can be implemented by adding a replica of the cubic volume to each surface of the cube. This has the affect of preserving the statistical properties of the original cubic volume. Another approach is to map spheres across the boundaries, such that a sphere close to $x \to x_n$ continues at x_1. This approach to replicating random distributions of spheres is not utilized here, as it will make implementation of no net flow boundary conditions (Equation 5.1.4.3) on the edge of the computational domain more complicated (see Section 5.2.3).

Figure 5.4.3.1 (a) shows the two point probability density function extracted from the random spheres models having volume concentrations of 0.01, 0.06, 0.11, 0.16, and 0.21. Figure 5.4.3.1 (b) Shows the normalised correlation function derived from the two point probability function. For these synthetic models, the side length of the cubic volume was fixed at $L_B = 2.95\,\mathrm{m}$, the model was discretised at a resolution of $\Delta x = 0.01\,\mathrm{m}$, and the sphere radius was $R_1 = 0.1\,\mathrm{m}$

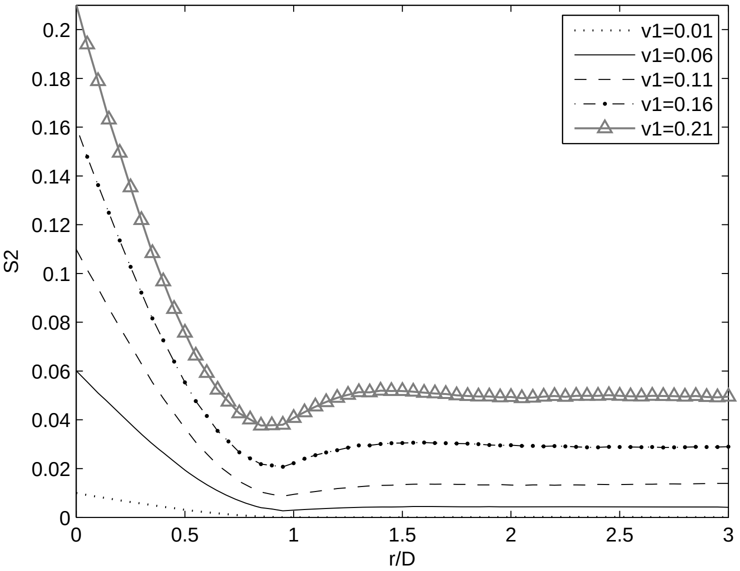

(a)

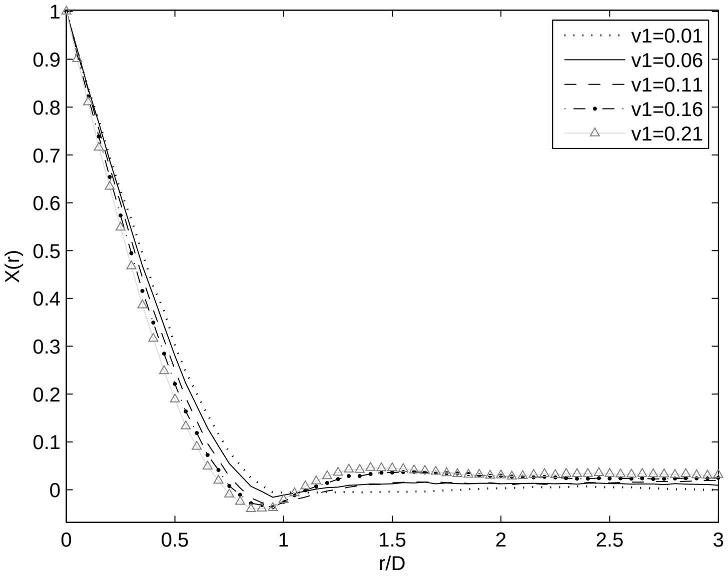

(b)

Figure 5.4.3.1: Spatial statistics of the randomly distributed sphere models of varying inclusion concentrations. (a) Shows the two point probability function and (b) correlation function for the non-overlapping randomly distributed spheres

If the correlation functions extracted from a statistical volume reach their respective theoretical limit as $r \to \infty$ (i.e when the offset becomes large); then the volume can be considered as a representative volume element (Torquato 2002). Figure 5.4.3.1 (b) shows that as the offset r increases, the correlation function for larger inclusion concentrations (i.e $v_1 = 21\%$) does not quite converge to zero. This indicates that spheres at offsets greater than twice the sphere diameter, are still slightly correlated. Hence, there may be small statistical errors in the non-overlapping sphere models at larger volume concentrations.

To further investigate the statistical characteristics of the generated models, I compare the extracted two point probability function (and correlation function) against a two point probability function (and correlation function) theoretically derived for randomly distributed non-overlapping spheres by Torquato and Stell (1986). Unfortunately, the evaluation of their two point probability function requires numerical integration and fast Fourier transforms etc, so I only make use results of their tabulated results.

In Figure 5.4.3.2 (a) the two point probability and (b) correlation function extracted from models having inclusion concentrations of $v_1 = 11\%$ and $v_1 = 21\%$ are compared against tabulated results (Torquato & Stell 1986) at inclusion concentrations of $v_1 = 10\%$ and $v_1 = 20\%$. The figure shows that the extracted curves are in good qualitative agreement with theoretical estimates when volume concentrations are similar. Hence, the models generated by RSA will provide a sufficient statistical representation of randomly distributed spheres.

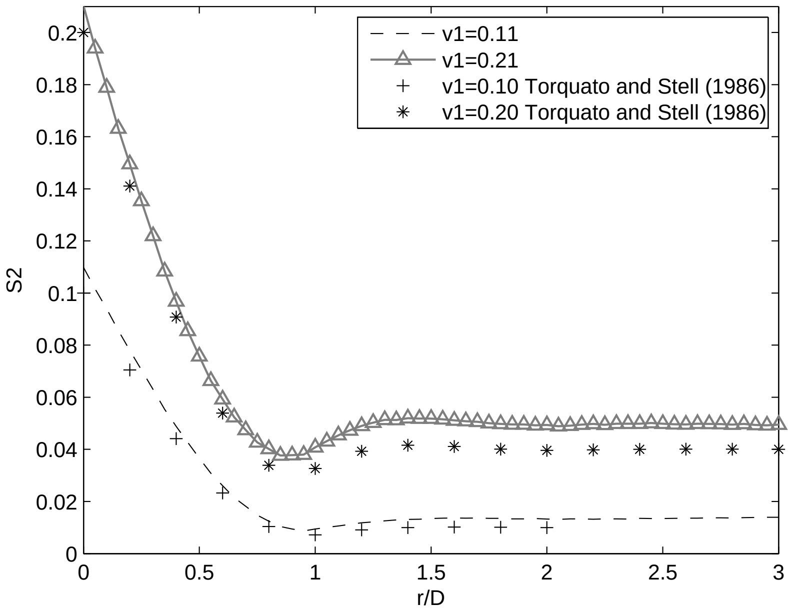

(a)

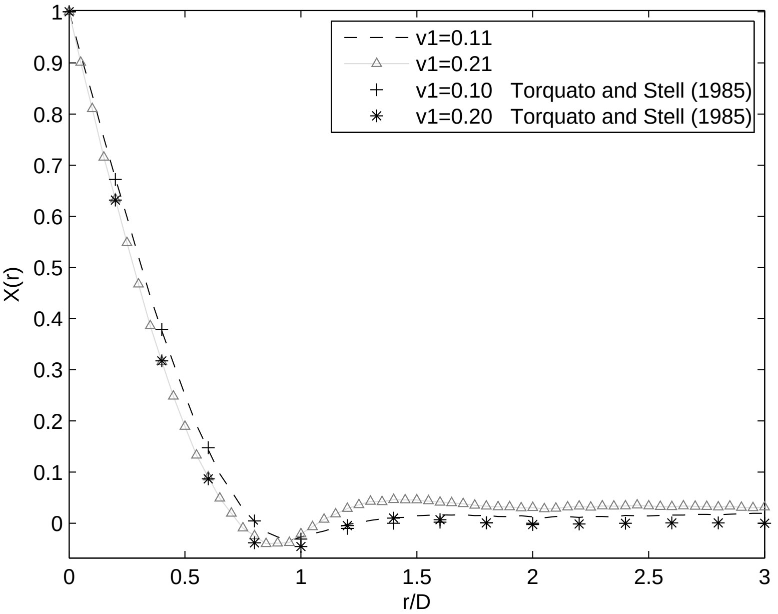

(b)

Figure 5.4.3.2 Theoretical (Torquato & Stell 1986) and extracted spatial statistics for randomly distributed sphere models. (a) Comparison of extracted and theoretical two point probability curves for randomly distributed spheres. (b) Comparison of extracted and theoretical correlation functions for randomly distributed spheres.

5.5 Numerical Shape Parameters for Random Distribution of Spheres

Here I calculate the numerical shape parameter ζ for a random distribution of non-overlapping spherical inclusions, in particular studying how ζ varies when spherical inclusion concentration and fluid contrast is altered. The numerical estimates of the shape parameter are compared against the analogous analytical shape parameters derived in Chapter 4 (Equations (4.3.1.8) and Equations (4.3.1.10)). My objective is to delineate the range of spherical inclusion concentrations and fluid bulk moduli contrasts for which the corresponding analytical shape parameters are accurate.

Three different fluid contrast scenarios are considered. For all models, it is assumed that the more compressible fluid is present as spherical inclusions within an otherwise water saturated host. The inclusion fluid bulk moduli for each case are (1) low contrast $Kf_i = 2GPa$ (2) moderate contrast $Kf_i = 1GPa$ and (3) high contrast $Kf_i = 0.01GPa$. As significant viscosity variation can affect the accuracy of the finite-difference solution, I set the inclusion fluid viscosity equal to the viscosity of water. For each fluid contrast scenario, I model spherical inclusion concentrations: starting at 1%, (or 99% water saturation) incrementing by 5%, to a maximum of 31% (or 69% water saturation).

In addition to calculating the analytical shape parameters (Equations (4.3.1.8) and Equations (4.3.1.10)) for randomly positioned non-overlapping spheres, I also calculate the analytical shape parameters for periodically distributed spheres and randomly positioned overlapping spheres for the equivalent volume concentrations and fluid contrasts. By doing this I can access how the shape parameter for the randomly positioned non-overlapping spheres changes with contrast and volume inclusion concentration, relative to changes observed for other distributions of spherical inclusions.

Scenario 1: Low Contrast

Figure 5.5.1 shows the numerical shape parameter (asterisks) and the analytical shape parameter (dashed line) for randomly positioned non-overlapping spheres. Clearly there is an excellent agreement between the shape parameters derived from numerical experiments and those derived from analytical considerations over a wide range of inclusion concentrations (6% to 31%). The numerical shape parameter differs significantly from the analytical shape parameter for 1% of inclusions. This is a numerical artefact, which is attributed to cancellation errors. After examining the finite-difference code, I traced the error back too very small differences between very large numbers, which occurs within one step when calculating the shape parameter. From my analysis performed in Chapter 4, I know that the theoretical limit on the shape parameter for low contrast and small volume concentration is 5/9; hence I expect that my finite-difference shape parameters would lye on the analytical curve at small volume concentrations given the trend observed between 6% to 31% inclusion concentrations.

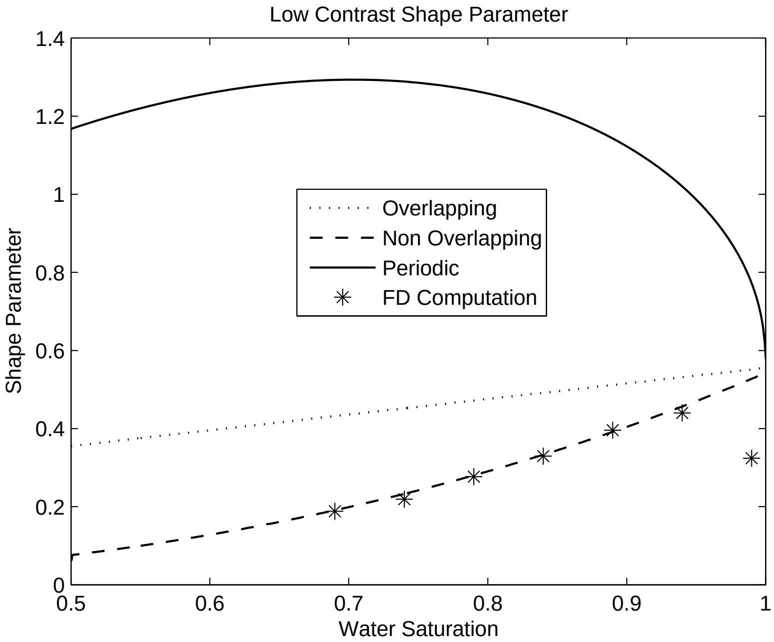

Figure 5.5.1: Numerical and analytical shape parameters for spherical inclusions having low fluid contrast with water. The numerical shape parameters (asterisks) follow the analytical relationship (dashed line) for low contrast random spheres.

Scenario 2: Moderate Contrast

Figure 5.5.2 shows the numerical shape parameter (asterisks) and two versions of the analytical shape parameter for randomly positioned non-overlapping spheres. These two analytical shape parameters correspond to shape parameters derived from DRM theory, with contrast assumptions (dotted line, Equation (4.3.1.10)) and without (dashed line, Equation (4.3.1.8)) contrast assumptions placed on the inclusion fluid, respectively.

Clearly there is excellent agreement between the numerical shape parameters and the shape parameters derived from DRM theory. Interestingly, for water saturations > 89% , the numerical shape parameters are situated on the un-approximated analytical shape parameter (Equation 4.3.1.8); otherwise they are situated on the low fluid contrast approximation (Equation 4.3.1.10) of this shape parameter.

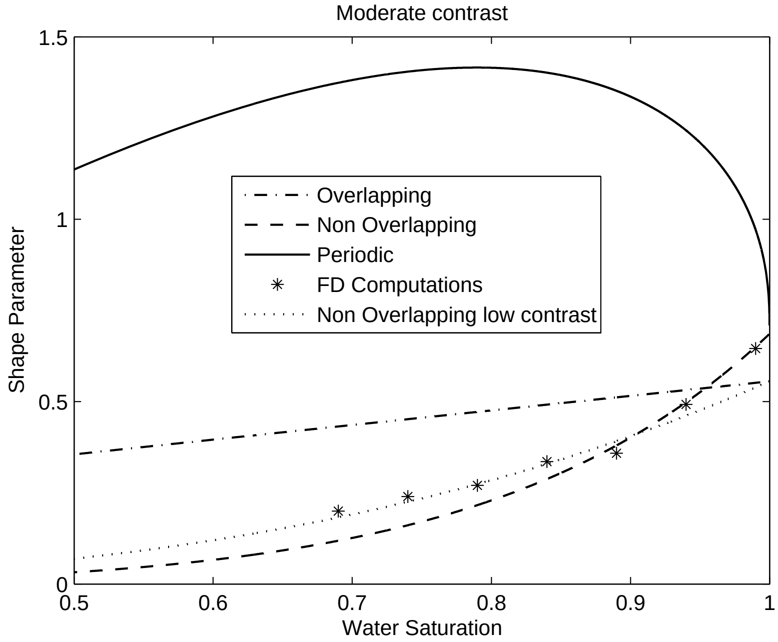

Figure 5.5.2: Numerical and analytical shape parameters for spherical inclusions having moderate fluid contrast relative to water. The numerical shape parameters (asterisks) follow two different analytical relationships. For water saturation >89% the numerical shape parameters follow the randomly distributed sphere (dashed line), whilst for water saturations <89% it follows the low contrast approximation of the randomly distributed sphere shape parameter (dotted line).

Scenario 3: High Contrast

Figure 5.5.3 displays the numerical shape parameter (asterisks) and the analytical shape parameters for randomly positioned non-overlapping spheres when fluid contrast between the inclusion and host fluid is large. Figure 5.3.3 shows that the numerical shape parameter does not seem to rest along either analytical shape parameter relationships (randomly distributed non-overlapping spheres (dashed line) Equation 4.3.1.8) nor does it correspond to the periodic (solid line) shape parameter. However, by zooming into the picture Figure 5.5.4 we see that the numerical shape parameters follow closely the analytical shape parameter for low fluid contrast (dotted line Equation 4.3.1.10) at water saturations less 81%. Clearly more modelling is required to understand how the shape parameter varies at high fluid contrast for randomly distributed spheres.

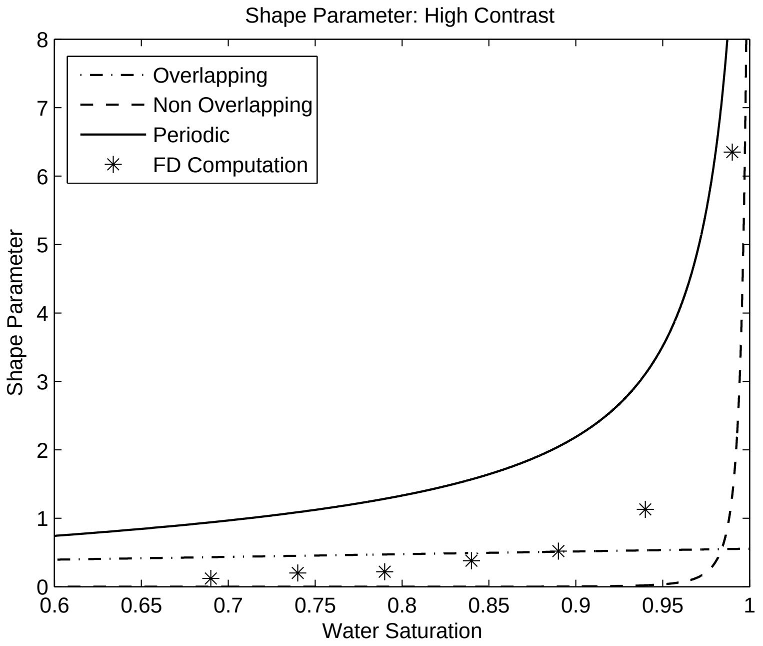

Figure 5.5.3 High contrast shape parameters for randomly distributed spheres. The numerical shape parameters (asterisks) do not follow either analytical derived shape parameter relationships given by overlapping spheres (dashed-dotted line), periodic spheres (solid line) or randomly distributed spheres (dashed line Equation 4.3.1.8)

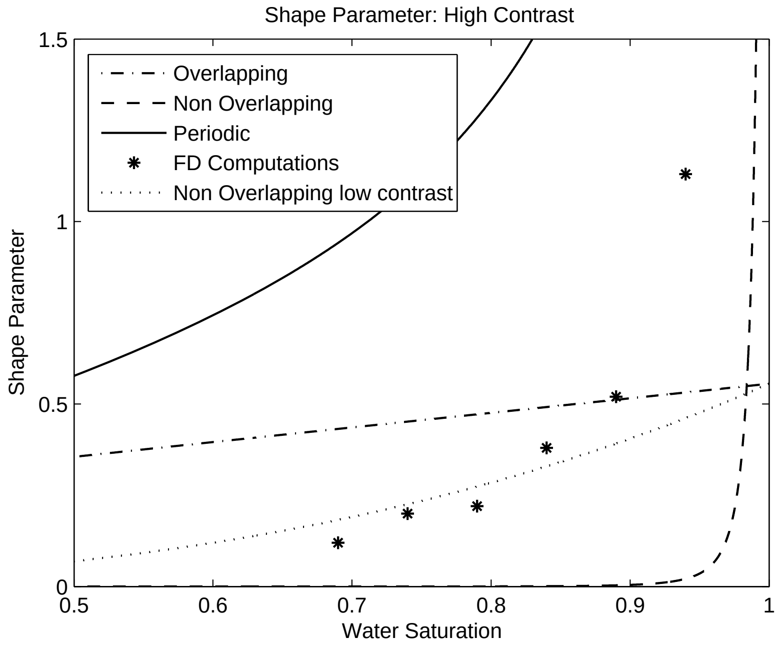

Figure 5.5.4: High contrast shape parameters for randomly distributed spheres. By zooming into Figure 5.5.3 the numerical shape parameters begin to follow the analytical shape parameter for randomly distributed spheres (dotted-line Equation 4.3.1.8) at water saturations less then 81 %.

5.6 An Example: Attenuation

Tserkovnyak and Johnson (2002) have inverted attenuation and velocity data obtained from experiments into shape and frequency scaling parameters, having in mind the object of determining spatial characteristics of partial fluid distributions. However, crucial to converting experimentally determined shape and frequency scaling parameters into quantities that reflect characteristics of the fluid saturated porous rock is an interpretation strategy. For partially saturated rocks, Tserkovnyak and Johnson (2002) assumed that water saturation can be modelled as an inclusion within the concentric circle geometry. This allowed shape and frequency scaling parameters to be related to volume to surface area and effective patch size. However, their method is only one way of possibly relating shape and frequency scaling parameters to physically meaningful quantities for partially saturated rock.

In this Chapter, I have shown how the shape parameter can change as both water saturation and contrast in fluid compressibility is increased. Moreover, I have demonstrated how the shape parameter changes for different types of 1D, 2D and 3D fluid distributions. This work is especially important when one contemplates inverting from attenuation and velocity data for information on saturation or geometry parameters such as V/S etc, without some prior knowledge of fluid distribution within partially saturated rock.

To illustrate this point, I will forward model the frequency-dependent attenuation curve for 21 % heavy gas inclusions within an otherwise water saturated rock. I assume two different fluid distribution geometries; they are randomly distributed spheres and periodically distributed spheres. To calculate the frequency-dependent attenuation curve for the random distribution of spheres, I use APS taking the shape parameter value given in Figure 5.6.1 (a). I also compute the attenuation for randomly distributed spheres using DRM (see Section 3.2), whilst the periodic attenuation curve is calculated using APS with Equation (1.3.2.7) given by the redline in Figure 5.6.1 (a).

Figure 5.6.1 (b) shows that the attenuation curves for randomly distributed spheres using APS (black curve) and DRM (blue curve) are different. Although not shown here, for this volume concentration and fluid contrast, DRM (Non Over Theor -blue curve) does not satisfy Gassmann–Wood limits on phase velocity. Hence, the DRM attenuation curve is erroneous. The frequency-dependent attenuation for periodic (red curve) and random (black curve) spheres generated using APS with appropriate shape parameters are significantly different at low frequencies, although there is good correspondence at high frequencies.

The importance of this example is that it shows that the value taken by the shape parameter will directly influence attenuation (and also velocity). The shape parameter in turn is affected by how fluids are distributed, percentage water saturation, fluid contrast etc. Hence by inverting experimental data into shape and frequency scaling parameters as a middle step to characterising partially fluid saturated rock, we must then determine how to transform the shape parameter (and also frequency scaling parameter) into the physically meaningful parameters we are interested in. For this purpose, relations such as those derived in Table 4.4.2 and Table 4.4.4 are crucial.

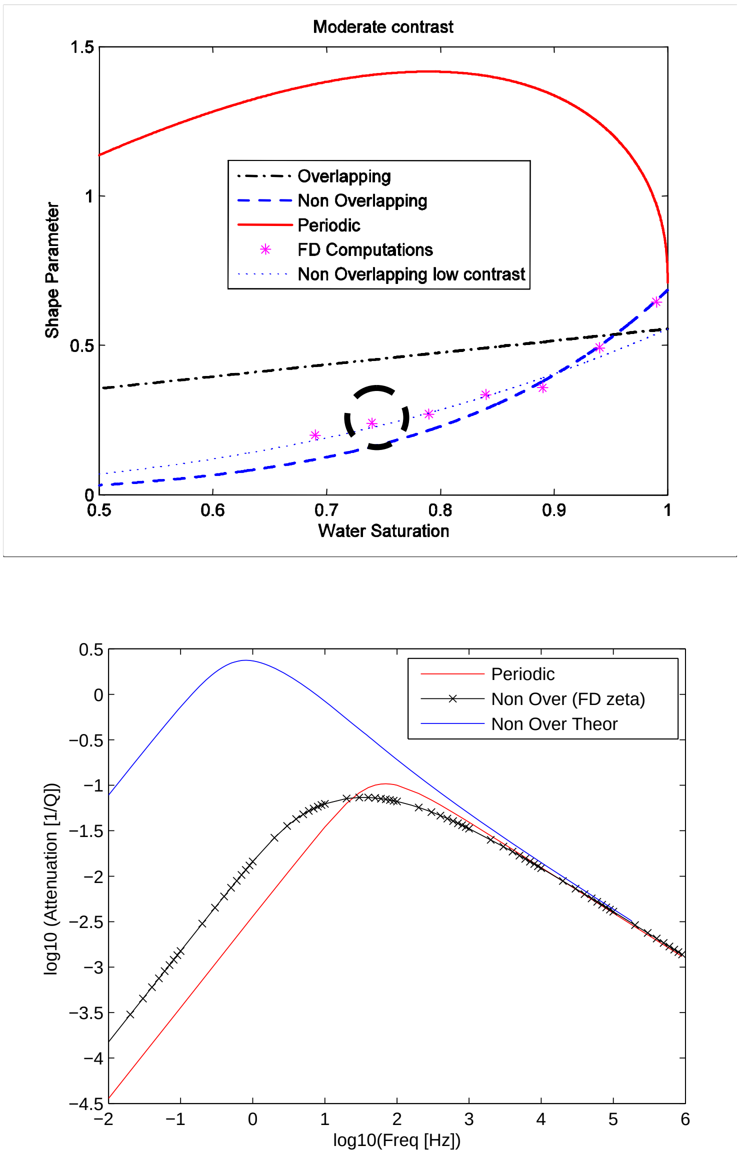

a)

b)

Figure 5.6.1: Shape parameter and frequency-dependent attenuation curves. (a) Shows the shape parameters for randomly and periodically distributed spheres containing a heavy gas. (b) Shows frequency-dependent attenuation curves calculated using APS with different shape parameters. Clearly there is a difference in the attenuation curves for randomly and periodically distributed spheres.

5.7 Chapter Conclusions

I have trialled a new way of numerically determining shape parameters for complicated fluid distributions, this method is promising. The approach was to numerically determine the T coefficient of the APS framework. This coefficient governs the low frequency approach of the saturated bulk modulus to the static limit by the Gassmann-Wood equations. It is defined in terms of the integral of an auxiliary function, which is the solution to a potential equation related to fluid pressure diffusion.

The potential equation was approximated using finite-differences. The resulting algorithm was tested for a variety of 1D, 2D and 3D modelling scenarios. In particular, I have shown that shape parameters can be determined accurately for a variety of fluid contrasts, fluid viscosities and fluid saturations. However, for synthetic models where viscosity contrast is of interest, the model must be treated carefully.

For 3D fluid distributions described by randomly distributed non-overlapping spheres, I have used my numerical approach to validate:

(1) the accuracy of the low contrast shape parameter (Equation 4.3.1.10) over a wide range of inclusion concentrations (1% to 31%) and fluid bulk moduli contrasts, ranging from low to moderate.

(2) the accuracy of the moderate contrast shape parameter (Equation 4.3.1.8) over a wide range of inclusion concentrations of intermediate fluid contrast.

Like any trial, there is still more work that can be performed. In particular, the algorithm could be run on many more models of large fluid contrast (such as with water and gas) to obtain a better idea of how large contrast will affect the shape parameter for randomly distributed spheres. By doing more trials of this kind, one could use the numerical shape parameter estimate to develop heuristic shape parameters, for situations where an analytical solution of shape parameter is too tough to derive.

Further work, which is yet to be performed is to validate (or invalidate) the other analytical shape parameters, derived in Chapter 4. The same process would be performed, by comparing the analytical shape parameters against numerically estimated shape parameters. However, one must be very careful and ensure that the model generated as input to the finite-difference code, does in fact satisfy the statistical requirements of the desired medium, such as with a particular correlation function etc. Otherwise, one may be comparing shape parameters which implicitly assume different types of fluid distributions.

Chapter 6

Conclusions and Recommendations

6.0 Introduction

Quantitative interpretation of seismic data and detection of hydrocarbon is largely based on seismic amplitudes at different offsets. As hydrocarbons are usually present in the reservoir alongside brine, which is especially true during production, knowledge of precise relationships between saturation and seismic attributes is important for exploration and especially for monitoring of production.

In this thesis, I have determined from first principles, how compressional wave attenuation and velocity is affected by partial fluid saturation of porous rock. Specifically, I focus on identifying changes in frequency-dependent attenuation and dispersion caused by altering the fluid distribution and contrast between pore fluids. I concentrate on mesoscale fluid heterogeneities which arise on a length scale greater than pore scale, but less than wavelength scale. I choose to investigate effects due to mesoscale fluid heterogeneities because significant attenuation and dispersion may result within the seismic frequency bandwidth (White 1975; Pride et al. 2004).

Below I summarise the key outcomes of my work.

6.1 Fluid Distribution from Saturation Experiments on Porous Rock

In Chapter 2, I studied core samples undergoing a drainage experiment, where pressurized nitrogen gas was injected into fully water saturated rock. Specifically, I looked for evidence that mesoscale fluid heterogeneities exist. I found sufficient evidence using X-ray tomographic images of partially saturated core samples, which I processed to form saturation maps. These saturation maps showed heterogeneous fluid patches. By applying statistical measures which are typically used in material science to describe the microstructure of materials I investigated how the saturation maps change as gas saturation increases. Specifically, I found that the correlation function and correlation length provided the most useful spatial information for characterising mesoscopic fluid heterogeneities and changes in fluid distribution patterns caused by increased gas saturation. The correlation function was shown to be well approximated by a single or superposition of two Debye correlation functions, whilst the Debye correlation length was observed to decrease almost linearly with gas saturation.

6.2 Patchy Saturation Models for Complex and Irregular Fluid Distributions

Models based on the theory of statistical wave propagation have the potential to accurately simulate the acoustic signatures of partially saturated rocks, because they implicitly assume that fluid distribution is described by a correlation function. In Chapter 3, I started by analysing one such approach, the 1D patchy saturation model of Müller and Gurevich (2004) which assumes layering of fluid heterogeneities. By deriving correlation functions for periodic layering and quasi-periodic layering, it was shown that small amounts of uncertainty in layer repetition had little effect on attenuation and dispersion signatures.

The main outcome of Chapter 3 was the development of a 3D patchy saturation model (3DCRM) which allows attenuation and dispersion to be estimated when fluid distribution is modelled using a correlation function. By substituting different correlation functions into the 3DCRM model, I showed that attenuation and dispersion could be estimated for many different types of fluids distributions. By comparing attenuation and dispersion curves generated using different correlation functions; I was able to show qualitatively that fluid distribution affects the frequency-dependent shape of attenuation and dispersion curves.

Another key result of Chapter 3 was the development of a methodology which allows one to incorporate statistical information obtained from saturation maps (like correlation functions etc) into the 3DCRM model. Having this methodology is very important, because it allows one to calculate frequency-dependent attenuation and dispersion due to spatial information obtained directly from realistic fluid distributions.

6.3 Extension of the APS Framework

The 3DCRM and 1DCRM models are precise for low fluid contrast and approximate at high fluid contrast. This occurs because the statistical approach underpinning the derivation of 3DCRM and 1DCRM models is precise for small fluctuations in physical properties. In reality, pore fluid contrast may be large, as the bulk moduli of two dissimilar fluids can vary by several orders of magnitude; such is the case with water and gas saturation. To compensate for effects due to fluid contrast, scaling functions were incorporated into each CRM model to ensure convergence to the Gassmann-Wood and Gassmann-Hill limits, for low and high frequencies, respectively. By making this approximation, it was implicitly assumed that the frequency-dependent character of the saturated P-wave modulus is independent of fluid contrast. That is, within the CRM framework, the fluid contrast affects only the magnitude of attenuation and dispersion, not the shape of attenuation and dispersion curves.

In order to test whether the frequency-dependent characteristics of attenuation and dispersion change with fluid contrast (for realistic fluid distributions); I utilized the APS framework of Johnson (2001). This is a regular cell model with a simple and general framework, which is valid for any fluid contrast. However, in its original implementation APS was limited to simplistic fluid distributions, such as concentric spheres. The first step in utilizing the APS framework was to recognize how to extend its range of applicability to arbitrary fluid distributions with low fluid contrast (or percent saturation). By doing this I could compare estimates of attenuation/dispersion with the random media models (1DCRM, DRM, 3DCRM) to check the accuracy of my approach.

In Chapter 4, I showed how the APS framework could be extended to model complicated fluid distributions. My approach was to modify two special parameters within this framework called “shape” and “frequency scaling” parameters. Specifically, I derived new equations for these parameters, which allowed other pore fluid distributions to be modelled. By substitution of the new shape and frequency scaling parameters into the APS framework, I was able to extend the APS framework to model attenuation and dispersion for different fluid distributions. Comparison of the APS estimates with the equivalent random media models (1DCRM, DRM, 3DCRM) showed that the APS branching function approximation was very accurate at intermediate frequencies.

Some notable results of this analysis are that the APS framework can be utilized to model random layering whereas it was originally designed for periodic layering. I also explicitly derived an equation showing how the shape parameter, which controls the shape of the frequency-dependent attenuation and dispersion curves, depends explicitly on the correlation function and volume to surface area of 3D arbitrary fluid distributions. I also showed how the shape and frequency scaling parameters are related to statistical measures which can be extracted from x-ray tomographic images.

6.4 Numerical Estimation of Shape and Frequency Scaling Parameters

The new shape and frequency scaling parameters derived in Chapter 4 were known to be accurate for certain fluid contrasts and volume concentrations. As such to examine whether these shape parameters are valid for arbitrary fluid contrasts and concentrations, I developed a new numerical approach.

In Chapter 5 I numerically determined the shape parameter for complicated fluid distributions. The approach was to numerically determine the T coefficient of the APS framework. This coefficient governs the low frequency approach of the saturated bulk modulus to the static limit as given by the Gassmann-Wood equations.

The T parameter is defined by an integral of an auxiliary function, which is determined from the solution to a potential partial differential equation governing wave-induced fluid pressure diffusion.

The potential equation was approximated using finite-differences. The resulting algorithm was tested for a variety of 1D, 2D and 3D modelling scenarios. In particular, I showed that shape parameters can be determined accurately for a variety of fluid contrasts, fluid viscosities and fluid saturations.

The outcome of this Chapter was to show that the APS framework could be utilized to model attenuation and dispersion due to complicated fluid distributions, such as randomly distributed spheres at any fluid contrast.

6.5 Recommendations for Future Work

There are four main areas of research work which could follow on from my PhD study. They can be categorized as:

(1) Comparison of experimental attenuation and velocity estimates against theoretical predictions using CRM with spatial information extracted from tomographic images of partially saturated rock.
(2) Validation of analytical shape and frequency scaling parameters using APS theory.
(3) Substitution of realistic rock and fluid properties into patchy saturation models and modelling seismic attributes.
(4) Case studies

6.5.1 Experiment versus theory

I have developed a methodology for relating gas saturation maps to the 3DCRM patchy saturation model through an autocorrelation function. This method enables estimation of phase velocity dispersion and attenuation due to mesoscopic fluid flow.

If acoustic measurements are made in parallel to X-ray tomographic images during a saturation experiment, one could compare 3DCRM theoretical predictions and experimental estimates for attenuation and velocity.

By comparing experimentally derived velocity and attenuation against theoretical estimates produced using 3DCRM (having incorporated spatial information extracted from tomographic images), one may gain insight into whether mesoscopic fluid flow is a controlling factor on the acoustic properties of partially saturated rock. This is important to evaluate as there are other possible attenuation mechanisms such as squirt flow (Gist 1994) or scattering (Gelinsky et al. 1998) which may be a factor, especially at ultrasonic frequencies.

If there are large discrepancies between 3DCRM theoretical estimates and experimental observations then it may indicate that mesoscopic fluid flow is not the controlling factor on the acoustic response of partially saturated rocks and that we should concentrate on modelling effects due to other mechanisms. Alternatively, it may indicate that frame heterogeneities, such as porosity, permeability, and dry frame bulk modulus variation need to be accounted for.

The advantage of using 3DCRM for this type of analysis, is that unlike other patchy saturation models (eg White 1975), the fluid distribution in 3DCRM is experimentally defined. This means that there are no parameters within 3DCRM theory which can be fiddled with to make theoretical and experimental measurements match.

6.5.2 Validation of analytical shape parameters

The analytical shape and frequency scaling parameters derived in Chapter Four provide a recipe on how to relate frequency-dependent signatures (attenuation and velocity) of partially saturated rock to measures which characterise partial fluid saturation, such as fluid distribution, correlation length, volume concentration etc. When these parameters are incorporated in the APS framework, a simple unified approach to modelling partial fluid saturation signatures is presented. Further work which can be performed is to use the numerical procedure demonstrated in Chapter 5 to validate and evaluate the accuracy of the shape parameters at a range of fluid contrasts and fluid saturations.

The validation of shape and frequency scaling parameters will be important for inversion from attenuation and velocity information to properties of partially fluid saturated rock.

6.5.3 Forward modelling patchy saturation signatures for specific rock properties

The focus of this thesis has been on getting the tools in place to be able to model partial fluid saturation signatures due to realistic fluid distributions and fluid contrasts. Further work which could be performed is to use these tools to specify likely attenuation and dispersion signatures for different rock types and fluid saturations. That is, model attenuation and dispersion for a range of rock properties having characteristic dry frame bulk modulus, porosity and permeability appropriate for carbonates, sandstones etc.

In particular, one could identify the range of permeability/correlation lengths for which attenuation and dispersion are a maximum within the seismic frequency bandwidth. Moreover, one could use the tools within this thesis to model AVO signatures including for frequency-dependent effects due to partial fluid saturation.

6.5.4 Case/Field Studies

There are two main areas of application for this research. The first is in exploration settings and the second is in production settings. Noting that, one will firstly require a reliable means of estimating attenuation from seismic data and secondly be able to distinguish attenuation as a result of intrinsic loss (wave induced fluid flow) from attenuation due to scattering losses (amplitude loss due to elastic scattering).

In exploration, there is a problem of differentiating between rock which is saturated by economic and uneconomic quantities of hydrocarbons using both seismic amplitudes (Gross & Hood 1998) and AVO signatures (O’Brien 2004). An interesting study would be to apply APS theory to see whether seismic amplitudes and AVO signatures (such as those discussed by Gross & Hood 1998) could be interpreted in terms of shape and frequency scaling parameters. For a number of fluid distributions (examined in Chapter 4) the shape and frequency scaling parameters were shown to be sensitive to percent fluid saturation and fluid contrast. Hence, a rock which is saturated by large percentages of hydrocarbon may have characteristically different shape parameters than for same rock saturated by small percentages of hydrocarbons. A study comprising of known exploration successes and failures would provide optimal data for this type of analysis.

To assist with production of hydrocarbon from reservoirs, time lapse studies are conducted. Time lapse seismic interpretation is based on relating differences in seismic sections obtained from repeating surveys over producing reservoirs to changes in reservoir fluids and pressures. Production techniques, such as waterflooding, gas injection and gas dissolution have the potential to create very complicated fluid distributions. These complicated fluid distributions often exist on a spatial scale far smaller than the resolution of cells within reservoir flow simulators (Sengupta et al. 2003; Sengupta & Mavko 2003). In order to track fluid front movements accurately it will be of benefit to model seismic velocities as accurately as possible, hence there will be a need to model affects due to complicated fluid distributions.

References

Ames, WF 1977, *Numerical Methods for Partial Differential Equations,* Academic Press, New York

Amos, CL, Sutherland, TF, Radezijewski, B & Doucette, M 1995, ‘A rapid technique to determine bulk density of fine grained sediments by X-ray computed tomography’, *Journal of Sedimentary Research*, vol. 66, pp. 1023-1025.

Arns, CH, Bauget, F, Limaye, A, Sakellariou, A, Senden, TJ, Sheppard, AP, Sok, RM, Pinczewski, WV, Bakke, S, Berge, LI, Oren, PE & Knackstedt, MA 2004 ‘Porescale characterization of carbonates using x-ray microtomography’, *Society of Petroleum Engineers, 2004 Annual Technical Conference and Exhibition*, Houston, September 2004, SPE 90368:1-12.

Arns, CH, Knackstedt, MA, Pinzewski, WV & Lindquist, WB 2001, ‘Accurate computation of transport properties from microtomographic images’, *Geophysical Research Letters*, vol. 28, pp. 3361-3364.

Arns, CH, Knackstedt, MA, Pinzewski, WV & Garboczi EJ, 2002, ‘Computation of linear elastic properties from microtomographic images: methodology and agreement between theory and experiment’, *Geophysics*, vol. 67, No. 5, September-October, pp. 1396-1405.

Arns, CH, Knackstedt, MA, Pinzewski, WV & Martys, NS 2004, ‘Virtual permeatry of microtomographic images’, *Journal of Petroleum Science and Engineering,* vol. 45, No. 1-2, pp. 41-46.

Assefa, S, McCann, C & Sothcott J 1999, ‘Attenuation of P- and S-waves in limestones’, *Geophysical Prospecting*, vol. 47, pp. 359-392.

Auriault, JL 1980, ‘Dynamic behaviour of a porous medium saturated by a newtonian fluid’, *International Journal of Engineering Science*, vol. 18, pp. 775-785.

Auriault, JL, Boutin, C, Royer, P & Schmitt, D 2002, ‘Acoustics of a porous medium saturated by a bubbly fluid undergoing phase change’, *Transport in Porous Media*, vol. 46, No. 1, pp. 43-76.

Bachelor, GK 1967, *An Introduction to Fluid Mechanics,* Cambridge University Press, Cambridge UK

Bear, J 1988, *Dynamics of fluids in porous media,* Dover, New York

Bedford, A & Stern, M 1982, ‘A model for wave propagation in gassy sediments’, *Journal of the Acoustical Society of America*, vol. 73, pp. 409-417.

Berkowitz, B & Hansen, D 2001 ‘A numerical study of the distribution of water in partially saturated porous rock’, *Transport in Porous Media*, vol. 45, pp. 303-319.

Berryman, JG 1985 ‘Scattering by a spherical inhomogeneity in a fluid-saturated porous medium’, *Journal of Mathematical Physics,* vol. 26, No. 6, pp. 1408-1419.

Berryman, JG 1988, ‘Seismic wave attenuation in fluid saturated porous media’, *Pure and Applied Geophysics,* vol. 128, pp. 424-432.

Berryman, JG & Blair, SC 1986, ‘Use of digital image analysis to analysis to estimate fluid permeability of porous materials: Application of two point correlation functions’, *Journal of Applied Physics*, vol. 60, pp. 1930-1938.

Best, AI, McCann, C & Sothcott, J 1994, ‘The relationship between the velocities, attenuations and petrophysical properties of reservoir sedimentary rocks’, *Geophysical Prospecting*, vol. 42, pp. 151-178.

Biot, MA 1956a, ‘Theory of propagation of elastic waves in a fluid in a fluid saturated porous solid. .I.-Low frequency range’, *Journal of the Acoustical Society of America*, vol. 28, pp. 168-178.

Biot, MA 1956b, ‘Theory of propagation of elastic waves in a fluid saturated porous solid. II. Higher frequency range’, *Journal of the Acoustical Society of America*, vol. 28, pp. 179-191.

Biot, MA & Willis, DG 1957, ‘The elastic coefficients of the theory of consolidation’, *Journal of Applied Mechanics*, vol. 24, pp. 594-601.

Biot, MA 1962, ‘Mechanics of deformation and acoustic propagation in porous media’, *Journal of Applied Physics*, vol. 33, pp. 1482-1498.

Bourbie, T, Coussy, O & Zinszner, B 1987, *Acoustics of Porous Media*, Technip, Paris

Brie, A, Pampuri, F, Marsala, AF & Meazza, O 1995, ‘Shear sonic interpretation in gas bearing sands’, *Society of Petroleum Engineers Annual Technical Conference and Exhibition, Dallas, 1995*. SPE 30595.

Buckingham, MJ 2000, ‘Wave propagation, stress relaxation, and grain-to-grain shearing in saturated, unconsolidated marine sediments’, *Journal of the Acoustical Society of America*, vol. 108, pp. 2796-2815.

Burridge, R & Keller, JB 1981 ‘Poroelasticity equations derived from microstructure’, *Journal of the Acoustical Society of America*, vol. 70, pp. 1140-1145.

Cadoret, T, Marion, D & Zinszner, B 1995, ‘Influence of frequency and fluid distribution on elastic wave velocities in partially saturated limestones’, *Journal of Geophysical Research*, vol. 100, pp. 9789-9803.

Cadoret, T, Mavko, G & Zinszner, B 1998, ‘Fluid distribution effect on sonic attenuation in partially saturated limestones’, *Geophysics*, vol. 63, pp. 154-160.

Calvert, R 2005, ‘4D technology: where are we, and where are we going to?’ *Geophysical Prospecting*, vol. 53, pp. 161-171.

Carcione, JM, Helle, HB & Pham, NH 2003, ‘White’s model for wave propagation in partially saturated rocks: Comparison with poroelastic numerical experiments’, *Geophysics*, Vol. 68, No. 4, July-August, pp. 1389-1398.

Chandler, RN & Johnson, DL 1981, ‘The equivalence of quasistatic flow in fluid-saturated porous media and Biot's slow wave in the limit of zero frequency’, *Journal of Applied Physics*, vol. 52, pp. 3391-3395.

Chang, R 1994, *Chemistry*, 5th Edition, McGraw-Hill Publishing Company

Ciz, R & Gurevich, B 2005, ‘Amplitude of Biot’s slow wave scattered by a spherical inclusion in a fluid-saturated poroelastic medium’, *Geophysical Journal International*, vol. 160, pp. 991-1005.

Ciz, R, Gurevich, B & Markov, M 2006, ‘Seismic attenuation due to wave-induced fluid flow in a porous rock with spherical heterogeneities’, *Geophysical Journal International*, vol. 165, No. 3, pp. 957-968.

Ciz, R, Toms, J & Gurevich, B 2005, ‘Attenuation and dispersion of elastic waves in a poroelastic medium with spherical inclusions’, in Abousleiman, YN, Cheng, AH-D & Ulm F-J (eds.), *Poromechanics III Biot Centenial (1905-2005)*, Taylor and Francis, London, pp. 201-208.

Coker, DA, Torquato, S & Dunsmuir, JH, 1996, ‘Morphology and physical properties of Fontainebleau sandstone via a tomographic analysis’, *Journal of Geophysical Research*,Vol. 101, pp. 17497-17506.

Commander, KW & Prosperetti, A 1989, ‘Linear pressure waves in bubbly fluids. Comparison between theory and experiments’, *Journal of the Acoustical Society of America*, vol. 85, pp. 732-746.

Cooper, DW 1988, ‘Random-sequential-packing simulations in three dimensions for spheres’ *Physical Review A*, vol.38, pp522-524.

Dai, N, Vafidis, A & Kanasewich, ER 1995, ‘Wave propagation in heterogeneous, porous media : a velocity-stress, finite-difference method’, *Geophysics*, vol. 60. No. 2, pp. 327-340.

Debye, P & Bueche, AM 1949, ‘Scattering by an inhomogeneous solid’, *Journal of Applied Physics*, vol.20, pp. 518-525.

Dee Kee, D & Chhabra, RP 1988, ‘A photographic study of shapes of bubbles and coalescence in non-Newtonian polymer solutions’, *Rheologica Acta*, vol. 27, pp. 656-660

De Gryze, S, Jassogne, L, Six, J, Bossuyt, H, Wevers, M, & Merckx, R 2006, ‘Pore structure changes during decomposition of fresh residue: X-ray tomography analyses’, *Geoderma*, vol. 134, pp. 82-96.

Deresiewicz, H & Skalak, R 1963, ‘On uniqueness in dynamic poroelasticity’, *Bulletin of the Seismological Society of America*, vol. 53, pp. 409-416.

Domenico, SN 1976 ‘Effect of brine-gas mixture on velocity in an unconsolidated sand reservoir’, *Geophysics*, vol. 41, pp. 882-894.

Dunsmuir, JH, Ferguson, SR, D’Amico, KM & Stokes, JP 1991, ‘X-ray microtomography: A new tool for the characterization of porous media’, Paper SPE 22860 presented at the 1991 SPE Annual Technical Conference and Exhibition, Dallas, Oct. 6-9

Dutta, NC & Ode, H 1979a, ‘Attenuation and dispersion of compressional waves in fluid-filled porous rocks with partial gas saturation (White model)- Part I. Biot theory’, *Geophysics* vol. 44, pp. 1777-1788.

Dutta, NC & Ode, H 1979b, ‘Attenuation and dispersion of compressional waves in fluid-filled porous rocks with partial gas saturation (White model)-Part II. Results’, *Geophysics* vol. 44, pp. 1789-1805.

Dutta, NC & Seriff, AJ 1979 ‘On White’s model of attenuation in rocks with partial gas saturation’, *Geophysics*, vol. 44, pp. 1806-1812.

Feder, J 1980, ‘Random sequential adsorption’ *Journal of Theoretical Biology*, vol. 87, pp. 237-254.

Frankel, SP 1950, ‘Convergence Rates of Iterative Treatments of Partial Differential Equations’, *Mathematical Tables and Other Aids to Computation*, vol.4, pp. 65-75.

Franks, LE 1969, *Signal Theory*, Prentice Hall, New Jersey

Frisch, HL & Stillinger, FH 1963, ‘Contribution to the Statistical Geometric Basis of Radiation Scattering’, *Journal of Chemical Physics*, vol. 38, pp. 2200-2207

Galvin, RJ, Toms, J & Gurevich, B 2007, ‘A simple approximation for seismic attenuation and dispersion in a fluid-saturated porous rock with aligned fractures’ *SEG Expanded Abstracts*, vol. 26, pp. 1679.

Gadjdošík, J, Zeman, J & Šejnoha, M 2006, ‘Qualitative analysis of fiber composite microstructure: Influence of boundary conditions’, *Probabilistic Engineering Mechanics* vol. 21, pp. 317-329.

Gassmann, F 1951, ‘Elastic waves through a packing of spheres’, *Geophysics, vol.* 16, pp. 673-685.

Gelinsky, S & Shapiro, SA 1997, ‘Dynamic-equivalent medium approach for thinly layered saturated sediments’, *Geophysical Journal International*, vol. 128, pp. F1-F4.

Gelinsky, S, Shapiro, SA, Müller, TM & Gurevich, B 1998, ‘Dynamic poroelasticity of thinly layered structures’, *International Journal of Solids and Structures* vol. 35, pp. 4739-4752.

Gist, GA 1994, ‘Interpreting laboratory velocity measurements in partially gas-saturated rocks’, *Geophysics*, vol. 59, pp. 1100-1109.

Gregory, AR 1976, ‘Fluid saturation effects on dynamic elastic properties of sedimentary rocks’, *Geophysics*, vol. 41, pp. 895-921.

Gross, OP & Hood, KC 1998, ‘Prospect failures in a world class hydrocarbon system: Definition, distribution and possible causes of low gas saturated sands in deepwater Gulf of Mexico’, *American Association of Petroleum Geologists Annual Meeting, Extended Abstracts,*

Gurevich, B & Lopatnikov, SL 1995, ‘Velocity and attenuation of elastic waves in finely layered porous rocks’, *Geophysical Journal International*, vol. 121, pp. 933-947.

Helle, HB, Pham, NH & Carcione, JM 2003, ‘Velocity and attenuation in partially saturated rock, poroelastic numerical experiments’, *Geophysical Prospecting* vol. 51, pp. 551-566.

Hill, R 1963, ‘Elastic properties of reinforced solids: some theoretical principles’, *Journal of the Mechanics and Physics of Solids*, vol. 11, pp. 357-372.

Homsy, GM 1987, ‘Viscous fingering in porous media’, *Annual Review of Fluid Mechanics*, vol. 19, pp. 271-311.

Hoshen, J & Kopelman, R 1976, ‘Percolation and cluster distribution. I. Cluster multiple labeling technique and critical concentration algorithm’ *Physical Review B*, vol. 14, pp. 3438-3445.

Hounsfield, GN 1972, ‘A method of and apparatus for examination of a body by radiation such as X- or gamma radiation’, British Patent No. 1,283,915, London

Johns, RA, Steude, JS, Castanier, LM, & Roberts, PV 1993, ‘Non destructive measurements of fracture aperture in crystal-line rock cores using X-ray computed tomography’, *Journal of Geophysical Research*, vol. 98, pp. 1889-1900.

Johnson, DJ, Koplik, & Dashen, R 1987 ‘Theory of Dynamic permeability and tortuosity in fluid-saturated porous media’ *Journal of Fluid Mechanics*, vol 176, pp. 379-402.

Johnson, DL 2001, ‘Theory of frequency-dependent acoustics in patchy-saturated porous media’, *Journal of the Acoustical Society of America*, vol. 110, pp. 682- 694.

Johnston, DH, Toksöz, MN & Timur, A 1979 ‘Attenuation of seismic waves in dry and saturated rocks. II: Mechanisms’, *Geophysics*, vol. 44, pp. 691-711.

Jones, TD 1986, ‘Pore fluids and frequency-dependent wave propagation in rocks’, *Geophysics*, vol. 51, pp. 1939-1953.

Karal, FC & Keller, JB 1964, ‘Elastic, electromagnetic and other waves in random medium’, *Journal of Mathematical Physics*, vol. 5, pp. 537-547.

Kelder, O & Smeulders, DMJ 1997, ‘Observation of the Biot slow wave in water-saturated Nivelsteiner sandstone’, *Geophysics*, vol. 62, pp. 1794-1796.

Ketcham, RA & Carlson, WD 2001, ‘Acquisition, optimization and interpretation of X-ray computed tomographic imagery: applications to the geosciences’, *Computers and Geosciences*, vol. 27, pp. 381-400.

Klimes, L 2002, 'Correlation Functions of Random Media', *Pure and Applied Geophysics*, vol. 159, pp. 1811-1831.

Knackstedt, MA, Arns, CH, Limaye, A, Sakellariou, A, Senden, TJ, Sheppard, AP, Sok, RM, & Pinczewski, WV 2004, 'Digital Core Laboratory: Properties of reservoir core derived from 3D images', *Society of Petroleum Engineers*, *2004 SPE Asia Pacific Conference on Integrated Modelling for Asset Management*, Kuala Lumpur, March 2004, SPE 87009:1-14.

Knight, R, Chapman, A & Knoll, M 1990, 'Numerical modelling of microscopic fluid distribution in porous media', *Journal of Applied Physics*, vol. 68, pp. 994-1001.

Knight, R, Dvorkin, J & Nur, A 1998, 'Acoustic signatures of partial saturation', *Geophysics*, vol. 63, pp. 132-138.

Knight, R & Nolen-Hoeskema, R 1990, 'A laboratory study of the dependence of elastic wave propagation of elastic wave velocities on porescale distribution', *Geophysical Research Letters*, vol. 17, pp. 1529-1532.

Krzikalla, F, Müller, T.M, Hardy, B & Gurevich, B 2006, 'Seismic wave attenuation and dispersion in patchy-saturated rocks- Numerical Experiments', *Abstract for Vienna 2006,68th EAGE Conference and Exhibition incorporating SPE Europec 2006*

Levin, BR 1968, *Theoretical Backgrounds of Statistical Radio Engineering* (in Russian). Nauka, Moscow

Levy, T 1979, 'Propagation of waves in a fluid-saturated porous elastic solid' *International Journal of Engineering Science*, vol. 17, pp. 1005-1014.

Lopatnikov, SL & Gorbachev, PY 1987, ‘Propagation and attenuation of longitudinal waves in a partially gas-saturated porous media’, *Izvestiya Earth Physics*, vol. 23, pp. 683-689.

Lopatnikov, SL & Gurevich, B 1986, ‘Attenuation of elastic waves in a randomly inhomogeneous saturated porous medium’, *Doklady Earth Science Sections*, vol. 291, No. 6, pp. 19-22.

Lu, B & Torquato, S 1992, ‘Lineal-path function for random heterogeneous materials’, *Physical Reveiw A*, vol. 45, pp. 922-929.

Markov, MG & Levin, VM 2007, ‘The role of surface tension in elastic wave scattering in an inhomogeneous poroelastic medium’, *Waves in Random and Complex Media*, vol. 17, pp. 615-626.

Mavko, G & Nur, A 1979, ‘Wave propagation in partially saturated rocks’, *Geophysics*, vol. 44, pp. 161-178.

Mavko, G & Mukerji, T 1998, ‘Bounds on low frequency seismic velocities in partially saturated rocks’, *Geophysics*, vol. 63, pp. 918-924.

Mecke, KR 1998, Integral geometry and statistical physics’, *International Journal of Modern Physics B*, vol. 12, pp 861-899.

Monsen, K & Johnstad, SE 2005, ‘Improved understanding of velocity-saturation relationships using 4D computer-tomography acoustic measurements’, *Geophysical Prospecting*, vol. 53, pp. 173-181.

Morten, KW & Mayers, DF 1995, *Numerical Solution of Partial Differential Equations: An Introduction*, Cambridge University Press, Cambridge UK

Müller, TM & Gurevich, B 2004, ‘One-dimensional random patchy saturation model for velocity and attenuation in porous rocks’ *Geophysics*, vol. 69, pp. 1166–1172.

Müller, TM & Gurevich, B 2005a, ‘A first order statistical smoothing approximation for the coherent wave field in random porous media’, *Journal of the Acoustical Society of America*, vol. 117, pp. 1796-1805.

Müller, T.M, & Gurevich, B 2005b, ‘Wave-induced fluid flow in random porous media: Attenuation and dispersion of elastic waves’, *Journal of the Acoustical Society of America*, vol. 117, pp. 2732-2741.

Müller, T.M, Lambert, G & Gurevich, B 2007, ‘Dynamic permeability of porous rocks and its seismic signatures’, *Geophysics*, vol.72, pp. E149-E158.

Müller, T.M, & Rothert, E 2006, ‘Seismic attenuation due to wave-induced flow: Why Q in random structures scales differently’ *Geophysical Research Letters*, vol. 33, No. 16, pp. L16305.

Müller, T.M, Toms-Stewart, J, & Wenzlau, F 2008 ‘Velocity-saturation relation for partially saturated rocks with fractal pore fluid distribution’ *Geophysical Research Letters*, In Press

Murphy, WF 1982, ‘Effects of partial water saturation on attenuation in Massilon sandstone and Vycor porous glass’, *Journal of the Acoustical Society of America*, vol. 71, pp. 1458-1468.

Murphy, WF 1984, ‘Acoustic measures of partial gas saturation in tight sandstones’, *Journal of Geophysical Research*, Vol. 89, No. B13, pp. 11549-11559.

Murphy, WF 1985, ‘Sonic and ultrasonic velocities: theory versus experiment’, *Geophysical Research Letters*, vol. 12, pp. 85-88.

Murphy, WA, Winkler, KW & Kleinberg, RA 1986 ‘Acoustic relaxation in sedimentary rocks- Dependence on grain contacts and fluid saturation’, *Geophysics*, vol. 51, pp. 757-766.

Nagy, PB, Alder, L & Bonner, BP 1990 ‘Slow wave propagation in air-filled porous materials and natural rocks’, *Applied Physics Letters*, vol. 56, pp. 2504-2506.

Norris, AN 1993, ‘Low-frequency dispersion and attenuation in partially saturated rocks’, *Journal of the Acoustical Society of America*, vol. 94, pp. 359-370.

O’Brien, J 2004, ‘Seismic amplitudes from low gas saturation sands’, *The Leading Edge*, vol 23, pp.1236-1243

Oh, W & Lindquist, WB 1999, ‘Image thresholding by indicator kriging’, *IEEE Transactions on Pattern Analysis and Machine Intelligence*, vol. 21, pp. 590-602.

Olafuyi, AO, Sheppard, AP, Arns, CH, Sok, RM, Cinar, Y, Knackestedt, MA & Pinczewski, WV 2006, ‘Experimental investigation of drainage capillary pressure using digitized tomographic images’, *Society of Petroleum Engineering*, 99897.

Orsi, TH & Anderson, A 1999, ‘Bulk density calibration for X-ray tomographic analyses of marine sediments’, *Geo-Marine Letters*, vol. 19, pp. 270-274.

Özdenvar, T & McMechan, GA 1997, ‘Algorithms for staggered-grid computations for poroelastic, elastic, acoustic, and scalar wave equations’, *Geophysical Prospecting* vol. 45, pp. 403-420.

Paterson, L & Lupton, G 2003, Laboratory notes, CSIRO Petroleum, Unpublished.

Palmer, ID & Traviola, ML 1980 ‘Attenuation by squirt flow in undersaturated gas sands’, *Geophysics*, vol. 45, pp. 1780-1792.

Peyton, RL, Haeffner, BA, Anderson, SH & Gantzer, CJ 1992, ‘Applying X-ray CT to measure macropore diameters in undisturbed soil cores’, *Geoderma*, vol. 53, pp. 329-340.

Plona, TJ 1980, ‘Observation of a second bulk compressional wave in a porous medium at ultrasonic frequencies’, *Applied Physics Letters*, vol. 36, pp. 259-261.

Pride, SR, Tromeur, E & Berryman, JG 2002, ‘Biot slow-wave effects in stratified rock’, *Geophysics*, vol. 67, pp. 271–281.

Pride, SR & Berryman, JG 2003a, ‘Linear dynamics of double-porosity and dual-permeability materials. I. Governing equations and acoustic attenuation’, *Physical Reveiw E*, vol. 68, pp. 036603.

Pride, SR & Berryman, JG 2003b, ‘Linear dynamics of double-porosity and dual permeability materials. II. Fluid transport equations’, *Physical Reveiw E*, vol. 68, pp. 036604.

Pride, SR, Berryman, JG & Harris, JM 2004 ‘Seismic attenuation due to wave-induced flow’, Journal of Geophysical Research, vol. 109, No. B1, B01201.

Pride, SR, Gangi, AF & Morgan, FD 1992, ‘Deriving the equations of motion for porous isotropic media’, *Journal of the Acoustical Society of America*, vol. 92, pp. 3278-3290.

Pride, SR, Morgan, FD & Gangi, AF 1993 ‘Drag forces of porous-medium acoustics’ *Physical Reveiw B,* vol. 47, pp. 4964-4978.

Pride, SR, Gangi, AF & Morgan, FD 1992, ‘Deriving the equations of motion for porous isotropic media’, *Journal of the Acoustical Society of America*, vol. 92, pp. 3278-3290.

Pride, SR, Tromeur, E & Berryman, JG 2002, ‘Biot slow-wave effects in stratified rock’, *Geophysics*, vol. 67, pp. 271–281.

Saenger, EH, Ciz, R, Krüger, OS, Schmalholz, SM, Gurevich, B & Shapiro, SA 2007, ‘Finite-difference modelling of wave propagation on microscale: A snapshot of the work in progress. *Geophysics*, vol. 72, pp. SM293-SM300.

Seidel, L 1874 ‘Über ein Verfahren, die Gleichungen, auf welche die Methode der kleinsten Quadrate führt, sowie lineare Gleichungen überhaupt, durch successive Annäherung zu lösen’, *Abh. Bayer. Akademie der Wiss. Math. Nat. Kl.* 11, 1874

Sengupta, M & Mavko, G 2003, ‘Impact of flow simulation parameters on saturation scales and seismic velocity’, *Geophysics* ,vol 68, 1267-1280.

Sengupta, M, Mavko, G & Mukerji, T 2003, “Quantifying subresolution saturation scales from time-lapse seismic data: A reservoir monitoring case study’, *Geophysics* ,vol 68, 803-814.

Shepp, LA & Logan, BF 1974, ‘Reconstructing interior head tissue from X-ray transmissions’, *IEEE Transactions on Nuclear Science*, vol. NS-21, pp. 228-236.

Silberman, EJ 1957, ‘Sound velocity and attenuation in bubbly mixtures measured in standing wave tubes’, *Journal of the Acoustical Society of America*, vol. 29, pp. 925-933.

Silverstein, DL & Fort, T 2000, ‘Prediction of air-water interfacial air in wet unsaturated porous media’, *Langmuir*, vol. 16, pp. 829-834.

Silverstein, DL & Fort, T 2000, ‘Incorporating low hydraulic conductivity in a numerical model for predicting air-water interfacial area in wet unsaturated particulate porous media’, *Langmuir*, vol. 16, pp. 835-838.

Silverstein, DL & Fort, T 2000, ‘Prediction of water configuration in wet unsaturated porous media’, *Langmuir*, vol. 16, pp. 839-844.

Smeulders, DMJ & van Dongen, MEH 1997, ‘Wave propagation in porous media containing a dilute gas-liquid mixture: theory and experiments’, *Journal of Fluid Mechanics*, vol. 343, pp. 351-373.

Smith, TM, Sondergeld, CH & Rai, CS 2003, ‘Gassmann fluid substitutions: A tutorial’, *Geophysics*, vol. 68, pp. 430-440.

Sneddon, IN 1957 *Elements of partial differential equations*, McGraw Hill, New York

Thomas, JW 1995 ‘Numerical partial differential equations: Finite-difference Methods’ *Texts in Applied Mathematics Number 22*, Springer, New York

Toms, J, Müller, TM, Ciz, R & Gurevich, B 2006, ‘Comparative review of theoretical models for elastic wave attenuation and dispersion in partially saturated rocks’, *Soil Dynamics and Earthquake Engineering*, vol. 26, pp. 548-565.

Toms, J, Müller, TM & Gurevich, B 2007, ‘Seismic attenuation in porous rocks with random patchy saturation’, *Geophysical Prospecting*, vol. 55, pp. 671-678.

Toms, J, Müller, TM, Gurevich, B, & Johnson, DL 2006, ‘Attenuation and dispersion in partially saturated porous rock: Random vs Periodic Models’, *68th EAGE Conference, Expanded Abstracts*, Vienna

Toms, J, Müller, TM, Gurevich, B, & Johnson, DL 2007, Acoustics of Random Patchy Saturation: *69th EAGE Annual Conference, Expanded Abstracts,* London

Toms-Stewart, J, Müller, TM, Gurevich, B, & Paterson, L 2008, ‘Statistical characterization of gas patch distributions in partially saturated rocks‘, submitted *Geophysics*

Torquato, S 2002, *Random Heterogeneous Materials: Microstructure and Macroscopic Properties*, Springer Verlag, New York

Torquato, S & Beasley, JD & Chiew, YC 1988, ‘Two-point cluster function for continuum percolation’, *Journal of Chemical Physics*, vol. 88, pp.6540-6547

Torquato, S & Stell, G 1985, ‘Microstructure of two-phase random media. V. The n-point probability functions for inpenetrable sphere’, *Journal of Chemical Physics*, vol. 82, No. 2, pp. 980-987.

Trefethen, LN 1982, ‘Group velocity in finite-difference schemes’, *SIAM Review*, vol. 24, pp113-136.

Tserkovnyak, Y & Johnson, DL 2002, ‘Can one hear the shape of a saturation patch’, *Geophysical Research Letters*, vol. 29, pp. 1108-1112.

Tserkovnyak, Y & Johnson, DL 2003, ‘Capillary forces in the acoustics of patchy-saturated porous media’, *Journal of the Acoustical Society of America*, vol. 115, pp. 2596-2606.

Turner, ML, Knüfing, L, Arns, CH, Sakellariou, A, Senden, TJ, Sheppard, A.P, Sok, RM, Limaye, A, Pinczewski, WV, & Knackstedt, MA 2004, ‘Three dimensional imaging of multiphase flow in porous media’, *Physica A*, vol. 339, pp. 166-172.

van Wijngaarden, L 1972, ‘One dimensional flow of liquids containing small gas bubbles’ *Annual Review of Fluid Mechanics*, vol. 4, pp. 369-396.

Vinegar, HJ & Wellington, SL 1986, ‘Tomographic imaging of three-phase flow experiments’, *Review of Scientific Instruments*, vol. 58, pp. 96-107.

Vogelaar, B & Smeulders, DMJ 2007, ‘Seismic attenutation models for partially saturated media’, *Abstract for London 2007,69th EAGE Conference and Exhibition*

Wang, Z 2001, ‘Fundamentals of seismic rock physics’, *Geophysics*, vol. 66, pp. 398-412.

Waterman, PC & Truell, R 1961, ‘Multiple scattering of waves’, *Journal of Mathematical Physics*, vol. 2 (4), pp.512 – 537.

Weissberg, HL 1963, ‘Effective diffusion coefficient in porous media’, *Journal of Applied Physics*, vol. 34, pp. 2636-2639

Wellington, SL & Vinegar, HJ 1987, ‘X–ray computerized tomography’, *Journal of Petroleum Technology*, vol. 39(8), pp. 885-898.

White, JE 1975, ‘Computed seismic speeds and attenuation in rocks with partial gas saturation’, *Geophysics*, vol. 40, pp. 224-232.

White, JE, Mikhaylova, NG & Lyakhovitskiy, FM 1976, ‘Low-frequency seismic waves in fluid-saturated layered rocks’, *Physics of the Solid Earth* (Transl. Izv.) vol. 11, pp. 654-659.

Winkler, K 1985, ‘Dispersion analysis of velocity and attenuation in Berea sandstone’, Journal of Geophysical Research, vol. 90, pp. 6793-6800.

Withjack, EM, Devier, C & Micheal, G 2003, ‘The role of X-ray computed tomography in core analysis’ *Society of Petroleum Engineering,* 83467.

Wood, AB 1941, *A textbook of sound,* Bell, London

Yamakawa, N 1962, ‘Scattering and attenuation of elastic waves’, *Geophysical Magazine*, (Tokyo), vol. 31, pp. 63-97.

Yeong, CLY & Torquato, S 1998a, ‘Reconstructing random media’, *Physical Review E,* vol. 57, pp. 495- 506.

Yeong, CLY & Torquato, S 1998b, ‘Reconstructing random media II, Three dimensional media from two-dimensional cuts’, *Physical Review E,* vol. 58, pp. 224-233.

Young, DM 1954, ‘Iterative methods for solving partial difference Equations of Elliptic Type’ *Transactions of the American Mathematical Society*, Vol 76, pp. 92

Zhou, MW & Sheng, P 1989, ‘First-principles calculations of dynamic permeability in porous media’ *Physical Review B*, vol. 39, pp. 12027-12039.